THERMAL SIGNATURES OF SKIN LESIONS USING COMPUTATIONAL THERMAL MODELING AND MEDICAL INFRARED IMAGING

by
Akanksha Bhargava

A dissertation submitted to Johns Hopkins University in conformity with the requirements for the degree of Doctor of Philosophy

Baltimore, Maryland

October, 2016

© 2016 Akanksha Bhargava
All Rights Reserved

Abstract

Infrared (IR) thermography is a valuable quantitative diagnostic tool that allows for non-invasive, accurate measurement of skin temperature variations in the presence of a lesion. Modeling the underlying thermal and physiological processes within the body offers excellent potential for improving the thermographic measurement system design and developing more exact, quantitative assessment criteria. Using computational modeling and infrared imaging experiments, this dissertation investigates the thermal signatures of lesions of varying geometrical and physiological characteristics.

We first performed a comprehensive sensitivity analysis of the computed skin temperatures in order to understand the relationships between healthy skin temperatures and the underlying thermophysical processes and tissue properties. These functional relationships provide a foundation for interpreting steady state and transient thermal signatures of skin lesions. We developed a computational thermal model for a heel deep tissue injury (DTI) to allow for an early thermographic detection and assessment capability for DTIs. The DTI models were used to develop thermographic measurement strategies and quantitative staging criteria that can be employed in a clinical setting. We analyzed the infrared images of various vascular tumors and pigmented skin lesions acquired from patient studies, using the combined white light-infrared image processing approaches. Our quantitative thermal analysis of lesions of different physiological characteristics, sizes, locations and depths will facilitate quantitative assessment and interpretation of other skin lesion thermographic images. A better understanding of the thermal behavior of skin

lesions, gained using computational modeling and infrared imaging experiments in this study, can contribute to the advanced use of quantitative infrared imaging in medical diagnostic applications.

Primary Reader: Cila Herman

Secondary Reader: Robert Ivkov

Tertiary Readers: Dmitri Artemov and Michael E. Thomas

Acknowledgements

First and foremost, I would like to thank my advisor, Dr. Cila Herman. This research journey would not have been possible without her guidance, support and presence. I am truly grateful to her for giving me the freedom to work on different topics and imparting valuable career skills to me.

I would like to thank the members of my thesis committee, Dr. Robert Ivkov, Dr. Dmitri Artemov and Dr. Michael Thomas for their valuable feedback on the thesis. I appreciate the feedback on image processing and thermal modeling from Dr. Arjun Chanmugam and clinical imaging support from Dr. Bernard Cohen and Dr. Annie Grossberg that have helped make this work successful. I would like to acknowledge the efforts of Dr. Müge Pirtini Çetingül in collecting imaging data of pigmented skin lesions.

I am thankful to the members of the Heat Transfer Lab, Tze-Yuan Cheng, Rajeev Hatwar, Xinrong You, Sri Kamal Kandala, Jinchen Tang and Yan Zhou, for their intellectual contributions in projects related to this dissertation. Special thanks to all my friends, especially Leen Alawieh, Parastou Eslami, Jasim Sadique, Kaushik Sampath, Prakruti Hoskere, Sarita Koride, Neha Dixit, Vijay Vedula, Princy Parsana, Anand Malpani, Siddharth Mahendran, Vishwa Parekh, Pooja Chaudhary and Amod Jog for making my stay in Baltimore enjoyable.

I appreciate the financial support provided for this research from the Department of Mechanical Engineering at the Johns Hopkins University, National Science Foundation, the Alexander and Margaret Stewart Trust through the Cancer Center of the Johns Hopkins University, and National Institutes of Health NCI Grant.

Lastly, I would like to thank my family: my parents, Sanjeev Bhargava and Sarita Bhargava, my brother, Suvrat Bhargava, my sister-in-law, Sakshi Braroo and my partner and best friend, Vikas Arya for being a great source of inspiration and encouragement during this journey. I would not have been able to complete it without your immerse love and support.

To Ma, Pa, Bhai and Vikas

Contents

List of figures

List of Tables

Chapter 1 Introduction

1.1 Background

The association between abnormal body surface temperature and disease has long been recognized in medicine [1]. Medical thermometers were introduced in the 17th century, however, the association between elevated body temperature and fever was recognized much earlier by the early physicians [1, 2]. A skin lesion (a tumor or an injury of the skin or the underlying tissue) changes the surrounding tissue temperature that may cause the skin surface temperature to increase or decrease, thereby leading to a thermal signature associated with that lesion [3]. The abnormality in tissue temperature may be due to abnormal blood flow and metabolic activity associated with the lesion, or abnormal vessel morphology and lack of homeostasis control, or due to a host of other physiological processes such as inflammation, ischemia, etc. [4]. The spatial and temporal variations of skin temperature can be measured accurately and non-invasively at high resolution using modern infrared (IR) imaging cameras [4, 5]. This temperature measurement capability has led to considerable efforts into using IR imaging for medical diagnostics and assessment purposes [6]. However, the lack of insights into the underlying thermal and physiological processes in the tissue can lead to ambiguous or inaccurate interpretations and diagnosis, which is one of the reasons for IR imaging being avoided or underutilized in the clinic. To address this challenge, this dissertation aims to improve the understanding of how skin temperature is influenced by the thermal and physiological processes within the underlying

tissue layers and apply this knowledge to enhance the thermographic detection and assessment capability for a variety of skin lesions and subcutaneous lesions.

Skin is the largest organ of the human body and it exhibits a heterogeneous multilayered physiological and thermal structure [7]. To model skin temperature, the superficial 10-20 mm thick tissue, encompassing the lesion and the surrounding healthy tissue, is considered as the region of interest in this study [8]. Depending on lesion location, size and the clinical application, a larger region of interest can be easily accommodated using the methodology described in the dissertation. This region consists of an avascular epidermis layer, a highly vascularized dermis layer and a subcutaneous region comprising of the fat, muscle and bone layers. The transport of heat from deep tissue to the skin surface is maintained by thermal conduction coupled with complex physiological processes such as blood flow (perfusion) and metabolism (heat generation) [4]. Therefore, the relevant thermophysical properties and physiological parameters for heat transport within tissue layers are: thermal conductivity, density, specific heat, blood perfusion rate (net rate of heat transport between tissue and flowing blood), metabolic heat generation rate (volumetric heat generation rate due to tissue metabolism). Each layer is described by a different set of the aforementioned properties, making tissue a complex thermal system. The physiological variations among different body locations and individuals [8-12] add further complexity to the mathematical description of the system, as these variations could potentially affect interpretations of the thermal model and the diagnostic accuracy or.

The objectives of this dissertation are threefold. **The first aim** is to conduct a sensitivity analysis of skin temperatures, with respect to the thermophysical properties affecting skin temperature, computed using the thermal model of healthy tissue. In order

to reduce model complexity and gain increased understanding of the biophysical system of the skin, we model and quantify the effects of different thermophysical parameters on the healthy skin temperature, identify important parameters of the model and test the variability of healthy skin temperature to changes in the most important inputs. These functional relationships will serve as a foundation for the understanding of measurement uncertainties, interpreting thermal signatures of skin lesions and improving the IR measurement system design for skin lesion diagnosis.

Infrared (IR) thermography is a valuable quantitative diagnostic tool that allows for non-invasive, accurate measurement of skin temperature variations in the presence of a lesion [5]. An IR camera detects the electromagnetic radiation emitted from a surface (skin) in the infrared region of the spectrum (0.7-1000μm wavelength range) [4] and transforms the measured signal into a 2D greyscale image. The corresponding color-coded temperature map of the surface is obtained by using appropriate calibration [13]. Over the last two decades, IR imaging technology has dramatically improved due to the advances in IR camera instrumentation, such as the introduction of focal plane arrays, new coolant materials and uncooled detectors, as well as the use of computer vision and image processing algorithms for IR image analysis [14]. IR imaging can be performed passively (to measure steady state temperature) or actively (to measure the transient thermal response of the skin to an external forcing such as heating or cooling) [15]. The technological advances in instrumentation led to a considerable amount of effort focused on using IR imaging in medical diagnostics and assessment, during the past decade [6]. IR imaging was used for the assessment of arthritis [6], peripheral neuropathy [16-19], vascular disorders [20], wound healing [21], thermoregulation [22], diagnosis of skin tumors [15, 20, 23-26],

burns [27], shoulder impingement syndrome [28] and evaluation and monitoring of flap surgery [29].

The second aim of this dissertation is to facilitate IR imaging based early detection capability for deep tissue injuries (DTIs), which are serious pressure injuries of the skin and the underlying tissue [30]. Early detection of DTIs is necessary to reduce mortality and morbidity among pressure ulcer patients and decrease financial and human burdens associated with these injuries [31, 32]. Early detection of DTIs is challenging because the injury starts to develop in the deep tissue layers and may remain invisible to the naked eye until substantial damage to the underlying tissue has already occurred [33]. While researchers have been attempting to develop thermographic techniques for the assessment of pressure injuries for almost four decades, they faced challenges associated with seemingly inconsistent skin temperature data (thermal signatures showed both skin temperature increase and decrease) that they could not explain [34]. The computational thermal models of DTI developed in this dissertation account for the pathophysiological processes associated with DTI damage, and they are extremely useful by allowing to gain insights into the seemingly inconsistent thermal signatures reported in previous studies. In addition to this, modeling skin temperature changes associated with DTIs provides data necessary for the design of an IR imaging measurement system for quantitative, objective detection and characterization of DTIs in early stages.

The third and final aim of this dissertation is to initiate a catalog of thermal and color signatures of skin lesions. A systematic catalog of IR and white light images of different lesions encountered in clinical practice would provide an invaluable training tool for clinicians using IR imaging in practice. Current methods for assessment of lesion color

rely on the subjective color and appearance interpretation of clinicians [35, 36]. In this study, we introduce objective, digital image processing tools for the analysis of lesion color. Clinical IR image analysis tools are needed for quantitative assessment of growth and regression of lesions and evaluation of treatment response for long term monitoring and evaluation. Current IR image analysis approaches for assessment of vascular tumors suffer from subjective interpretation and reliance on single point measurements [20, 26, 37, 38]. Single point measurements only provide reference values for large lesions such as infantile hemangiomas, which exhibit significant temperature variations across the lesion. These variations can be associated with pathophysiological processes within the lesion and single point measurements are ineffective for lesions that demonstrate rapid changes in size and vascularity over the course of their lifecycle [39]. A collection of thermal signatures would serve as a reference database for the studies attempting to use quantitative infrared imaging for evaluation and assessment of skin lesions. This dissertation contributes to the catalog of thermal signatures by including IR and white light images of infantile hemangioma, port-wine stain, venous malformation, junctional dysplastic nevus, and compound dysplastic nevus.

1.2 Organization of the thesis

Using computational thermal modeling and quantitative infrared imaging, we address the aforementioned aims organized in the following chapters

Chapter 2: Sensitivity analysis of healthy skin temperature

The goal of this chapter is to better understand the behavior of the steady state skin temperature and the transient thermal response of skin to cooling. We performed a

comprehensive sensitivity analysis to quantify the relationships between healthy skin temperature and the parameters of the underlying tissue layers. The analysis provides a basis for interpreting the steady state and transient thermal signatures of skin lesions as well as an insight into the magnitude of possible temperature variations caused by the uncertainties in property data and their impact on measurement uncertainties in clinical applications of IR imaging. A systematic analysis of the transient thermal response to skin cooling with respect to the skin layers and their properties is invaluable to applications of dynamic IR imaging and the development of sensitive quantitative IR diagnostic techniques.

Chapter 3: Heat transfer model for deep tissue injuries (DTIs) – a step towards an early thermographic diagnostic capability

In order to explain the inconsistent temperature findings associated with DTIs in prior studies and to advance the use of IR imaging for early DTI detection and characterization, we developed a computational thermal model of a heel DTI. The model accounts for the pathophysiological processes during tissue damage and can explain the diverse thermal signatures of DTIs observed in prior thermographic studies. Using our model, based on both computed results and clinical observations, we introduced new and more accurate clinical thermal staging for DTI lesions. This novel staging can serve as a means to evaluate the severity of the DTI injury and determine management strategies for the injury. Additionally, our thermal model, coupled with inverse reconstruction techniques, demonstrated the feasibility of using IR imaging for estimating the depth, size and blood perfusion rate of DTIs.

Chapter 4: Quantitative assessment of infantile hemangioma using combined infrared and white-light imaging

The research objective is to analyze the steady state thermal signatures and color signatures of infantile hemangioma lesions obtained from infrared and white light images acquired from patient studies. We quantitatively assessed the extent of subcutaneous involvement for different morphological types of infantile hemangiomas (superficial, deep and mixed); interpreted the thermal signatures in terms of their vascular activity during proliferation, plateau and involution phases; quantified the color differences by comparing the color of the hemangioma lesion with the surrounding healthy skin color; and developed a dimensionless temperature difference formulation for comparing IR images captured at different times during longitudinal studies.

Chapter 5: Thermal signatures of skin lesions

The aim of this chapter is to provide an atlas of thermal signatures of vascular and pigmented skin lesions. We selected lesions varying in physiological characteristics, sizes and depths. The collection will facilitate the analysis and interpretation of other vascular anomalies, pigmented lesions and soft tissue injuries.

Chapter 6: Conclusions

This chapter summarizes the knowledge and experience gained from previous chapters and addresses the prospects of quantitative infrared imaging for the assessment and evaluation of skin lesions.

Chapter 2 Sensitivity analysis of healthy skin temperature

Overview

The aim of this chapter is to perform a comprehensive sensitivity analysis of healthy skin temperature with respect to tissue thermophysical properties and layer thicknesses. With a focus on medical applications of infrared imaging, our analysis includes sensitivities of both steady state skin temperature and the dynamic thermal recovery of the skin from a cooling excitation. In section 2.1, we introduce sensitivity analysis as a tool to address the model response to variation of input parameters. Prior sensitivity analysis studies for bioheat transfer models are reviewed in section 2.1. In section 2.2, we first develop the mathematical model for simulating skin temperatures during steady state, cooling and subsequent thermal recovery. Next, we use the computed skin temperatures to evaluate the sensitivities. Computed results for skin temperature sensitivities to relevant tissue parameters are discussed for the steady state and transient cases in section 2.3.

The key contributions from this portion of this study are: (1) insights into the thermal behavior of the skin during steady state and transient thermal recovery from a cooling excitation and the relationships between healthy skin temperatures and thermophysical properties and thicknesses of tissue layers, (2) insights into why transient thermal recovery of skin from a cooling excitation is a better indicator of the underlying physiology compared to steady state skin temperature, (3) identification of the most important and least important tissue properties for skin temperature assessment, (4)

improved insight into the impact of uncertainties in thermophysical properties on surface temperature distributions to help assess the uncertainties in data interpretation.

2.1 Introduction

Heat transfer in living tissue and skin tissue is a complex process. The heat exchange between the skin surface and the underlying tissue takes place through the combined effects of thermal diffusion, blood perfusion, metabolic heat generation and thermal interactions between the skin and its surroundings [4]. A deviation from the normal physiological functioning, caused by a disease or an injury, is accompanied by changes in body temperature, which can also affect the temperature of the skin [40]. For example, deep tissue injury lesions that exhibit tissue ischemia cause skin temperature decrease [34]. Malignant melanoma lesions require increased blood supply to the lesion that causes skin temperature increase [41]. A better understanding of the relationships between skin surface temperatures and associated physiological variables can provide insights into the complex thermal behavior of the skin and serve as the foundation for the interpretation of thermal images captured in a clinical setting.

The analysis of spatial and temporal distribution of the skin tissue temperature is central to thermal diagnostic applications of infrared imaging and thermal treatments involving skin tissue [3, 42, 43]. Computational thermal models are a convenient means to study the thermal behavior of the biophysical system of the skin and develop understanding of the thermal behavior of skin in the presence of a tumor or an injury. For example, heat transfer models of hyperthermia can provide detailed understanding of the thermal response of the tumor and the surrounding healthy skin to local thermo-stimulation, in order to develop criteria for effective thermal dose delivery [44-46]. Similarly, thermal

models of lesions are used to develop IR image based diagnostic and assessment criteria for lesions [8, 41].

Skin tissue has a heterogeneous multilayered structure [7]. The thermophysical properties vary within tissue layers, from one body location to another and from one individual to another [7, 9, 11, 47]. The skin layer thicknesses also show location-dependent variations [7, 47]. Additionally, accurate property data for some locations may not be available, as measurements of thermophysical properties of the human tissue are difficult to perform [11, 12] and property values can exhibit individual variations. In most of the thermal models involving the skin, the computational domain is represented as a multilayered structure, in which each layer is characterized by average data for thermophysical properties and thicknesses. The thermal characteristics of each layer contribute to the heat transport process and other physiological processes associated with blood flow and metabolic heat generation. Owing to the heterogeneous tissue structure and non-uniform tissue properties, the skin temperature depends on a large number of thermophysical parameters, which we will call input parameters in the sensitivity analysis. The uncertainties in the input parameters (due to individual or physiological variations or errors in measurement data) add further complexity to the model, as they could potentially affect the accuracy of diagnosis/interpretations of the thermal model. In order to reduce model complexity and gain an understanding of the thermal behavior of healthy skin tissue, we modeled and quantified the effects of different input variables on the healthy skin temperature, identified important input variables of the thermal model of the skin and tested the variability of healthy skin temperature to variations in the most significant inputs.

The manner in which a model output depends on the input parameter values can be studied using sensitivity analysis, which is a tool widely used in various disciplines, including control engineering [48], chemistry [49, 50] and environmental modeling [51]. The nature of the sensitivity analysis can be global (where model behavior is addressed for wide ranges of inputs) or local (where attention is focused on behavior near a specific point in the parameter space or a nominal operating point) [52]. Local parametric sensitivities are easier to compute, have a relatively low computational cost and can be compared across different parameters [52].

Using the local measure, the sensitivity of a model output Y to a parameter x_1 is the rate of change of Y with respect to x_1, expressed mathematically as dY/dx_1. Local sensitivity analysis can be used to (1) establish quantitative relationships between a model output (skin surface temperature) and an uncertain input, (2) address model behavior with respect to these inputs and (3) identify the most sensitive or important input parameters of the model [49, 53]. The local, partial derivative based sensitivity measures can be computed using the direct method (where the differential equations for the sensitivities are solved simultaneously with the model) or by applying the one-factor-at-a time (OAT) method (where the sensitivities are obtained from the computed model output using finite difference approximations) [49]. In this study, we used the OAT method to perform sensitivity analysis with respect to thermophysical properties and thicknesses of tissue layers for steady state skin temperature as well as for the dynamic thermal response of the skin to a cooling excitation.

Some form of sensitivity analysis has been performed on bioheat transfer models prior to this study for optimizing thermal treatment processes [46, 54-56], identifying

important parameters for burn injuries [10, 57-59] and improving thermographic diagnosis of lesions [41, 60]. Skin tissue exhibits a complex thermal process that involves many tissue layers and their thermal and physiological characteristics. However, prior studies addressed the influence of only a subset of these characteristics in their models. Some studies used global methods such as analysis of variance (anova), however they did not address the variations in thermophysical properties in individual layers of the tissue. Using the Taguchi design of experiments, Jamil and Ng [46] demonstrated that the electromagnetic parameters are the most important design parameters affecting hyperthermia treatment. Using a seven parameter based anova design, Ng [58] demonstrated that low metabolic heat generation, subcutaneous blood perfusion rates and low ambient temperature can yield better results for clinical thermographic assessment of breast cancer lesions. Ng et al [58] analyzed the sensitivity of thermal damage caused by a burn injury with respect to eight parameters using the anova design. Blood perfusion rate of the dermis layer, heat transfer coefficient and heating temperature were found to be significant parameters affecting skin temperature in a burn injury. Liu [54] adopted partial derivative based approach to calculate the uncertainties in temperature predictions resulting from uncertain parameters for a hyperthermia model. However, their study used a single-layered tissue model and did not apply the method to transient temperature distributions [54]. Jasinski [55] performed transient sensitivity analysis of the model for a thermal injury using an injury dependent blood perfusion term. Thus, the focus of prior studies was on limited number of properties specific to the bioheat application. A comprehensive sensitivity analysis of the healthy skin temperature with respect to thermophysical properties and layer thicknesses of all tissue layers has not been carried out. The current

study attempts to fill the gap by evaluating sensitivities of both steady state skin temperature and the transient thermal response to skin cooling. We used a 6 layered thermal model of the skin consisting of epidermis, papillary dermis, reticular dermis, fat, muscle and bone and focused on the influence of thermophysical properties, such as thermal conductivity, specific heat, density, blood perfusion rates and metabolic heat generation rates, as well as layer thicknesses.

The objective of the sensitivity analysis in this dissertation is to (1) identify the most important thermophysical properties and layer thicknesses of the model, (2) compare the steady state sensitivities with the sensitivities of the dynamic thermal response and (3) demonstrate that large variations in the most input parameters lead to small skin temperature changes. It should be noted that, that the current study assumes that the tissue thermophysical properties are constant over the timescale of interest and do not change with temperature for the investigated temperature ranges which are relatively small (10-37°C). In the context of thermoregulation mechanisms, the blood perfusion rates may be modified when the skin is subjected to a mild cooling excitation [61], however, at this stage of the study these feedback mechanisms are neglected and will be considered in future research.

2.2 Method

In sections 2.2.1 and 2.2.2, we develop the mathematical model and the numerical model for computing steady state healthy skin temperatures and thermal recovery of the skin surface from a cooling excitation and provide model validation. In section 2.2.3, we first explain the partial derivative based sensitivity analysis method, using a simple function of two input variables. Next, we apply this method to our healthy skin tissue model

in section 2.2.4. Using the skin temperatures computed in section 2.2.1, we derive the formulations for skin temperature sensitivities, both for the steady state and transient situations.

2.2.1 Mathematical model and simulation method

The general bioheat equation is the most commonly used representation of the spatial and temporal temperature distribution in human skin tissue [7]. It was first introduced by Pennes in 1948 [62] in the following form

$$\rho c \frac{\partial T}{\partial t} = \nabla \cdot (k \nabla T) + \omega \rho_b c_b (T_b - T) + \dot{q}, \tag{2.1}$$

where $T(x, y, z, t)$ is the tissue temperature (K), a function of location and time, ρ the tissue density (kg/m^3), c the specific heat (J/kg·K), k the thermal conductivity (W/m·K), ω the blood perfusion rate (m^3/s per m^3 of the tissue), $\dot{q}$ the rate of metabolic heat generation (W/m^3), ρ_b the blood density (kg/m^3), c_b the blood specific heat (J/kg·K), and T_b the arterial blood temperature (K). The term on the left hand side represents the rate of change of change of thermal energy stored in a unit tissue volume. It is equal to the sum of the rates at which the thermal energy enters or leaves the control volume in a unit time due to heat conduction, heat exchange between the blood and the tissue, and tissue metabolism. Equation 2.1 assumes that the blood enters the differential control volume at a given rate ω at temperature T_b [62]. The rate of heat transfer between the blood and the tissue is proportional to the volumetric blood perfusion rate and the temperature difference between them [62]. Although, numerous studies [7, 63] have suggested modifications to the Pennes bioheat equation to account for variations in vascular geometries and blood temperature,

the model described by Equation 2.1 is widely applied to understand temperature distribution in human tissue [3, 7].

The temperature distribution in the tissue $T(x, y, z, t)$ for a given geometry and application is determined by solving Equation 2.1 for the appropriate set of boundary conditions. To account for the heat loss from the skin due to radiation, evaporation and convection, Deng and Liu and Wilson [3] and Wilson and Spence [8] incorporated these terms in the energy balance equation at the skin surface. To evaluate different skin cooling methods for dynamic thermographic detection of lesions, Cheng and Herman [64] used different boundary conditions at the skin surface in their thermal model: - constant temperature cooling (cooling by high heat capacity cooling patch), contact cooling (cooling using a water-soaked cotton patch) and convective cooling (blowing cold air over the skin). To account for tissue heating during a thermal treatment process, heat source terms are added either on the right hand side of the bioheat equation for volumetric heating or accommodated by the appropriate boundary condition for surface heating [7].

In this study, the general model described by Equation 2.1 is modified to accommodate the physical situation illustrated schematically in Figure 2.1(a). Since the dominant temperature variations develop in the direction perpendicular to the skin surface, the general bioheat equation, Equation 2.1 can be simplified by considering a single spatial dimension *y*, reducing it to a one-dimensional (1D) model. The 1D computational domain for the heat transfer model is shown in Figure 2.1(b). The domain has six subdomains, one subdomain for each of the tissue layers from Figure 2.1(a). The nodes represent the layer interfaces. For simplicity, we assumed that the thermophysical properties to be temperature-independent for the investigated temperature range which is relatively small

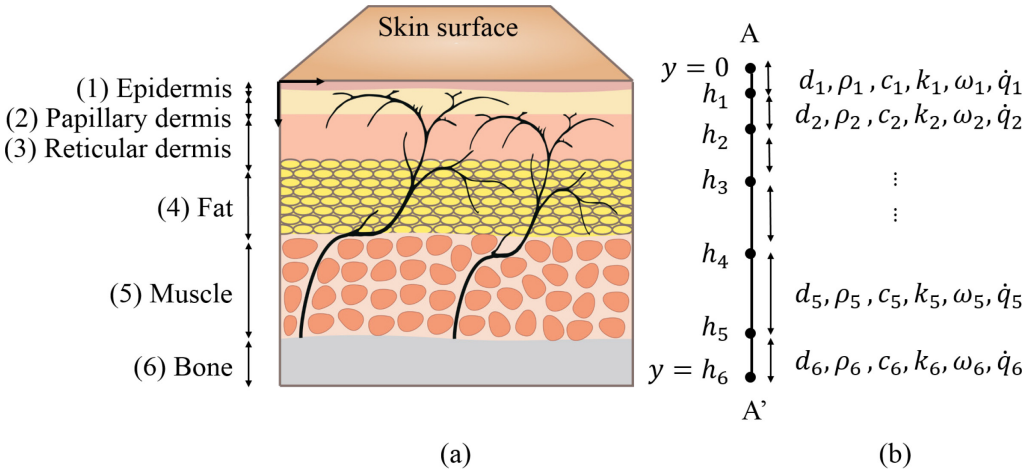

Figure 2.1 Schematic of the skin tissue: (a) Cross section of the skin illustrating the tissue layers and the blood vessels, (b) simplified 1D computational domain for the skin used in the simulations. The subscripts 1 to 6 refer to the tissue layers. Each layer is characterized by a thickness d, density ρ, specific heat c, thermal conductivity k, blood perfusion rate ω and metabolic heat generation rate $\dot{q}$. The symbol h represents the location of the interfaces.

(10 - 37°C). The blood density, specific heat and temperature are also assumed to be constant. The property and thickness data for the tissue layers used in the models are summarized in Table 2.1. The range of physiological property variations and the corresponding average value for each property that is used in the computations are also provided in Table 2.1.

A set of six coupled bioheat equations (one equation for each of the six layers)

$$\rho_n c_n \frac{\partial T(y,t)_n}{\partial t} = \mathrm{k_n} \frac{\partial^2 T(y,t)_\mathrm{n}}{\partial^2 \mathrm{y}} + \omega_\mathrm{i} \rho_b c_b (T_\mathrm{b} - T(y,t)_n) + \dot{q}_n \qquad (2.2)$$

$h_{n-1} < y < h_n, h_0 = 0$ and $n = 1, 2, ..6$

is solved to obtain the temperature distribution $T(y,t)$ in the computational domain. Equation 2.2 is solved by imposing appropriate initial and boundary conditions at the skin surface (topmost node, node 0, in Figure 2.1(b)) and the bottom node, node 6, and the

continuity conditions for temperature and heat flux at each layer interface. The continuity for temperature is given by

$$T_n(y = h_n, t) = T_{n+1}(y = h_n, t) \qquad n = 1,2,3,4,5 \tag{2.3}$$

and the continuity of heat flux is described as

$$-k_n \frac{\partial T_n(y = h_n, \mathrm{t})}{\partial y} = -k_{n+1} \frac{\partial T_{m+1}(y = h_n, \mathrm{t})}{\partial y} \quad n = 1,2,3,4,5 \tag{2.4}$$

Equations 2.3 and 2.4 are satisfied at all times at the layer interfaces. The bottom-most node ($\mathrm{y} = \mathrm{h}_6$) is maintained at a constant core body temperature at all times as

$$T(\mathrm{y} = h_6, t) = 37℃. \tag{2.5}$$

We aim to solve for the steady state temperature distribution as well as for the transient thermal response of the skin tissue to a cooling excitation. The solution is obtained in three steps: (1) compute the steady state temperature distribution with the skin surface exposed to ambient conditions (t =0), (2) apply cooling for a short duration ($0 < t < t_c$) and (iii) compute the thermal recovery of the tissue as a function of time after the removal of cooling load and exposing the skin to ambient conditions. The thermal boundary conditions for the top and bottom nodes of the computational domain during these steps are illustrated in Figure 2.2. In step 1, we assumed a convective boundary condition as

$$q'' = h_\infty(T(\mathrm{y} = h_0, t) - T_\infty), \quad t < 0 \text{ and } \ t > t_c \tag{2.6}$$

with an ambient temperature of $T_\infty = 22℃$ and a convective heat transfer coefficient, $h_\infty = 12\ W/m^2 \cdot K$ for the steady state conditions. The skin surface ($\mathrm{y} = \mathrm{h}_0$) is exposed to these ambient conditions before the beginning of skin cooling ($t < 0$) (Figure

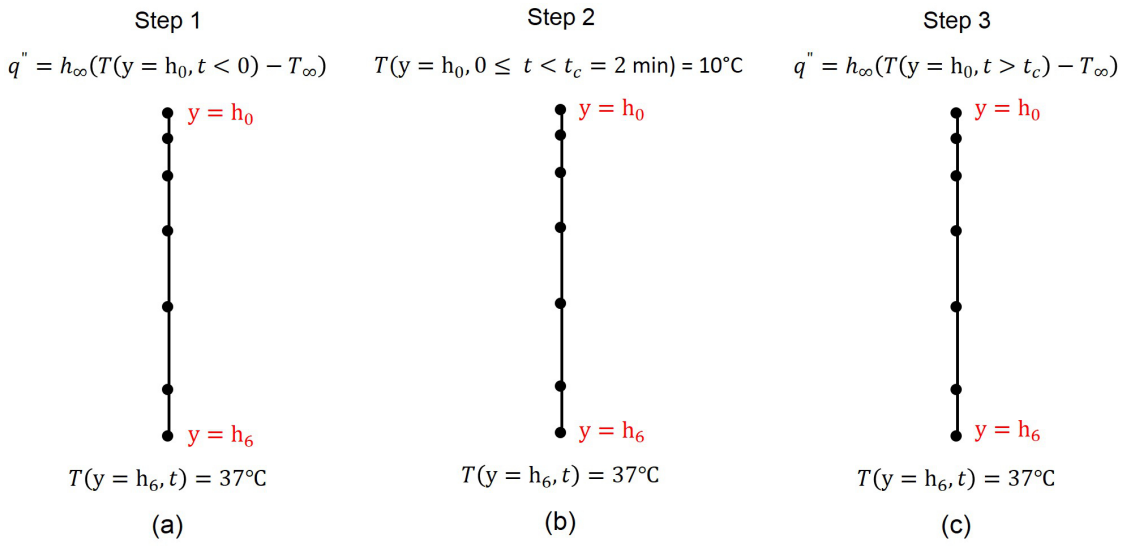

Figure 2.2 Thermal boundary conditions at the top ($y = 0$) and bottom ($y = h_6$) nodes of the computational domain used for computing (a) steady state temperatures in step 1, (b) temperatures during skin cooling in step 2 and (c) transient thermal recovery temperatures in step 3. $T_\infty = 22°C$, $h_\infty = 12\ W/m^2 \cdot K$, $t_c = 2$ min.

2.2(a)) and after the removal of cooling load ($t > t_c$) (Figure 2.2(c)). Steady state temperatures were computed by solving Equations 2.2 – 2.6.

In step 2, we applied a constant temperature cooling load on the skin surface (Figure 2.2(b)) as

$$T(y = h_0, t) = 10°C, \quad 0 \leq t < t_c = 2\ \text{min} \tag{2.7}$$

The previously obtained (Step 1) steady state solution was used as the initial condition for the transient cooling process.

Finally in step 3, we computed the transient thermal recovery of the skin tissue from the cooling load. The skin was again exposed to the convective boundary condition (Equation 2.6) (shown in Figure 2.2 (c)) and the temperatures were computed until the skin surface reached its steady state temperature. The computations were carried out using the finite

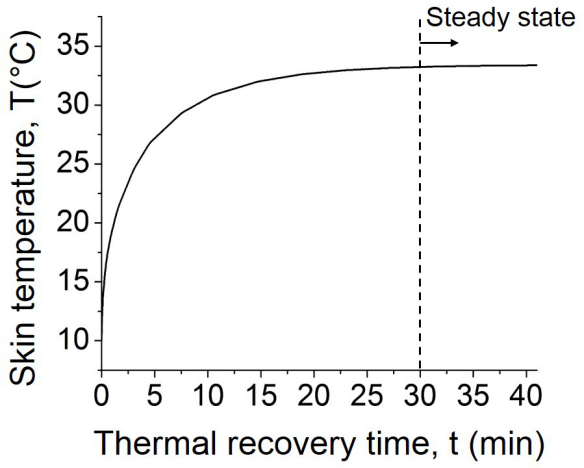

Figure 2.3 Transient thermal recovery of the skin from a cooling excitation (10°C applied for 2 min). The time t = 0 corresponds to the removal of the cooling load and t = 40 min corresponds to the end of the thermal recovery, the time when the skin surface has regained its steady state temperature of 33°C.

element software COMSOL Multiphysics v4.4a. To verify the convergence with respect to the mesh size, the smallest element size was set to 0.18mm. The results differed by less than 1% before and after mesh refinement. The convergence of the solution was ensured by setting the time step Δt as 0.1s for cooling and thermal recovery periods. Figure 2.3 shows the temperature as a function of time during the thermal recovery, computed by solving Equations 2.2 to 2.7 for the average values of the tissue properties summarized in Table 2.1.

2.2.2 Model validation

The multi-layered model for healthy skin considered in this study is based on the heat transfer model of skin tissue introduced [41] and validated experimentally by Çetingül and Herman [5] and Cheng and Herman [64]. Çetingül and Herman [5] demonstrated a good agreement between model predictions for healthy skin temperature and measurement data obtained in a clinical study. In this section, we compare our model predictions for the

temperature distribution in a single-layered tissue (with properties: $k = 0.185$ W/m·K, $\omega =$

Table 2.1 Tissue thermophysical properties and thicknesses used in the simulations. Property data are taken from Centigul and Herman [41] unless otherwise stated

Tissue layer	Thermal conductivity, $\boldsymbol{k}$			Blood perfusion, $\boldsymbol{\omega}$ $(\times \mathbf{10^{-3}})$			Metabolic heat generation rate, $\dot{\boldsymbol{q}}$			Specific heat capacity, $\boldsymbol{c}$			Density, $\boldsymbol{\rho}$			Layer Thickness, $\boldsymbol{d}$		
	W/m·K			$m^3/ m^3·s$			W/m^3			J/kg·K			Kg/m^3			mm		
	Avg	Min	Max	Avg	Min	Max	Avg	Min	Max	Avg	Min	Max	Avg	Min	Max	Avg	Min	Max
Epidermis	0.23	0.21	0.26	0	0	0	0	0	0	3589	3578	3600	1200	1080	1320	0.26	0.03	0.50
Papillary Dermis	0.44	0.37	0.52	1.9	0.20	3.6	368	276	460	3300	3200	3400	1200	1080	1320	1.1	0.5	1.7[a]
Reticular dermis	0.44	0.37	0.52	1.9	0.20	3.6	368	276	460	3300	3200	3400	1200	1080	1320	1.1	0.5	1.7[a]
Fat	0.18	0.16	0.21	0.05	0	0.1	368	276	460	2674	2288	3060	1000	900	1100	5.0	2.0	8.0[a]
Muscle	0.50	0.45	0.56	5.7	0.5	10.9	684	513	855	3790	3770	3810	1085	976.5	1193.5	7.5	6.0	10[a]
Bone	0.4[b]	0.24[c]	0.56[c]	0[b]	0[c]	0[c]	0[b]	0[c]	0[c]	1300[b]	1105[c]	1495[c]	1030[b]	927[c]	1133[c]	3.0[b]	1.8	4.2[a]

a [91]
b [34]
c - assumption

0.5e^{-4} 1/s, $\dot{q}$ = 368 W/m^3, d = 7.5 mm, ρ_b= 1060 kg/m^3, c_b= 3770 J/kg·K and T_b= 37°C) against the analytical solution obtained for the 1D thermal model, subjected to the same boundary conditions. The steady state, 1D analytical solution for a single-layered tissue is derived below. For a tissue domain of thickness d under steady state conditions, Equation 2.2 for n = 1 reduces to

$$k\frac{\partial^2 T}{\partial^2 y} + \omega\rho_b c_b(T_b - T) + \dot{q} = 0 \quad 0 \le y \le d\,. \tag{2.8}$$

The boundary condition for the skin surface ($y = 0$) is

$$-k\frac{\partial T}{\partial y}\Big|_{y=0} = h_\infty\big(T|_{y=0} - T_\infty\big). \tag{2.9}$$

The boundary condition for the bottom surface (core) ($y = d$) is

$$T|_{y=d} = 37℃ \tag{2.10}$$

To obtain an analytical solution, we substitute $\theta = T_b - T$ and $\xi = (d - y)/d$ into Equations 2.8 -2.10. Equation 2.8 reduces to

$$\frac{\partial^2\theta}{\partial^2\xi} - \gamma^2\theta = \phi \quad 1 \ge \xi \ge 0 \tag{2.11}$$

where $\gamma = d\sqrt{\omega\rho_b c_b/k}$ and $\phi = d\sqrt{\dot{q}/k}$. The general solution of Equation 2.11 is

$$\theta = C_1\cosh\gamma\xi + C_2\sinh\gamma\xi - \phi/\gamma^2 \tag{2.12}$$

The boundary condition at the skin surface ($\xi = 1$) (Equation 2.9) becomes

$$\frac{k}{d}\frac{d\theta}{d\xi}\Big|_{\xi=1} = h(T_b - T - \theta|_{\xi=1}) \tag{2.13}$$

The boundary condition at the bottom boundary ($\xi = 0$) (Equation 2.10) becoms

$$\theta|_{\xi=0} = 37°\text{C} \tag{2.14}$$

Solving Equation 2.11 with Equations 2.12 and 2.13 yield C_1 and C_2 as

$$C_1 = \frac{\phi}{\gamma^2} \tag{2.15}$$

$$C_2 = \frac{h\left((T_b - T_\infty) + \frac{\phi}{\gamma^2}\right) - \frac{\phi}{\gamma^2}((k\gamma/d)\sinh(h\gamma) + h\cosh(h\gamma))}{(k\gamma/d)\cosh(h\gamma) + h\sinh(h\gamma)} \tag{2.16}$$

Figure 2.4 shows that the model prediction obtained using Comsol matches the analytical solution exactly. Based on results of the experimental validation from previous studies [5, 64] and the good agreement with the simple analytical model presented in this section, we conclude that our model represents the biophysical system of the skin with good fidelity.

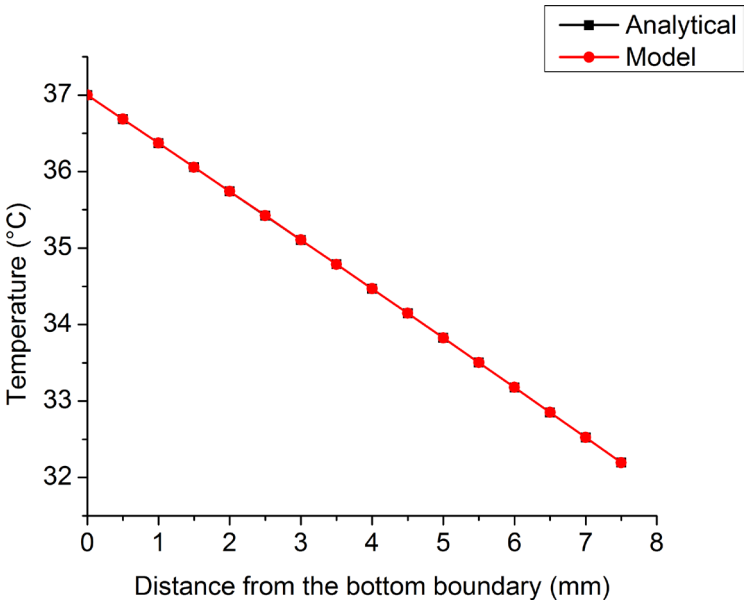

Figure 2.4 Comparison of the computational model prediction with analytical solution for the1D bioheat model of a single–layered tissue

2.2.3 Sensitivity analysis method

In this study, we used the one-factor-at-a-time (OAT) method of sensitivity analysis [65, 66]. The OAT approach refers to determining parameter sensitivities by varying each input variable of the model independently, while holding the remaining variables fixed at their nominal values. The ratio of the change in the model output to the change in the model input, while other input variables remain fixed, is used as the sensitivity measure [65, 66].

Figure 2.5 conceptualizes the OAT approach of computing the sensitivities in the form of partial derivatives. The method is illustrated using a two input parameter model, $Y = f(x_1, x_2)$. In our study the input parameters are the thermophysical properties of the tissue layers (30 properties) and layer thicknesses (6 layers). The output Y is the skin surface temperature $T(y,t)$ in our model. The large number of parameters affecting the thermal behavior of the system makes the problem very complex and serves as the motivation for identifying the most important input parameters that will determine the thermal response of the system. The influence of the model inputs x_1 and x_2 on the output Y is illustrated by the surface plot in Figure 2.5. Let $Y = Y^*$ be the nominal response, when the input parameters are fixed at their nominal values (NVs), given by $x_1 = x_1^*$ and $x_2 = x_2^*$. The nominal values in our system are the average values of the thermophysical properties and tissue layer thicknesses listed in Table 2.1. The sensitivities of Y to x_1 and x_2 at their nominal values can be expressed in terms of the partial derivatives $\partial Y/\partial x_1$ and $\partial Y/\partial x_2$, respectively [48] by sensitivity coefficients S_{x_1} and S_{x_2} as

$$S_{x_1} = \left.\frac{\partial Y}{\partial x_1}\right|_{x_1^*, x_2^*}, \; S_{x_2} = \left.\frac{\partial Y}{\partial x_2}\right|_{x_1^*, x_2^*}, \tag{2.17}$$

as illustrated in Figure 2.5. To compute S_{x_1}, the nominal value of x_1 is varied by a small amount Δx_1 around $x_1$while x_2 is fixed at x_2^* . Then the resulting effect on the output Y is calculated. The sensitivity $S_{x_1} = \left.\frac{\partial Y}{\partial x_1}\right|_{x_1^*, x_2^*}$ is the magnitude of the slope of a tangent (shown by the red line in Figure 2.5) that points in the direction of increasing values of x_1 and meets the output surface at the point $(x_1^*,\ x_2^*)$. This slope is also the ratio of the change in Y due to a small change in x_1 and therefore is the sensitivity measure of Y with respect to x_1. Similarly, the value for S_{x_2} is the effect of changing x_2 by a small amount Δx_2 on the output Y, while x_1 is fixed at x_1^*. In order to compare the effects of different inputs (whose values may differ by orders of magnitudes), relative or normalized sensitivity coefficients are used [48]. The normalization is done by multiplying the sensitivity coefficients (Equation 2.17) by the ratio of the nominal value of the input to the nominal values of the output. The normalized sensitivities $\bar{S}_{x_1}$ and $\bar{S}_{x_2}$ are calculated as

$$\bar{S}_{x_1} = \left.\frac{x_1^*}{Y^*}\frac{\partial Y}{\partial x_1}\right|_{x_1^*, x_2^*}, \qquad \bar{S}_{x_2} = \left.\frac{x_2^*}{Y^*}\frac{\partial Y}{\partial x_2}\right|_{x_1^*, x_2^*} \tag{2.18}$$

In the skin temperature model (Equations 2.2 – 2.7) there are a total of 36parameters, consisting of a set of five thermophysical properties (ρ_n, c_n, k_n, ω_n, $\dot{q}_n$) and a thickness value d_n in the y direction, for each of the six constituent layers ($n = 1, \dots, 6$). The values of these properties are listed in Table 2.1. The average values of the input parameters (skin properties), used to compute skin temperatures, will be used as the nominal values. We are interested in computing two kinds of sensitivities: (1) steady state sensitivities (using steady state temperatures as the model output) and (2) transient sensitivity functions (using transient thermal recovery of skin surface as the model output). The steady state and transient skin temperature sensitivities lay foundations for interpreting

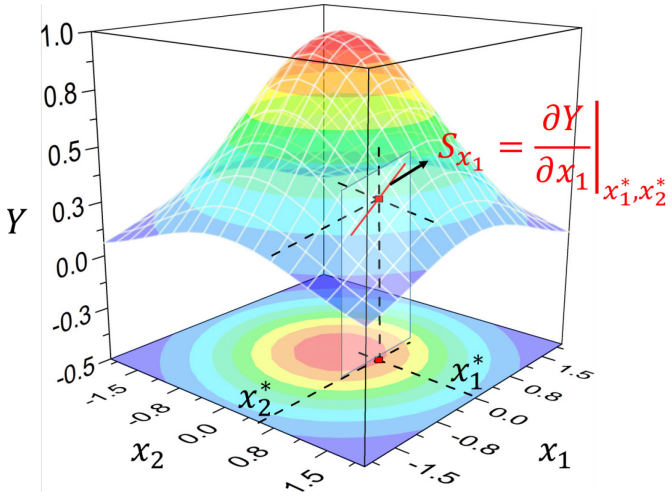

Figure 2.5 Illustration of the OAT method of sensitivity analysis. The sensitivity of the model outout Y with respect to an input paramter x_1 is the partial derivative $\partial Y/\partial x_1$, computed at the nominal value (x_1^*, x_2^*) in the input parameter space.

steady state and transient thermal signatures of lesions in Chapters 3-5. Table 2.1 shows that the input parameters for the skin temperature model differ by orders of magnitudes. Therefore, we will use normalized sensitivities to express the sensitivity measures of skin temperatures to thermophysical properties and thicknesses.

2.2.4 Computation of sensitivities of skin temperature

In this section, we apply the OAT method of sensitivity analysis to our thermal model of the skin. Let the vector β consist of the thirty six input parameters of the skin tissue model.

$$\beta = [\rho_{i=1\ldots6}, c_{i=1\ldots6}, k_{i=1\ldots6}, \omega_{i=1\ldots6}, \dot{q}_{i=1\ldots6}, d_{i=1\ldots6}] \tag{2.19}$$

Let $\beta^* = [\rho_i^*, c_i^*, k_i^*, \omega_i^*, \dot{q}_i^*, d_i^*]$ represent the nominal values of the inputs (shown in Table 2.1), where i = 1,…,6 denote the tissue layers. The independent effect of an input on the

model output can be derived by expanding the model output using Taylor series in terms small increments of the input. For example, the independent effect of the blood perfusion rate can be derived by expanding the skin temperature T using Taylor series, in terms of small increments $\pm\Delta\omega$ around the nominal value ω^*, while other inputs are fixed at their nominal values β^* as

$$T(t, \beta_1^*, \ldots \omega^* + \Delta\omega, .., \beta_{36}^*) = T^*(t, \beta^*) + \frac{\partial T(t)}{\partial \omega}\Big|_{\beta^*} \Delta\omega + \frac{1}{2}\frac{\partial^2 T(t)}{\partial^2 \omega}\Big|_{\alpha^*} (\Delta\omega)^2 + .. \quad (2.20)$$

and

$$T(t, \beta_1^*, \ldots \omega^* - \Delta\omega, .., \beta_{36}^*) = T^*(t, \beta^*) - \frac{\partial T(t)}{\partial \omega}\Big|_{\beta^*} \Delta\omega + \frac{1}{2}\frac{\partial^2 T(t)}{\partial^2 \omega}\Big|_{\alpha^*} (\Delta\omega)^2 - .. \quad (2.21)$$

In Equations 2.20 and 2.21, $T^* = T\,(t, \beta_j^*)$ denotes the nominal value of the skin temperature computed for the nominal value β^* by solving Equations 2.2 to 2.7. By summing Equations 2.20 and 2.21, we get a measure of $S_\omega(\mathrm{t})$, which is the sensitivity of skin temperature $T(t)$ to the blood perfusion rate ω. We used the central difference finite difference scheme for calculating the partial derivatives of skin temperatures with respect to the thermophysical properties and tissue layer thicknesses. The sensitivity is expressed in terms of a second order accurate partial derivative, $\partial T/\partial\omega$, computed at β^*as

$$S_\omega(\mathrm{t}) = \frac{\partial T(t)}{\partial \omega}\Big|_{\beta^*} \approx \frac{T\,(t, \beta_1^*, .., \omega^* + \Delta\omega, .., \beta_{36}^*) - T\,(t, \beta_1^*, .., \omega^* - \Delta\omega, .., \beta_{36}^*)}{2\Delta\omega} \quad (2.22)$$

The resulting change in skin temperature, $\Delta T(℃)$ to a small change $\Delta\omega$ of the blood perfusion rate ω^* is determined as

$$\Delta T(\mathrm{t}) = \Delta\omega S_{\omega}(\mathrm{t}) \tag{2.23}$$

According to Equation 2.3, a positive sensitivity value means that the input increases the skin surface temperature and a negative sensitivity means that the input decreases the skin surface temperature. In this study, we will present the skin temperature sensitivities in the normalized form (Equation 2.18), which is a more relevant form allowing quantitative comparisons between inputs whose nominal values differ by orders of magnitudes. The normalized sensitivity, $\bar{S}_{\omega}(\mathrm{t})$, for the blood perfusion rate is

$$\bar{S}_{\omega}(\mathrm{t}) = \frac{\omega^*}{T^*(t)} \frac{\partial T(t)}{\partial \omega}\Big|_{\beta^*} \tag{2.24}$$

The temperatures on the right hand side of Equation 2.22 are obtained by solving Equations 2.2 to 2.7. First, the nominal skin temperature value $T^* = T\ (t, \beta_j^*)$ is obtained by keeping all inputs fixed at their nominal values. In the next step, the skin temperature calculations are repeated for the values $\omega = \omega^* + \Delta\omega$ and $\omega = \omega^* - \Delta\omega$ (where $\Delta\omega = 0.1\omega$), while the rest of the parameters remain fixed. The sensitivities of the steady state temperature are obtained by substituting the steady state skin temperatures (from Equations 2.2 – 2.6) into Equations 2.22 – 2.24. The sensitivities of the transient thermal recovery of the skin (shown in Figure 2.3) are obtained by substituting transient skin temperatures (from Equations 2.2 – 2.7) in Equation 2.22 and Equation 2.24. The sensitivity coefficient was calculated at each time instant. This process is repeated for all thirty six input parameters (Equation (2.19) to obtain the sensitivities of steady state and transient skin temperatures.

2.3 Results and discussion

In this section, we evaluate the sensitivities of the steady state temperature and the dynamic thermal response (thermal recovery from a cooling excitation) of the skin. By ranking the normalized sensitivities in the order of their absolute values, we identify the most important tissue layers and thermophysical properties for the steady state thermal model. The sensitivity analysis of the dynamic thermal response is performed considering 24 inputs (the epidermis and the bone were not included as they were the least important layers for the steady state thermal model). The independent effects of ρ, c, k, ω, $\dot{q}$ and d on the dynamic thermal response are compared with the corresponding effects on the steady state skin temperature. For the transient skin temperatures, we also considered the sensitivities to the interactions between thermal conductivity, k, and specific heat, c, of the layers, to account for the effect of thermal diffusivity, $\alpha = k/\rho c$. The sensitivities are presented in the form of mixed partial derivatives, $\partial^2 T/\partial k \partial c$.

2.3.1 Sensitivity analysis of steady state skin temperature

We computed the sensitivity of steady state skin temperature to each of the 36 input parameters using Equation 2.24, by considering a change of 10% in the nominal value. In order to compare the effects of thermophysical properties on steady state skin temperature, we plot the normalized sensitivities in Figure 2.6. A positive sensitivity coefficient indicates that the skin temperature increases by increasing the parameter (shown by $\bar{S}_k$ in Figure 2.6(a), $\bar{S}_\omega$ in Figure 2.6(b) and $\bar{S}_{\dot{q}}$ in Figure 2.6(c)). The effects of metabolic heat generation rates (Figure 2.6(c)) on steady state temperature were an order of magnitude

smaller ($\bar{S}_{\dot{q}} \sim 10^{-3}$) than the effects of the blood perfusion rates and thermal conductivities ($\bar{S}_k \sim 10^{-2}$, $\bar{S}_\omega \sim 10^{-2}$).

A negative sensitivity coefficient indicates that skin temperature decreases by increasing the parameter. The thicknesses of the epidermis, fat and bone layers, all of which have either low or no perfusion, showed negative sensitivity values (Figure 2.6(d)). The

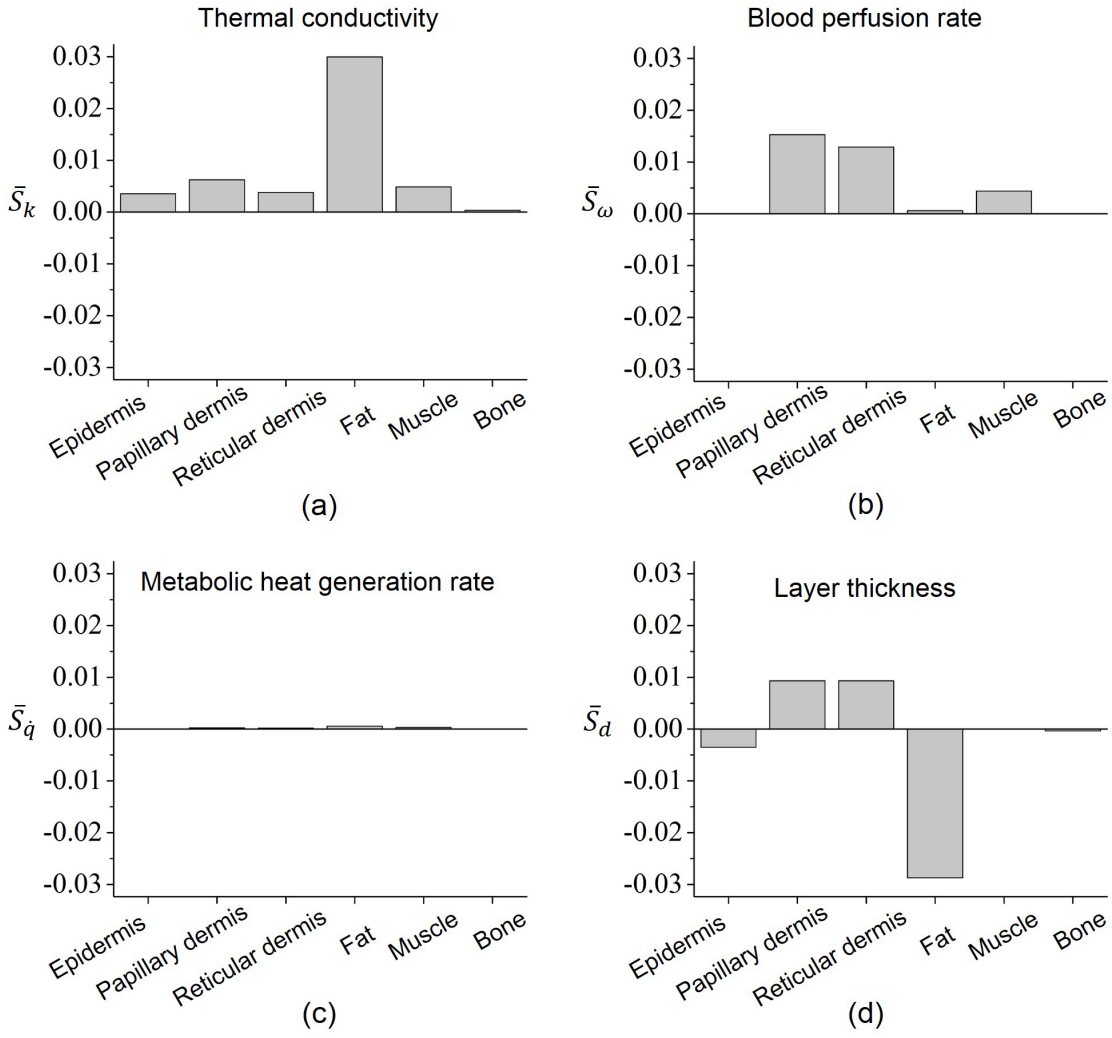

Figure 2.6 Sensitivity of the steady state skin temperature to (a) thermal conductivities, $\bar{S}_k$, (b) blood perfusion rates, $\bar{S}_\omega$, (c) metabolic heat generation rates, $\bar{S}_{\dot{q}}$, and (d) thicknesses, $\bar{S}_d$ of the epidermis, papillary dermis, reticular dermis, fat, muscle and bone.

thicknesses of the reticular dermis and papillary dermis, which are highly vascular, showed positive sensitivities. Increasing the muscle layer thickness did not affect the steady state skin temperature. Very small sensitivities to tissue densities, $\bar{S}_\rho \sim 10^{-13}$ and specific heats, $\bar{S}_c \sim 10^{-13}$ (not shown in Figure 2.6) demonstrate that these properties do not affect the steady state skin temperatures, since the rate of change of the energy storage term in the bioheat equation is zero and these properties are simply not present in the steady state mathematical model.

To identify the most important thermophysical properties for the steady skin temperature, we arranged the normalized sensitivities of all 36 inputs by their magnitudes in Figure 2.7(a). The most important parameters are the thermal conductivity of the fat layer, blood perfusion rates of dermis layers and the fat layer thickness. The least important thermophysical properties are the specific heats and densities. Overall, thermal and physiological processes of the epidermis and bone layers affected the skin temperature by the least amount (Figure 2.7(a)).

To compare the order of magnitude of effects on the skin temperature in response to 10% changes in input parameters, we computed steady state skin temperature changes $\Delta T\,(℃)$ using Equation 2.23. The results are shown for all the 30 thermophysical properties in Figure 2.7(b) and the 6 layer thicknesses in Figure 2.7(c). The maximum skin temperature increases of 0.1°C correspond to the fat thermal conductivity variations (Figure 2.7(b)), 0.06°C corresponding to the dermal blood perfusion rates (Figure 2.7(b)), 0.04°C corresponding to the dermal thicknesses (Figure 2.7(c)) and the maximum temperature decrease of 0.1°C is caused by changes of the fat layer thickness (Figure 2.7(c)). These results demonstrate that large variations in the most important parameters

lead to very small variations of the skin surface temperature, which makes IR diagnostic methods quite robust when considering the influence of uncertainties in thermophysical property data and individual variations.

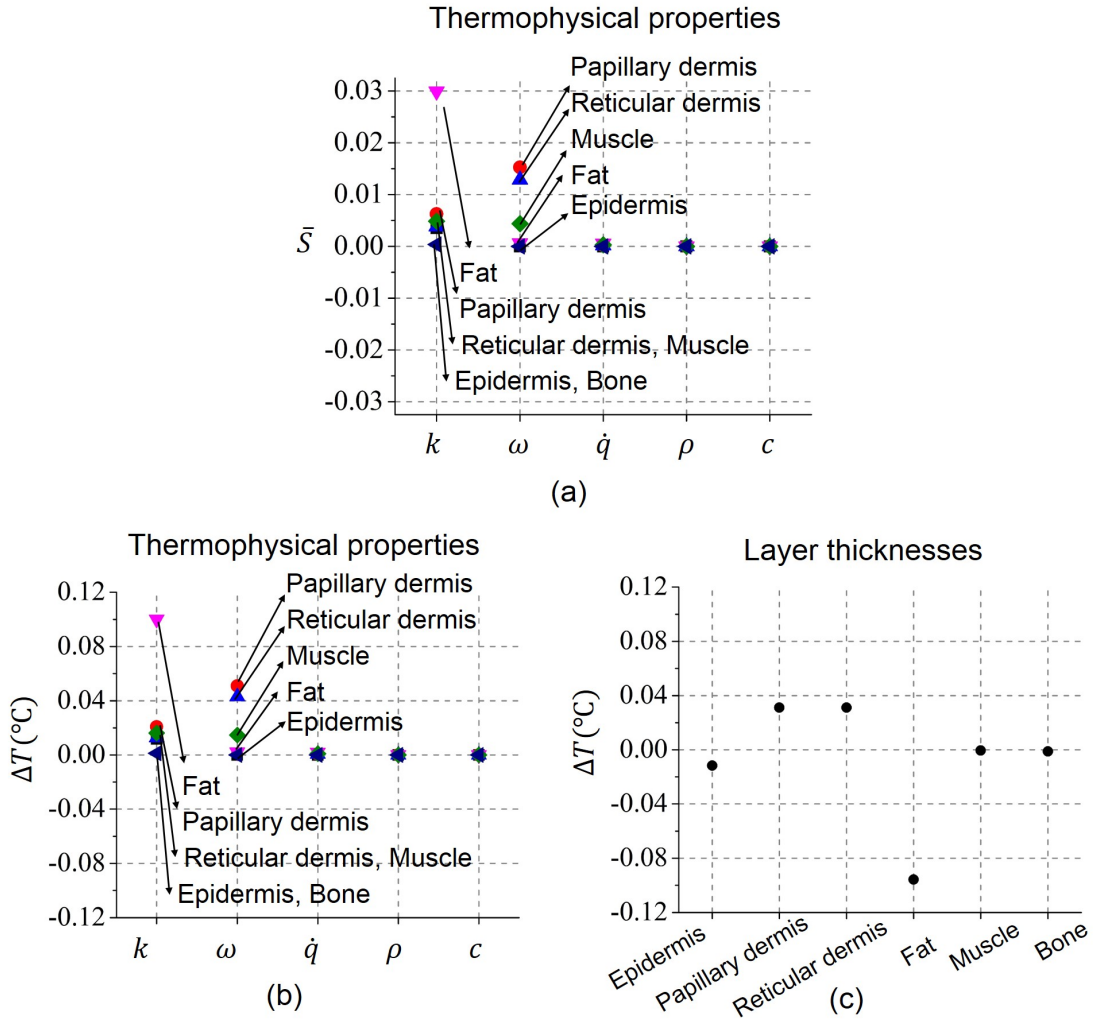

Figure 2.7 Ranking of the steady state skin temperature sensitivities. (a) Steady state sensitivities $\bar{S}$, to thermophysical properties k, ω, $\dot{q}$, ρ and c of all tissue layers. Changes in skin temperature, ΔT(°C), when a change of 10% was made to each of the (b) tissue properties k, ω, $\dot{q}$, ρ, c and (c) tissue layer thicknesses.

2.3.2 Sensitivity analysis of transient thermal recovery of the skin to a cooling excitation

Figure 2.8 shows the transient temperature profiles of different skin layers computed during cooling and subsequent thermal recovery. The temperature of the top-most surface (skin) corresponds to the point at h = 0 in the domain, that was subjected to the cooling stress of 10°C. The temperature of each layer was computed at the mid-thickness point i.e.at h = 0.13 mm for the epidermis, h = 0.8 mm for the papillary dermis, h = 1.9 mm for the reticular dermis, h = 5 mm for the fat layer and h = 9 mm for the muscle. The time t < 0 (shaded grey region) on the abscissa corresponds to a period of 2 mins of constant temperature cooling at 10°C. The time t = 0 coincides with the removal of the cooling load from the top-most surface. Different layers cooled down to different degree under the influence of the cooling stress. The temperature decreased from 34°C to 12°C for the epidermis layer (red), from 34°C to 15°C for the papillary dermis layer (blue), from

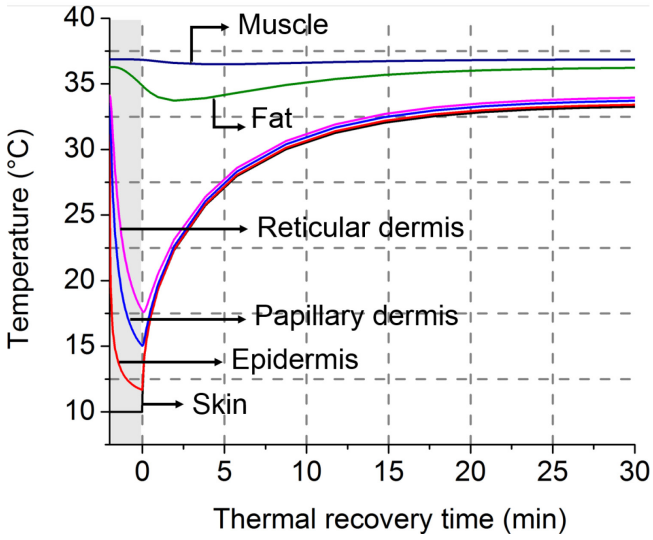

Figure 2.8 Cooling and thermal recovery of skin tissue layers. A constant temperature cooling boundary condition of 10°C was imposed on the skin surface for 2 min (shaded region). The cooling was removed from the skin surface at time t = 0.

34°C to 18°C for the reticular dermis layer (magenta), from 36°C to 35°C for the fat layer (green) and from 36.87°C to 36.83°C for the muscle layer (dark blue). The epidermis and dermis layers started recovering their temperatures at t = 0 (when cooling load was removed). However, the fat (h = 5 mm depth) and muscle (h = 9 mm depth) layers continued to cool down until t = 2 min and t = 5 min respectively, during which the temperatures continued to decrease from 35°C to 34°C (for the fat layer) and from 36.83°C to 35.5°C (for the muscle layer). The continued cooling of the fat and muscle layers is due to the cooling wave that penetrated into the tissue during the cooling period. The differences in the thermal behavior of different skin layers during cooling and thermal recovery can be employed for improving skin cooling techniques for dynamic IR imaging applications. For example, the self-cooling behavior of the fat and muscle layers can be employed in optimizing skin cooling [64] for quantitative dynamic IR imaging of deep tissue injuries [34], to achieve shorter scan times in a clinical setting and improve patient comfort.

The transient sensitivity functions, $\bar{S}(t)$, are plotted as a function of the thermal recovery time, t (t = 0 corresponds to the beginning of the thermal recovery period and t = 40 min is the time to reach steady state) in Figure 2.9. Figure 2.9(a) shows the transient sensitivity functions, $\bar{S}_k(t)$, associated with thermal conductivities of papillary dermis, reticular dermis, fat layer and muscle. Figures 2.9(b) – (d) display the sensitivity functions associated with the densities and specific heats ($\bar{S}_\rho(t)$ and $\bar{S}_c(t)$), blood perfusion rates ($\bar{S}_\omega(t)$) and thickness ($\bar{S}_d(t)$), respectively. The sensitivity functions associated with metabolic heat generation are not shown in Figure 2.9, as they were an order of magnitude smaller (~10^{-3}) than other parameters (~10^{-2}).

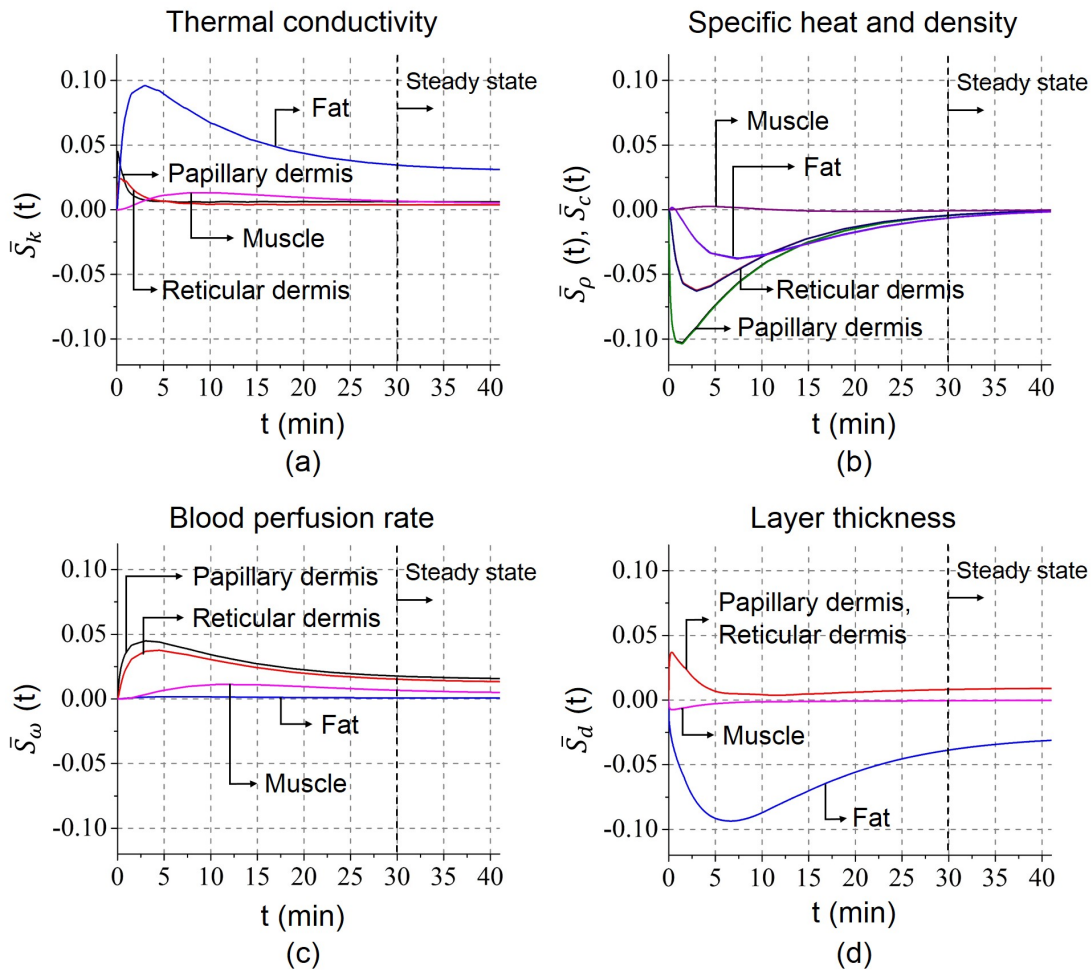

Figure 2.9 Sensitivity of the transient thermal recovery of the skin to variations of (a) thermal conductivities, $\bar{S}_k(t)$, (b) densities and specific heats, $\bar{S}_\rho(t)$ and $\bar{S}_c(t)$, respectively, (c) blood perfusion rates, $\bar{S}_\omega(t)$ and (d) thicknesses, $\bar{S}_d(t)$ of the papillary dermis, reticular dermis, fat and muscle layers.

The absolute values of the transient sensitivity coefficients are larger than the corresponding steady state sensitivities (transient sensitivities reach steady state values by t = 40 min, when skin temperature recovers its steady state), as shown by the maxima/minima during the t = 0 to 30 mins (Figures 2.9(a) – (d)) time interval. Some of the sensitivity functions, e.g. those associated with layer k (Figure 2.9 (a)), ω (Figure 2.9 (c)) and $d_{\text{papillary dermis}}$ and $d_{\text{reticular dermis}}$ (Figure 2.9 (b)), first increase from zero to

reach a maximum and then decrease from the maximum value to their steady state level. The positive values correlate with the increasing effect of these parameters on the steady state skin temperature (Figure 2.6). Other functions, e.g. those associated with layer ρ and c (Figure 2.9 (b)) and d_{fat} and d_{muscle} (Figure 2.9(b), first decrease from zero to a minimum and then increase from the minimum value to the steady state level. Unlike steady state, the transient functions $\bar{S}_{\rho}(t)$ and $\bar{S}_{c}(t)$ are not zero because of the presence of the energy storage term on the left hand side of Equation 2.1. Additionally, the negative values for the layer thickness curves correlate with the effect of the thicknesses of fat and muscle on decreasing steady state skin temperature (Figure 2.6). The larger values of the transient sensitivity coefficients can be explained in the following way: cooling the skin surface increases the temperature gradients across the tissue, which activates different thermal and physiological processes within each tissue layer and leads to an enhanced thermal response of the skin. This means that the thermal recovery of the skin from a cooling excitation is a better, more sensitive indicator of the thermal state of the tissue underneath and provides more information than the steady state skin temperature. Our finding is consistent with the studies showing that the transient thermal response of the skin to cooling can detect very small temperature differences between malignant lesion and healthy tissue, which cannot be measured using static IR imaging [15, 67, 68]. For example, early stage melanoma do not exhibit measureable temperature differences during static imaging, but have a strong thermal signature, suitable for quantitative diagnostic applications, during dynamic imaging [15]. In our previous study [34], we demonstrated that the transient thermal recovery of the skin from a cooling excitation can provide more information about the physiological state of a deep tissue injury (inflammation, ischemia

or a combination of ischemia and inflammation) when compared to steady state skin temperature. The transient sensitivity analysis improves our understanding of the thermal response of healthy skin tissue to skin cooling.

The timing of the maxima/minima for the sensitivity curves associated with a given property varies with the depth of the layer (Figures 2.9(a) – (d)). The peaks for a given property represent its maximum contribution to the increase/decrease of skin temperature during thermal recovery. For all properties (Figures 2.9(a) – (d)), the sensitivity curves associated with the fat and muscle layers showed late maxima/minima (after t = 2 mins), compared to the peaks for the papillary dermis and reticular dermis layers (before t = 2 mins). The differences in the timings of maxima/minima can be tied to the skin cooling results displaying the temperature evolution in the tissue layers as a function of time, as shown in Figure 2.8. The differences in the timing of the minima in Figure 2.8 reflect the observations based on the sensitivity plots. The deeper layers started recovering late from the cooling excitation (t = 2 and 5 mins for the fat and muscle layers vs. t = 0 min for the dermis layers) and, therefore, the maximum contributions from these layers occur late (after t = 2 min) into the thermal recovery. This means that a deep tissue lesion (situated in fat or muscle layers) would present the strongest measurement signal late into thermal recovery (t = 2 to 10 mins from our analysis). A near surface lesion (involving epidermis or dermis layers) would present the strongest measurement signal early (t = 0 to 2 mins). Therefore, the optimum duration for a thermographic scan, that yields the best measurement sensitivity, would vary with the depth of the lesion.

The positive (k, ω and $\dot{q}$) and negative (ρ, c and d) signs for the sensitivities (Figure 2.9(a) – (d)) show that there are competing effects within the tissue that determine the rate

of skin temperature increase during transient thermal recovery. To study the contributions from each layer, we grouped the sensitivity data by tissue layers in Figure 2.10 and Figure 2.11. During rapid increase of skin temperature (first 10 - 30s shown in Figure 2.3), thermal recovery of the skin is mainly a function of dermal thermal conductivity ($\bar{S}_k$) and depends to a lesser extent on dermal perfusion ($\bar{S}_\omega$), specific heat ($\bar{S}_\rho$) and density ($\bar{S}_c$) (Figures

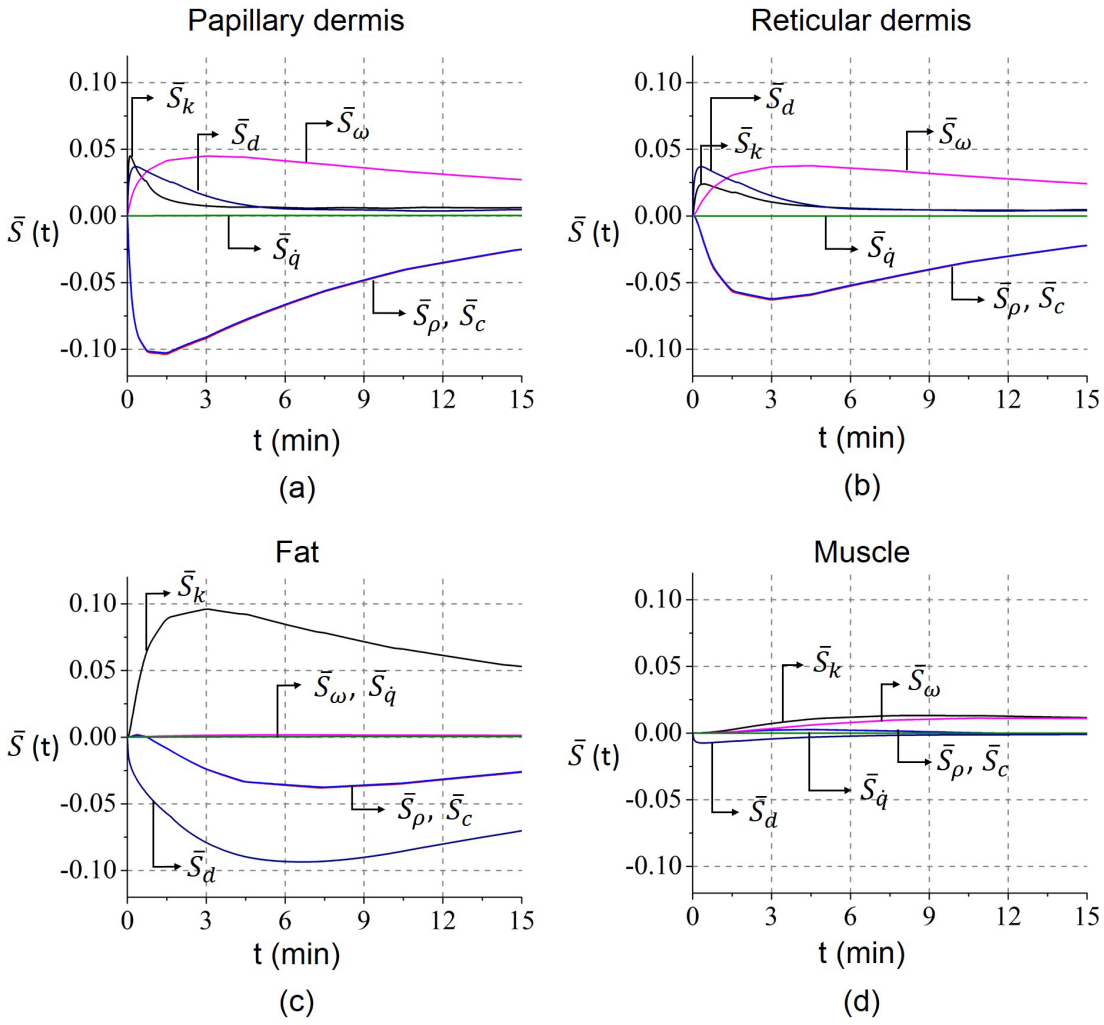

Figure 2.10 Sensitivity of the transient thermal recovery of the skin with respect to the parameters of the (a) papillary dermis, (b) reticular dermis, (c) fat and (d) muscle layer. The sensitivities $\bar{S}_k(t)$, $\bar{S}_\rho(t)$, $\bar{S}_c(t)$, $\bar{S}_\omega(t)$, $\bar{S}_{\dot{q}}(t)$ and $\bar{S}_d(t)$ are shown for each layer.

2.10 (a) and (b)). When the rate of increase is less pronounced (after 30s), the temperature increase is dominated by the effects of dermal perfusion ($\bar{S}_\omega$), specific heat ($\bar{S}_\rho$) and density ($\bar{S}_c$) (Figures 2.10 (a) and (b)). The effect of the metabolic heat generation ($\bar{S}_{\dot{q}}$) is negligible in comparison to other effects (Figures 2.11 (a) and (b)).

The sensitivities to layer thicknesses are shown in to compare the order of magnitude of the effects of thickness with thermophysical properties. The contributions from the fat and muscle layers (Figures 2.10(c) and (d)) appear late into the thermal recovery (due to prolonged cooling experienced by these layers). The contributions of fat perfusion ($\bar{S}_\omega$) and metabolic heat generation ($\bar{S}_{\dot{q}}$) (Figure 2.10(c)) are negligible in comparison to other fat layer parameters (also shown in Figure 2.7). Smaller sensitivity values and flatter maxima/minima of the muscle sensitivity curves (Figure 2.3) can be explained in terms of lesser cooling of the muscle layer in comparison to other layers (Figures 2.10(d)). The contributions from the muscle layer may be increased, for example for detecting a deep lesion of the muscle, by extending the duration of cooling in dynamic IR imaging.

We also analyzed the contributions of the interactions between thermal conductivity k and specific heat c on the transient skin temperature, to account for the effects of layer thermal diffusivities, $\alpha = k/\rho c$ (a measure of the ability to conduct thermal energy relative to the ability to store thermal energy). Each parameter was simultaneously changed by 10% and the skin temperatures were computed for the following four combinations: $(k + \Delta k, c + \Delta c)$, $(k - \Delta k, c - \Delta c)$, $(k + \Delta k, c - \Delta c)$ and $(k - \Delta k, c + \Delta c)$. It should be noted that the thermal diffusivity changes only when the parameters are varied in the opposite directions i.e. for $(k + \Delta k, c - \Delta c)$ and $(k - \Delta k, c + \Delta c)$. The

second order skin temperature sensitivities were expressed in terms of mixed partial derivatives, $\partial^2 T(t)/\partial k \partial c$, using the finite difference approximations for the second-order derivative [69]. When compared to the first order sensitivities (independent effects of the individual parameters), only the fat layer exhibited larger second order effects (interaction effects). From Figure 2.11(c), $(\bar{S}_k(t))$ and $(\bar{S}_c(t))$ varied between -0.1 and 0.1, while $\partial^2 T/\partial k \partial c\ (t)$ varied from -0.35 to 0.35, suggesting that the parameters intensified the

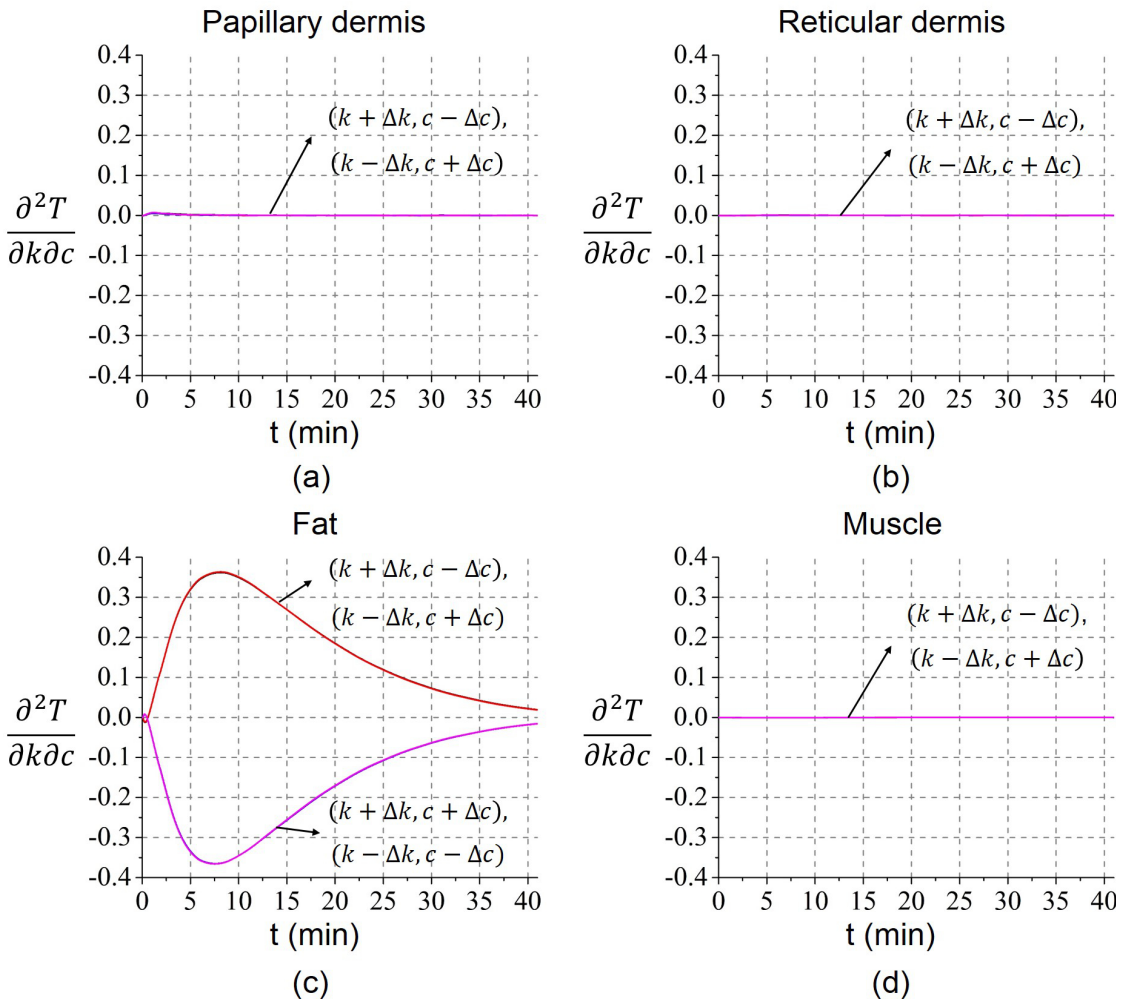

Figure 2.11 Mixed partial derivatives, $\partial^2 T/\partial k \partial c$, showing the effects of interactions between thermal conductivity and specific heat for (a) papillary dermis, (b) reticular dermis, (c) fat and (d) muscle.

effects of each other for the fat layer. For dermis and muscle layers, the changes caused by these parameters cancelled each other, resulting in very small second order the effects for these layers (Figures 2.11 (a), (b) and (d)).

2.3.3 Summary and conclusions

We performed a sensitivity analysis of healthy skin temperature with respect to 36 tissue parameters (30 thermophysical properties and 6 layer thicknesses) in order to gain insights into the complex thermal behavior of the skin tissue. Both steady state skin temperatures (skin was exposed to ambient temperature) and transient thermal recovery of the skin to a cooling excitation were included in the analysis, with an emphasis on medical diagnostic applications of static and dynamic IR imaging (that relies on cooling methods). The partial derivative based normalized sensitivities allowed us to quantify and compare the independent effects of input parameters on skin temperatures. Large variations in the most important tissue parameters (thermal conductivity of the fat layer, blood perfusion rates of dermis layers and the fat layer thickness) had a negligible influence on the computed skin temperatures. Additionally, the metabolic heat generation rate is one of the least important parameters in the thermal model. Larger values of the transient sensitivity coefficients compared to their steady state values demonstrate that the thermal recovery of the skin from a cooling excitation is a better indicator of the thermal state of the tissue underneath and provides more information than the steady state skin temperature. This means that in diagnostic applications of IR imaging, thermal contrasts between lesion and healthy skin can be enhanced by subjecting the skin to cooling. We also analyzed the contributions of the thermal and physiological characteristics of each layer to the transient thermal recovery of the skin, in order to gain insights for improving the dynamic IR

measurement system design. Fat and muscle layers exhibited late onset of thermal recovery (after 2 and 5 minutes, respectively, following the removal of the cooling load) and subsequently, late maxima in the sensitivity curves in comparison to epidermis and dermis layers. This means that a deep tissue lesion (situated in the fat or muscle layers) would present the strongest measurement signal late into thermal recovery (t = 2 to 10 mins in our analysis). A near surface lesion (involving epidermis or dermis layers) would present the strongest measurement signal early (t = 0 to 2 mins in our analysis). Therefore, the optimum duration for a thermographic scan, that gives the best measurement sensitivity, would vary with the depth of the lesion. Additionally, the differences in the thermal behavior of the different skin layers during cooling and thermal recovery can be employed for improving skin cooling techniques for dynamic IR imaging applications. The fundamental understanding of the thermal system of the skin gained from this study is invaluable for the design of dynamic IR measurement systems, as well as systems for cryotherapy or hyperthermia treatments, and lays the foundations for interpreting the thermal signatures of lesions analyzed in Chapters 3 -5.

Chapter 3 Heat transfer model for deep tissue injuries (DTIs) – a step towards an early thermographic diagnostic capability

Overview

The aim of this chapter is to develop a computational thermal model for deep tissue injuries (DTIs) to study their thermal signatures and assess the possibility of early thermographic detection and diagnosis. An introduction to DTIs and the current pressure injury staging system is provided in section 3.1. The imaging techniques that are currently used to assess DTI damage are reviewed in section 3.2. We also reviewed the seemingly inconsistent thermographic findings of pressure injuries reported in prior literature in section 3.2. To explain the inconsistencies reported in prior thermographic literature, we discuss the DTI etiologies (direct tissue damage, ischemic damage and ischemia – reperfusion injury) in section 3.3. We identified upward and downward trends for blood perfusion, metabolic heat generation and tissue temperature associated with physiological events occurring during ischemia and ischemia reperfusion injuries in section 3.4. These trends are incorporated into the thermal models of DTIs (ischemia model, inflammation model and multilayer DTI model) that are developed in section 3.5. Finally, the results are presented in section 3.6. We propose a novel thermal staging for DTIs as 'reversible-damage DTIs' and 'irreversible-damage DTIs' and analyze the long-term skin temperature

variations during these stages, incorporating ischemia and ischemia-reperfusion injuries. Next, we quantify the thermal signatures of reversible and irreversible DTIs using our computational heat transfer models for the steady state situation and the transient thermal recovery from a cooling excitation. Using these results, we conclude that the skin temperature changes associated with incipient DTIs can be measured non-invasively using static and dynamic thermographic imaging.

The key contributions from this study are – (1) the explanations for the inconsistent thermographic findings reported in prior literature for pressure injuries, (2) heat transfer models for DTI that account for tissue physiology during ischemia and ischemia – reperfusion, (3) computational evaluation of thermal signatures of DTIs during steady state conditions and transient thermal recovery from a cooling excitation for early thermographic diagnosis, (4) new and more accurate thermal staging for DTIs that could serve as a means to identify and quantify the severity and properties of DTI (ischemia or inflammation) and tailor suitable management strategies for the injury.

3.1 Introduction to deep tissue injuries (DTIs)

Deep tissue injuries (DTIs) are severe pressure injuries of the skin and the underlying tissue resulting from sustained tissue loadings [30]. The patients experiencing limited mobility due to a physical or cognitive impairment are at most risk of developing DTIs [31], as illustrated in Figure 3.1. The locations on the body that are most susceptible to DTIs are those that are subjected to pressure loadings in a seated (Figure 3.1(a)) or a supine (Figure 3.1(b)) position, such as the heel, the ischial and the sacral regions [70]. Early detection of DTIs is challenging because the injury develops first in the deep tissue

near a bony prominence with intact overlying skin and fat layers [33]. By the time visible clinical signs of the injury appear on the skin surface, the injury has progressed to the vicinity of the surface. A severe DTI injury causes substantial damage to the underlying tissue [33]. Pressure injuries affect more than 2.5 million patients each year in the US, causing morbidity and mortality among patients across the health care facilities. The incidence rates vary between 0.4% – 38% among acute care patients and 2% - 24% among long term care patients [71]. The costs of pressure injuries pose huge financial burden to the US healthcare system, with more than $11 billion spent annually on the treatment and extended hospitalization stays of the affected patients [72]. Early diagnosis of DTIs is necessary to develop effective interventions and reduce the financial and human burdens associated with pressure injuries.

DTIs are classified as the sixth type of pressure injury in the current pressure injury staging system defined by the National Pressure Ulcer Advisory Panel (NPUAP) [30, 73]. The staging system classifies pressure injuries on the basis of the visual signs of the injury and depth of tissue damage [30]. The classification includes stage I through IV pressure

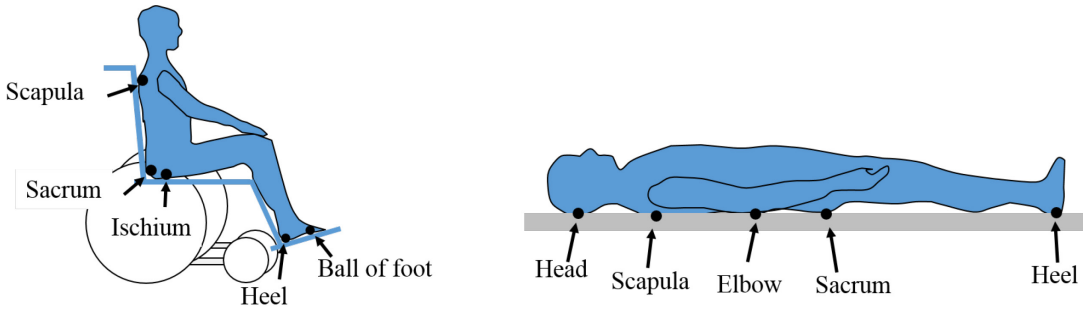

Figure 3.1 Common body sites where DTIs develop in a (a) seated and (b) supine position.

ulcers (with stage I ulcers defined as the least severe ulcers - to stage IV ulcers that involve full tissue thickness loss), unstageable pressure ulcers and DTIs. The visual signs and the extent of tissue damage as defined by the NPUAP are depicted in Figure 3.2, for a stage I pressure ulcer (Figure 3.2(a)), stage IV pressure ulcer (Figure 3.2(b)) and a severe DTI (Figure 3.2(c)). Pressure ulcers begin to develop at the skin surface compared to DTIs that begin to develop in the subcutaneous tissue. The damage is likely to begin at the skin surface in the form of a pressure ulcer if the compressive pressure loading is accompanied by the shearing of the skin layers against the support surface [74]. Additionally, a pressure ulcer may be identified early by the presence of non-blanchable erythema on the skin surface [73], as illustrated by Figure 3.2(a). In contrast, a DTI results primarily from

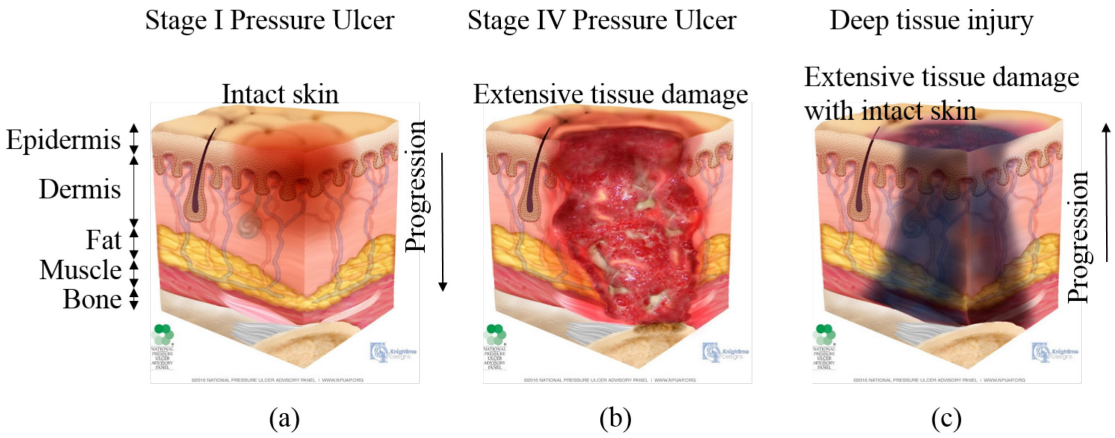

Figure 3.2 Characteristic features of tissue damage for pressure ulcers and deep tissue injury (http://www.npuap.org). Tissue layers are added to the schematics to emphasize the extent of tissue damage in each case. The arrow indicates the direction of propagation of the injury from the incipient phase to an advanced stage. A pressure ulcer injury progresses from the skin surface at the top, as illustrated by (a) stage I pressure ulcer to the deep tissue at the bottom, as shown by (b) stage IV pressure ulcer. Stage I pressure ulcers present non-blanchable erythema of the intact skin and damage that is limited to the dermis. Stage IV pressure ulcers have a crater-like appearance and damage extends to the bone. (c) A DTI develops first in the deep tissue with an intact skin and progresses to the skin surface while causing extensive damage to the underlying tissue. A late stage DTI presents deep purple/maroon discoloration of the intact skin and damage that extends to the bone.

compressive loading [74] and occurs when the subcutaneous tissue is compressed between a bony prominence and a support surface for an extended period of time. The initial injury occurs in the subcutaneous tissue with the overlying skin remaining intact. In later stages, it progresses upwards to the skin surface [33]. By the time DTIs present visible signs (non-blanchable deep red, maroon or purple discoloration) on the skin (as illustrated in Figure 3.2(c)), the underlying tissue is extensively damaged [33]. Thus, it is challenging to diagnose a DTI related damage in an early stage of the injury, when no visible signs are present on the skin surface. The DTI may rapidly evolve as a stage IV pressure ulcer (shown in Figure 3.2(b)) causing damage across the entire tissue thickness [33], if not managed properly. According to Black et al [75], a full thickness wound may develop within 7-10 days from the appearance of DTI related skin discoloration.

The current pressure ulcer staging system is not suitable for accurately evaluating and diagnosing an early phase DTI that first develops in the subcutaneous tissue. Diagnostic imaging methods are needed for the early detection of incipient DTIs and the evaluation of the associated tissue damage. New and more accurate staging definitions for DTIs would enable more accurate clinical assessment of tissue damage and prevent misclassification of severe DTIs as milder stage I pressure ulcers that present visible skin discolorations similar to DTIs. The aim of this study is to demonstrate, using computational modeling, that the subcutaneous tissue damage associated with early stage DTIs can be detected quantitatively using thermographic imaging. Based on these results, new and improved staging of early DTI is proposed.

3.2 Current assessment techniques for DTI

In the past decade, a limited number of imaging studies focused on early detection and assessment of DTIs. Ultrasonography was used for detecting the extent of soft tissue damage in DTI [76-79]. However, the ultrasound imaging based assessment of DTI related damage is subjective and difficult to interpret without a trained radiologist. Additionally, it is difficult to distinguish DTI related features from the heterogeneities of the healthy tissue in an ultrasound image [79]. Hamaluik et al [79] proposed using ultrasound elastography, which is based on measurement of the relative stiffness of the tissue, as a tool to determine soft tissue damage. Their method does not take into account DTI etiologies. For establishing diagnostic accuracy, certain biomarkers of tissue damage have been identified [80], but their applicability on human subjects is not established yet.

Thermographic imaging has been attempted many times since the 1970s for the diagnosis and assessment of pressure related injuries [17, 81-86], however, the results of these studies have been inconclusive. Some studies measured elevated skin temperature for pressure injury cases when compared to the surrounding healthy skin [81, 86]. Other studies reported skin temperature decreases for pressure injuries [17, 83]. Using IR thermography, Goller et al [84] performed measurements of skin temperatures of human skin at pressure loading site and reported both skin temperature increases and decreases relative to healthy skin. Sprigle et al [85] performed skin temperature measurements in pressure injuries using thermocouples and reported both temperature increases and decreases. The subjective interpretation of thermal images and limited insights into the underlying physiological and thermal responses to tissue damage explain the inconsistent skin temperature patterns observed in prior studies.

In this study, our goal is to develop computational models of heat transfer for deep tissue injuries that account for the pathophysiological processes during tissue damage, such as ischemia and ischemia reperfusion, and provide a means for early assessment of DTIs and interpretation of their thermal signatures. The computational models will allow us to analyze the skin temperature responses associated with these processes and improve the understanding of the inconsistent skin temperature patterns reported in prior thermographic studies [17, 81-86]. Specifically, we demonstrate that the influence of ischemia and inflammation on the skin temperature, that can be measured with IR thermography can also be computed using these computational models. We postulate that our computational models will facilitate interpretation of thermographic images and therefore help to improve its diagnostic capability by decreasing reliance on subjective interpretation. Even more important is that these models can serve as the foundation for a more rigorous, quantitative interpretation of other soft tissue thermographic images, which can lead to more exact quantitative detection and diagnostic criteria.

We will first discuss the likely etiologies for DTIs namely – direct tissue damage, ischemia damage and ischemia – reperfusion injury in section 3.3. Next, we will propose two sequences of the underlying biophysical and chemical processes in section 3.4 that lead to both ischemia mediated and ischemia-reperfusion mediated damage in DTI. In both cases, we identify the processes leading to changes in blood perfusion, metabolic heat generation and tissue temperature (either increase or decrease). These trends are incorporated into the thermal models of heel DTIs (ischemia model, inflammation model and multilayer DTI model) that are developed in section 3.5. Finally, the results are presented in section 3.6. We first propose thermal stages (reversible and irreversible tissue

damage) for DTIs, incorporating ischemia and ischemia reperfusion injuries, and next analyze the evolution of skin temperature with time in the presence of DTIs. The stages we introduced can explain the influence of sequential progression of ischemia and inflammation on skin temperature distributions. Next, we quantify the thermal signatures of reversible and irreversible DTIs during the steady state conditions and transient thermal recovery from a cooling excitation. The thermal signatures are computed for a range of lesion depths and thermophysical properties. Using these results, we show that the skin temperature changes associated with incipient DTIs can be measured non-invasively using static and dynamic thermographic imaging.

3.3 DTI etiologies

The experimental studies by Loerakker et al, (2010) [87] and Loerakker et al, (2011) [88] demonstrated that pressure induced tissue deformation, ischemia (occlusion of the subcutaneous vasculature) and ischemia reperfusion (revascularization of the ischemic tissue) are the likely etiologies for DTIs. These damage mechanisms are illustrated in Figure 3.3 for a heel DTI, which is the representative model for DTIs in this study. The heel is the most common site where DTIs develop [32] (Figure 3.3(a)). Although the heel is equipped to endure walking/running/standing-related routine mechanical loadings, the soft tissue becomes susceptible to DTI under immobile conditions that cause unfavorable sustained loadings [89]. The posterior portion of the heel tissue (as shown in Figure 3.3(a)) consists of a large heel bone (the calcaneus), a thin muscle layer (the panniculus carnosus) and a thick fat pad that has overlying dermal and epidermal skin layers [90]. These anatomical layers are illustrated for the cross section aa' in Figure 3.3(b). The muscle layer is fed by a rich vascular supply from the subdermal and periosteal plexuses and is a region

of high metabolic activity [91]. In contrast, the fat layer has a marginal blood supply and is relatively avascular [90, 91].

Under immobile conditions, the soft tissue of the heel remains under sustained compression from the calcaneus against a support surface (Figure 3.3(a)). The compression causes deformation in the tissue and a direct injury (Figure 3.3(b)). The injury is exacerbated by tissue ischemia that results from pressure - induced partial or complete occlusion of blood vessels [88] (Figure 3.3(c)). The low levels of oxygen and glucose during ischemia affect tissue metabolism and cause ischemia injury. Cichowitz et al [91] postulated that the muscle layer of the heel (Figure 3.3(b)) is inherently susceptible to ischemia damage because of its rich vascularity. The fat layer (Figure 3.3(b)) is also vulnerable to pressure - induced ischemia damage because of its inability to dissipate external pressures. Therefore, the fat and muscle layers are the likely primary sites of early tissue damage in heel DTIs [91]. The DTI lesion involving the fat and muscle layers, as displayed in Figure 3.3(b), represents an early DTI damage. The magnitude and duration of external loading, baseline blood perfusion levels, vascular integrity and immunocompetence of the subject are the major factors determining the extent of ischemic damage in a DTI [70]. A tissue unloading event may reverse the effects of ischemic damage by increasing blood supply in the affected tissue. Loerakker et al, (2011) [88] observed that the ischemic tissue in a DTI may develop an ischemia - reperfusion injury when the blood rushes back to the ischemic tissue upon tissue unloading (Figure 3.3(d)). In an ischemia-reperfusion injury, the elevated blood perfusion aggravates the damage further by generating undesirable oxidative stresses and inflammation in the tissue [89]. According to Mak et al [89], these etiological factors may be present concomitantly. The injury during

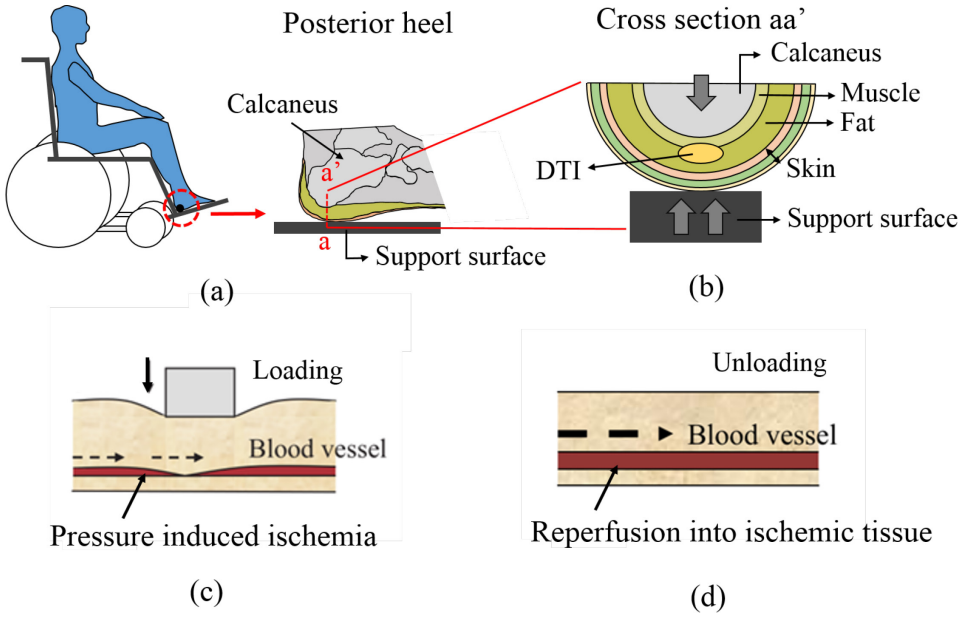

Figure 3.3 DTI of the heel tissue acquired during sitting. (a) The soft tissue of the heel (including muscle and fat) is continuously compressed by the calcaneus bone against a support surface (wheelchair footrest in this case) when the patient is confined to a wheelchair for prolonged durations. (c) Prolonged loading of the tissue causes partial or complete occlusion of the blood vessels causing an ischemia injury. (d) At unloading, reperfusion of the previously ischemic tissue causes increase in blood flow and the resulting oxidative stress can cause ischemia-reperfusion injury.

tissue loading caused by tissue deformation and subsequent ischemia and tissue unloading due to ischemic reperfusion will depend on the relative magnitudes and time scales of ischemia and reperfusion [89].

3.4 Physiological responses of the tissue to ischemic injury and ischemia reperfusion injury

We identified sequential physiological events during ischemia and ischemia-reperfusion injury, from prior literature [92-98]. The characteristic sequences of physiological events (chemical and biophysical processes) are presented in Figure 3.4 for

an ischemia injury and in Figure 3.5 for an ischemia-reperfusion injury. Next to the boxes that represents these events, we introduce the trends for tissue blood perfusion (ω), metabolic heat generation (q) and temperature (T), which can be increasing, decreasing or remain constant. An upward arrow represents parameter increase and a downward arrow represents parameter decrease. This information allows us to incorporate the physiological changes occurring during ischemia and ischemia reperfusion mediated damage into our computational model for DTIs. We will use this information to propose thermal classification (reversible-damage and irreversible-damage injury) for deep tissue injury in section 3.6.1.

3.4.1 Ischemic injury during tissue loading

The physiological responses of the tissue to pressure induced ischemia injury are illustrated in Figure 3.4(a). Each block in the schematic is marked with a letter: when we refer to Figure 3.4(c), for example, we discuss events in block (c) of Figure 3.4. The soft tissue near bony prominences, such as the heel, experiences sustained pressure loadings when the patient is recumbent for extended periods during hospitalization or due to a profound disability (Figure 3.4(a)). An ischemic injury occurs when the pressure loading exceeds the levels at which the blood vessels are partially or completely occluded [95] (Figure 3.4(b)). Jennings and Reimer [92] demonstrated that the duration of loading and the level of occlusion (percentage of baseline blood perfusion present) are both important in causing the ischemia-led tissue damage. During an ischemic injury, the tissue does not get enough blood supplied as needed for adequate oxygen delivery as well as for the removal of the products of metabolism to maintain tissue viability. The reduced blood perfusion levels affect the aerobic metabolism (Figure 3.4(c)). In the presence of

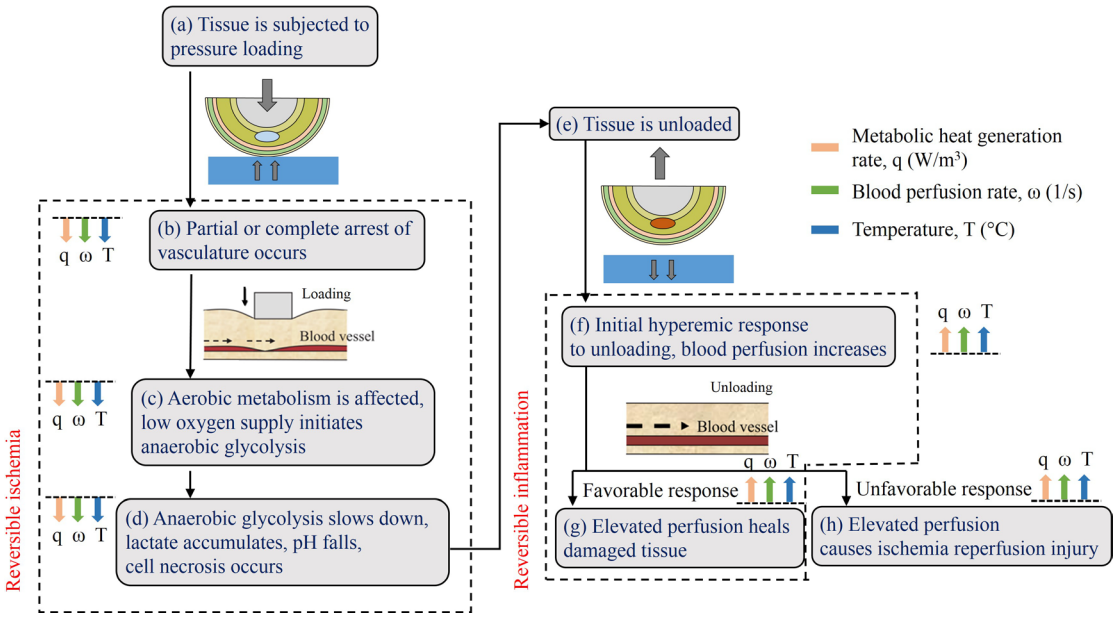

Figure 3.4 Ischemia mediated DTI mechanism and physiological responses of the affected tissue. An arrow pointing up indicates an increasing trend in a parameter and vice versa. Blocks denote key events and the arrows indicate paths between the events. Relevant references are provided in the text.

insufficient oxygen levels, the tissue resorts to anaerobic glycolysis (or non-oxygen condition) mechanisms for metabolic heat generation, which are detrimental to tissue health [92] (Figure 3.5(c)). The rates at which the cells are able to generate energy are less than the rates at which the energy is being consumed by the cells. This process causes a shortage of oxygen and glucose levels in the tissue. Cell necrosis occurs if there is a deficit in ATP (energy) levels, leading to an accumulation of lactate and a subsequent drop in pH levels [92, 93]. These unfavorable physiological responses cause an ischemic injury resulting from a prolonged pressure application (Figure 3.4(d)). We have associated downward trends for blood perfusion, metabolic heat generation and temperature during ischemia injury, as illustrated in steps Figure 3.4(b), Figure 3.4(c) and Figure 3.4(d). The downwards trends account for reduced blood perfusion levels due to blood flow occlusion and low metabolic heat generation due to anaerobic metabolism conditions. Variations of

these properties are incorporated in our computational heat transfer model of DTI ischemia, which allows us to quantify the tissue temperature responses to ischemia-led tissue damage in a DTI.

3.4.2 Favorable hyperemic response during tissue unloading

Prior studies have measured a characteristic hyperemic response to tissue unloading (Figure 3.4(e)) [74, 94]. The response is similar to an inflammatory response that is characterized by a significant increase in blood perfusion (when compared to the baseline perfusion levels) in the affected tissue (Figure 3.4(f)) [94]. Depending on the severity of the ischemic injury, physiological mechanisms (such as thermoregulation) may be able to compensate for the prior loss of blood perfusion by restoring oxygen and other vital nutrients to the tissue. The tissue will recover from an ischemic injury by means of the favorable hyperemic response (Figure 3.4(g)) [94]. To account for tissue hyperemia and restored oxygen supply, we have associated upward trends for blood perfusion, metabolic heat generation and temperature during a favorable hyperemic response, as illustrated in steps Figure 3.4(f) and Figure 3.4(g). These increases in property values are incorporated into our computational heat transfer model of DTI inflammation, which allows us to quantify tissue temperature during a hyperemic response to tissue unloading.

3.4.3 Unfavorable ischemia-reperfusion injury during tissue unloading

An ischemia-reperfusion injury is caused by an unfavorable revascularization event during tissue unloading [99]. The physiological responses of the tissue to an ischemia-reperfusion injury during tissue unloading are illustrated in Figure3.5. During an ischemia-

reperfusion event, the re-entry of oxygen into the previously hypoxic tissue aggravates tissue damage, by initiating a reperfusion cascade (Figure 3.5(d)) [93, 96, 97]. The tissue responds with an inflammatory response which is characterized by the generation and accumulation of reactive oxygen species (ROS), reduction in the nitric oxide levels (Figure 3.5(f)), and the activation of the complement cascade (Figure3.5 g)) [96, 97]. According to [93], some portions of the tissue may circumvent a reperfusion injury as a result of local swelling in the endothelium. These portions will remain ischemic, become necrotic over time and may show decreased temperatures (Figure3.5(c)). The activation of the

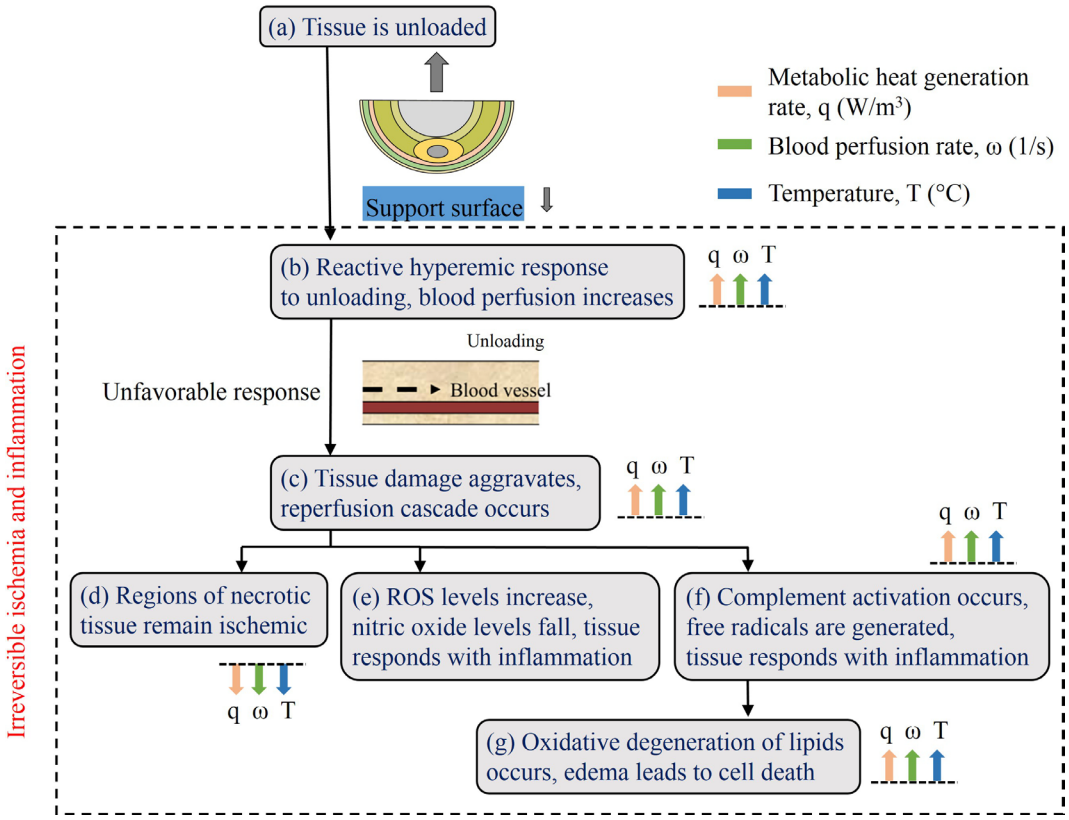

Figure3.5 Ischemia-reperfusion mediated DTI mechanism and physiological responses of the affected tissue, leading to a permanent tissue damage. An arrow pointing up indicates an increasing trend in a parameter and vice versa. Blocks denote key events and the arrows indicate paths between the events. Relevant references are provided in the text.

complement cascade stimulates local endothelial white blood cell adhesion [93] releasing more cytotoxic enzymes and oxygen free radicals (Figure3.5 (f)). These events cause lipid per-oxidation, edema, cell wall abnormalities and eventually cell death [96] (Figure3.5 (g)). These unfavorable physiological responses ultimately lead to an ischemia – reperfusion injury that is more severe than the previous ischemic injury. We associated upward trends for blood perfusion, metabolic heat generation and temperature during the unfavorable inflammatory response, as illustrated in steps shown in Figure3.5(b) – (c) and Figure3.5(e) – (g). The upward trends account for increased blood perfusion levels and high metabolic heat generations due to the reperfusion cascade. We associated downward trends for blood perfusion and metabolic heat generation with severely ischemic regions (Figure 3.5(d)). These property trends of ischemia-reperfusion injury are incorporated into our computational heat transfer model of a multilayer DTI lesion (consisting of a necrotic wound bed surrounded by an inflammation layer) that exhibits both DTI ischemia and DTI inflammation. This physiological model allows us to quantify the tissue temperature responses to an unfavorable hyperemic response to tissue unloading.

3.5 Methods

The goal of the computational model is to predict the skin temperature distributions of the healthy heel tissue and tissue with DTI and assess the possibility of an early thermographic diagnosis of the injury. The motivation for understanding the temperature distributions is the better interpretation of IR images captured in a clinical setting. Understanding the skin surface temperature distributions during different stages of the DTI holds the potential to be able to stage DTI from IR images. The thermal signatures (characteristic thermal responses) of DTIs are defined in terms of skin temperature

increases, decreases or no change with respect to the temperature of the healthy heel tissue. We included a steady state analysis (corresponding to data for steady state infrared imaging) and a transient analysis (that matches the conditions for dynamic infrared imaging). The steady state thermal signatures of DTIs are computed by exposing the skin to ambient conditions. The goal of the transient analysis is to enhance the temperature differences between the healthy and the injured tissue, when compared to the steady state situation. A prominent DTI can often be identified from the steady-state analysis alone. The transient analysis can yield a stronger measurement signal in a clinical application and may provide additional information on the type of DTI (ischemia, inflammation, multilayer DTI) when compared to the steady state condition. Therefore, the understanding of the transient thermal signatures is critical. The transient analysis begins with the skin (heel) exposed to ambient conditions, such as in the steady state analysis. At time t = 0, a cooling excitation is applied to the skin surface (constant surface temperature of 15°C for one minute in the present study). In a clinical setting, this can be accomplished by applying a gel pack at 15°C to the skin surface. The duration of cooling and the cooling temperature can be optimized for clinical applications to minimize patient discomfort, while achieving maximum temperature differences [64]. After the cooling is removed, the tissue is again exposed to ambient conditions, and it gradually warms up to reach steady state temperature. This reheating process is called the thermal recovery. We demonstrate that the thermal recovery of tissue previously subjected to cooling would result in a transient thermal signature yielding a capability to quantitatively detect deep tissue injury, both at the early ischemic and inflammatory stages. The details of our mathematical model and computational solution method are presented in the following sections.

3.5.1 Mathematical model and solution method

In this study, the computational thermal model of the heel tissue serves as the representative model for DTIs. The computational domain in this model is the 2D cross section aa' of the heel, as shown in the schematic in Figure 3.6(a). The semi – elliptical computational domain (Figure 3.6(b)) consists (1) epidermis, (2) papillary dermis, (3) reticular dermis, (4) fat, (5) muscle and (6) bone and (7) the deep tissue injury lesion. The

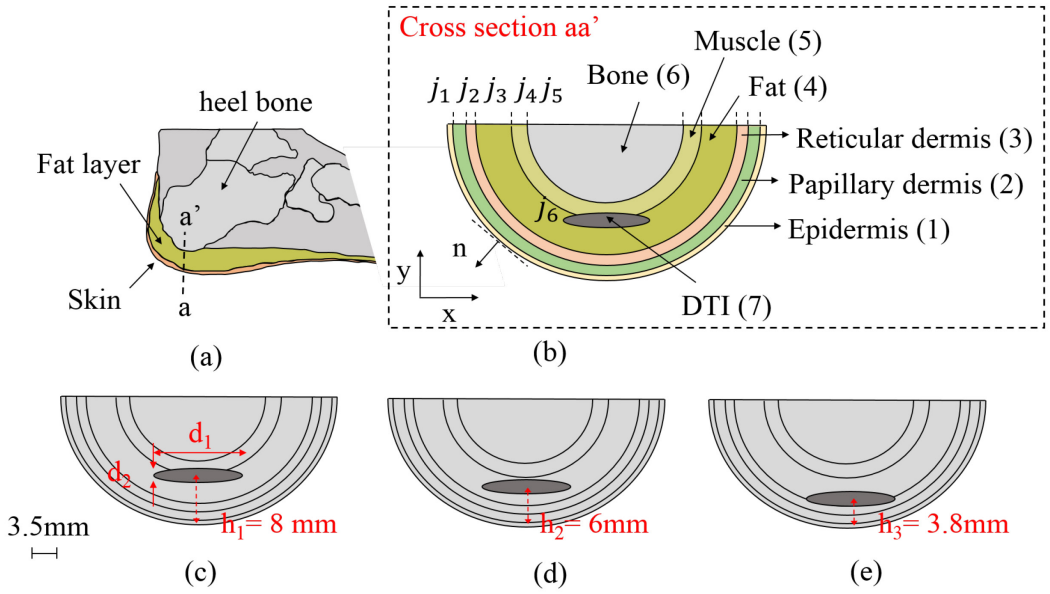

Figure 3.6 Schematics of the heel tissue and computational domain for modeling early stage heel DTI. (a) Lateral view of the heel showing the talus bone, fat pad and skin layers. Section aa' is the projection of the computational domain. (b) Computational domain showing detailed heel tissue anatomy across section aa' and a DTI lesion in fat and muscle layers. Early stage DTI of heel is modeled by considering three possible lesion depths for onset of tissue damage: (c) h = 8 mm (DTI exists in the fat and muscle), (d) h = 6 mm (DTI exists in fat layer) and (e) h = 3.8 mm (DTI exists in the fat and reticular dermis), where the depth h is measured from the skin surface (outermost boundary). The early stage DTI lesion is modeled as an ellipse with dimensions: d_1 = 1.5 cm (major axis), d_2 = 0.25 cm (minor axis). One form of an advanced stage DTI is modeled by considering a multilayer lesion (not shown) consisting of a 1.5 cm by 0.25 cm ellipse surrounded by a 1.25 mm thick layer.

layer thicknesses are overemphasized and not to scale in the schematics to show the anatomical details of the heel tissue. Our modeling efforts include an analysis for three lesion depths, since the exact location where the DTI begins in the heel tissue is not known in advance. The depths considered in this study are: (1) h = 8 mm (the injury begins in the muscle and fat layers), (2) h = 6 mm (the injury begins in the fat layer) and (3) h = 3.8 mm (the injury begins in the fat and reticular dermis layers). The schematics of computational domains for these depths are shown in Figures 3.6(c)-(e). We assume that each layer is homogenous, has a uniform thickness and a set of constant thermophysical properties that do not change with temperature, within the temperature range considered in this study. The thermophysical properties of tissue layers and lesion, tissue layer thicknesses and lesion dimensions were obtained from the prior literature [77, 91, 94, 100-102] and they are summarized in Table 3.1 and Table 3.2.

The governing equation for the heat transfer model in this study is the Pennes bioheat equation [62], that we first introduced in Chapter 2, in section 2.1. Our mathematical heat transfer model is described by a set of seven ($i = 1, 2, 7$) coupled bioheat transfer equations (one equation for each tissue layer and one for the lesion) as

$$\rho_i c_i \frac{\partial T_i}{\partial t} = \nabla \cdot (k_i \nabla T_i) + \omega_i \rho_i c_i \left(T_{b_i} - T_i\right) + q_i \tag{3.1}$$

Equation 3.1 is solved in the computational domain using the appropriate initial, boundary and interface conditions. The continuity of temperature and heat flux is satisfied at the six interfaces (Figure 3.6(b)), m =1, 2, 3, 4, 5 and 6 as

$$T_m(x, y, t)|_{j_m} = T_{m+1}(x, y, t)|_{j_m} \tag{3.2}$$

$$-k_m \frac{\partial T_m(x,y,t)}{\partial n}\Big|_{j_m} = -k_{m+1} \frac{\partial T_{m+1}(x,y,t)}{\partial n}\Big|_{j_m} \quad (3.3)$$

In Equation 3.3, n is the direction of the normal to a boundary and m represents the interfaces, as shown in Figure 3.6(b). The distance between the lesion center and the top surface is sufficiently large (2.2 cm) for the top surface to not feel the thermal effect of the lesion. Therefore the boundary condition of zero heat flux

$$-k \frac{\partial T(x,y,t)}{\partial n}\Big|_{\text{top surface}} = 0 \quad (3.4)$$

is used at the top horizontal surface of the domain (Figure 3.6(b)). The direction of the heat flux from the skin layers is radially outwards and a uniform core body temperature is assumed at the muscle-bone interface (Figure 3.6(b)) as

$$T(x,\mathrm{y},t)|_{\mathrm{j_5}} = 37°\mathrm{C} \quad (3.5)$$

Using Equations 3.1 to 3.5, the computational model is solved in three steps: (i) compute the steady state temperature distribution with the skin surface exposed to ambient conditions, (ii) for transient analysis apply skin cooling for a short cooling period t_c and

Table 3.1 Thermophysical properties of heel tissue used in the simulations

Layer	Thickness (mm)	Specific heat (J/kg·K)	Thermal conductivity (W/m·K)	Perfusion rate (10-3) (1/s)	Metabolic heat generation (W/m3)	Arterial blood temperature (°C)	Density (kg/m3)
Epidermis	0.46[a]	3589[b]	0.235[b]	0[b]	0[b]	0[b]	1200[b]
Papillary dermis	1.67[a]	3300[b]	0.445[b]	0.18[b]	368.1[b]	37[b]	1200[b]
Reticular dermis	1.67[a]	3300[b]	0.445[b]	1.26[b]	368.1[b]	37[b]	1200[b]
Fat layer	5[a]	2674[b]	0.185[b]	0.08[b]	368.3[b]	37[b]	1000[b]
Muscle	2.5[a]	3600[b]	0.51[b]	2.7[b]	684.2[b]	37[b]	1085[b]
Bone	3[a]	1300[c]	0.4[c]	0[d]	0[d]	0[d]	2000[c]

[a][91]
[b][41]
[c][102]
[d][100]

Table 3.2 Thermophysical properties of DTI used in the simulations

Damage mechanism	DTI dimensions (cm)	Specific heat (J/kg·K)	Thermal conductivity (W/m·K)	Perfusion rate (10-3) (1/s)	Metabolic heat generation (W/m3)	Arterial blood temperature (°C)	Density (kg/m3)
Ischemia	d1=1.25[e]	2450[f]	0.1[f]	0.262[g]	342.1[f]	35[f]	1037[f]
	d2=0.25[e]						
Inflammation	d1= 1.5[e]	2450[f]	0.558[b]	6.95[b]	5262.5[b]	37[b]	1037[b]
	d2=0.25[e]						

[b][41]
[e][77]
[f][101]
[g][94]

(iii) compute the transient thermal recovery of the skin surface as a function of time after the removal of the cooling load (the skin surface is exposed to ambient conditions again). For this study, we assumed an ambient temperature of $T_\infty = 22°C$ and a convective heat transfer coefficient $h_\infty = 12$ W/m^2·K for the steady state condition. The steady state solution describes the thermal state of the tissue before the skin cooling begins ($t < 0$) and also the thermal state which the tissue gradually attains during the thermal recovery process($t \to \infty$). The thermal boundary condition at the skin surface for the steady state situation with skin exposed to ambient air is

$$q'' = h_\infty (T(x, y, t)|_{\text{skin}} - T_\infty) \quad t < 0, t > t_c \tag{3.6}$$

The temperature distribution computed for the steady state solution (Equations 3.1 to 3.6) was used as the initial condition for the transient cooling process. In the transient analysis, we applied a cooling excitation to the skin surface. The boundary condition for skin cooling is constant temperature of 15°C for the cooling duration of $t_c = 1$ min described as

$$T(x, y, t)|_{\text{skin}} = 15°C, \ 0 \leq t < t_c = 1 \text{ min} \tag{3.7}$$

The boundary condition described by Equation 3.7 can be approximated in a clinical setting by applying a cold gel pack to the skin surface. The cooling duration and temperature can be optimized to minimize patient discomfort and scan time, while yielding a satisfactory temperature difference. After the cooling was removed ($t > t_c$), the convective boundary condition described by Equation 3.6 was applied again to the skin surface to compute the thermal recovery of the skin surface from the cooling excitation.

The computations were carried out using the finite element software COMSOL Multiphysics v4.3a. The mesh consisted of 4932 free triangular elements. Figure 3.7 shows the computational mesh in the entire domain. The magnified region shown to the right shows the mesh around the DTI lesion. The temperatures at the skin surface and around the lesion were of primary interest in the study. To achieve high spatial resolution, the maximum element size for the epidermis, the muscle and fat layers was set as 1.3mm, whereas the maximum mesh size was 2.4mm for the remaining domains. The computational results differed by less than 1% when the smallest element size was set as 0.65mm. The convergence of the solution was ensured by setting the time step Δt as 0.1s for the first 5 minutes of thermal recovery and 1s for the rest of the thermal recovery period.

In this study, the early stages of a DTI lesion are characterized either by ischemia or inflammation, and thermal models were developed for these two cases. Table 3.2 summarizes the thermophysical properties for these two DTI models. Staging the injury in terms of ischemia and inflammation is useful because it helps to explain the inconsistency in previously reported thermographic measurements of pressure ulcers. Temperatures computed for these models were compared with temperatures from the healthy tissue model. A multilayer model was also developed to account for the advanced stages of DTI.

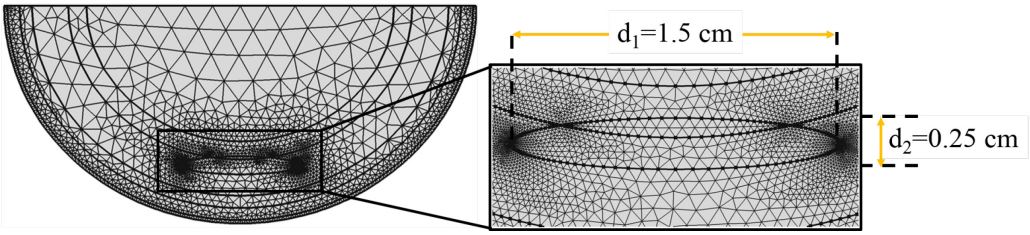

Figure 3.7 Computational mesh for the heel cross section aa' from Figure 3.6 with an 8 mm deep elliptical DTI lesion with d_1 and d_2 being the major and the minor axis, respectively. The mesh consists of 4932 free triangular elements.

3.5.1.1 Healthy tissue model

The healthy tissue model serves as the baseline model for comparisons between the healthy tissue and tissue with DTI. The healthy heel model does not have any lesion. The thermophysical properties for healthy tissue for the mathematical model are summarized in Table 3.1.

3.5.1.2 Ischemia model

The ischemia model predicts the temperature distributions in the heel tissue in the presence of an ischemic lesion. The ischemic injury is characterized by low blood perfusion due to blood vessel occlusion and low metabolic heat generation due to anaerobic metabolic processes [94, 98], as illustrated in Figure 3.4. A decrease in the effective thermal conductivity and density of the tissue is likely due to lipid accumulation in the damaged tissue [77, 101]. The thermophysical properties of DTI ischemia lesions for the mathematical model are summarized in Table 3.2.

3.5.1.3 Inflammation model

The inflammation model predicts the temperature distributions in the heel tissue in the presence of DTI inflammation. A favorable hyperemic response to a prior ischemia injury (Figure 3.4) and an unfavorable hyperemia response to an ischemia – reperfusion injury (Figure3.5) are both characterized by an inflammatory response in the tissue. We incorporated elevated blood perfusion levels, high metabolic heat generation and high thermal conductivity [94] to characterize DTI inflammation. The thermophysical properties of DTI inflammation used in the mathematical model are summarized in Table 3.2.

3.5.1.4 Multilayer model

The multilayer DTI model predicts temperature distributions in the heel in the presence of a more advanced injury. At an advanced stage, the initial ischemia lesion may transform into a DTI inflammation lesion followed by a multilayer DTI lesion, which is represented by a thin inflammation layer surrounding the ischemic core. The outer layer of the multilayer DTI lesion is characterized by thermophysical properties of DTI inflammation and the inner ischemic core is characterized by thermophysical properties of DTI ischemia (Table 3.2).

3.6 Thermal signatures of DTIs

In this section, we present the computed thermal signatures of DTIs during steady state conditions and transient thermal recovery from a cooling excitation, using the thermal models developed in section 3.5. Our aim is to demonstrate the possibility of steady state and dynamic thermographic early detection, identification and characterization of DTIs. In section 3.6.1, we first introduce ‘reversible-damage DTIs’ and ‘irreversible-damage DTIs’

as two clinical stages or categories of DTIs. Next, we present the long-term skin temperature variations during the evolution of these stages. These projections are based on the tissue temperature trends that were identified in section 3.4. In sections 3.6.2 and 3.6.3, we quantify the thermal signatures of reversible and irreversible DTIs using our computational heat transfer models. To account for the unknown depth of the early damage, three possible lesion depths are considered for each stage DTI, as discussed in section 3.5.1.

3.6.1 Thermal classification for DTIs

To enable more accurate clinical assessment of tissue damage during the evolution of DTI, we propose two thermal stages: reversible-damage DTI (representing an early stage injury) and irreversible – damage DTI (representing an aggravated injury). These definitions are based on the tissue temperature trends that we identified in section 3.4 for ischemia-led tissue damage (Figure 3.4) and ischemia – reperfusion-led injury (Figure3.5). A reversible DTI refers to an incipient ischemic injury to the subcutaneous tissue (caused during tissue loading) that could be reversed by a hyperemic response (or inflammation) to tissue unloading (Figure 3.4 (a) – (g)). The tissue eventually recovers its baseline healthy state (Figure 3.4(g)). The skin temperature evolution during the occurrence and progression of a reversible DTI is displayed in Figure 3.8(a). It can be detected by infrared imaging of the affected lesion during the time period of interest. The initial temperature decrease in Figure 3.8(a), during reversible ischemia, indicates low blood perfusion and metabolic heat generation (Figure 3.4(b) – (d)). The following increase in temperature, during reversible inflammation, is a hyperemic response (elevated blood perfusion) to tissue unloading (Figure 3.4(e) – (f)). The subsequent temperature decrease to the baseline healthy state temperature (shown in Figure 3.4(g)) indicates the recovery of the damaged tissue to a

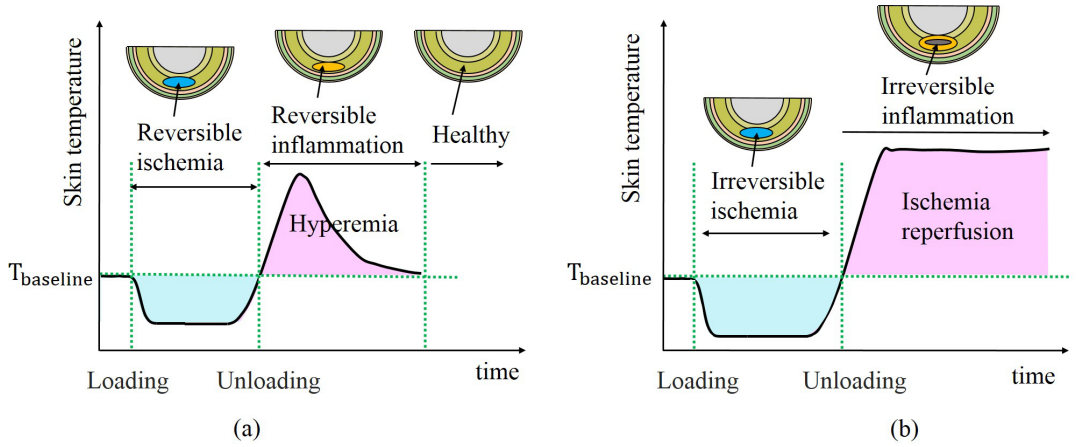

Figure 3.8 Qualitative display of skin surface temperature evolution over time for two clinical outcomes of DTI. (a) Case I: tissue recovers from a brief ischemic episode. (b) Case II: tissue suffers irreversible damage as a result of a severe inflammatory response and ischemia – reperfusion injury.

healthy state. Further research is necessary to examine the time scales for the temperature decreases and temperature increases. The magnitude of temperature decreases and increases during reversible DTI ischemia and inflammation will depend on the magnitude and duration of sustained loading, leading to ischemia, as well as on the dimensions and depth of the DTI lesion. Quantitative skin temperature data for a reversible DTI lesion, computed using DTI ischemia and inflammation models will be presented in section 3.6.2.

An irreversible DTI develops from a pre-existing ischemic injury (caused during tissue loading) that is aggravated by an ischemia-reperfusion injury during tissue unloading (Figure 3.4(h) and Figure 3.5(a) – (g)). Advanced stage damage can be classified as thermally and clinically irreversible. The ischemic DTI lesion may evolve into a single thin inflammation layer around the ischemic core region and transform into a multilayer DTI or into a DTI inflammation lesion over time. The skin temperature variations during irreversible DTI occurrence and progression are qualitatively displayed in Figure 3.8(b).

The initial temperature decrease (in Figure 3.8(b)) indicates the state of low blood perfusion and metabolic heat generation (Figure 3.4(b) – (d)) and Figure 3.5(d)), during ischemia, similar to the situation in Figure 3.8(a)). The subsequent sustained temperature elevation (in Figure 3.8(b)), contrasted to short duration in Figure 3.8(a), suggests an extended unfavorable inflammatory response (elevated blood perfusion levels), caused by the ischemia-reperfusion event following tissue unloading (Figure 3.4(h) and Figure3.5 (b) – (c), (e) – (g)). The temperature rise may also be due to the presence of a thin inflammation layer around the pre-existing ischemic lesion or inflammation occurring in the full volume of the DTI. In the presence of an aggravated injury, the tissue metabolism fails to restore the baseline healthy temperatures (Figure 3.8(b)) over time. Quantitative skin temperature data for an irreversible DTI lesion computed from the multilayer DTI models will be presented in section 3.6.3.

3.6.2 Thermal signatures of reversible DTIs

In this section, we present computed skin temperatures in the presence of reversible ischemia and inflammation damage. The characteristic responses are computed for a 1.5 cm by 0.5 cm large heel DTI lesion situated at three depths: (1) h = 8 mm (muscle and fat layer are damaged), (2) h = 6 mm (fat layer is damaged) and (3) h = 3.8 mm (fat and reticular dermis layers are damaged). Steady state thermal signatures of reversible DTIs are presented in section 3.6.2.1 (steady state thermographic assessment) and the transient thermal signatures in section 3.6.2.2 (dynamic thermographic assessment).

3.6.2.1 Steady state signatures (reversible DTIs)

Steady state heel temperatures were computed for healthy tissue and DTI models for ischemia and inflammation using Equations 3.1 to 3.6. Figure 3.9 displays the computed temperature distributions for DTI ischemia and DTI inflammation cases. The results are shown for the ROI outlined by a dashed red box in the top right schematic. The temperature plots are color coded: dark blue color is the lowest temperature and red color is the highest temperature. The boundaries of different layers are indicated by the black lines. A temperature decrease is observed during ischemia, due to low blood perfusion levels (Figure 3.9 (a), (c) and (e)). A temperature increase is observed during an inflammatory response, due to elevated blood perfusion levels (Figures 3.9 (b), (d) and (f)). These effects

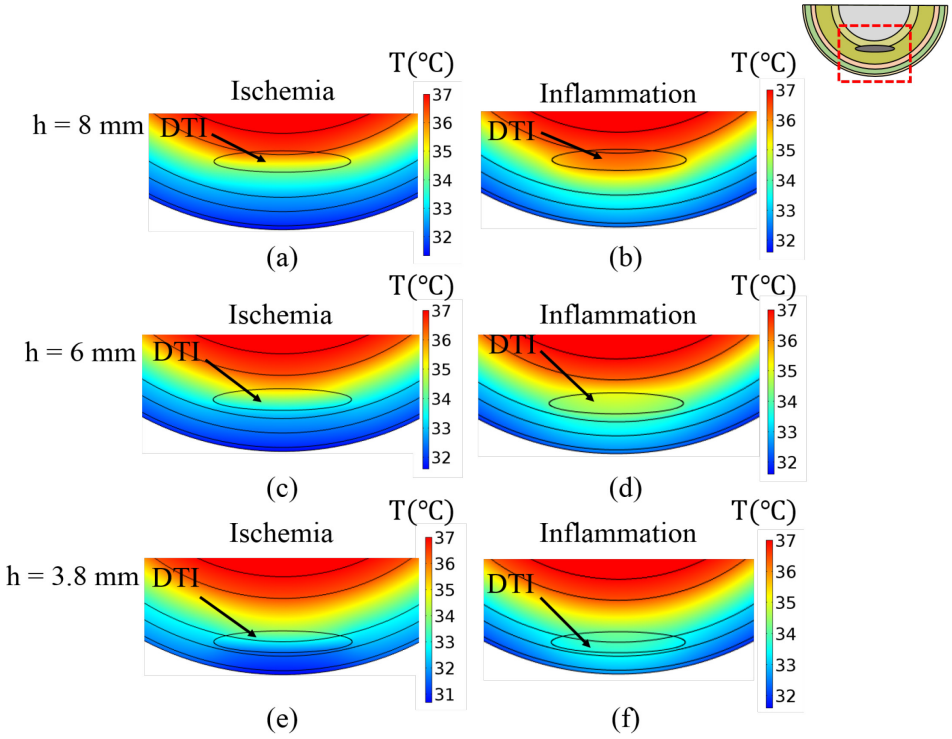

Figure 3.9 Computed steady state temperatures for DTI models of ischemia and inflammation. The red box in the top right schematic shows region of interest. Temperature distributions are shown for lesion depths h = 8 mm (a) ischemia and (b) inflammation; h = 6 mm (c) ischemia and (d) inflammation; and h = 3.8 mm (e) ischemia and (f) inflammation. Temperatures increase from dark blue to red.

are illustrated for the three depths of DTI lesion: h = 8mm ischemia and inflammation in Figures 3.9 (a) and (b); h = 6mm ischemia and inflammation in Figures 3.9(c) and (d); and h = 3.8mm ischemia and inflammation in Figures 3.9(e) and (f).

The steady state skin surface temperature profiles for the healthy model, DTI ischemia and DTI inflammation are compared in Figure 3.10 for the three lesion depths. The ordinate shows the skin temperature during steady state. The distance l on the x axis is the distance measured along the curved surface of the heel periphery, as indicated in the

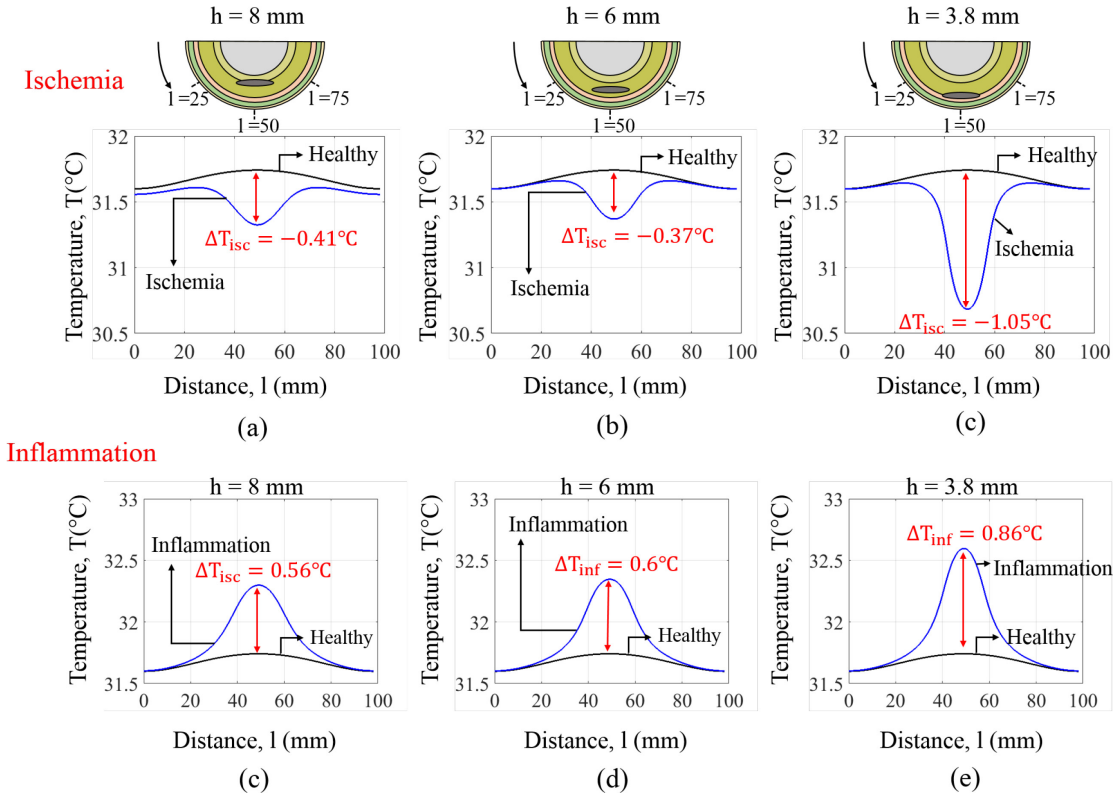

Figure 3.10 Steady state thermal signatures for DTI ischemia and inflammation. Skin surface temperature profiles from the healthy tissue model and ischemia models compared for depths (a) h = 8 mm, (b) h = 6 mm and (c) h = 3.8 mm. Skin surface temperature profiles from the healthy tissue model and inflammation models compared for depths (d) h = 8 mm, (e) h = 6 mm and (f) h = 3.8 mm depths. Temperature differences are computed as $\Delta T_{isc} = T_{ischemia} - T_{healthy}$ for DTI ischemia and ΔT_{inf} $(T_{inflammation} - T_{healthy})$ for DTI inflammation. The ordinate is the distance along the circumference of the heel, as shown in the schematic.

top heel schematics. The healthy skin temperature profiles are shown by the black lines and the blue lines represent the skin temperature profiles for ischemia (top row images) and inflammation (bottom row of images). With respect to the healthy skin profile, the computed temperature decreases during ischemia ($\Delta T_{isc} = T_{ischemia} - T_{healthy}$) and the temperature increases during inflammation ($\Delta T_{inf} = T_{inflammation} - T_{healthy}$) are indicated in each plot. The maximum temperature decreases and increases are observed for the location l = 48mm, which is the location above the lesion center. During steady state, the skin temperature decreases for a DTI ischemic lesion by 0.41°C for the h = 8mm depth (Figure 3.10(a)) depth, 0.37°C for the h = 6 mm depth (Figure 3.10(b)) and 1.05°C for the h = 3.8mm depth (Figure 3.10(c)) case. The skin temperature increases for a DTI inflammation lesion by 0.56°C for the h = 8mm depth (Figure 3.10(d)), 0.6°C for the h = 6mm (Figure 3.10(e)) and 0.86°C for the h = 3.8 mm (Figure 3.10(f)) depth case. As expected, the temperature difference and the corresponding measurement signal is larger, the closer the lesion is to the skin surface. The thermal signatures of this magnitude can easily be measured using modern IR cameras, resulting in a steady state thermographic diagnostic capability for heel DTI ischemia and inflammation.

3.6.2.2 Transient thermal signatures (reversible DTIs)

While the steady state situation can yield relatively large temperature differences that are easy to measure, especially for larger DTIs relatively close to the skin surface, even more information can be gained and the temperature differences between the healthy and DTI cases can be enhanced (when needed, for example for small lesions) by considering transient thermal recovery temperatures of the skin. In the present study, the skin surface

was subjected to a cooling load of 15°C for 1 min duration and its transient thermal recovery was computed using the healthy tissue and DTI models, by solving Equations 3.1 to 3.7. Figure 3.11 displays the transient thermal recoveries of the healthy tissue, and of an 8mm deep lesion characterized by ischemia as well as inflammation. The transient temperatures are plotted for point P (shown in the top right heel schematic), which corresponds to the l = 48 mm location on the skin surface. At this location, the maximum steady state thermal signatures were detected. The characteristic transient thermal signatures of DTI ischemia and inflammation lesions are shown as function of thermal recovery time in Figure 3.11(a). For a cooling load of 15°C of 1 minute duration, the complete thermal recovery takes about 20-25 minutes (Figure 3.11(a)). However, key information regarding the nature of the DTI (ischemia vs. inflammation) is available within

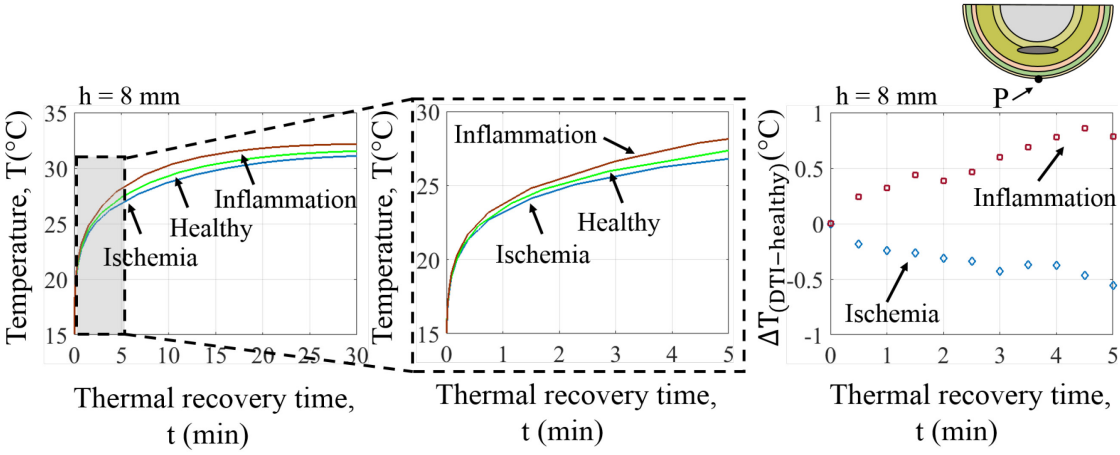

Figure 3.11 Transient thermal recovery of skin surface temperature for healthy tissue and DTI models of ischemia and inflammation. Top right schematic shows point P where recoveries were computed. (a) Complete thermal recovery – until temperature of the skin reaches steady state, (b) magnified region of the early thermal recovery period (the first five minutes of particular interest in clinical applications) (c) Temperature difference $\Delta T_{DTI-healthy}$ shown for the first five minutes of thermal recovery. Red curve shows temperature increase for inflammation and blue curve shows temperature decrease for ischemia.

the first five minutes of the thermal recovery period. DTI ischemia can be identified by a slower recovery (light blue curve) and DTI inflammation can be identified by a faster recovery (red curve) when compared to the healthy tissue (green curve) during the first five minutes of thermal recovery (Figure 3.11(b)).

For the 8 mm deep DTI case, the computed temperature decrease $\Delta T_{isc} = T_{ischemia} - T_{healthy}$ was in the range of $0.25°C - 0.5°C$ (Figure 3.11(c)). The computed temperature increase $\Delta T_{inf} = T_{inflammation} - T_{healthy}$ was in the range of $0.5°C - 0.9°C$, during the first five minutes of the thermal recovery (Figure 3.11(c)). These results show that the tissue affected by DTI ischemia and DTI inflammation can be distinguished from the healthy tissue by cooling down the skin surface and measuring the thermal recovery of the skin above the lesion as a function of time. The 8 mm deep DTI case serves as the worst case depth scenario in our model for detecting the changes associated with DTI ischemia and inflammation. Deep tissue injuries can develop deeper, in locations with a thicker fat layer, such as the sacral area. Dynamic IR imaging can be particularly valuable for the detection of such lesions. We have demonstrated that the transient thermal signatures of the 8 mm deep ischemia or inflammation lesions are measurable with modern IR cameras. Therefore, depending upon the location and size of the lesion as well as the tissue properties, the duration of a transient measurement would be 1-5 minutes, which is acceptable in a clinical setting. These transient thermal signatures suggest that the entire diagnostic measurement can be carried out within 6 minutes, which is acceptable in a clinical practice.

Figure 3.12 illustrates that our transient analysis can enhance the temperature differences between healthy and tissue affected by DTI in a clinical setting and provide

stronger thermal signatures compared to the steady state case. The steady state temperature profiles (shown in green) are plotted along the tissue depth line hh' (shown schematically in the top right schematic). The position h = 0 is located on the skin surface and h'= 11.3 mm is the bone-muscle interface in Figure 3.12. With respect to healthy skin, a temperature decrease of 0.35°C is observed for ischemia (Figure 3.12(b)) and an increase of 0.6°C is observed for inflammation for a 6 mm deep DTI (Figure 3.12(c)) in steady state. The temperature profiles computed at 3.5 minutes into the thermal recovery are shown by the black lines. At this time, a temperature decrease of 0.41°C is observed for ischemia (Figure 3.12(b)) and an increase of 0.7°C is observed for inflammation (Figure 3.12(c)), when compared to skin temperature of healthy tissue at the same time (Figure 3.12(a)). This time

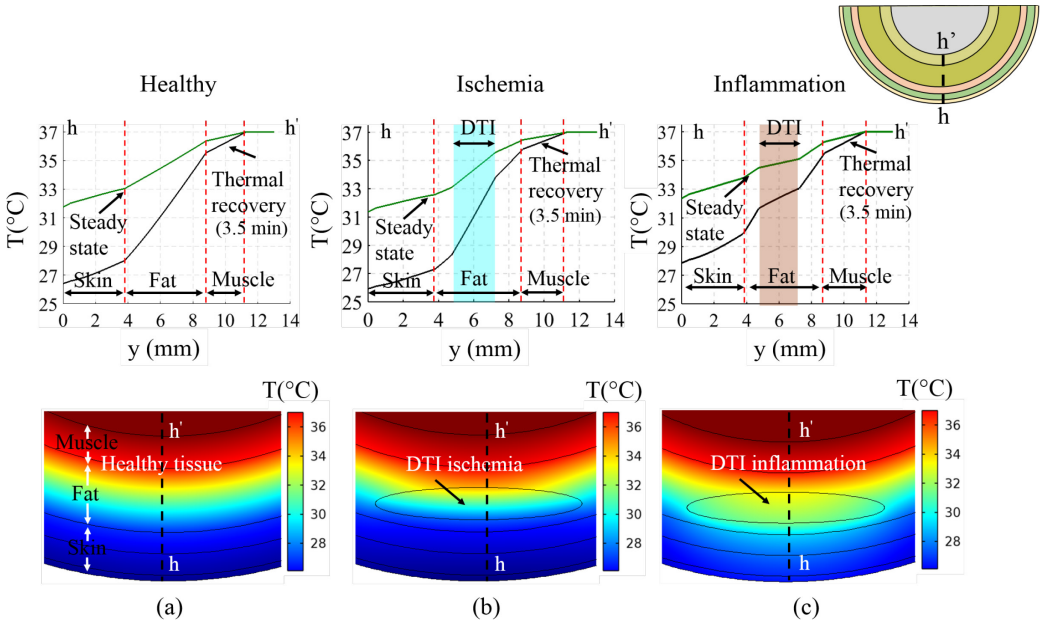

Figure 3.12 Skin temperature profiles plotted along depth line hh' during steady state and transient thermal recovery (top row) and 2D color-coded temperature distributions during thermal recovery (bottom row) for (a) healthy tissue, (b) tissue with a 6 mm deep DTI ischemia and (c) inflammation lesion. In the top row, the green curves show steady state and the black curves show transient tissue temperature profiles at 3.5 minutes into the thermal recovery, at a time when the temperature differences of interest are large.

instant is selected for comparison because the temperature difference between healthy tissue and DTI responses is largest in the 3-4 minute time range. Both the 0.41°C temperature decrease and the 0.7°C temperature increase (with respect to the healthy situation) at the skin surface are larger than in the steady state situation (0.35°C decrease and 0.6°C increase, respectively) and can easily be measured with modern, relatively low cost IR cameras.

The bottom row of images shown in Figure 3.12 displays the 2D color coded heel tissue temperature distributions computed at 3.5 minutes into thermal recovery for the healthy tissue model (left), DTI ischemia model (middle) and DTI inflammation model (right) for a 6 mm deep DTI. The blue regions in the color-coded images correspond to low temperatures and red regions to the high temperatures. A temperature decrease is visible in the region of the lesion and its surroundings for ischemia (Figure 3.12(b)), whereas the temperature increases in this region for inflammation (Figure 3.12(c)), when compared to the healthy tissue shown in Figure 3.12(a).

Figure 3.13 displays the transient skin surface temperatures computed for DTI ischemia and inflammation, along the perimeter of the heel (location, l shown in top schematics) as a function of the thermal recovery time, t. The plots for ischemia lesions for depths h = 8 mm (Figure 3.13(a)) and h = 3.8mm (Figure 3.13(b)) show temperature decreases. The plots for inflammation lesions for depths h = 8 mm (Figure 3.13(c)) and h = 3.8 mm (Figure 3.13(d) show temperature elevations. The increases or decreases in the skin temperatures are most pronounced for the location range from l = 35 to l = 65 mm, the area above the lesion. The width of the region characterized by temperature increases or decreases scales with major axis of the DTI. The results demonstrate that key quantitative

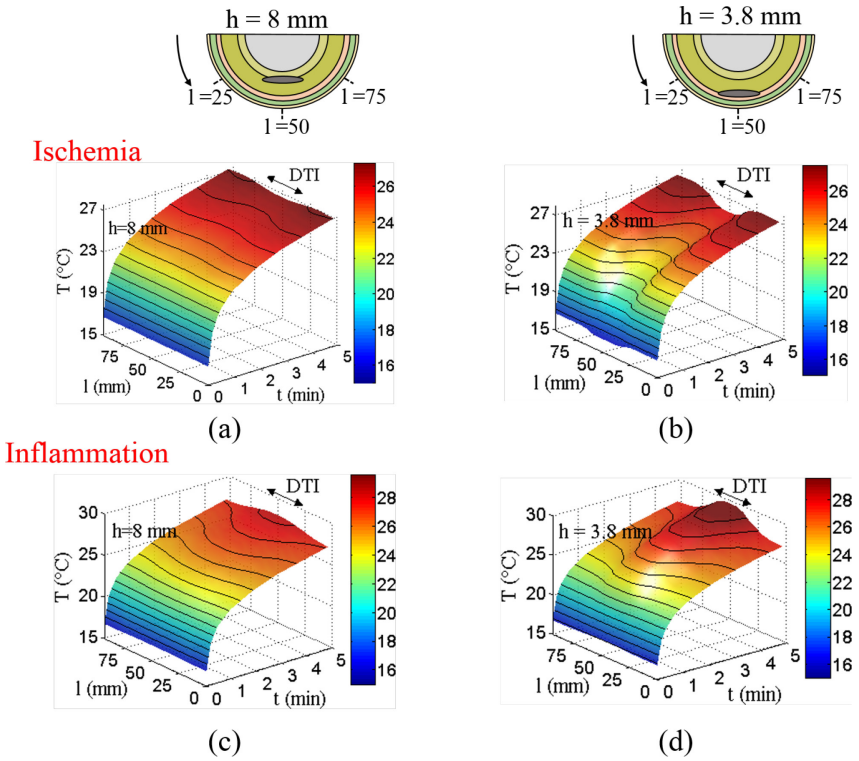

Figure 3.13 Skin surface temperature distribution as a function of location and thermal recovery times for DTI lesions. Ischemia lesions at (a) h = 3.8 mm and (b) h = 8 mm depth and inflammation lesions at (c) h = 3.8 mm and (d) h = 8 mm depth. The locations l = 35 to 65 mm along the skin surface and the thermal recovery times from t = 2 to 5 minutes provide best sensitivity for measurement. DTI dimensions: d_1 = 1.5 cm (major axis), d_2 = 0.25 cm (minor axis).

information regarding the nature of the DTI (ischemia vs. inflammation) is available within the first 2-5 minutes of thermal recovery.

The impact of lesion depth on the transient skin temperatures is illustrated for DTI ischemia lesions in Figure 3.14 and DTI inflammation in Figure 3.15. For the three depths of DTI ischemia and DTI inflammation lesions, the skin surface thermal response was computed during the first five minutes of the thermal recovery process. The results are compared with the skin temperatures of the healthy tissue for the same times of the thermal recovery process in Figure 3.14 (ischemia) and Figure 3.15 (inflammation). As expected,

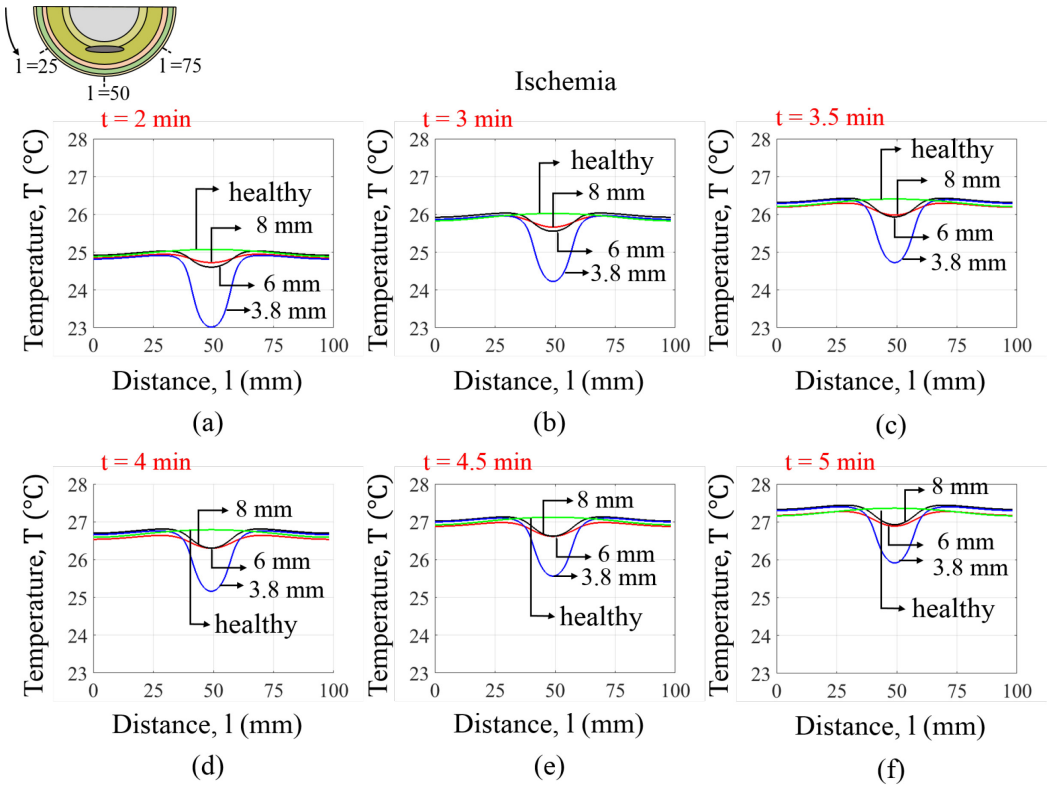

Figure 3.14 Impact of DTI ischemia lesion depth on the transient skin surface temperature profiles. Skin surface temperatures are plotted along the perimeter of the heel (l shown in top left schematic) for healthy (green) tissue and lesions at depths h = 3.8 mm (blue), 6 mm (black) and 8 mm (red). The results are shown at thermal recovery times of (a) t = 2 min, (b) t = 3 min, (c) t = 3.5 min, (d) t = 4 min, (e) t = 4.5 min and (f) t = 5 min, when the temperature differences of interest are large. DTI dimensions: d_1 = 1.5 cm (major axis), d_2 = 0.25 cm (minor axis).

the 3.8 mm deep DTI (blue line) results in the most pronounced temperature decrease/increase in skin surface temperature with respect to the healthy tissue (green line) in both ischemia (Figure 3.14) and inflammation plots (Figure 3.15). The trends for the 3.8mm depth DTI indicate that the lesion closer to the skin surface will have stronger thermal signatures. Skin temperatures for the 6mm and 8 mm deep ischemia lesions do not differ as much as the skin temperatures for the inflammation lesions at the same depths (Figure 3.14 and Figure 3.15), suggesting weaker thermal signatures for ischemia when

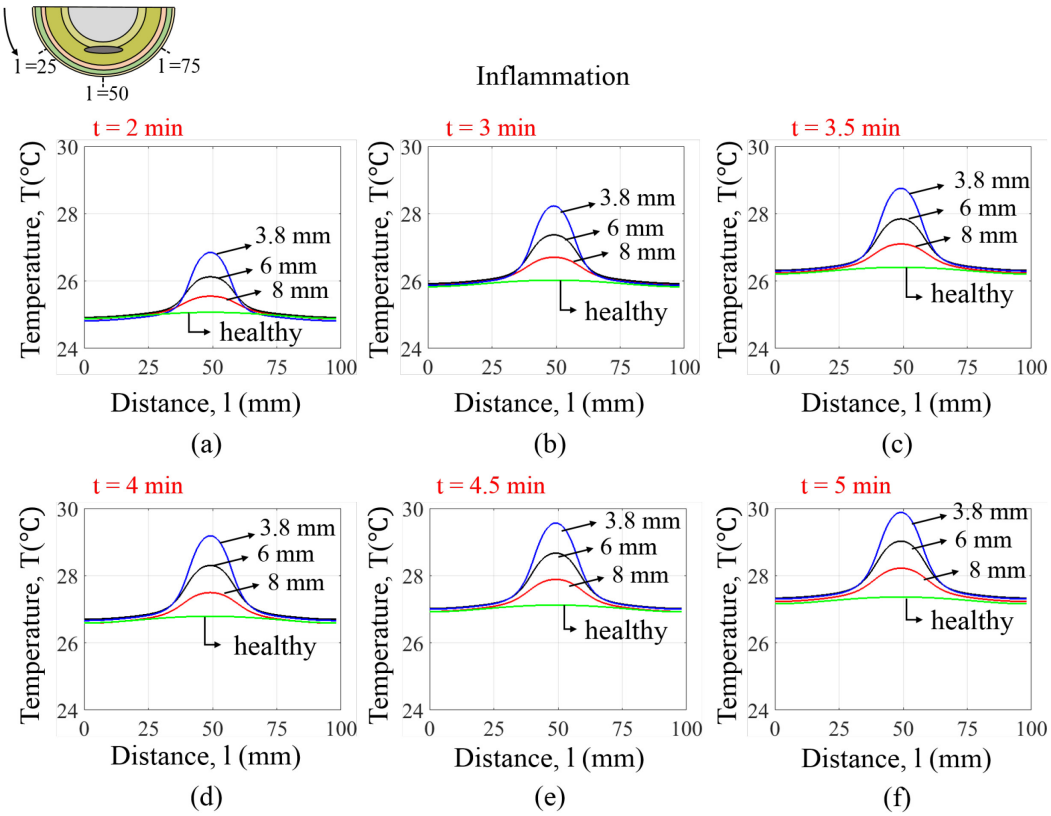

Figure 3.15 Impact of DTI inflammation lesion depth on the transient skin surface temperature profiles. Skin surface temperature profiles are plotted along the perimeter of the heel (l shown in top schematic) for healthy tissue (green) and lesions at depths h = 3.8 mm (blue), 6 mm (black) and 8 mm (red). The results are shown for thermal recovery times of (a) t = 2 min, (b) t = 3 min, (c) t = 3.5 min, (d) t = 4 min, (e) t = 4.5 min and (f) t = 5 min, when the temperature differences of interest are large. DTI dimensions: d_1 = 1.5 cm (major axis), d_2 = 0.25 cm (minor axis).

compared to inflammation. These trends can be explained by our findings from Chapter 2, section 2.3 indicating that the skin temperature is less sensitive to changes in fat perfusion (the 6 mm depth ischemia lesion, mainly located in the fat layer) when compared to changes in muscle perfusion (the 8 mm depth ischemia lesion, mainly in the muscle layer). The thermal signatures of the ischemia lesions are affected by the competing effects of the lesion depth and the sensitivity of the skin temperature to the blood perfusion in the tissue layer affected by the DTI.

Figure 3.16 displays the computed transient thermal signatures ΔT_{isc} for DTI ischemia and ΔT_{inf} for DTI inflammation lesions for the duration of 2- 5 minutes of the thermal recovery process. The results are shown along the heel perimeter for the location range l = 25 mm to 75 mm (l is shown in top schematics), that provides the best spatial sensitivity for detecting the thermal signatures of the DTI lesions (dimensions: d_1 = 1.5 cm major axis, d_2 = 0.25 cm minor axis) of this study. The early thermal recovery times from 2-5 minutes were selected because they are sufficient for best sensitivity in dynamic thermal imaging. The temperature differences computed from the healthy and DTI

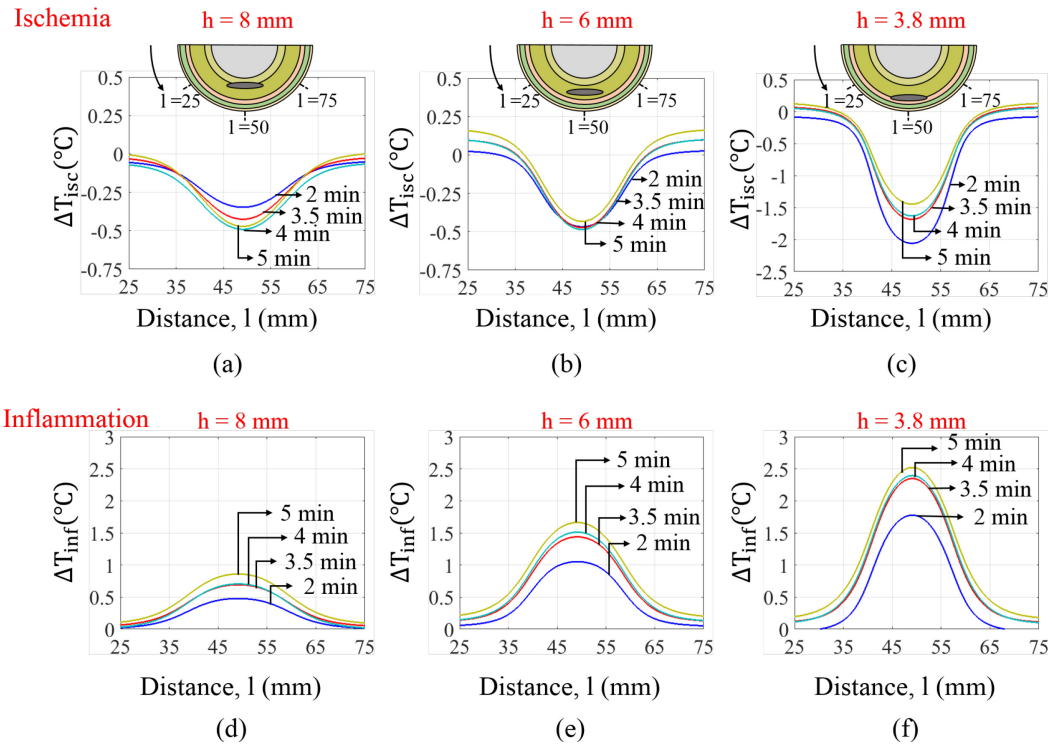

Figure 3.16 Thermal signatures of DTI ischemia and DTI inflammation from transient analysis. Skin surface temperature differences, ΔT ($T_{DTI} - T_{healthy}$), plotted from l = 25 mm to 75 mm (l shown in top schematics) at thermal recovery times t = 2, 3.5, 4 and 5 minutes for DTI ischemia lesions (ΔT_{isc}) at (a) h = 8 mm, (b) h = 6 mm and (c) h = 3.8 mm depth and for DTI inflammation lesions (ΔT_{inf}) at (d) h = 8 mm, (e) h = 6 mm and (f) h = 3.8 mm depth.

ischemia models ($\Delta T_{isc} = T_{isc} - T_{healthy}$) are shown in the top row of Figure 3.16. During the first 2 - 5 minutes of the thermal recovery period, the temperature decreases ΔT_{isc} varied in the range of 0.38°C to 0.5°C for an 8 mm deep lesion (Figure 3.16 (a)), 0.45°C to 0.5°C for a 6 mm deep lesion (Figure 3.16(b)) and 1.4°C to 2°C for a 3.8 mm deep lesion (Figure 3.16(c)). These are relatively large temperature differences can easily be measured with modern IR cameras in a clinical setting. The temperature differences obtained from healthy and DTI inflammation models ($\Delta T_{inf} = T_{inf} - T_{healthy}$) are shown in the bottom row of Figure 3.16. ΔT_{inf} varied in the range 0.25°C to 0.9°C for an 8 mm deep lesion (Figure 3.16(d)), 1.0°C to 1.6°C for a 6 mm deep lesion (Figure 3.16(e)) and 1.7°C to 2.5°C for a 3.8 mm deep lesion (Figure 3.16(f)). Again, these temperature differences can be measured with modern IR cameras in a clinical setting.

We observed that early recovery times (2–4.5 minutes).present stronger measurement signal for ischemia lesions in comparison to later recovery times. The values for ΔT_{isc} for the 3.8 mm deep ischemia lesion decreased after t = 2 minutes into the thermal recovery period (Figure 3.16(c)). For the 6 mm and 8 mm deep ischemia cases, this decrease in the values for ΔT_{isc} was observed after t = 4.5 minutes of the thermal recovery period (Figures 3.16 (a) and (b)). In contrast, the thermal signatures of the inflammation cases increased with increasing recovery times, reaching a maximum at t = 5 minutes. These results suggest that the imaging times of 1-5 minutes of the thermal recovery will be sufficient for best sensitivity in dynamic thermal imaging of both DTI ischemia and DTI inflammation lesions.

3.6.3 Thermal signatures of irreversible DTIs

Irreversible damage can occur in DTIs if the initial ischemic lesion evolves as a pure inflammation lesion or turn into a multilayer DTI. A pure inflammation lesion could also turn into a multilayer DTI if the central portion becomes necrotic. The thermal signatures of a pure inflammation lesion will be similar to reversible inflammation DTI which are discussed in section 3.6.2. In this section, we discuss the thermal signatures of a multilayer DTI that represents a case of an irreversible DTI damage. We model an irreversible DTI as a multilayer DTI. A 1.5cm by 0.5 cm large elliptical ischemic lesion is surrounded by a 1.25 mm thick inflammation layer. It should be noted that the multilayer DTI is larger than the single layer DTI, considered previously. The thermal signature of the multilayer DTI on the skin surface will be affected by the combined effects of ischemia and inflammation. The analysis is presented for three lesion depths: h = 8mm, h = 6 mm and h = 3.8 mm. The steady state signatures are presented in section 3.6.3.1 and the transient signatures are presented in section 3.6.3.2.

3.6.3.1 Steady state signatures (irreversible DTIs)

Steady state heel temperatures were computed using healthy tissue and multilayer DTI models by solving Equations 3.1 to 3.6. Figure 3.17 displays the color coded temperature distributions computed for three depths of multilayer DTI lesions: h = 8mm (Figure 3.17(a)), 6 mm (Figure 3.17(b)) and 3.8 mm (Figure 3.17(c)). The ROI for displaying the temperature distributions is outlined by a dashed red box in the top left schematic. The locations of the tissue layers and DTI are indicated by the black lines. For the steady state conditions, the tissue temperature patterns for the multilayer DTI matched

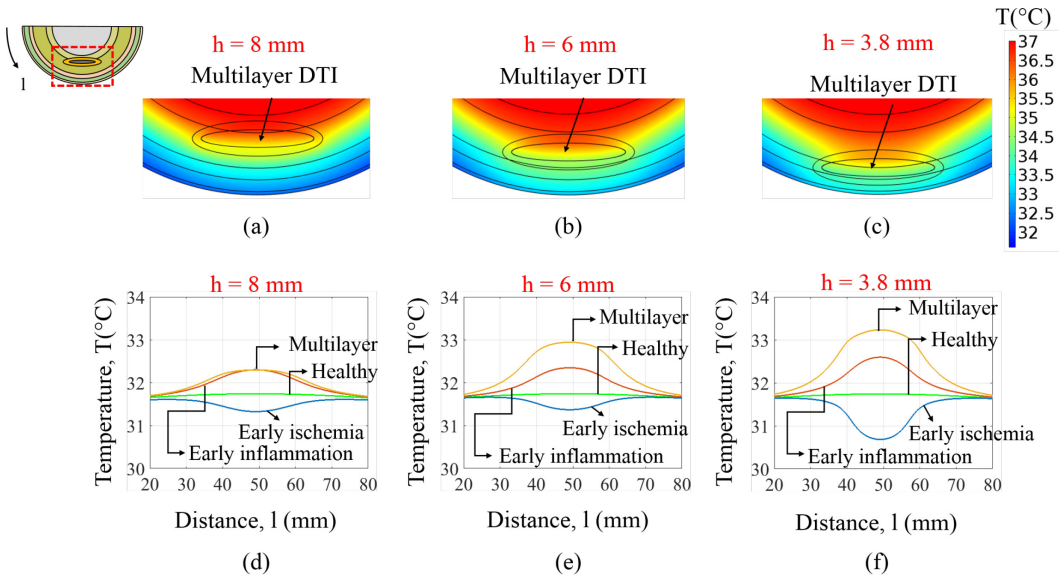

Figure 3.17 Steady state temperature distributions for the multilayer DTI cases. Color coded 2D temperature distributions for multilayer DTI lesion at depths (a) h = 8 mm, (b) h = 6 mm and (c) h = 3.8 mm. Skin surface temperature profiles plotted along the perimeter of the heel (from l = 20 to 80 mm) for multilayer DTI lesions at depth (c) h = 8 mm, (d) h = 6 mm and (e) h = 3.8 mm. The skin surface temperature profiles for healthy tissue and DTI ischemia, DTI inflammation at the same depth are also shown in the bottom row plots.

the temperature patterns for the DTI inflammation lesions (discussed in section 3.6.2.1). An increase in tissue temperature was observed for all three multilayer DTI cases (Figure 3.17 (a) – (c)). The net temperature increase for a multilayer DTIs indicates that the effects of tissue inflammation (present in the outer rim) dominate the effects of tissue ischemia (present in the central portion) in steady state conditions.

Figure 3.17 (d) – (f) display the steady state skin surface temperatures in the presence of multilayer DTIs (yellow) for the three lesion depths. The computed steady state temperature profiles of the healthy skin (green), reversible DTI ischemia (blue) and reversible DTI inflammation (red) at same depths are also shown in the plots. It should be noted that the width of the multilayer DTI is larger than reversible DTIs, due to an outer

inflammation layer. An increase in skin surface temperature was observed for all multilayer cases (Figure 3.17 (d) – (f)). The temperature increase for an 8mm deep multilayer DTI (Figure 3.17 (d)) was equal in magnitude to the increase for an 8 mm deep reversible DTI inflammation lesion , which is smaller (1.5cm by 0.5 cm large). For the 6mm (Figure 3.17 (e)) and 3.8 mm (Figure 3.17 (f)) deep multilayer DTI lesions, the temperature increases are larger in magnitudes when compared increases for reversible DTI inflammation lesions at the same depths. The skin temperature decreases due to tissue ischemia are dominated by the temperature increases due to tissue inflammation, resulting in a net temperature increase in the healthy tissue in steady state conditions.

3.6.3.2 Transient thermal signatures (irreversible multilayer DTIs)

Figure 3.18 shows the transient thermal recoveries of the skin surface in the presence of multilayer DTI lesions. The thermal recovery as a function of time was computed for the three multilayer DTI depths and results were compared with healthy tissue as well as DTI ischemia, inflammation results for the same lesion depth (Figures 3.18 (a)– (c)). Again, when compared to the steady state analysis (section 3.6.3.1), the transient analysis for multilayer DTIs can provide more information about the properties of DTIs and allow us to distinguish between inflammation only and multilayer DTIs.

Figure 3.19 displays the steady state skin surface temperature distributions and the transient skin temperatures during early recovery times (t = 10 to 210s) for three multilayer DTI depth cases (schematically shown in Figure 3.19(a), (d) and (i)). The surface temperatures are displayed for the locations l = 20 to 80 mm along the heel periphery. The

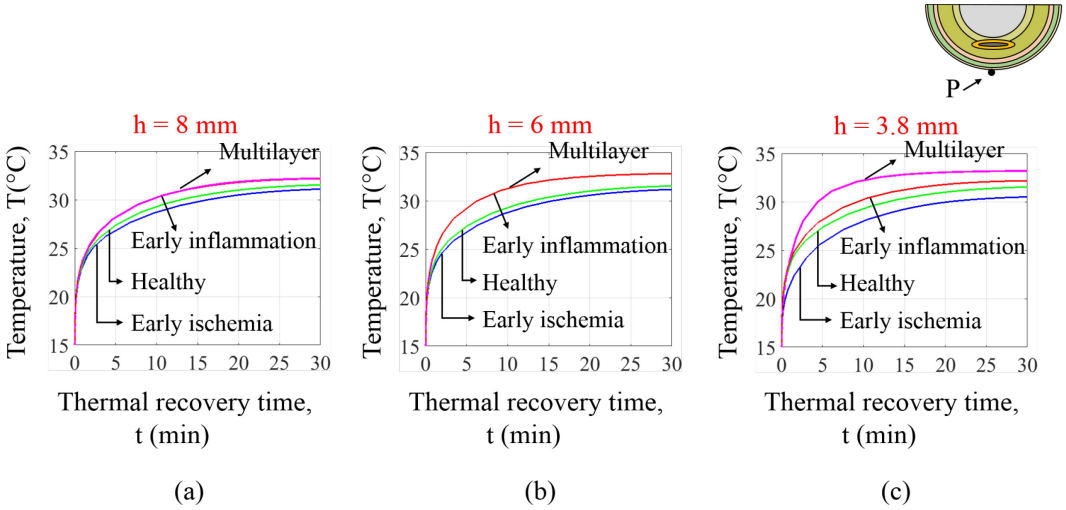

Figure 3.18 Skin temperature as a function of thermal recovery time for healthy tissue, multilayer DTIs, DTI ischemia, DTI inflammation for the DTI lesions at depths (a) h = 8 mm, (b) h = 6 mm and (c) h = 3.8 mm. The skin temperature was computed at point P shown in the top right schematic.

steady state temperatures show only a temperature increase with respect to the healthy tissue case as shown for h = 8mm in Figure 3.19(b), h = 6mm in Figure 3.19 (e) and h = 3.8 mm depth case in Figure 3.19 (j). In contrast, the transient temperatures show both a local temperature decrease (ischemia dominated thermal signature) and a local temperature increase (inflammation dominated thermal signature) compared to the healthy tissue. The surface temperature distribution is a result of the competing effects of temperature decrease, an indication of ischemia, and temperature increase, an indication of inflammation. Temperature decrease is detectable on the skin surface only during the early stages of the transient analysis and not during steady state. The temperature decrease was observed within the first 30s for the multilayer DTI cases (Figure 3.19 (c), (f) and (i)). After this period, only temperature increase was observed as the skin surface temperature recovered further (Figure 3.19 (c), (f) and (i)). These results clearly illustrate the possibilities of generating larger temperature differences (measurement signals) and

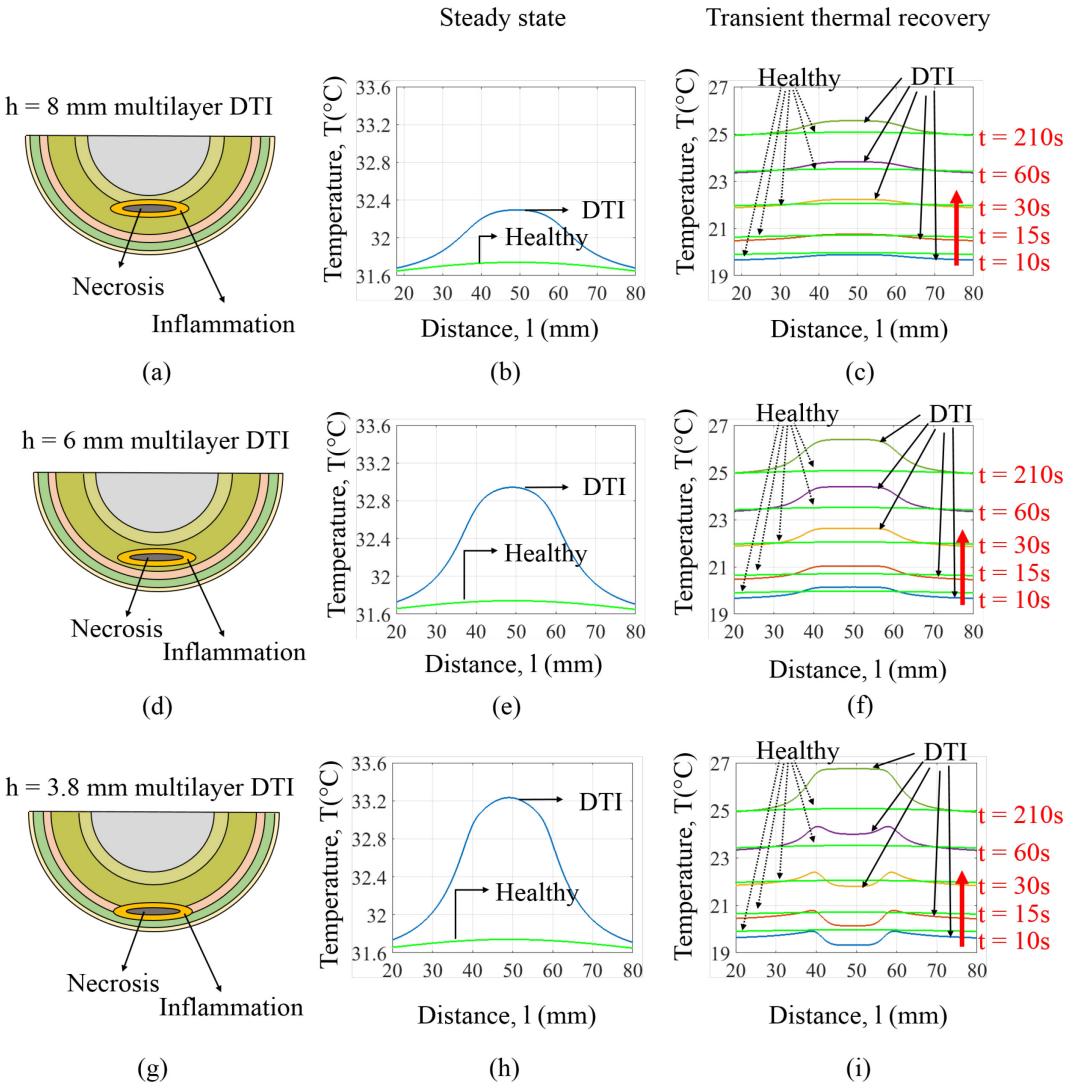

Figure 3.19 Steady state and transient thermal signatures of multilayer DTI lesions. Schematics of multilayer DTI lesions are shown for (a) h = 8 mm, (d) h = 6 mm and (g) h = 3.8 mm deep lesions. The central grey portion represents the necrotic region and the surrounding orange portion represents inflammation. The steady state thermal signatures of multilayer DTI lesions are shown for the depths (b) h = 8mm, (e) h = 6 mm and (h) h = 3.8 mm. The temperature is plotted as a function of the distance l along the heel periphery (shown in left schematics) between l = 20 mm to l = 80 mm where the temperature differences of interest are large. The transient thermal signatures of multilayer DTI lesions are shown for thermal recovery times t = 10s, 15s, 30s, 60s and 210s for (c) h = 8mm, (f) h = 6mm and (i) h = 3.8 mm deep lesions.

reducing measurement errors by using dynamic IR imaging contrasted to steady state

techniques.

Also, using dynamic infrared imaging and the transient analysis, we are able to quantitatively detect the presence of irreversible multilayer DTIs. This feature is important in a clinical setting, as the clinician is able to gain better insight into the level of damage as well as detect irreversible damage soon. In this way, measures to alleviate further damage can be implemented sooner and the overall impact on the health of the patient can be reduced.

3.7 Discussion - thermal signatures of DTIs

Quantitative diagnostic imaging tools are needed for the early detection of DTIs to gain better insight into the state and level of tissue damage. Our computational modeling analysis for DTIs shows that infrared imaging can be used for detecting the manifested skin temperature changes associated with ischemia and inflammation in DTIs. Since infrared imaging offers a non-invasive, non-contact and quantitative method that could be used in clinics, it could be a valuable tool to the clinicians for diagnosing and assessment of DTIs.

Our computational modeling results provide better insights into the biophysical processes underlying the temperature changes manifested on the skin surface during DTI occurrence and progression. The results show that the previous thermographic findings of temperature increases and temperature decreases for pressure injuries can be explained in terms of tissue inflammation and ischemia, respectively. The proposed thermal stages for DTIs are based on the long-term skin temperature evolution during DTI occurrence and progression. A reversible-damage DTI is associated with a milder incipient injury that is reversible in nature with proper clinical care and characterized by milder ischemia and

inflammation. An irreversible damage DTI is represents an aggravated injury that is characterized by unfavorable chemical and biophysical processes occurring during ischemia-reperfusion. The thermal labeling of DTIs as reversible-damage and irreversible-damage injuries offers a quantitative, objective and a convenient method to classify the severity and the type of the DTI which is suitable for clinical use. The proposed thermal classification derived from this computational study would complement the longitudinal thermographic scans of the at risk patients.

Thermographic scans of the tissue at risk for DTI will either show temperature decrease, increase or no temperature difference, when compared to the temperature of the surrounding healthy skin or the healthy tissue temperature of the same body part (unaffected symmetrical location) measured at an earlier time. We have incorporated ischemia and inflammation as key thermal variables in our computational models to account for the sequential progression of DTIs by ischemia or ischemia – reperfusion mechanisms. The quantitative thermal signatures associated with tissue ischemia, inflammation and with the combination of ischemia and inflammation have been computed in this study. We demonstrated that the tissue with early ischemia and inflammation DTI or a multilayer DTI can be identified by measuring either steady state temperature distributions or the thermal response to the cooling stress and comparing it with the thermal response of the healthy tissue. By obtaining thermographic measurements of DTI subjects and comparing measurement data to the data computed from the ischemia, inflammation and multilayer models, clinicians can gain better quantitative insight into the properties and stages of DTIs. Additionally, the temperature data obtained by IR imaging can be coupled

with inverse reconstruction techniques [103] to obtain key parameters of the DTI lesion, such as dimensions, depth, blood perfusion rate and metabolic heat generation rates.

Furthermore, our computational modeling study illustrates the advantages of dynamic infrared imaging over static infrared imaging for the diagnosis and assessment of DTI. We demonstrated that the thermal signatures of DTIs during steady state conditions can be enhanced by considering transient thermal recoveries of the skin surface from a cooling excitation. Additionally, we showed that the transient analysis can provide more information about the type of DTI (ischemia or inflammation or multilayer) when compared to the steady state analysis. Our analysis for the multilayer DTI case is an example to demonstrate that considering the transient skin temperatures has advantages over the steady state thermal analysis. The transient thermal recovery of the affected area can detect the effects of ischemia and inflammation present in the multilayer DTI lesion, in contrast to the steady state analysis that could only detect inflammation and could potentially underestimate the severity of the injury in a clinical setting. To illustrate the potential of inverse reconstruction techniques coupled with IR imaging for DTI assessment, we show examples of reconstruction of DTI size, blood perfusion and depth based on the computed steady state temperature data in the next section.

3.8 Inverse method applied to the bioheat transfer model for DTIs – measuring DTI properties from thermal signatures

In the previous sections, we solved a direct bioheat transfer problem by computing the skin surface temperatures for known geometrical and thermophysical properties of DTIs. Our model demonstrated that the characteristic thermal responses of DTI ischemia

and inflammation lesions can be measured using thermographic imaging. In this section, our aim is to solve an inverse bioheat transfer problem of estimating the geometrical and thermophysical properties of DTIs using the skin surface temperature distributions [103]. We applied the Levenberg – Marquardt (LM) method [104] to solve the inverse problem of estimating the depth, size and blood perfusion rate of the DTI. This preliminary analysis is based on the steady state characteristic responses of DTIs and a 15 mm by 6 mm large elliptical DTI ischemia lesion (with 50% blood perfusion rate when compared to the surrounding healthy tissue) was used as the test case for the simulations.

The LM method is a minimization technique [104] that is used for solving the least squares curve fitting problems. The damping term in the minimization formulation of the LM method makes it more robust when compared to the traditional least square approaches. In this study, the LM algorithm estimates the best set of lesion parameters by minimizing the difference between the measured and the computed skin surface temperatures in a least squared sense. The mathematical details [105] are provided in the Appendix. Initially, a measured skin temperature profile and an initial guess of the unknown parameters is provided to the algorithm. The measured data in this study correspond to the data obtained from our computational phantom for the selected test case. The skin temperature profile is computed for the guessed parameters and is compared with the measurement data. The next set of parameters is estimated iteratively until the sum of the squared error between the measured and the computed data is minimized. We can simultaneously and accurately estimate two parameters using the steady state skin surface temperatures [105]. In this study, we focused on three parameters– the depth h, the size d_1 (major axis of the lesion) and the blood perfusion rate ω, that are most relevant for DTIs.

To evaluate these parameters using the steady state temperatures, we tested three cases (1) the size and the depth are unknown, (2) the size and the blood perfusion rate are unknown and (3) the depth and the blood perfusion rate are unknown [105]. In the next section, we will present the results for these three cases.

3.8.1 Results of the inverse problem

Reconstructing DTI geometry (known blood perfusion rate) – Our goal is to estimate the depth and the size (dimension of the major axis) for an ischemic DTI lesion that has 50% blood perfusion rate of the surrounding healthy tissue. We modeled a 15 mm by 6 mm large DTI lesion at the depths of 8mm, 6 mm and 3.8mm from the skin surface. For these three lesions, the skin temperature data obtained from the computational phantom serve as the measurement data for the LM algorithm. Table 3.3 summarizes the actual values and the initial guesses used for estimating the sizes and depths for each lesion. The top row in Figure 3.20 illustrates the iterative progression of the initial guesses (set 2 from Table 3.3) to the actual values of the DTI parameters. The black lines correspond to the depth estimates and the blue lines correspond to the size estimates. The bottom row shows the variation of the sum of the squared error, S with the number of iterations. The parameter

Table 3.3 Initial guesses for the inverse estimation of depths and sizes for an ischemic DTI. The blood perfusion levels are assumed to be 50% of that of the surrounding healthy tissue.

Actual values	ω = 50% ischemia		ω = 50% ischemia		ω = 50% ischemia	
	h = 8 mm	d_1 = 15 mm	h = 6 mm	d_1 = 15 mm	h = 3.8 mm	d_1 = 15 mm
Guess 1	6	12	5	13	2.5	10
Guess 2	9	13	4	10	2.9	12
Guess 3	7	12	3	19	1.5	10

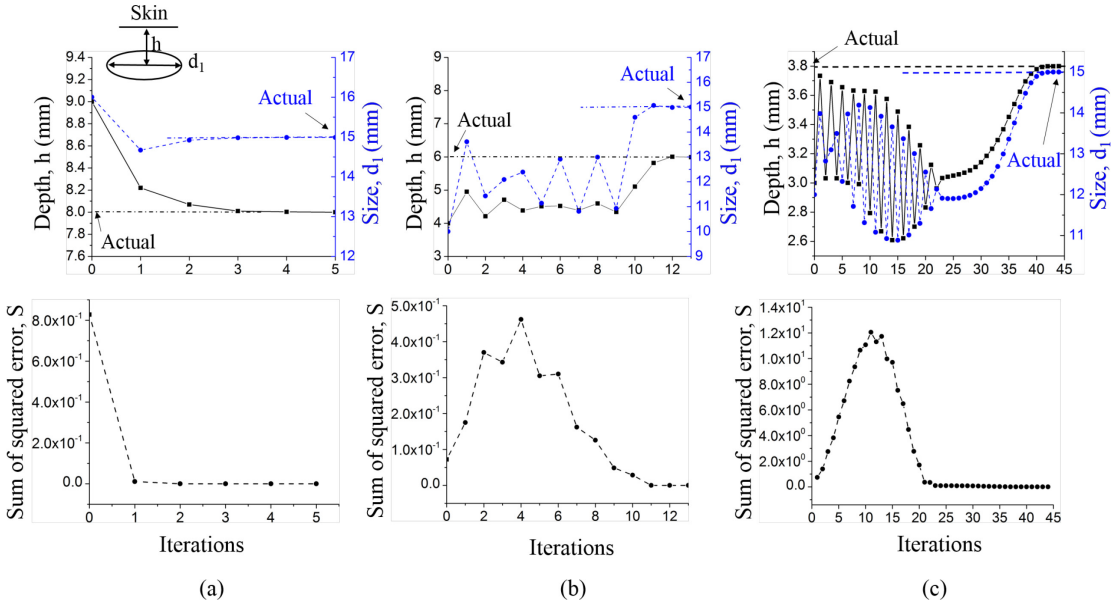

Figure 3.20 Size (d_1) and depth (h) estimates for an ischemic DTI lesion which has 50% blood perfusion rate of the surrounding healthy tissue. The inverse estimates are shown for a DTI lesion which is (a) 8 mm deep, (b) 6 mm deep and (c) 3.8 mm deep, all with a 15 mm large major axis. The minor axis of the lesion is assumed to be 0.5 times to the dimension of the major axis.

values converged to their actual values within 5 iterations for the 8 mm depth lesion (Figure 3.20 (a)), 12 iterations for the 6 mm depth lesion (Figure 3.20 (b)) and 45 iterations for 3.8 mm depth lesion (Figure 3.20 (c)). The other two sets of initial guesses (sets I and III from Table 3.3) also converged to the actual values indicating the uniqueness of the solution. These results demonstrate that, by using the steady state analysis, it is possible to estimate the depth and the size of the DTI simultaneously. We were able to estimate a 15 mm by 6 mm large DTI ischemia lesion between 3.8 to 8 mm depths.

Reconstructing DTI size and blood perfusion rate (known depth): The objective is to determine the size (dimensions of the major axis) and the blood perfusion rate for a DTI ischemia lesion which is 3.8 mm deep. We modeled a 15 mm by 6 mm large DTI lesion with a blood perfusion rate of $\omega = 0.0005$ 1/s. For this lesion, the skin temperature data

obtained from the computational phantom serve as the measurement data for the LM algorithm. Table 3.4 summarizes the actual values and the initial guesses for the major axis dimensions and the blood perfusion rates. The different values of initial guesses were used to test the uniqueness of solution. Figure 3.21 illustrates the iterative progression of the solution from the initial guesses (set 1 from Table 3.4) to the actual values. The black lines correspond to the size estimates and the blue lines correspond to blood perfusion estimates. The bottom row shows the variation of the sum of the squared error S with the number of iterations. The parameter values converged to their actual values within 18 iterations for guess 1, 5 iterations for guess 2 and 5 iterations for guess 3. These results demonstrate that, by using the steady state analysis, it is possible to estimate the size and the blood perfusion rate of an ischemic DTI.

Reconstructing lesion depth and blood perfusion (known size): The goal is to estimate the depth and the blood perfusion rate for an elliptical DTI lesion which is 15mm by 6mm. We modeled a 3.8 mm deep lesion with a blood perfusion rate of $\omega = 0.0005$ 1/s. For this lesion, the skin temperature data obtained from the computational phantom serve as the measurement data for the LM algorithm. Table 3.5 summarizes the actual values and the initial guesses for the depth and the blood perfusion rate of the lesion. These different values of initial guesses were used to test the uniqueness of the inverse reconstruction.

Table 3.4 Initial guesses for the inverse reconstruction of DTI size and blood perfusion rate for a known depth

Actual values	h = 3.8 mm	
	d1 = 15 mm	ω = 0.0005 1/s (50% ischemia)
Guess 1	11	0.001
Guess 2	12	0.0003
Guess 3	12	0.001

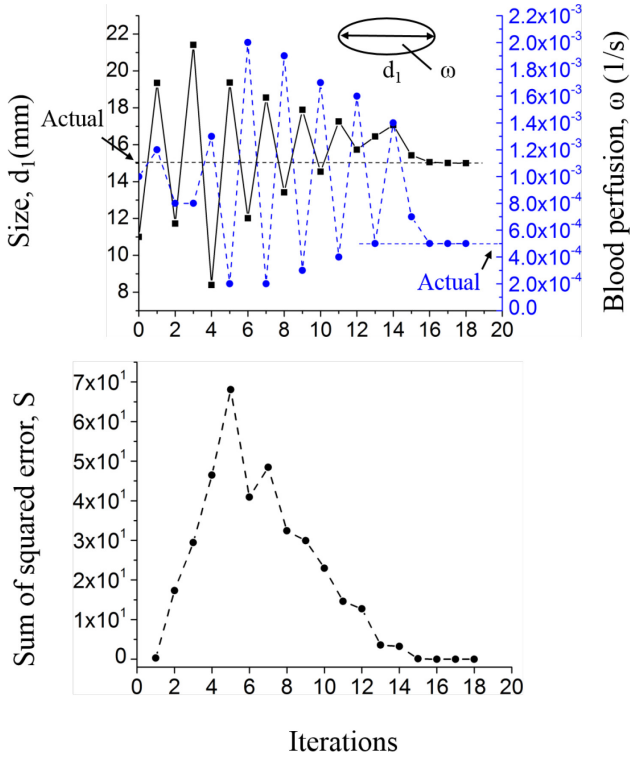

Figure 3.21 Size (d_1) and blood perfusion rate (ω) estimates for an ischemic DTI at 3.8 mm depth (top row) and the convergence of the iterative inverse computation (bottom row).

Figure 3.22 illustrates the iterative progression of the solution from the initial guesses to the actual values for initial guesses (set 3 in Table 3.5) for the size and blood perfusion. The black lines correspond to the size estimates and the blue lines to blood perfusion estimates. The bottom row shows the variation of the sum of the squared error, S with the

Table 3.5 Initial guesses for the inverse estimation of DTI depth and blood perfusion rate for a given size

Actual values	d1 = 1.5 cm, d2 = 0.6 cm	
	h = 3.8 mm	ω = 0.0005 1/s (50% ischemia)
Guess 1	3	0.0003
Guess 2	2.5	0.0003
Guess 3	2	0.0003

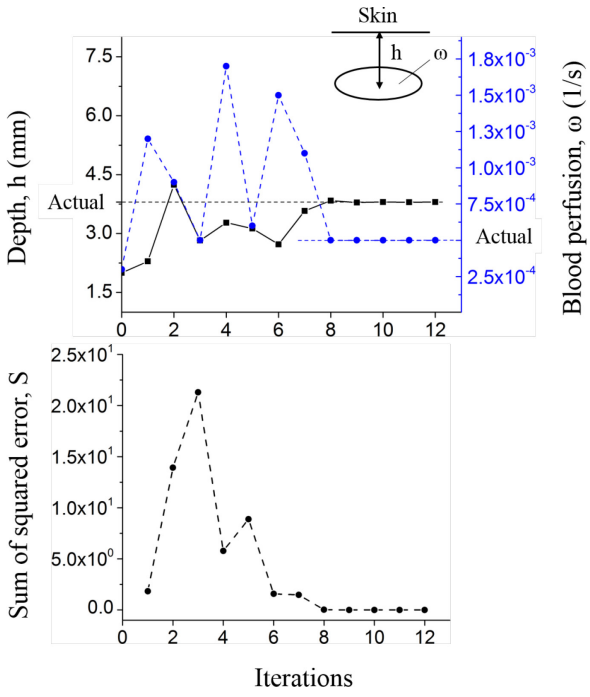

Figure 3.22 Depth (h) and blood perfusion rate (ω) estimates for an ischemic DTI lesion of size 1.5 cm by 0.6 cm (top row) and the convergence of the iterative inverse computation (bottom row).

number of iterations. The two lesion parameters converged to their actual values within 9 iterations for guess 1, 7 iterations for guess 2 and 12 iterations for guess 3. These results demonstrate that, by using the steady state analysis, it is possible to estimate the size and the blood perfusion rate of an ischemic DTI.

In summary, our computational thermal model and inverse reconstruction approach will help the clinicians relate thermographic findings with key physiological changes, to identify patients at risk at an early stage of the injury, and to provide necessary intervention to prevent the spreading of the DTI. The proposed thermal classification from this computational study for quantitatively documenting the stage of the DTI, would benefit

from the longitudinal thermographic scans combined with ultrasound or MRI images of the at risk patients. IR imaging coupled with inverse reconstruction techniques for DTIs provides a quantitative, inexpensive and non-invasive tool to assess tissue damage, which is suitable for a clinical setting.

Chapter 4 Quantitative assessment of infantile hemangiomas using combined infrared and white-light imaging

Overview

The aim of this chapter is to present quantitative assessment of vascular infantile hemangiomas (IHs) with the combined white – light and infrared imaging technique. First, IHs are introduced in section 4.1, with brief descriptions of their life-cycle (proliferation, plateau and involution phases) and the depth of subcutaneous involvement based classification (superficial, mixed and deep). A review of current assessment techniques for infantile hemangiomas is presented in section 4.2. Next, the white-light and steady state infrared imaging and image processing for obtaining the color and thermal signatures of lesions are discussed in sections 4.3 through 4.4. Sample hemangioma cases are assessed using the combined imaging technique in section 4.5. Finally, the main findings of the study are summarized in section 4.6.

The major contributions from this chapter are: quantitative assessment of the extent of subcutaneous involvement in different morphological types of infantile hemangiomas (superficial, deep and mixed); interpretation of the thermal signatures in terms of the hemangioma vascular activity in proliferation, plateau and involution phases;

quantification of color differences by comparing hemangioma color and surrounding healthy skin color; and the dimensionless temperature difference formulation for comparing the IR images captured at different times during longitudinal studies.

4.1 Introduction to infantile hemangiomas (IHs)

Infantile hemangiomas (IHs), often referred to as "strawberry" birthmarks, are the most common vascular tumors of infancy [106-109]. They affect approximately 10% of the infant population, while the risks are higher for female subjects and preterm infants born with low body weight [110, 111]. They most often appear present within the first few weeks after birth, with 60% tumors affecting the head and neck region [112]. IHs grow rapidly in size during the first 3-10 months of age and slowly regress with time. Some IHs may be completely resolved by 7-10 years of age [113]. Though most IHs are benign, the location of the IH may be problematic [114] if it impacts vital functioning [106] such as vision (IHs near the eye), airway (IHs involving the nose), feeding (IHs involving mouth or lip). Furthermore, some IHs can cause excessive cosmetic disfigurement or may be complicated by ulceration [106, 107]. Objective, quantitative imaging tools are needed to assess IH growth and regression and evaluate treatment response for long term monitoring of IHs in routine clinical practice. Early assessment and treatment can prevent complications and will benefit IH subjects in the long run.

4.1.1 Life cycle

Infantile hemangiomas demonstrate unique characteristics during their life cycle that differentiate them from other vascular malformations [112], such as venous malformations and arterio - venous malformations. However, their pathogenesis is still not

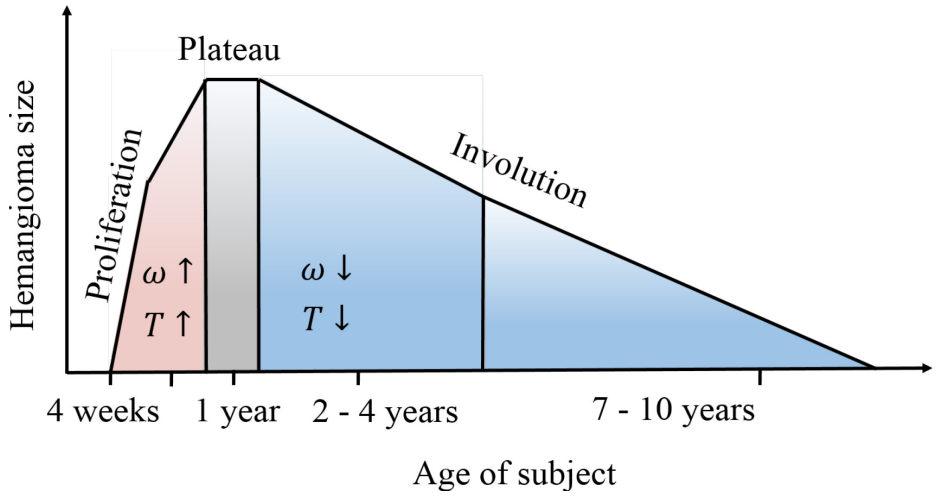

Figure 4.1 Lifecycle of an infantile hemangioma. Hemangiomas enter a rapid growth phase of proliferation (pink region) that lasts for almost 1 year characterized by rapid growth of lesion, increase in vascularity (or blood perfusion ω) and tissue temperature, T. Upward arrows indicate increase in these two parameters. Proliferation is followed by a short plateau phase of growth arrest (grey region) and finally by a long involution phase (blue region). Involution phase shows slow regression that is marked with decrease in blood perfusion ω and temperature, T. Downward arrows represent the decrease in these two parameters.

well understood, which drives the research for new treatment drugs [113, 115]. The schematic in Figure 4.1 illustrates the lifecycle of an IH lesion where the evolution phases are marked along with their characteristic features. Hemangiomas appear within few weeks after birth, enter into a rapid growth (proliferation) phase of almost one year, which is followed by a phase of slow regression (involution phase) that may last 7-10 years [39, 112], as shown in Figure 4.1. A short period of growth arrest (plateau phase) also occurs between proliferation and involution (Figure 4.1) [113]. The proliferation phase shows increase in lesion size [39], vascularity [116] and temperature [117]. Formation of new capillaries occurs during the proliferative growth phase [112]. The upward arrows shown for blood perfusion, ω and temperature, T in Figure 4.1 indicate increased vascularity and IH temperature. The involution phase shows decrease in lesion size, decrease in lesion

vascularity and increase in replacement of tumor tissue by fibrous fatty tissue [112]. Downward arrows for blood perfusion and lesion temperature during lesion involution illustrate this trend in Figure 4.1.

4.1.2 Classification

Infantile hemangiomas are classified on the basis of their appearance (color) and the depth of subcutaneous tissue involved as superficial, deep and mixed [106]. Examples of IH in each category are shown in Figure 4.2. The top row shows the white-light (WL) images or digital photographs of the three sub-types of IHs – superficial (left), mixed (middle) and deep (right). The bottom row shows schematics including the cross sections of the subcutaneous region of the tissue affected by the IH lesion (shown in red). The depth of IH is measured by the extent of the subcutaneous tissue involving each category. The schematics are based on histological findings that show IHs infiltrating dermal and subcutaneous layers of the tissue during proliferating stages [118]. Superficial (or strawberry) IHs have a visible superficial portion that is limited to the regions above the skin surface (Figure 4.2(a), bottom row). They are easy to diagnose due to their bright red color and the characteristic flat or raised appearance (top row, Figure 4.2(a)). In contrast to superficial hemangiomas, deep (or cavernous) hemangiomas have a deep subcutaneous portion that is covered with an overlaying healthy skin layer (bottom row, Figure 4.2(b)). The hemangioma may either be lightly visible, as shown in top row of Figure 4.2(b), or not visible at all. Subcutaneous hemangiomas are difficult to diagnose by their appearance, as they only present light red or light blue discoloration of the skin (top row, Figure 4.2(b)). Mixed hemangiomas consist of both superficial (visible) and subcutaneous (less visible or

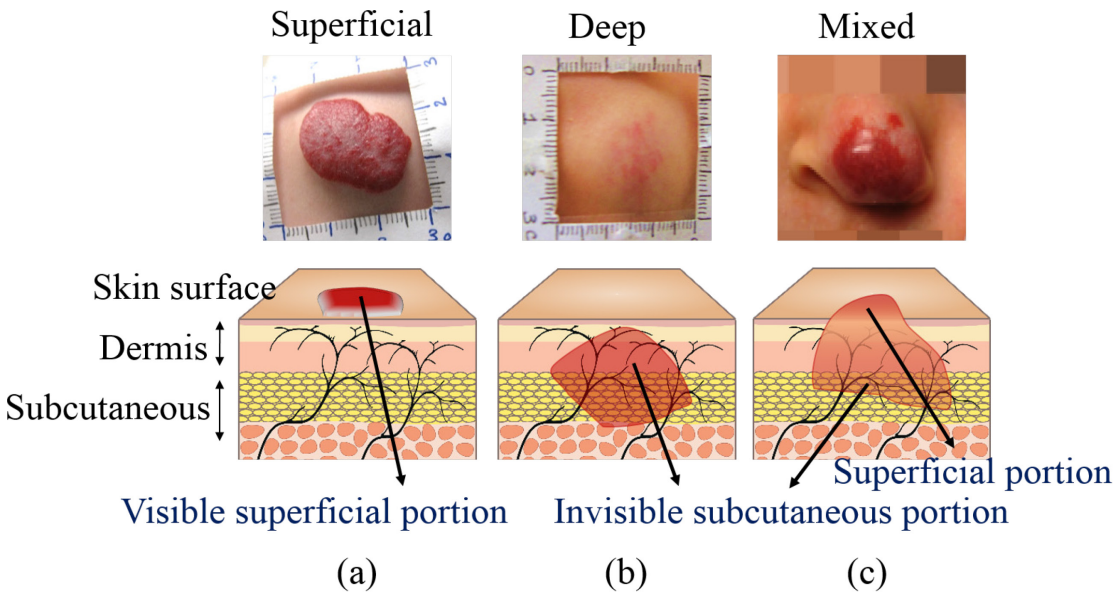

Figure 4.2 Clinical classification of IH based on the depth of subcutaneous involvement. The top row shows the WL images of a (a) superficial, (b) deep and (c) mixed IH. The bottom row depicts the depth of subcutaneous involvement for a (a) superficial IH (the skin layers are affected, lesion is visible in the WL), (b) deep IH (the subcutaneous tissue is mostly affected, subtle discoloration of the skin might be present) and a (c) mixed IH (the skin and subcutaneous tissue are affected. The WL image shows the superficial portion but the subcutaneous portion is invisible).

invisible) portions [106] (top and bottom rows of Figure 4.2 (c)). Figure 4.2 illustrates that we can only identify the extent of the visible portion of hemangiomas by WL imaging. It is important to note that the extent of the subcutaneous portion of the IH lesion cannot be identified by WL imaging alone.

4.2 Current assessment techniques for IHs

Documentation of lesion appearance (i.e. size, shape and color) by capturing a series of digital photographs is a well-established approach in medicine and dermatology [108, 109]. A white-light camera (or a digital camera) captures the light reflected from the skin surface in the visible spectrum (0.4–0.7 μm wavelength) of electromagnetic radiation,

with the light source being white-light (natural, incandescent, neon light, LEDs etc.). A color image of the scene is produced by the WL camera sensor by combining color information from the red, green and blue color filters of the color filter array [119]. Infantile hemangiomas demonstrate changes in lesion appearance as they evolve from proliferation to involution [35]. Drolet [109] documented changes in IH color from bright red during proliferating phase to dull red during involuting phase. Recent studies on assessment of IH color either used subjective color descriptors such as bright red, dull red, blue etc. [35], or a measurement score varying from 0 for mild discoloration to 2 for severe symptoms [36]. These methods rely on the subjective color and appearance interpretation of the clinicians. In this study, we introduced objective, digital image processing tools for the analysis of IH color. Our approach involves representation of lesion and healthy skin colors in a color coordinate system (Figure 4.3(a)) or a color space [120] to quantify the color differences between them. We chose the CIE 1976 (L*, a*, b*) color model (Figure 4.3 (a)), often referred to as the CIELAB color model [121] (CIE stands for Commission internationale de l'éclairage). The advantages of this color model over other conventional color models, such as RGB, CYMK etc., are that it is device independent (not dependent on the parameters of capture device or display equipment) and perceptually uniform (suitable for computing color differences) [121-123]. Additionally, the CIELAB color model can be represented by a simple three dimensional coordinate system with L*, a* and b* as the three coordinates. L* represents the lightness of color (0 for dark to 100 for bright), a* represents the balance between red and green hue (typically -120 for green to 120 for red) and b* represents the balance between yellow and blue hue (typically -120 for blue to 120 for yellow) [122] (as shown in Figure 4.3(a)). Prior studies demonstrate that the CIELAB

model is suitable for color based lesion segmentation [124, 125], relative lesion color assessment in vascular lesions such as hemangiomas [126] and port wine stains [127]; and assessment of skin conditions such as erythema [128, 129]. The CIELAB model has been shown as an effective tool to objectively quantify color differences between lesion and the healthy skin in subjects with hemangiomas and ota (melanocytic) naevi [126]. Kim et al [126] demonstrated that the visually perceived changes in lesion color can be expressed in terms of uniform changes of the three components L*, a* and b* of the CIELAB color space. Madooei and Drew [124] developed a color palette for visualization of the blue-white veil of melanoma lesions by presenting information from the CIELAB color space in the form of Munsell representation of colors.

In this study, we have combined the merits of the CIELAB based color difference analysis [126] and color visualization analysis [124] for color assessment of IH lesions. The color difference maps at lesion location and the average color difference values between lesion and healthy skin could be used for objective, quantitative assessment of IH color with respect to the healthy skin color. Additionally, the representation of colors in the cylindrical Munsell color space, achieved by conversion from the CIELAB to the Munsell though the intermediate CIELCh color space [120, 124, 130], offers an intuitive method of visualization of IH and healthy skin colors. An intuitive representation of color is possible because of the way information is displayed in the cylindrical coordinate system (that is used by both CIELCh model and Munsell color space [120]). In such a system, the color lightness L* (dark vs light) is displayed on the z axis, color saturation or chroma C* (weak vs strong color) is displayed on the radial axis; and color hue h* (e.g. red, yellow,

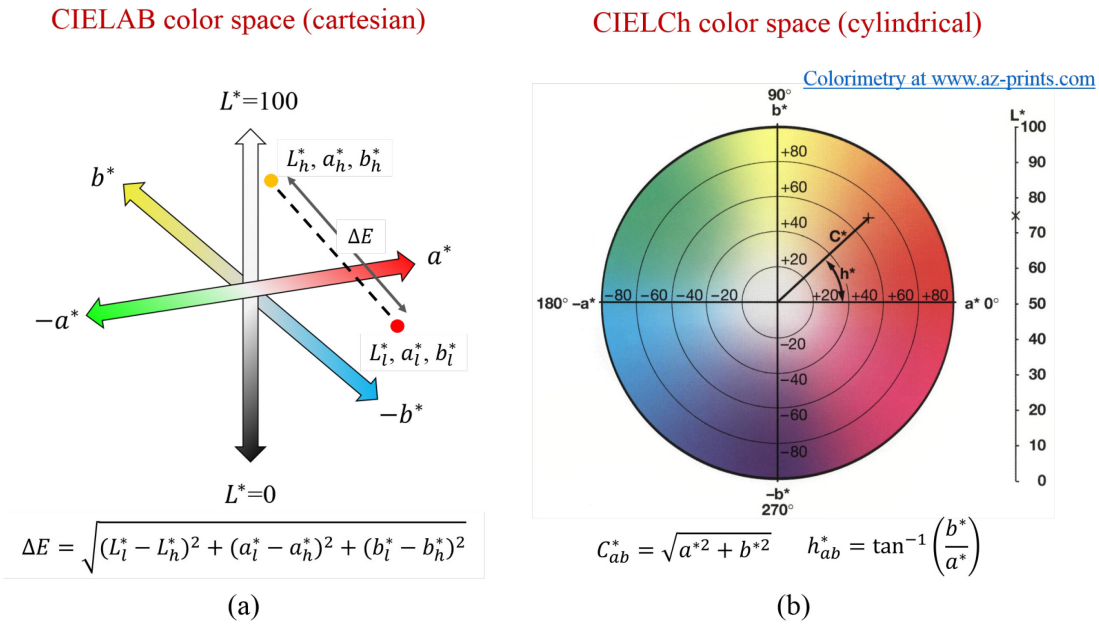

Figure 4.3 Illustrations of the CIELAB and CIELCh color spaces for color analysis of lesions. (a) The CIELAB color space is represented by a 3D cartesian geometry. The vertical axis shows color lightness L^* ($L^* = 0$ for dark, $L^* = 100$ for light); the green – red axis, a^* accounts for the balance between greenness (a^*=*-120*) and redness (a^*=*120*) of a color; yellow – blue axis b^* accounts for the balance between blueness (b^*=*-120*) and yellowness (b^*=*120*) of color. The formula for the color difference ΔE between the two color coordinates L_l^*, a_l^* b_l^* (lesion) and L_h^*, a_h^*, b_h^* (healthy skin) is the distance formula in a cartesian geometry. (b) The CIELCh color space is represented by a cylindrical coordinate system. The vertical axis describes color lightness L^* ($L^* =$ 0 for dark, $L^* = 100$ for light); the radial coordinate C^*or chroma shows color saturation or strength (increases radially outwards). $C_{ab}^* = \sqrt{a^{*2} + b^{*2}}$; the polar coordinate h^* shows color hue ($h^* = 0$ for red, $h^* = 90°$ for yellow etc.) with $h_{ab}^* = \tan^{-1}\frac{b^*}{a^*}$.

green, blue etc.) represents the polar angle (as illustrated in Figure 4.3(b)). Figure 4.2 illustrates the WL imaging technique alone is not suitable for accurate assessment of the extent and activity of IH lesions. The visual observations of WL imaging cannot accurately assess the extent of subcutaneous portions of lesions as illustrated in Figure 4.2 (b) and Figure 4.2 (c). Tsang et al [131] proposed assessment of IH volume by assuming the lesion to be spherical or hemispherical [131], since measurements of diameter or area from the

WL images or paper tapes were not sufficient in cases of subcutaneous or mixed hemangiomas. Tsang et al [131] noted the limitations of this approach due to uncertainties in the assumptions about lesion shape in these calculations. Still, most trials that evaluated treatment response of IHs relied on imprecise area or volume approximations bolstered by qualitative assessments of color and texture, documented with photographs or reported by individual physicians [113, 132-134]. While imaging methods, such as ultrasound, computed tomography (CT) and magnetic resonance (MR) are suitable for imaging subcutaneous tissue structures, except for serious cases, they are not recommended for routine clinical assessment of young infants due to the requirement of sedation or anesthesia or exposure to radiation and high costs [112, 131, 135].

Infrared (IR) imaging is a powerful tool to image and accurately measure small temperature differences on the skin surface with high spatial and temporal resolutions [15, 136]. An infrared camera detects the electromagnetic radiation naturally emitted by a surface (skin) in the 0.7-1000μm wavelength range, which can be related to surface temperature using appropriate calibration methods [15, 136]. As highly vascularized lesions, IHs are uniquely suited for thermographic (IR) assessment, since the increased blood flow through the lesion [116] results in a locally elevated temperature relative to the surrounding healthy tissue [117]. Both IH size and the activity of the hemangioma's vascular network can be assessed using the IR images [117]. The potential for temperature measurements (using IR thermography and other temperature sensors) to track hemangioma over time and manage treatment methods has been recognized prior to this study [20, 26, 37, 38, 117, 137, 138]. The first use of infrared thermography in infantile hemangiomas was reported by Miki [138] and Desmons et al [117]. They independently

observed that deep (cavernous) IHs showed elevated temperatures relative to surrounding healthy skin and maximum temperature differences exceeded 2°C [117, 138]. These studies demonstrated that IR thermography can be used for differentiating IHs from port-wine stains, which do not exhibit elevated temperatures and in determining therapeutic effects in these lesions [117, 138]. Saxena and Willital [20] reported significant temperature increases of 3.0±0.4°C in proliferating IHs, followed by temperature decreases to 1.5±0.3°C above healthy tissue values in involuting IHs. The authors used these data to reach treatment decisions. In prior studies, the temperatures were either measured at the mid-point of IH [38, 117, 138] or along the center line of the IH lesion [20] or an average temperature measure was considered [26, 37]. Such measurements can only serve as reference values, given the large sizes of IH lesions and the temperature variations within the lesions. Burkes et al [137] reported spatial temperature distributions of IHs in their results, but did not explain why elevated temperatures extend beyond the visible boundary. Other studies used contact temperature measurements using digital touch probes to study IHs [26, 38]. The studies demonstrated that the temperature of the lesion can be used to study proliferation and involution [26, 38].

As can be seen, only limited number of temperature measurement studies [20, 26, 37, 38, 117, 137, 138] were carried out either using IR thermography or other temperature sensors. The majority of these studies involved single point measurements and some were contact measurements. Hemangiomas are large lesions (with surface areas that can reach more than 20cm^2 in some cases) that demonstrate changes in vascularity from proliferation to involution [116]. Therefore, single/two point measurements can only provide reference values of IH temperature and vascularity. They do not accurately represent the thermal and

vascular state of the entire hemangioma lesion during the proliferation or involution phases. Furthermore, non-contact temperature measurement methods such as IR imaging demonstrate superior performance compared to contact temperature measurements, especially in medical diagnostic applications. Quantitative measurements, such as temperature distribution over the total lesion surface and estimation of affected area (both superficial and subcutaneous portions), using IR thermography are necessary in quantitative diagnostic applications.

We aim to integrate the advantages of infrared (IR) imaging and white – light (WL) imaging in a combined IR – WL imaging framework for non-invasive, quantitative assessment of IH color, temperature and vascular activity. The imaging method and image processing techniques for quantitative assessment of IHs are presented in section 4.3 and section 4.4. We were able to sample IHs from different anatomical locations – lip (case I), nose (case II), scalp (cases III and IV), back (case V), arm (case VI) and glabella (case VII) at various stages - proliferation, plateau and involution. Two of the lesions analyzed were superficial (cases III and IV), four were mixed (case I, case II, case V, VI) and one was deep (case VII). The assessment of color, temperature and vascular activity of these seven IHs is presented in sections 4.5 and 4.6. The analyzed IR images for cases IV [139], VI [140] and VII [139] are included in the chapter for the sake of completeness of the interpretations in this chapter.

4.3 Combined infrared (IR) and white – light (WL) imaging

We describe a non-invasive, non-contact imaging method for accurate quantitative assessment of infantile hemangiomas. This method is suitable for clinical assessment of

young IH subjects because it requires no sedation or anesthesia. The physical principles of IR imaging and IR camera calibration are presented in sections 4.3.1 and 4.3.2. The details of the clinical study, the experimental setup and imaging method using combined IR and WL imaging are discussed in sections 4.3.3 and 4.3.4.

4.3.1 Physical principles of IR imaging

Infrared imaging relies on the basic laws of blackbody radiation. The spectral radiance, $I(\lambda, T)$, of a blackbody at an absolute temperature, T (K) is given by the Planck's law [141]

$$I_{\lambda,b}(\lambda, T) = \frac{2hc_0^2}{\lambda^5[\exp(hc_0/\lambda kT) - 1]} \tag{4.1}$$

where h = 6.6256 $\times 10^{-34}$ J·s is the Planck's constant, k = 1.3805$\times 10^{-23}$ J/K the Boltzmann constant and c_0= 2.998$\times 10^8$ m/s the speed of light. The spectral emissive power of a blackbody [141] $E_{\lambda,b}(\lambda, T)$ is

$$E_{\lambda,b}(\lambda, T) = \pi I_{\lambda,b}(\lambda, T) = \frac{C_1}{\lambda^5[\exp(C_2/\lambda T) - 1]} \tag{4.2}$$

where C_1= $2\pi hc_0^2$ W·μm^4/m^2 and $C_2 = hc_0/k$ μm·K are the first and second radiation constants. The wavelength corresponding to the maximum emissive power moves to the shorter wavelengths as the temperature increases, which is given by the Wien's displacement law [141]

$$\lambda_{max} T = C_3 \tag{4.3}$$

where C_3 is the third radiation constant. The total emissive power of the blackbody E_b is obtained by integrating Equation 4.2 over all wavelengths that leads to the Stefan – Boltzmann law [141]

$$E_b = \sigma T^4 \tag{4.4}$$

where $\sigma = 5.67 \times 10^{-8}$ W/m^2·K^4 is the Stefan – Boltzmann constant. The emission from a real surface (that does not absorb all incident radiation) is expressed in the form

$$E = \varepsilon \sigma T^4 \tag{4.5}$$

where the emissivity ε is defined as the ratio of the radiation emitted by the surface to the radiation emitted by a blackbody at the same temperature [141]. The emissivity of human skin is constant at a value of 0.98±0.01 in the wavelength range of 2-14μm [4, 142].

4.3.2 IR camera calibration

For temperature measurements with an IR camera, the radiation detected by the camera is converted into temperature information using camera calibration. The response of an IR camera, $I(T)$, to the incident radiation can be represented in the form [13, 143]

$$I(T) = \int_{\lambda_{min}}^{\lambda_{max}} p(\lambda, T) r(\lambda) d\lambda \tag{4.6}$$

where the function $p(\lambda, T)$ describes the spectral radiance of the source (described by Equation 4.1 for a blackbody), $r(\lambda)$ characterizes the spectral response function of the camera and the limits of integration are defined by the wavelength band of the detector (3-5μm for mid-wave, 7-14 μm for long-wave etc.). I must be determined by calibrating the

IR camera against a blackbody of known temperature, T [143]. The radiation incident on the camera consists of radiation emitted by the object attenuated by the atmosphere; radiation from the surroundings reflected by the object and attenuated by the atmosphere; and radiation emitted by the atmosphere. The corresponding relationship [144] is expressed as

$$I = \tau\varepsilon I(T_0) + \tau(1-\varepsilon)I(T_{sur}) + (1-\tau)I(T_{atm}) \tag{4.7}$$

where τ is the atmosphere's transmittance over the wavelength range of interest and ε is the emissivity of the object. T_0, T_{sur} and T_{atm} are the temperatures of the blackbody, surroundings and atmosphere, respectively. For shorter distances from the object surface, the atmospheric absorption is negligible, therefore τ = 1 in Equation 4.7. As shown in Equation 4.7, the object radiation is a function of the emissivity of the object that can vary within the measurement wavelength range.

The procedure for an IR camera calibration that was followed to calibrate our IR imager has been described in detail by Çetingül and Herman [13]. We summarize the procedure here for the sake of completeness. Our IR camera was calibrated against a blackbody (CI Systems SR800) of temperature uniformity of 0.025°C, whose temperature was varied at increments of 0.5°C in the range of 5 - 35°C [13, 145]. While the camera was positioned at a fixed distance (30cm) from the blackbody (with τ = 1 in Equation 4.7) and the ambient temperature was held constant, IR images of the blackbody were captured at each temperature level [13]. The calibration curve that relates pixel intensity to temperature was obtained using a polynomial fit. Because of the radial intensity gradients present in the image, the average intensity of the central pixels (60 x 60) was used for calibration [13].

The calibration procedure was performed three times and the mean difference in the blackbody temperatures between three attempts was 0.026°C, demonstrating the correctness of the procedure [13]. The polynomial fit is of the form [13]

$$\mathrm{T}(℃) = -28 + 0.0018 \times \mathrm{g} - 1.2 \times 10^{-8} \times \mathrm{g}^2 \qquad (4.8)$$

where g denotes the pixel intensities. In the next step of the calibration procedure, the image non-uniformities due to the presence of dead pixels in focal plane array matrix and radial temperature gradients were corrected [13]. The intensity of every dead pixel was replaced by an average intensity of the neighboring four pixels. To correct the radial gradients, a pixel based error map (difference between pixel temperature and blackbody temperature) was calculated for all temperature levels. Çetingül and Herman [13] showed that this error is a function of both pixel location (shown by the bell shaped distribution) as well as the blackbody temperature and needs to be corrected to give accurate temperature information. To account for these dependencies, Çetingül and Herman [13] fitted polynomial models to the error first in terms of pixel position (using multiple least square regression) and then in terms of temperature (using a least square 3rd order polynomial) [13] to obtain correction masks for each temperature level. As a preprocessing step in the image processing of IR images of the skin, this correction mask was added to the uncorrected IR images to account for the inherent image deteriorations [13].

4.3.3 Clinical study

The clinical imaging study was conducted at the Johns Hopkins Children's Harriet Lane Clinic (Department of Dermatology at the Johns Hopkins Medical Institutions) between September 2012 and March 2013 (IRB protocol:NA_00014694, Retrospective

Study to Measure Treatment Outcomes of Vascular Anomalies, and Pediatric Interventional Radiology Procedures). Inclusion criteria consisted of clinical diagnosis of infantile hemangiomas by pediatric dermatologists at Johns Hopkins. The steady state and dynamic infrared imaging technique developed at the Heat Transfer Lab at The Johns Hopkins University [5, 15, 146] was used to image and analyze young subjects of age groups ranging from 1 month to 30 months.

4.3.4 Equipment and imaging method

Infrared imaging in combination with white – light imaging was used in the study to analyze infantile hemangioma lesions. The imaging setup is shown in Figure 4.4. Figure 4.4 (a) shows the Merlin® midwave infrared camera (FLIR Systems Inc., Wilsonville, OR), the PC connected to the infrared camera for IR image acquisition and storage and a Canon PowerShot G11™ digital camera (Canon U.S.A., Inc., One Canon Park, Melville, NY) used for capturing the WL images. Figure 4.4 (b) shows the cold gel pack used for skin cooling during dynamic IR imaging. A sample WL image (0.4 – 0.7 μm spectral range) of a hemangioma of the forehead is shown in Figure 4.4 (c). The IR camera is equipped with a 320x256 pixel indium antimonide (InSb) focal plane array (FPA) and can record 16-bit raw data with a frame rate of 60 Hz. It has a temperature sensitivity of 0.025°C and field of view (FOV) of 22x16 degrees. Figure 4.4 (d) shows a sample grey scale IR image (3 – 5 μm wavelength range) of the same lesion as the WL image in Figure 4.4 (c). Figure 4.4 (e) displays the color coded IR image of the lesion obtained after IR camera calibration [147] . An adhesive white paper marker was applied to the skin at the beginning of the imaging session, as shown in Figure 4.4(c). The marker was used as a reference to measure lesion size (major and minor axis dimensions) from its WL image. Since the marker is

visible in the WL and IR images, it was also used as a reference for WL-IR image alignment [146]. During the imaging process, a reference WL image of the lesion (shown in Figure 4.4 (c)) was acquired first using the WL camera. Next, a steady state IR image sequence of 20 images was acquired at 2 fps for 10 seconds. Recording multiple images offered the option of selecting the best quality image in the sequence as well as the possibility of time averaging. A greyscale IR image is displayed in Figure 4.4(d) and the corresponding color

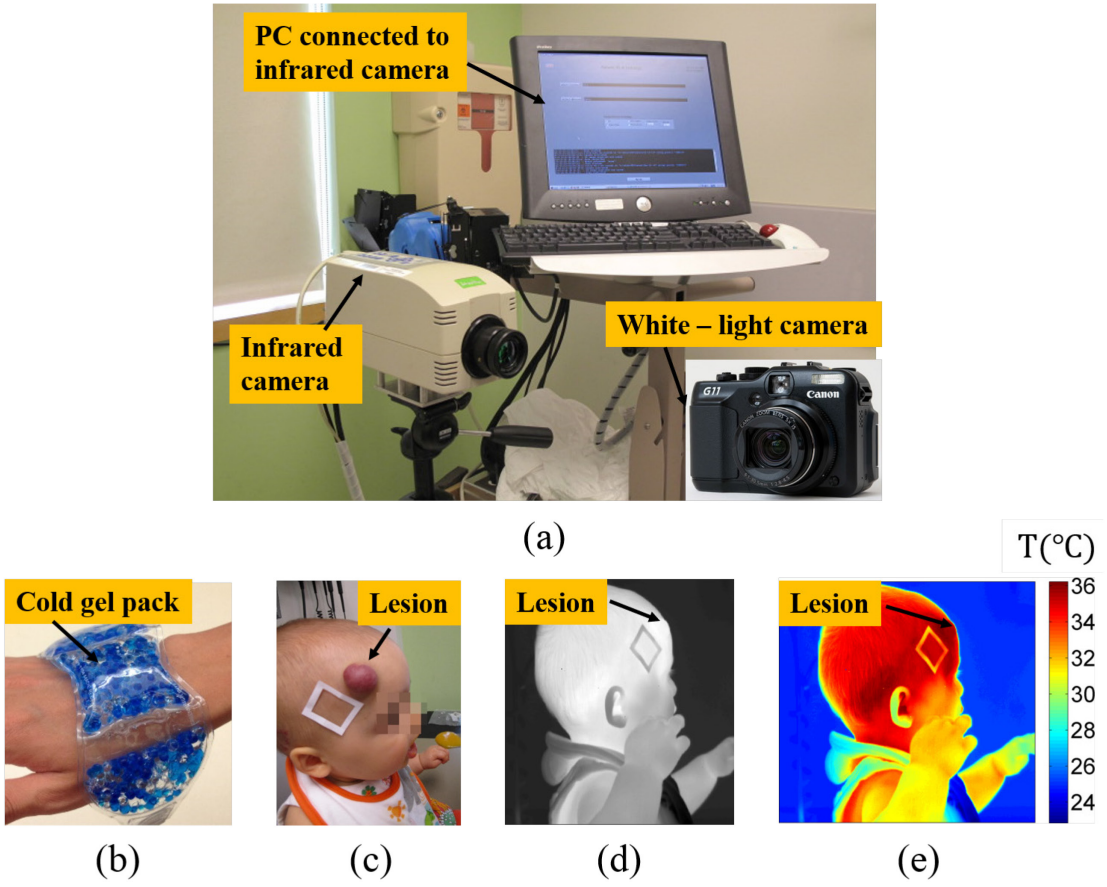

Figure 4.4 Combined IR – WL image acquisition setup for imaging of IHs. The imaging setup consists of the (a) Merlin midwave (3-5 µm) IR Camera, the Canon PowerShot G11™ WL (0.4 – 0.7 µm) camera, the PC for saving the IR images and (c) a cold gel pack for skin cooling during dynamic IR imaging. The bottom row shows the (c) WL image of an IH lesion, (d) the corresponding greyscale IR image before calibration and (c) the matching color coded IR image of the IH lesion after calibration.

coded IR image is shown in Figure 4.4 (e). Dynamic IR imaging, measuring the change of temperature distribution with time, was also used to image some vascular lesions. For such cases, the lesion was cooled down for a period of 60 seconds with a cold gel pack (shown Figure 4.4 (b)). Finally, a dynamic IR image sequence of 120-360 images was acquired at a rate of 2 fps for 2-3 minutes. This allowed capturing the thermal recovery of the lesion from cooling excitation.

Imaging of young infants, especially those who were under treatment, was quite challenging. Imaging was usually performed after the routine evaluation or the treatment of the subject was completed. The young subjects would often feel tired after their lengthy stay at the clinic, limiting our ability to repeat imaging scans (in case the subject moved a lot or removed the paper marker during the initial scan). Dynamic infrared imaging that would require subject's cooperation throughout the combined sessions of skin cooling and subsequent thermal recovery was not always feasible.

4.4 Image processing

We implemented computational techniques used in image processing and computer vision for extraction and analysis of information from WL [124, 126] and IR [146] images of lesions. Our image processing pipeline involves techniques for lesion color analysis [126], lesion boundary segmentation [5], planar homography for image registration [119] and computational photography for IR – WL image overlay [140]. Section 4.4.1 introduces the WL image processing pipeline for performing color analysis and area calculations of lesions and section 4.4.2 focuses on the IR image processing steps for thermal analysis and area calculations of lesions based on the IR images.

4.4.1 White – light image processing

Figure 4.5 summarizes our WL image processing pipeline for computing lesion dimensions, lesion and healthy skin colors and color differences between them from the WL images. The flowchart in the top panel show the image processing steps. The bottom rows of images illustrate the results of these steps. The WL images were captured using the digital camera (section 4.3.4) using the sRGB (standard red, green and blue) color space setting (Figure 4.5(a)). The first step in the WL image processing is the segmentation of the superficial portion of the lesion and a region representing the healthy skin (Figure 4.5(d) – (f)) in the WL image. Next, the dimensions of the lesion including the lesion size and area are measured from the WL image. The segmentation of the lesion and healthy skin and measurement of key dimensions are discussed in section 4.4.1.1. In the next step, the color differences between lesion and healthy skin are measured in the CIELAB space (Figure 4.5(a), (b), (i) – (k)). We present the color difference calculation method in section 4.4.1.2. In the final step, the quantitative representation of lesion and healthy skin colors in the Munsell color space (Figure 4.5(a), (b), (i), (l) – (m)) is presented in section 4.4.1.3.

4.4.1.1 Lesion size from the WL image

The lesion was manually segmented from the WL image. The lesion boundary is outlined with green dots in Figure 4.6(a). This region will be referred to as the superficial portion of the lesion because it is visible in the WL image. Next, a binary lesion mask was created from the lesion boundary by setting pixels inside the boundary be 1 and those outside as 0 (Figure 4.6(b)). The area of the superficial portion is determined by counting

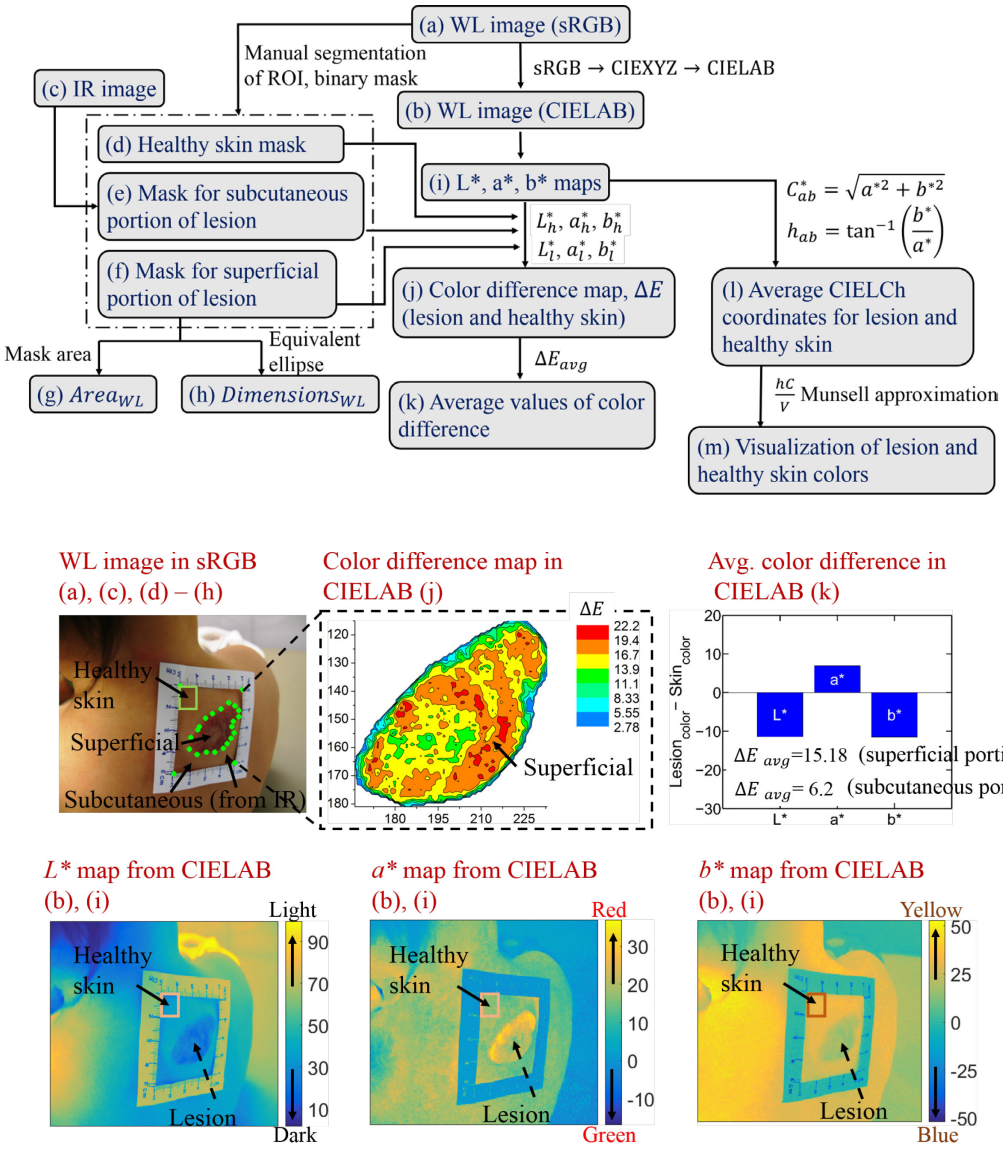

Figure 4.5 WL image processing pipeline. The letter labels marked in each box of the flowchart are associated with the images that are obtained by the means of processing those steps. The lesion size and area is computed in steps (a), (c), (d) – (h). The color difference between lesion and healthy skin is computed in steps (a), (b), (i) – (k). The quantitative color visualization using Munsell representation of colors is achieved in steps (a), (b), (i), (l) – (m).

the number of pixels inside the boundary and converting this area into cm^2 using the length scale provided by the paper marker (Figure 4.6 (c)). This area will be referred to as $Area_{WL}$.

The IH lesion may have an irregular shape. In this case, the lesion was approximated by an

equivalent ellipse, such that it has the same area and the same center of mass as the lesion. As a result, the longest axis of the lesion shape is approximated by the major axis and the length perpendicular to the longest axis by the minor axis.

4.4.1.2 Color difference between lesion and healthy skin

The color difference between lesion and healthy skin is calculated in the CIELAB color space. We converted the WL image originally captured in the sRGB (standard RGB) color space to the CIELAB color space and used the CIELAB color coordinates to compute the color differences between lesion and healthy skin. We used the sRGB setting in the digital camera to capture the color images. This setting specifies the color of each pixel in terms of a tristimulus vector $[R\ G\ B]^T$ in the sRGB format, where R represents the red channel, G represents the green channel and B represents the blue channel. The measured RGB values were first converted into CIEXYZ (intermediate color space) values by a linear transformation, and finally into CIELAB by a non-linear transformation [120, 122]. The conversion to an intermediate CIEXYZ color space is necessary to obtain positive values of the tristimulus [123, 126]. All conversions were implemented in Matlab. The conversion to CIELAB can be expressed as

$$
\begin{aligned}
L^* &= 116\, f(Y/Y_n) - 16 \\
a^* &= 500[f(X/X_n) - f(Y/Y_n)] \\
b^* &= 200[f(Y/Y_n) - f(Z/Z_n)]
\end{aligned}
\tag{4.9}
$$

$$
\text{where} \quad f(\mathrm{x}) = \begin{cases} \mathrm{x}^{1/3}, & x > \left(\frac{6}{29}\right)^3 \\ \frac{1}{3}\left(\frac{29}{6}\right)^2 \mathrm{x} + \frac{4}{29}, & x \le \left(\frac{6}{29}\right)^3 \end{cases}
$$

In Equation 4.9, X_n, Y_n and Z_n are the CIEXYZ tristimulus values for the reference white (standard illuminant D65 was used in this study). The CIELAB data are presented in the cartesian coordinate system. A more intuitive representation of color is obtained by representing CIELAB values (shown in Figure 4.3(a)) in an equivalent cylindrical coordinate system, CIELCh (shown in Figure 4.3(b)) that matches more closely with the visual experience of colors [120, 123]. The transformation can be described as

$$\begin{aligned} L^* &= L^* \\ C^*_{ab} &= \sqrt{a^{*2} + b^{*2}} \\ h^*_{ab} &= \tan^{-1}\left(\frac{b^*}{a^*}\right) \end{aligned} \tag{4.10}$$

where L^* or lightness is shown along the z axis, C^*_{ab} or chroma correspond to the radial coordinate and h^*_{ab} or hue is represented by the angular coordinate of the cylindrical coordinate system (Figure 4.3(b)). The values of L^*, C^*_{ab} and h^*_{ab} will be utilized in this study for visualization of lesion color and healthy skin color. Next, the color difference between lesion color and healthy skin color was computed using the CIELAB values for healthy and lesion pixels. Let L^*_h, a^*_h and b^*_h represent healthy skin color coordinates and L^*_l, a^*_l and b^*_l represent lesion color coordinates in the CIELAB color space. The cartesian distance between the two coordinate points gives a measure of the color difference between them [122, 126].

$$\Delta E = \sqrt{(\Delta L^*)^2 + (\Delta a^*)^2 + (\Delta b^*)^2} \tag{4.11}$$

In Equation 4.11, ΔE is the measure of the color difference and $\Delta L^* = L^*_l - L^*_h$, $\Delta a^* = a^*_l - a^*_h$ and $\Delta b^* = b^*_l - b^*_h$. The ΔE value combines the individual differences in

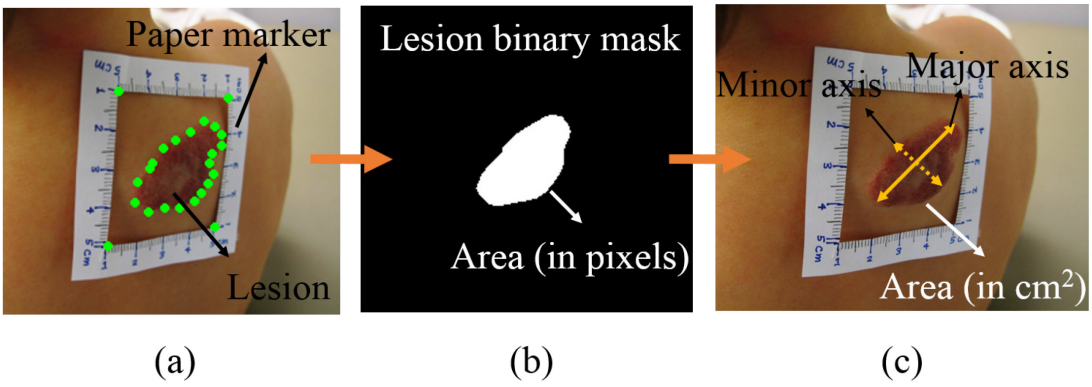

Figure 4.6 Illustration of lesion size and area calculation from the WL image. (a) The WL image of an IH surrounded by a 5 cm x 5 cm paper marker. The lesion boundary is outlined with green dots. (b) Binary mask of the lesion (lesion pixels = 1 (white), other pixels = 0 (black). The area in pixel units is the total number of lesion pixels. (c) Major axis (longest axis of the lesion shape) and minor axis (axis perpendicular to the longest axis) determined from the binary mask. The cm units for lesion size (cm) and area (cm^2) are estimated with the help of the reference length scale provided by the paper marker.

color lightness (ΔL^*), redness (Δa^*), and blueness (Δb^*) into one quantitative metric that is proportional to the visually perceived color difference between lesion and healthy skin [148]. This means that large ΔE values represent larger color differences between lesion and healthy skin and small ΔE values represent smaller color differences. For each clinical case considered in this study, we report mean color differences between (1) superficial portion and healthy skin and (2) subcutaneous portion and healthy skin.

4.4.1.3 Quantitative visualization of lesion and healthy skin color

In this study, we introduced quantitative visualization of IH lesion color and healthy skin colors, achieved by the means of CIELAB to Munsell color space approximation [130]. In Munsell representation of colors, a color is specified in the form HV/C where H

is the hue, V is the value or the lightness, and C is the chroma [120]. The cylindrical Munsell color space [120] is displayed in Figure 4.7(a) showing the color lightness on the y-axis, chroma on the radial axis and hue as the polar angle. The lightness varies from 1 to 10. The hue is specified by a combination of a letter and a numeric designator, as illustrated in the hue circle shown in Figure 4.7(b). The single letter designators represent the primary hues – R (red), Y (yellow), G (green), B (blue) and P (purple) and the double letter designators denote a combination of the primary hues – YR (yellow –red), GY (green – yellow), BG (blue – green), BP (blue – purple) and RP (red – purple) [120]. The numeric designator is greater than 1 and less than or equal to 10, where the number 5 is associated with the primary hues (Figure 4.7(b)). For example, a 5R would represent the primary red, a 2.5R would represent red-purple hue and an 8R would represent a yellow – red hue [120].

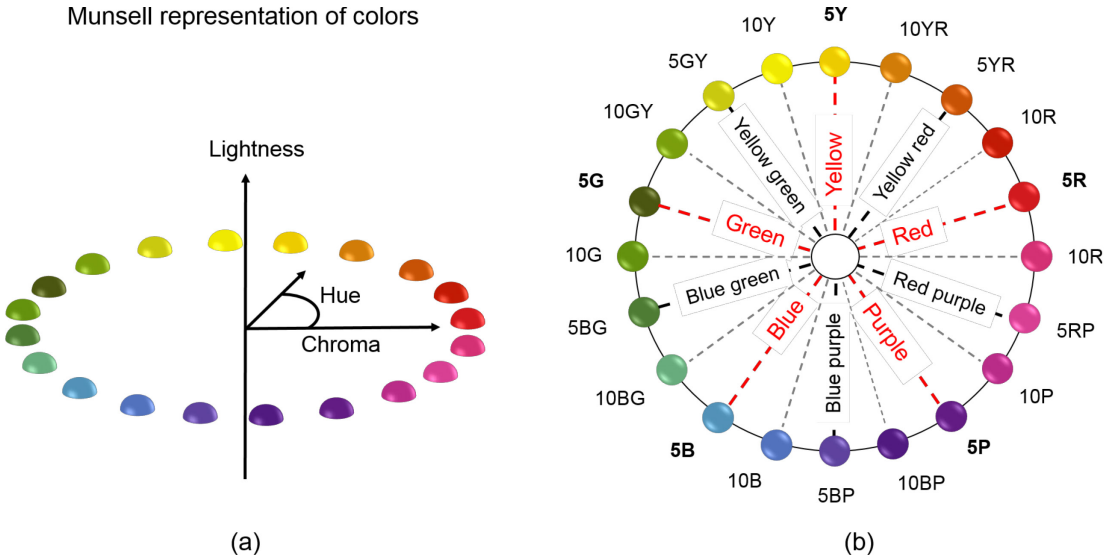

Figure 4.7 Munsell representation of colors. (a) A color is represented by its lightness (y-axis), chroma (radial axis) and hue (polar angle) in the cylindrical coordinate system of the Munsell color space. (b) The Munsell hue circle showing the five primary hues – 5R (red), 5Y (yellow), 5G (green), 5B (blue) and 5P. The double letter designators represent the intermediate hues – YR (yellow – red), GY (green – yellow) etc. The number designator is greater than 1 and less than equal to 10.

If the color lies on the Y-axis, its chroma is equal to 0. This description of colors in the Munsell representation is more intuitive when compared to the CIELAB representation (Figure 4.3(a)) and provide a quantitative means to assess colors of the IH lesion and healthy skin [120]. We approximated the Munsell colors from the respective CIELAB coordinates using the approximations adopted by Centore [130] and Madooei and Drew [124]. The Munsell value V is equivalent to L^* and varies from 1 to 10, the chroma C is approximately 1/5 times C^*_{ab} (Equation (4.10) and is a positive value, and the hue H corresponds to h^*_{ab} (Equation (4.10). The primary yellow hue corresponds to $h^*_{ab} = 90°$ and the other nine hues are located at evenly spaced hue angles during the conversion process [120, 130], as illustrated by Figure 4.7(b). The color conversion was implemented in Matlab [130].

4.4.2 Infrared image processing

Figure 4.8 summarizes our IR image processing steps for the detection of lesion boundary in the IR image, visualization and quantification of the total affected area from the IR image, thermal image overlay onto the WL image, comparison of lesion areas from the WL and IR images and finally the computing the dimensionless temperature difference images. The flowchart in the top panel elucidates the IR image processing steps. The bottom rows of images illustrate the results of these steps. As the first step in IR image processing, the greyscale image is converted into a color coded IR image using the temperature calibration for the IR camera [147] (Figure 4.8 (a) and (c)). The rest of the IR image analysis will be performed on the color coded IR image. Next, the superficial boundary is detected in the IR image (Figure 4.8 (a) - (e) and (g)) using the WL to IR image registration technique [119, 139] . The mapping of the lesion boundary from the WL image

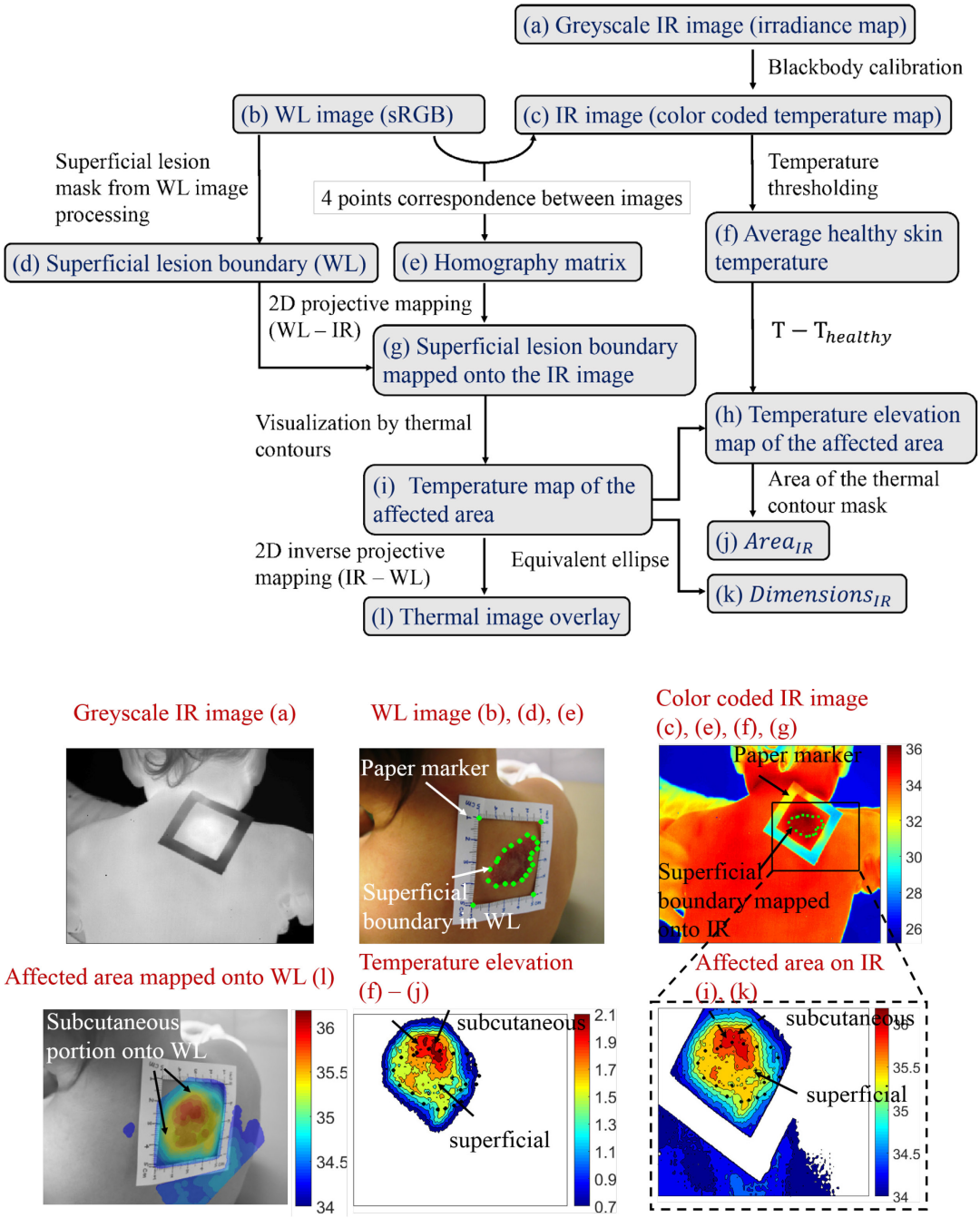

Figure 4.8 IR image processing pipeline. The letter labels marked in each box of the flowchart are associated with the images shown below, that are obtained by the means of processing those steps. The superficial lesion boundary in the IR image is identified in (a) – (e) and (g). The affected area in the IR image is determined in (f) – (k). The affected area is back-mapped onto the WL image in (l).

onto the IR image is explained in section 4.4.2.1. The total affected area in the IR image is

quantified in steps in Figure 4.8(f) – (j). The method of thermal contours is presented for quantification and visualization of the total affected area is presented in section 4.4.2.2. The affected area is back mapped onto the WL image in Figure 4.8(i) and (l). The method of thermal image overlay [140] is discussed in section 4.4.2.3. The total affected area from the IR image is compared with the area of the lesion from the WL image in section 4.4.2.4. In the final step, the dimensionless temperature difference maps are computed from the IR images in section location over time during longitudinal studies.

4.4.2.1 Detection of lesion boundary in the IR image

Infantile hemangiomas can affect significant subcutaneous portions of the tissue in addition to their superficial portion. In this study we consider two boundaries: the boundary of the superficial lesion (visible in the WL image, section 4.4.1) and the boundary of the entire lesion to be determined from the IR image as explained in this section. The boundary of the entire lesion, in general, may not be distinguished from the surrounding healthy skin by visible inspection. Small lesions such as melanomas show small temperature differences (or low thermal contrast) with respect to healthy skin [5]. We observed that the region of elevated temperature for IHs is often significantly larger than the visible portion of the lesion. For large lesions, such as infantile hemangiomas, the problem is to identify both the superficial and subcutaneous portions.

We used WL – IR image registration [119, 139] to identify the superficial lesion boundary in the IR image. First, the IR image was registered with the reference WL image using the four–points-correspondence based 2D projective transformation, referred to as homography [119]. The registration process is illustrated in Figure 4.9. The four corners of

the paper marker (that is visible in the WL and IR images) served as the points of correspondences between the two image planes. The corners were marked manually on the WL image as P1, P2, P3 and P4 (marked by green dots in Figure 4.9(a)) and on the IR image as P1', P2', P3' and P4' (marked by black dots in Figure 4.9(b)). Based on these point correspondences, a 3x3 homography matrix H was solved using the DLT (direct linear transformation) algorithm [139].

$$H = \begin{bmatrix} h_1 & h_4 & h_7 \\ h_2 & h_5 & h_8 \\ h_3 & h_6 & h_9 \end{bmatrix} \tag{4.12}$$

In Equation 4.12, the matrix H describes a two dimensional mapping from the WL image plane, given by (x, y), to the IR image plane, given by (x', y'), as shown in Figure 4.9. The elements $h_1 \ldots . h_8$ of the matrix represent the eight degrees of freedom and by

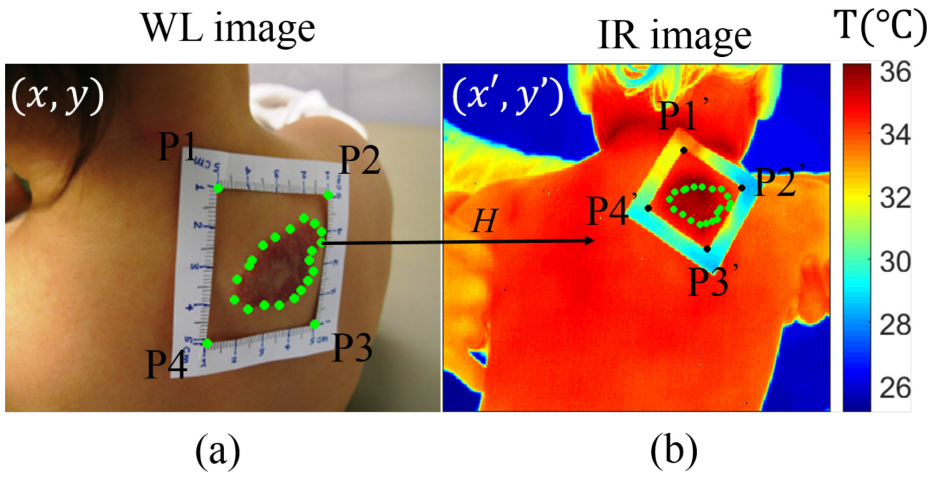

Figure 4.9 2D projective transformation from the WL image (with image coordinates, (x, y)) to the IR image (with image coordinates (x', y')). (a) The green corner points of the paper marker P1, P2, P3 and P4 in the WL image are mapped into the corresponding (b) black corners points P1', P2', P3' and P4' in the IR image to obtain the WL – IR 2D projection matrix H. This matrix was used to map the lesion boundary (outlined with green dots) in the (a) WL image into the (b) IR image to locate the superficial lesion boundary in the IR image.

convention $h_9 = 1$ [119]. Similarly, an inverse mapping H^{-1} maps points from the IR image plane to the WL image plane. The latter mapping is used later for the thermal image overlay.

In the next step, the homography matrix H was used to map the lesion boundary points from the WL image plane to the IR image plane. The mapping assumes that the points on the boundary lie in the same plane as the four points selected for computing homography. Let us assume that a point P_{WL} in the WL image is described by the vector $[x, y]^T$ in cartesian coordinate notation. Using homogenous coordinates notation [119], the coordinates of point P_{WL} are expressed by the vector $[x, y, 1]^T$. The corresponding coordinates of this point P_{IR}, in the IR image can be computed using H. The output coordinate vector $[u, v, w]^T$ is in the projective space of the IR camera.

$$\begin{bmatrix} \mathrm{u} \\ v \\ w \end{bmatrix} = [H] \begin{bmatrix} x \\ y \\ 1 \end{bmatrix} \tag{4.13}$$

In cartesian coordinates, the coordinates of the point P_{IR} in the IR image are given by the vector $[x', y']^T$ where $x' = \frac{u}{w}$ and $y' = \frac{v}{w}$. The image in Figure 4.9(b) shows the mapped lesion boundary (green dotted boundary) in the IR image, which is the superficial lesion boundary in the IR image.

4.4.2.2 Visualization of the total affected area in the IR image (thermal contours)

We used thermal contours to visualize temperature distribution at lesion location and its surroundings. The thermal contours or isotherms are imaginary lines that connect regions of equal temperature in the IR image (thermal map). The color coded IR image of

a hemangioma lesion is shown in Figure 4.10(a). A region of interest, ROI (a region surrounding the lesion) is indicated by the black rectangle in the IR image in Figure 4.10(a). The superficial lesion boundary is outlined with green dots. A magnified IR image of the ROI is displayed in Figure 4.10(b), where the temperature is visualized using thermal contours. The thermal contours allow better visualization of the temperature gradients in the IR image. The IR image in Figure 4.10(b) visualizes temperature distribution in the temperature range of 34 – 36°C with a temperature increment of 0.25°C. The black dotted boundary is the superficial lesion boundary mapped from the WL image, as explained in the previous section. The superficial portion is marked with a solid black arrow and the subcutaneous portions of the lesion is marked with dashed black arrows. The 3D temperature map shown in Figure 4.10(c) visualizes temperature elevation with respect to the surrounding unaffected skin temperature using thermal contours.

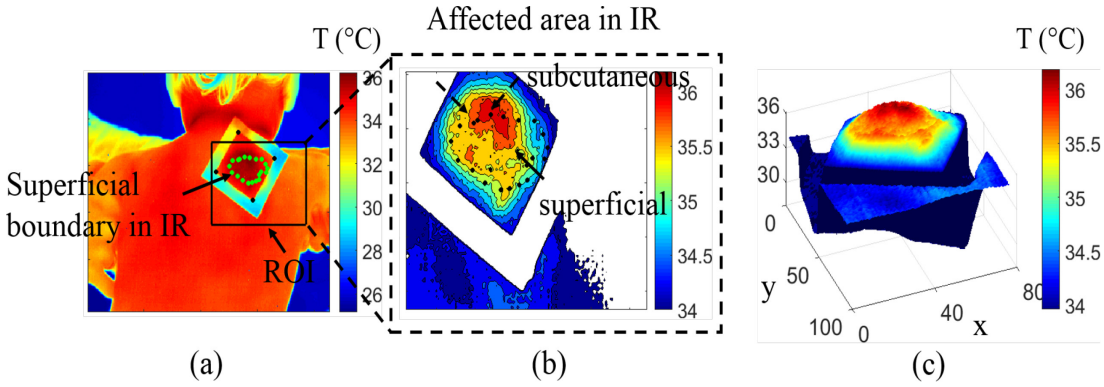

Figure 4.10 Visualization of the affected area in the IR image using the thermal contours. (a) An IR image of an IH of the upper back. The superficial lesion boundary shown in green is mapped into the IR image from the WL image. (b) Temperature distribution in the magnified ROI (80 pixels by 140 pixels large) displayed using thermal contours (34 – 36.5°C temperature range, with an increment of 0.25°C). The white areas are regions below 34°C which are not considered. The superficial and subcutaneous portions are marked with arrows. (c) 3D visualization of temperature distribution within the ROI using thermal contours

4.4.2.3 Visualization of the total affected area in the WL image (thermal image overlay)

The thermal image overlay is the overlay of thermal contours (determined from the IR image) onto the WL image using an inverse homography estimation (Equation 4.13) [140]. We mapped the total affected area determined using thermal contours onto the WL image for better, more intuitive visualization of the total affected area in the WL image. The visualization of the total affected area in a single image allows for easy interpretation of results of WL imaging and IR imaging and better evaluation of the total affected area.

An example of the thermal image overlay is shown in Figure 4.11. The WL image of an IH of the forehead is shown in Figure 4.11(a). Using thermal contours, the temperature of the lesion is visualized in Figure 4.11(b) in the temperature range of 31°C and 36.2°C with an increment of 0.5°C. The image indicates that the total affected area

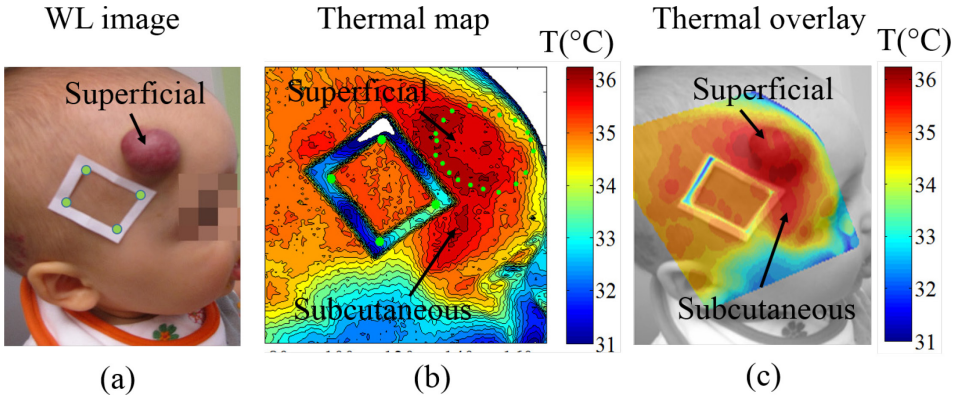

Figure 4.11 Area affected by the hemangioma mapped onto the WL image using thermal contours. (a) Area affected by the IH lesion in the WL image. The superficial visible portion of the IH is marked with a black arrow. (b) Total area affected by the lesion in the IR image. The thermal map is displayed using thermal contours with an increment of 0.25°C for the temperature range 31°C - 36°C. (c) Total area affected by the lesion in the WL image. The superficial and subcutaneous portions are marked with the black arrows.

extends well beyond the superficial lesion boundary (identified by green dots). The solid black arrows point towards the superficial and subcutaneous portions of the lesion. The temperature information is back mapped onto the WL image (Figure 4.11 (a)), as illustrated in Figure 4.11(c). By setting the transparency of the thermal contours at 0.6 value, the superficial and subcutaneous portions can be simultaneously visualized in the WL image. For clinicians, it is convenient to simultaneously visualize the superficial portion and its surroundings and the skin temperatures, in order to better evaluate the total affected area.

4.4.2.4 Lesion area ratio

We calculated the lesion area ratio, $Area_{IR}/Area_{WL}$, which is the ratio of the lesion area measured from the IR image ($Area_{IR}$) to the superficial lesion area measured from the WL image ($Area_{WL}$). From the WL image, $Area_{WL}$ was computed from the binary mask of the superficial portion of the lesion (section 4.4.1). From the IR image, $Area_{IR}$ was computed using the temperature elevation map of the lesion, as shown in Figure 4.12(a). The temperature elevation map is obtained by subtracting the reference healthy skin temperature value from the temperature of each pixel of the IR image. The resulting temperature elevation distribution at the lesion location is visualized using thermal contours in Figure 4.12 (a). A temperature rise in the range of 1°C to 2.2°C is observed with respect to the healthy skin temperature. Figure 4.12 (b) illustrates the regions of the map in Figure 4.12 (a) that are 1°C, 1.8°C and 2°C above the healthy skin temperature. The number of pixels in the temperature elevation contour (dark blue contour in this case with $\Delta T \geq 1$℃) were counted to get an estimate for $Area_{IR}$ in pixels. The units were then converted into cm^2 using the length scale provided by the paper marker.

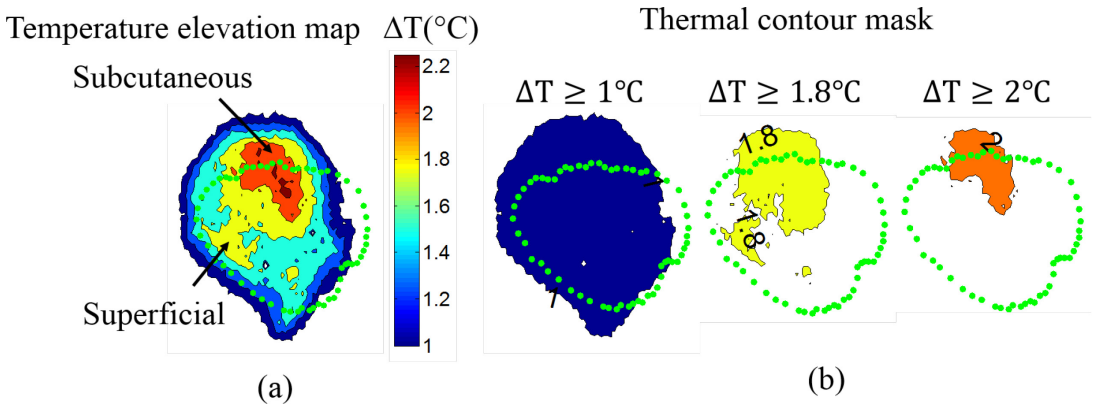

Figure 4.12 Lesion area calculation from the IR image using thermal contour masks. (a) The temperature elevation at lesion location relative to the surrounding healthy skin temperature. (b) The thermal contour masks of regions in (a) that are 1°C, 1.8°C and 2°C above the surrounding healthy skin temperature. The green dotted boundary on the masks outlines the superficial lesion.

4.4.2.5 Dimensionless temperature difference maps

The dimensionless temperature difference maps were introduced to compare the temperature distributions (on a scale of 0 to 1) at lesion location over time in longitudinal studies (Figure 4.13). Let $0 \leq \theta^* \leq 1$ represent the dimensionless temperature difference between the lesion and healthy skin, where

$$\theta^* = \frac{T - T_{ref}}{T_{max} - T_{ref}} \tag{4.14}$$

In Equation 4.14, T is the local skin temperature, T_{ref} is the temperature of a reference healthy location and T_{max} is the maximum skin temperature. $\theta^* = 0$ at the reference healthy location and $\theta^* = 1$ at the location where $T = T_{max}$ (warmest point of the IH lesion). Figure 4.13 illustrates the use of this method for comparison of temperature distributions of an IH lesion (of the nasal region) from two clinical visits (first imaging and

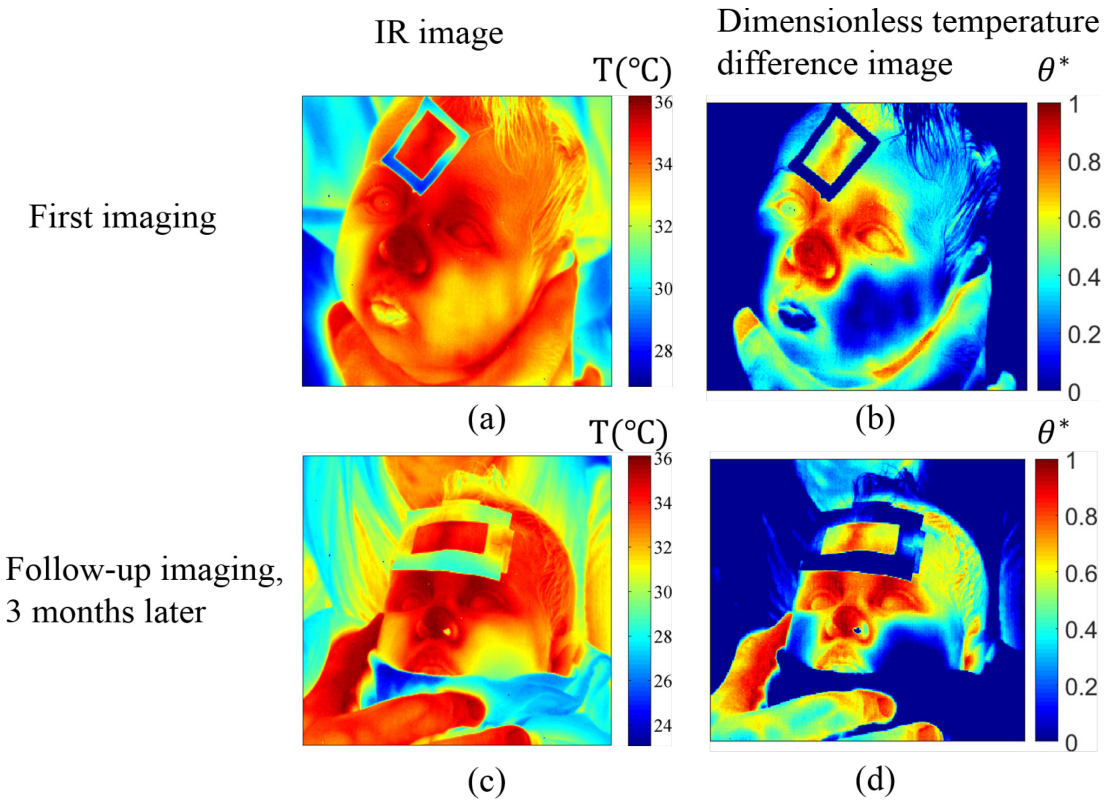

Figure 4.13 Original IR images of an IH of the nasal region and the corresponding dimensionless temperature difference (θ^*) maps. (a) The IR image at the first imaging and (b) the corresponding dimensionless temperature difference image. (c) The IR image at the follow-up imaging three months later and (d) the corresponding dimensionless temperature difference image obtained using Equation (4.14. $\theta^* = 0$ at the left cheek in both cases and $\theta^* = 1$ at the location where lesion temperature is highest.

follow-up imaging three months later). The IR image at first imaging session is shown in Figure 4.13 (a). The average healthy skin temperature is in approximately 33°C and the temperature of the hemangioma lesion is in the range of 34.5 - 36°C.At the second imaging session three months later, the average healthy skin temperature is approximately 31°C and the temperature of the hemangioma lesion in in the range of 34 - 36°C (Figure 4.13(c)). The dimensionless temperature difference maps were obtained using Equation (4.14. The left cheek temperature was used as the reference for the healthy skin in both cases,

assuming that the temperature distribution of the left cheek would mirror that of the right cheek in the absence of the lesion. The dimensionless temperature difference $\theta^* = 0$ at the left cheek and $\theta^* = 1$ at the lesion in both cases, as displayed in Figure 4.13(b) and Figure 4.13(d)). The normalized temperature differences between the lesion and reference healthy location can be used to compare the temperature distribution at the lesion location and its surroundings at different times in longitudinal studies.

4.5 Results

In this section, the thermal analysis and color characterization of IHs by the combined WL – IR imaging approach are illustrated by considering seven sample IH cases. The key clinical characteristics of the lesions are summarized in Table 4.1. For descriptive purposes, the cases are grouped into the stages of evolution and arranged in the order of increasing age of the subjects. All subjects were female ranging from two to thirty months. This distribution does align with studies indicating that the female gender is a risk factor for the development of IH [109]. Out of the seven cases, two IHs were in their proliferation phase and were located on the subject's lip (case I) and nose (case II), two IHs were in their plateau phase and were located on the subject's scalp (cases III and IV) and three IHs were in their involution phase and were located on the subject's back (case V), arm (case VI) and glabella (case VII). A follow – up analysis for case II before and after Propranolol treatment is also presented. All lesions were focal hemangiomas. Two were superficial (strawberry or capillary) hemangiomas, one was deep (cavernous) and four were mixed (capillary cavernous), with both superficial and deep components. Three of the subjects were treated with propranolol and one was treated with Timolol prior to imaging. The remaining three patients received no treatment prior to imaging.

4.5.1 Organization of results

In this study, we introduce a novel way of presenting imaging data (Figure 4.14 to Figure 4.20) using a six-step imaging strategy. The top row of each figure displays the WL image (top left), WL image overlaid with temperature information (middle) and color difference data between the lesion and healthy skin (top right). The bottom row of the figures shows the original IR image (bottom left), the magnified IR image within the ROI, showing temperature map at lesion location (middle) and temperature elevation with

Table 4.1 Summary of patient information and clinical features of IHs included in this study

Case No	Subject Age (months)	Subject Gender	Stage by Clinical Impression	Location of IH	Morphologic Subtype	Description	Treatment
I	1.2	Female	Proliferating	Lip	Focal	Mixed	None
II	2.2	Female	Proliferating	Nasal tip	Focal	Mixed	None
III	8.5	Female	Plateau/early involution	Left temporal scalp	Focal	Superficial	None
IV	9.8	Female	Plateau	Right forehead and parietal scalp	Focal	Superficial	Propranolol
V	13.7	Female	Involuting	Right upper back	Focal	Mixed	Timolol
VI	16.7	Female	Involuting	Left arm	Focal	Mixed	Propranolol
VII	29.3	Female	Involuting	Glabella	Focal	Deep	Propranolol

respect to healthy skin (bottom right). The WL images of the hemangiomas (top left images) show the superficial portion of the IH lesion that is identifiable by visual inspection. In some of the cases, the superficial portion of the IH visible in the WL image represents the entire hemangioma (cases II and III). However, the majority of cases showed that the portion of the IH visible in the WL image is merely the superficial component of a mixed hemangioma or the subcutaneous tumescence of a deep hemangioma. We observed that some cases have 'suspicious areas' around the superficial portion that cannot be detected in the WL image (cases II and III). The advantage of our combined WL – IR imaging approach is that it also shows these suspiciously warm regions. The color differences between the lesion and healthy skin in terms of the individual color attributes L*, a* and b* of the CIELAB color space are displayed in top right images. The computed color differences in terms of ΔE (Equation (4.11) are summarized in Table 4.2 (proliferating IH cases), Table 4.4 (plateau phase IH cases) and Table 4.6 (involuting IH cases). A green dotted boundary outlining the superficial lesion is presented in the bottom left IR image. The information in the ROI (outlined with a black box in the same IR image) is presented using thermal contour maps in the magnified image (bottom middle images). Finally, this temperature map is mapped onto the WL image (middle top images).

We first present results of the characterization of IH cases in proliferative phase (section 4.5.2), plateau phase (section 4.5.3) and involuting phase (section 4.5.4). A summary of the analysis of IHs in each phase is presented at the end of the section using tables. The computed color differences in terms of ΔE (Equation (4.11) are summarized in Table 4.2 (proliferating IH cases), Table 4.4 (plateau phase IH cases) and Table 4.6 (involuting IH cases). The geometrical and thermal features of IHs, i.e. maximum lesion

temperature, range of temperature elevation at the lesion location, lesion sizes (cm) and areas (cm^2) from the WL and IR images are summarized in Table 4.3 (proliferating IH cases), Table 4.5 (plateau phase IH) and Table 4.7 (involuting IH cases). Next, lesion colors and healthy skin colors are visualized in the Munsell color space in section 4.5.5. Finally, the IR images of a proliferating IH lesion (case II) before and after treatment are compared in section 4.5.6. We discuss and summarize key results of our analysis in section 4.6.

4.5.2 Characterization of IHs in proliferative phase

The proliferation phase of hemangioma lesion is characterized by rapid growth. During proliferation, there is formation of new capillaries that increase the vascularity of the growing lesion. The lesion may infiltrate the dermal and/or the subcutaneous tissue [118], forming a subcutaneous component that may or may not show visible traces on the skin surface. The increase in lesion vascularity causes a temperature rise that can be measured non-invasively by infrared imaging. We demonstrate the applicability of the IR – WL imaging technique in quantitatively assessing proliferating IHs in case studies I and II. We discuss the applicability of IR imaging as a quantitative assessment tool for comparing proliferating IHs over time (at different clinical visits) in section 4.5.6. The summaries of analysis of lesion color and temperature in proliferative cases I and II are presented at the end of this section in Table 4.2 and Table 4.3.

Case I Proliferating IH of the lip: Figure 4.14(a) shows a proliferating, mixed hemangioma of lip in a 1-month-old Caucasian female. The lesion did not receive any treatment prior to imaging. The lesion appears as a bump on the lip covering 60% of its mucosal and cutaneous regions. It was ulcerated and had been bleeding on an intermittent

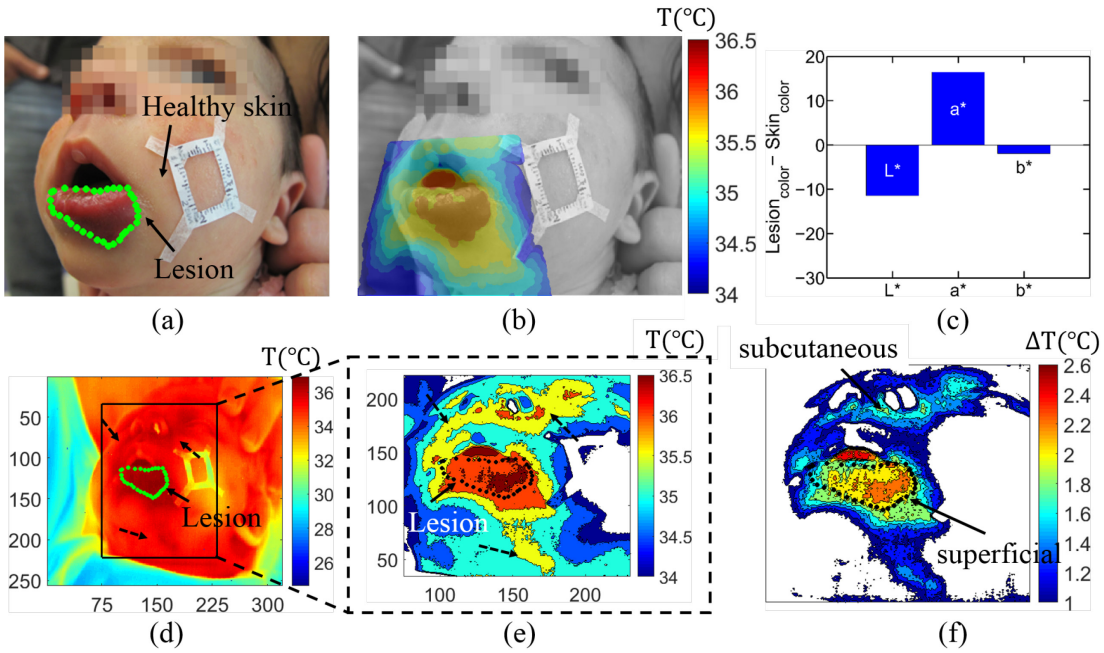

Figure 4.14 Case I - Proliferating hemangioma of the lower lip in a 1-month-old Caucasian female that was ulcerated and bleeding intermittently. The lesion did not receive treatment prior to imaging. (a) WL image. The green boundary outlines the superficial visible portion of the lesion. (b) The superficial affected area mapped onto the WL image. (c) Color difference data between the lesion and healthy skin in terms of color attributes L^*, a^* and b^*. (d) The color coded IR image. The green boundary is the superficial boundary mapped from the WL image. The black arrows mark the extent of the subcutaneous involvement and the black rectangle outlines the ROI. (e) The magnified IR image within the ROI, showing temperature map at lesion location and (f) temperature elevation with respect to healthy skin (1 – 2.2°C). Lesion area ratio: $Area_{IR}/Area_{WL} = 5.8$. Color differences: $\Delta E_{avg} = 32.17$ (superficial, healthy skin) and $\Delta E_{avg} = 13.71$ (subcutaneous, healthy skin).

basis, which resulted in an abated vermilion border. The color difference analysis shown in Figure 4.14(c) suggests that the lesion is darker in color (ΔL* = -10) and has dark reddish (Δa* = 17) and light bluish (Δb* = -3) hues when compared to the healthy skin.

From the WL image (in Figure 4.14(a)), the dimensions of the lesion are 3.3 cm (major axis) by 1.9 cm (minor axis), its surface area is 4.6cm^2 and it covers the lower lip of the subject. These dimensions describe the superficial portion of the lesion visible in the

WL image (Figure 4.14(a)). The IR images (Figure 4.14(d) – (e)) show that the lesion also affects some areas on the neck as well as the face. The subcutaneous portion of the lesion is marked with three dashed black arrows in Figure 4.14(d) - (e). The affected areas include the submandibular triangle, the left portion of the chin, the cutaneous and mucous lip, the philtrum and the left nasal sidewall region (Figure 4.14 (d)). The large subcutaneous involvement of the lesion is easily noticeable in an IR image because of the elevated temperature (35.5– 36.5°C) relative to the surrounding healthy skin (34.8°) (Figure 4.14 (e)). The hypervascular regions (with high blood perfusion) present in the vascular tumor during its proliferation phase [116] cause local increase in skin temperature that is identifiable in an IR image. The total area affected by the lesion as determined from the IR image is 26.8 cm^2. This means that the region affected by the hemangioma is 5.8 times larger than the lesion area visible in the WL image. This result suggests that the assessment of IH by visual inspection alone can severely underestimate the true extent of the affected region.

Additionally, we observed that the temperature increase is larger for the superficial portion of the lesion (1.8 – 2.6°C) than the subcutaneous portion (1.0 – 1.8°C), as shown in Figure 4.14(f). This difference in the temperature distribution is due to the presence of healthy skin layer overlying the subcutaneous portion of the IHs that decreases the effect of subcutaneous vasculature on the skin temperature. Finally, the temperatures of the superficial and (some of the) subcutaneous portions of the lesion are displayed in Figure 4.14(b) for easy visualization of the lesion extent.

Case II Proliferating IH of the nose: Figure 4.15(a) shows a proliferating, mixed hemangioma of the nasal tip in a 2-month-old Caucasian female. The lesion did not receive

any treatment prior to imaging. The lesion's appearance resembled an elevated rubbery mass that had softened, flattened and greyed particularly on the right side compared to the appearance during a previous visit. The visual inspection of the lesion showed light reddish-bluish discoloration left of the nasal tip (shown by an arrow on Figure 4.15(a)), suggesting deeper involvement. Figure 4.15(c) shows that the lesion is darker in

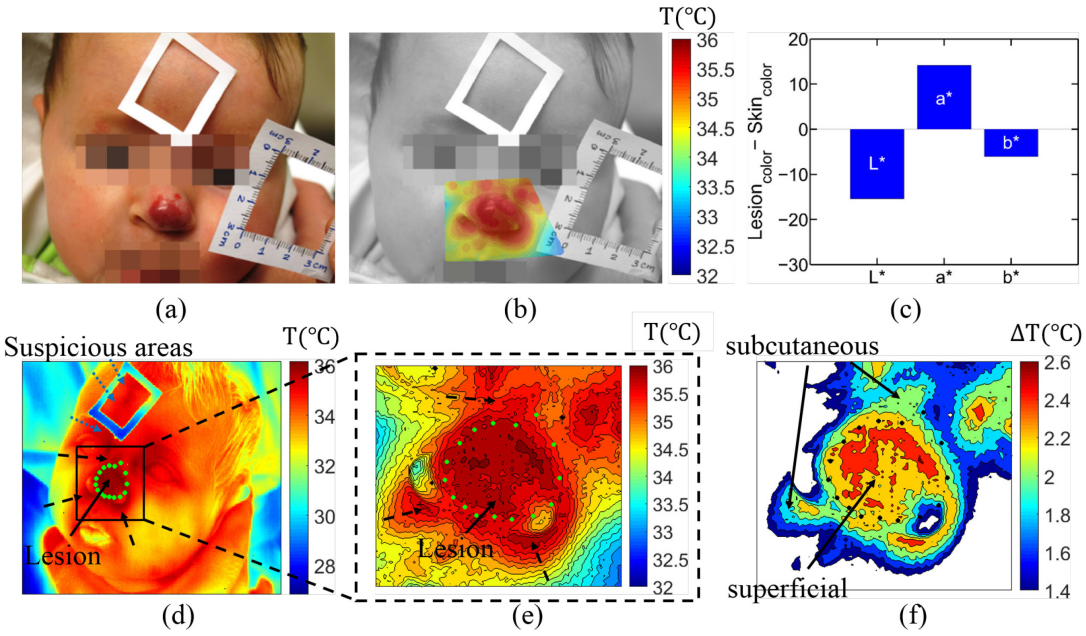

Figure 4.15 Case II – Proliferating hemangioma of the nasal tip in a 2-month-old Caucasian female. The lesion did not receive treatment prior to imaging. (a) WL image, (b) Total affected area mapped onto the WL image, (c) color difference analysis between lesion and healthy skin in terms of ΔL^*, Δa^* and Δb^*. (d) Color-coded IR image. The superficial boundary mapped from the WL is shown in green and marked with a solid black arrow. The dashed black arrows indicate the extent of subcutaneous involvement and the blue dashed arrows point to the suspiciously warm regions that might belong to the subcutaneous portion of the lesion. The black rectangle shows the ROI. (e) The magnified IR image showing temperature in the ROI and (f) temperature elevation at lesion location with respect to surrounding healthy skin (1.4 – 2.6°C). Lesion area ratio: $Area_{IR}/Area_{WL} = 1.6$. Color differences: $\Delta E_{avg} = 32.17$ (superficial, healthy skin) and $\Delta E_{avg} = 13.71$ (subcutaneous, healthy skin).

appearance ($\Delta L^* = -15$) and has more reddish ($\Delta a^* = 15$) and bluish ($\Delta b^* = -5$) hues when compared to the healthy skin.

From the WL image (in Figure 4.15 (a)), we determined that the superficial lesion is 1.7 cm (major axis) by 1.3 cm (minor axis) large, with a surface area of approximately 1.5 cm^2 and it covers the nasal tip. This is the superficial portion of the mixed lesion visible in the WL image (Figure 4.15 (a)). The IR images (Figure 4.15 (d) - (e)) show that the nasal base, the ala of the nose and the portions of the nasal ridge are also affected. These subcutaneous portions determined in the IR image are marked with dashed black arrows in Figure 4.15(d) - (e) and solid black arrows in Figure 4.15(f). Relative to the surrounding healthy skin temperature (33 – 34°C), we measured a temperature increase in the range of 1.4 – 2.6°C at the lesion location (shown in Figure 4.15(f)). The hypervascular regions (with high blood perfusion) present in the vascular tumor during its proliferation phase [116] are responsible for this local increase in skin temperature. The IR image shows that the dimensions of the entire lesion are 1.9 cm (major axis) by 1.6 cm (minor axis) and a surface area of approximately 2.3 cm^2. This is 1.6 times larger than the area visible from the WL image.

Additionally, we detected suspiciously warm areas in the middle forehead. These regions seem to be connected to the high temperature areas of the original lesion's subcutaneous portions. These suspicious areas are marked in Figure 4.15(a) with blue dashed arrows. We cannot confirm whether the temperature elevation in this region is due to the effect of subcutaneous vasculature of the lesion or the combined effect of the physiological blood circulation of the forehead and the abnormal, proliferating vasculature of the lesion. Therefore, we excluded this region from our calculations of lesion area based

on the IR image. Additional imaging by ultrasound or MRI would be needed to more accurately interpret the causes of the elevated temperatures on the forehead.

Summary for the proliferating IHs – Case studies I through II demonstrated the applicability of the combined IR – WL imaging technique in quantitatively assessing proliferation phase IHs. The color, thermal and geometrical features of the proliferating phase IHs are summarized in Table 4.2 and Table 4.3. Both lesions were classified as mixed subtypes. Case I was an elevated IH covering the lower lip and case II was a flat raised lesion at the nasal tip. We demonstrated that the color differences computed using the CIELAB model are proportional to the visually perceived color differences. The measured color differences between the superficial lesion and healthy skin are larger than the measured color differences between the subcutaneous portion and healthy skin. We also demonstrated that the total affected area, which is visualized by IR imaging, extends significantly beyond the visible superficial lesion boundary. The measured surface area of the elevated temperature region is 5.8 times larger than the measured surface area from WL images for case I and by 1.6 times for case II. The significant subcutaneous involvement can be associated with the proliferating subcutaneous portion of the lesion. The temperature

Table 4.2 WL image based color differences between lesion and healthy skin for proliferating IHs (from WL images)

Case No	Description	Location	ΔE_{avg} (superficial, healthy skin)	ΔE_{avg} (subcutaneous, healthy skin)
I	Mixed	Lip	32.17	13.71
II	Mixed	Nasal tip	28.11	27.62

Table 4.3 Geometrical and thermal features of proliferating IHs (from WL and IR images)

Case No	Maximum lesion temperature Tmax (℃)	Temperature elevation ΔT (℃)	Major Axis(WL) Minor Axis(WL) (cm)	Major Axis(IR) Minor Axis(IR) (cm)	$\mathbf{Area_{WL}}$ (cm^2)	$\mathbf{Area_{IR}}$ (cm^2)	Area ratio $(\frac{\mathbf{Area_{IR}}}{\mathbf{Area_{WL}}})$
I	36.6	1.0-2.6	3.3, 1.9	5.0, 3.8	4.6	26.8	5.8
II	36.2	1.4-2.6	1.7, 1.3	1.9, 1.6	1.5	2.3	1.6

elevation with respect to surrounding healthy skin was between 1 - 2.6°C for both cases. This temperature rise is due to the presence of hypervascular regions during the proliferating phase. These cases demonstrate the applicability of IR imaging as an inexpensive, non-invasive imaging technique for identifying the subcutaneous involvement in proliferating cases of mixed subtype. Accurate assessment of the subcutaneous involvement of IH early in the proliferative stage can prevent complications and will allow better tailoring of treatment strategies which will benefit IH subjects in the long run.

4.5.3 Characterization of IHs in plateau phase

The proliferative phase is followed by a short period of growth arrest, referred to the plateau phase (as illustrated in Figure 4.1). The plateau phase marks the transition of the IH lesion from proliferation (hypervascularity) to involution (both hypovascular and hypervascular regions may be present). We demonstrate the applicability of the combined IR – WL imaging technique in assessing the plateau phase of IHs through case studies III and IV. A summary of lesion color and plateau phase temperature characteristics for cases III and IV is presented at the end of this section using Table 4.4 and Table 4.5.

Case III Plateau phase IH of the scalp: Figure 4.16(a) shows a plateau/early involution phase, superficial hemangioma of the scalp in a 9-month-old Caucasian female. The lesion was deeply erythematous, very soft to palpation and had a greyish to dark purplish color by clinical observations. It did not receive treatment prior to imaging. Figure 4.16(c) shows

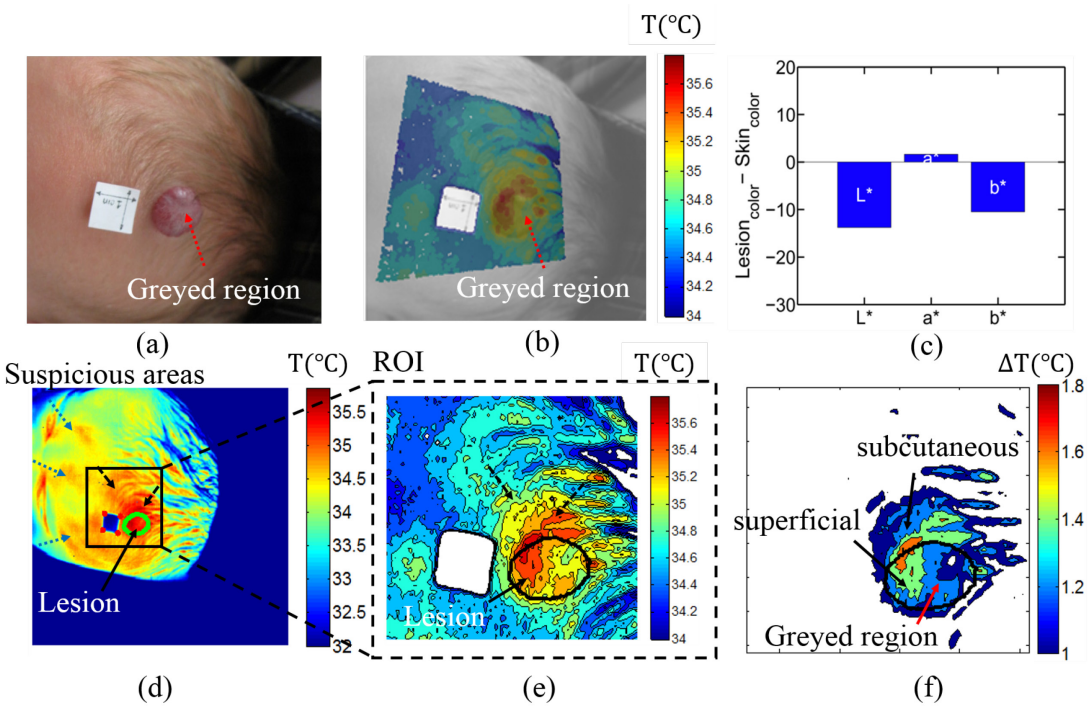

Figure 4.16 Case III - Plateau phase hemangioma of scalp in a 9-month-old Caucasian female [139]. The lesion was deeply erythematous and very soft to palpation. The superficial portion of the lesion had a somewhat grey, dark purple appearance. The patient did not receive treatment prior to imaging. (a) WL image. The dashed red arrow points at the central grey region b) Total affected area mapped onto the WL image. (c) Color difference between lesion and healthy skin in terms of ΔL^*, Δa^* and Δb^*. (d) Color-coded IR image. The solid black arrow indicates the superficial portion, the dashed black arrows point to the subcutaneous portions. The blue dashed arrows point to the suspiciously warm regions that might represent extensions to the subcutaneous portion. The black rectangle outlines the ROI. (e) Magnified IR image showing temperature in the ROI and (f) temperature elevation at lesion location (1 – 1.8°C) with respect to the surrounding healthy skin. The lesion area ratio is $Area_{IR}/Area_{WL} = 1.75$. The measured color differences are $\Delta E_{avg} = 14.15$ (superficial, healthy skin) and $\Delta E_{avg} = 7.27$ (subcutaneous, healthy skin).

that the lesion is darker in appearance ($\Delta L^* = -10.3$), has more bluish hues ($\Delta b^* = -9.7$) and similar reddish hues ($\Delta a^* = 1.2$) when compared to the healthy skin color.

From the WL image (in Figure 4.16(a)), the superficial portion of the lesion is 1.4 cm (major axis) by 1.1 cm (minor axis) large and covers an area of $1.2cm^2$ on the left temporal scalp of the subject. The IR images (Figure 4.16(d) – (e)) show that the lesion affects a larger area on the scalp than detected in the WL image. The black dashed arrows indicate the subcutaneous involvement of the lesion in Figure 4.16(e). The dimensions of the entire lesion, measured from the IR image, are 1.5 cm (major axis), 1.4 cm (minor axis) and a total area of 2 cm^2. This area is 1.7 times larger than the area measured from the WL image. This result suggests that the assessment of IH by visual inspection alone can underestimate the true extent of the affected region. We detected suspiciously warm areas in the forehead that seem to be connected to the high temperature areas of the original lesion's subcutaneous portions. These suspicious areas are indicated in Figure 4.16(d) by dashed blue arrows. We cannot confirm if the elevated temperatures in these areas is the result of the subcutaneous vasculature of the IH or the combined effect of the healthy blood vessels of the forehead region and the subcutaneous lesion vasculature. The IR image in Figure 4.16(d) detects additional areas of elevated temperatures which are partially covered by the subject's hair. Therefore, we excluded these regions from our calculations of lesion area based on the IR image. Additional imaging by ultrasound or MRI would be needed to more accurately interpret the causes of the elevated temperatures on the forehead. At the time of imaging, the central portion of the lesion exhibited greying (Figure 4.16(a)), which is considered an early sign of lesion regression [39]. In addition to the color change, IHs experience decrease in vascularization during regression [116]. The IR image (in Figure

4.16(f)) shows that the central greyish region has a smaller temperature elevation (1 – 1.2°C) than the top left boundary of the superficial portion (1.6 – 1.8°C). This temperature distribution can be explained in terms of decreased vascularization in the central portion of the lesion that shows lower temperature than the surrounding portion. The thermal map in Figure 4.16(e) is overlaid onto the WL image for better visualization (Figure 4.16(b)). This case illustrates the capability of IR imaging to quantitatively identify changes in lesion vascularity from the proliferative period to the involution period.

Case IV Plateau phase IHs of the forehead and scalp: Figure 4.17 shows two plateau phase hemangiomas in a 10-month-old Caucasian female subject. Lesion 1 was on the right forehead (Figure 4.17(a)) and lesion 2 was in the right parietal scalp region (Figure 4.17(g)). Lesion 1 was a 3.25 cm (major axis) x 1.8 cm (minor axis) large, elevated dome shaped hemangioma, as determined from the WL image. Lesion 2 resembled an oval shaped plaque that has overlying purple papules. The top left portion is labeled as L1 (2.5cm (major axis) x 1.4cm (minor axis) large) and bottom right portion is labeled as L2 (2.2 cm (major axis) x 0.7cm (minor axis)). These dimensions were measured form the WL image and represent the superficial portion of lesion 2. Lesion 2 was treated with topical Timolol gel. The average color differences between the superficial portion and healthy skin are - $\Delta E_{avg} = 21.45$ for lesion 1 and $\Delta E_{avg} = 29.5$ for lesion 2 (Table 4.4). The average color differences between the subcutaneous portion and healthy skin for both lesion 1 and lesion 2 are $\Delta E_{avg} = 2.55$ (Table 4.4).

The IR image of the subject is displayed in Figure 4.17(d), where ROI1 corresponds to lesion 1 and ROI2 corresponds to lesion 2. The temperature distributions in the ROIs are visualized in Figure 4.17(e) for lesion 1 and Figure 4.17(h) for lesion 2. These results show

that larger portions of the scalp region are affected by the combined effect of the lesions. The temperatures of the affected areas are 2.4 – 4.2°C above the healthy skin temperature as illustrated in Figure 4.17(f) for lesion 1 and Figure 4.17(i) for lesion 2. The solid black

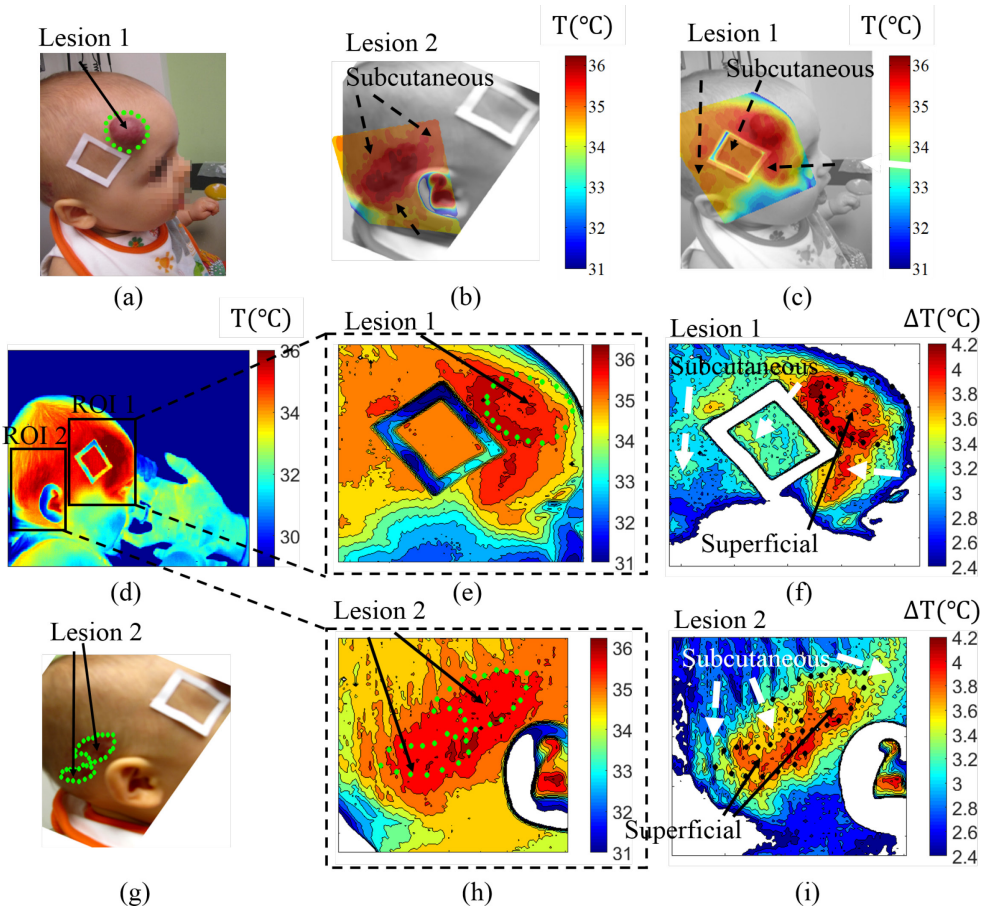

Figure 4.17 Case IV – Plateau phase hemangiomas of the forehead (lesion 1) and the scalp (lesion 2) in a 10-month-old, Caucasian female. (a) WL image of lesion 1. (b) Total affected area mapped onto the WL image for (b) lesion 2 and (c) lesion 1. (d) Color-coded IR image: the two black rectangles outline the ROIs for lesions 1 and 2. (e) Magnified IR image showing temperatures in ROI1 and the corresponding (f) temperature elevation map for lesion 1. (g) WL image of lesion 2. (h) Magnified IR image showing the temperatures in ROI2 and the corresponding (i) temperature elevation map for lesion 2. The temperature elevation with respect to the healthy skin is 2.4 to 4.2°C for lesions 1 and 2. The lesion area ratios are $Area_{IR}/Area_{WL} = 9$ for lesion 1 (forehead) and $Area_{IR}/Area_{WL} = 2.8$ for lesion 2 (scalp). The color differences are $\Delta E_{avg} = 21.45$ (superficial, healthy skin) for lesion 1 and $\Delta E_{avg} = 29.5$ for lesion 2. $\Delta E_{avg} = 2.55$ (subcutaneous, healthy skin) for both lesions.

arrows point to the superficial portions and the dashed white arrows indicate the subcutaneous involvement for both cases. The dimensions of the entire lesion measured from the IR images are: 8.9 cm (major axis), 6.6 cm (minor axis) with a surface area of 41 cm^2 for lesion 1; and 7.3 cm (major axis), 3.5 cm (minor axis) and 15.5 cm^2 for lesion 2. The areas of the affected portions measured from the IR images are 9.1 times larger for lesion 1 and 2.8 times larger for lesion 2, than the respective areas measured from the WL image. The total extent of the affected area, color coded to show the local temperature, was mapped onto the WL images and results are visualized in Figure 4.17(b) and (c). When considering the thermal signatures of the two lesions, we conclude that the entire scalp portion between lesion 1 on the right forehead and lesion 2 on the right parietal scalp seems to be affected. The temperature elevation in the affected region is due to the combined effect of the subcutaneous vasculature of lesions 1 and 2. The superficial portions of the lesions show higher temperature elevations (3.8 – 4.2°C for lesion 1 and 3.4 – 4.2°C for lesion 2) than the subcutaneous portions (2.4 – 4.0°C for lesion 1 and 3 – 4.0°C for lesion 2). The healthy skin layer (with lower perfusion and vasculature) overlying the subcutaneous portion decreases the heating effect of the subcutaneous vasculature on the skin temperature. The central portion of the elevated dome shaped lesion 1 is colder (35.5°C) when compared to the superficial boundary (36.2°C) close to the paper marker, as illustrated in Figure 4.17(e) – (f). Two explanations are possible for the lower temperature elevation in the central portion of the dome-shaped lesion. First, the higher central portion of the lesion can cool down more when exposed to ambient natural convection than the base of the lesion which is heated by perfusion from the subcutaneous lesion and thermal conduction from the tissue underneath. Alternatively, the low

temperature increase at the center of lesion 1 may be an indicator of the regression of the central portion. This explanation can be validated by observing the thermal signatures of the lesion over time.

Summary for the plateau phase IHs – Case studies III and IV demonstrated the applicability of the combined IR – WL imaging technique as an inexpensive, non-invasive imaging technique to quantitatively assess vascular patterns associated with plateau phase and early involuting phase IHs. The color, thermal and geometrical features of the plateau phase IHs are summarized in Table 4.5 and Table 4.4. Both lesions were clinically classified as superficial subtype and were located on the scalp. Lesion 1 had a raised dome shaped structure and lesion 2 resembled an oval shaped plaque overlaid with papules. The measured color differences between the superficial lesion and healthy skin are larger than the measured color differences between the subcutaneous portion and healthy skin. We demonstrated that the total affected area, which is visualized by IR imaging, extends well beyond the visible superficial lesion boundary. The area ratios were: $Area_{IR}/Area_{WL} = 1.7$ for case III; $Area_{IR}/Area_{WL} = 9$ for lesion 1 of case IV; and $Area_{IR}/Area_{WL} = 2.8$ for lesion 2 of case IV. These results suggests that the assessment

Table 4.4 Geometrical and thermal features of plateau phase IHs (from WL and IR images)

Case No	**Maximum lesion temperature Tmax** (℃)	**Temperature rise** Δ**T** (℃)	**Major Axis(WL) Minor Axis(WL)** (cm)	**Major Axis(IR) Minor Axis(IR)** (cm)	$\mathbf{Area_{WL}}$ (cm^2)	$\mathbf{Area_{IR}}$ (cm^2)	**Area ratio** $(\frac{\mathbf{Area_{IR}}}{\mathbf{Area_{WL}}})$
III	35.1	1.0-1.8	1.4, 1.1	1.5, 1.4	1.2	2.1	1.7
IV(1)	36.0	3.0-4.2	3.25, 1.8	8.9, 6.6	4.5	41.0	9.0
IV(2)	36.0	3.0-4.0	2.5,1.4(L1) 2.2,0.7(L2)	7.3, 3.5	5.6	15.5	2.8

Table 4.5 WL image based color differences between lesion and healthy skin for plateau phase IHs

Case No	Description	Location	ΔE_{avg} (superficial, healthy skin)	ΔE_{avg} (subcutaneous, healthy skin)
III	Superficial	Left scalp	14.15	7.27
IV (1)	Superficial	Right forehead	21.45	2.55
IV (2)	Superficial	Right parietal scalp	L1:28.74 L2:31.93	2.55

of an IH lesion by visual inspection alone can significantly underestimate the true extent of the affected region. We demonstrated that the lesion geometry and vascularity can affect the temperature elevation distributions. Early accurate identification of the subcutaneous involvement and assessment of the subcutaneous vascular patterns in IHs would be useful during longitudinal studies. It would allow taking clinical measures to prevent complications and quantitative treatment evaluations.

4.5.4 Characterization of involuting phase IHs

The final phase of lesion evolution is the involution phase, which is marked by slow regression of the lesion. According to [112], the fibrous fatty tissue replaces the deep vascular portions of the tumor, resulting in decreased size and vascularity [116] of IHs during the involution phase. The lesion becomes softer to the touch and shows greying of the visible portion [106, 110, 112, 137]. We demonstrate the applicability of the combined IR – WL imaging technique in assessing involuting IH cases V, VI and VII. A summary

of lesion color and temperature characteristics for the involution phase cases V to VII is presented at the end of this section in Table 4.6 and Table 4.7.

Case V Involuting IH of the back: Figure 4.18 (a) shows an involuting, mixed hemangioma of the back in a 14-month-old Caucasian female. The focal hemangioma resembled a soft red vascular plaque. The central portion of the lesion shows greying, indicating involution. A significant deep component was appreciated clinically and the

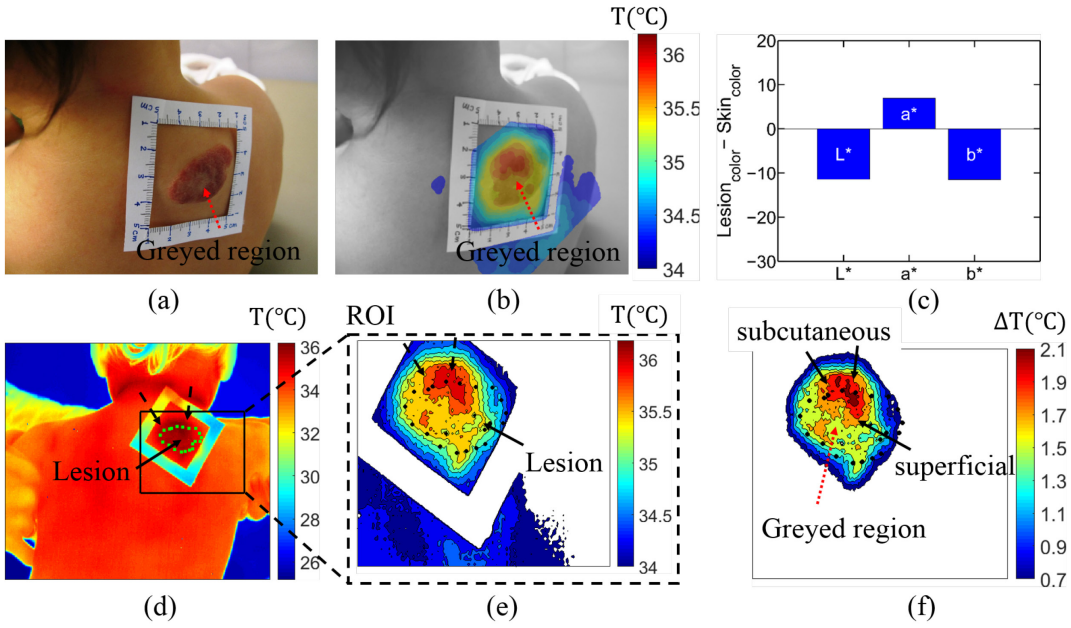

Figure 4.18 Case V - Involuting hemangioma of the back in a 14-month-old Caucasian female. The lesion resembled a soft red vascular plaque with central greying. A significant deeper component was clinically appreciated and the lesion was treated with Timolol gel. (a) WL image. (b) Total affected area mapped onto the WL image. It is color coded to show local temperature. (c) Color difference between the lesion and healthy skin in terms of L^*, a^* and b^*. (d) Color-coded IR image. The solid black arrow points to the superficial portion, the dashed black arrows point to the subcutaneous portion and the black rectangle outlines the ROI. (e) Magnified IR image showing temperature in the ROI and (f) temperature elevation (0.7°C – 2.1°C) at the lesion location with respect to the surrounding healthy skin. Lesion area ratio: $Area_{IR}/Area_{WL} = 2.1$ .Color difference: $\Delta E_{avg} = 12.09$ (superficial, healthy skin) and $\Delta E_{avg} = 6.05$ (subcutaneous, healthy skin).

lesion was treated with Timolol gel. Figure 4.18 (c) shows that the lesion is darker in appearance ($\Delta L^* = -11$) and has a dark reddish ($\Delta a^* = 7$) and bluish hue ($\Delta b^* = -11$) when compared to the healthy skin color. From the WL image, the dimensions of the superficial portion are 4.4 cm (major axis), 2.3 cm (minor axis) and a surface area of approximately 7.8 cm^2. The IR images (in Figure 4.18 (d) - (e)) show that larger portion of the back is affected than the region apparent by visual inspection. The dashed black arrows in Figure 4.18 (d) and Figure 4.18 (e)) point to the areas of subcutaneous involvement. The total affected portion of the lesion was mapped onto the WL image and the result is visualized in Figure 4.18(b). With respect to the surrounding healthy skin at 34°C (Figure 4.18 (d)), the temperature rise at lesion location is 1.1 – 2.1°C (Figure 4.18 (f)). Figure 4.18 (f) shows that the maximum temperature rise (1.7 - 2.1°C) is present in the region just outside the superficial boundary (outlined by black dotted line). The temperature rise is due to the hypervascular portions of the tumor. The greying of the central portion of the lesion (marked with a dashed red arrow in Figure 4.18(a) and (b)) is a sign of lesion regression. The temperature rise of the central region, that exhibits greying, is 0.7°C less than the temperature rise at the top rim of the lesion (Figure 4.18(e)). This temperature distribution at the central portion can be explained by the decreased vascularity of the involuting portion of the lesion. The lesion measures 5.1 cm (major axis) by 4.2 cm (minor axis) in the IR image with a total area of 16.3 cm^2. This is 2.1 times larger than the area measured from the WL image. This results suggests that the affected area is likely to be underestimated if considering the visible portion of lesion in the WL image alone.

Case VI Involuting IH of the arm: Figure 4.19(a) shows an involuting, mixed hemangioma of the arm in a 16-month-old Caucasian female. The focal hemangioma resembled a nodular red vascular plaque with some central greying. The lesion was treated with Propranolol. Figure 4.19 (c) shows that the lesion is darker in color (ΔL* = -11), has

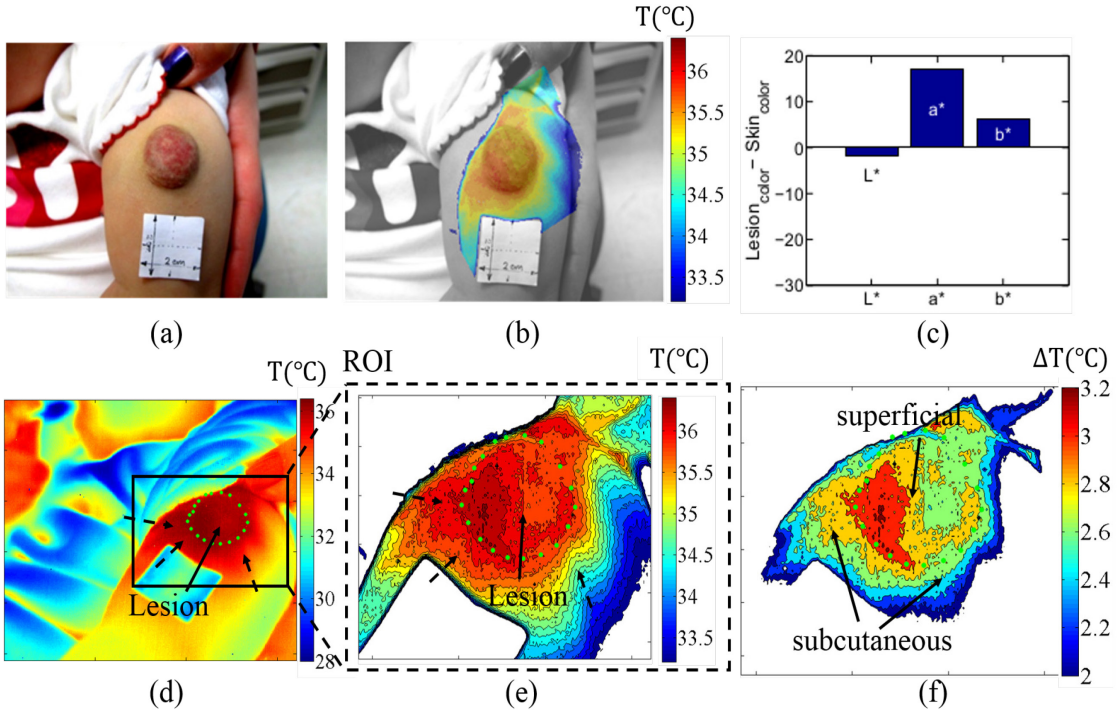

Figure 4.19 Case VI - Involuting hemangioma of the arm in a 16-month-old Caucasian female [140]. The lesion resembled a nodular red vascular plaque with some central greying. It was treated with Propranolol. (a) WL image. (b) Total affected area mapped onto the WL image. The map is color coded to show local temperature. (c) Color difference between the lesion and healthy skin in terms of L^*, a^* and b^*. (d) Color-coded IR image. The solid black arrow points to the superficial portion of lesion, and the dashed black arrows point to the subcutaneous portion. The black rectangle outlines the ROI. (e) The magnified IR image showing temperature in the ROI and (f) temperature elevation at the lesion location (2 – 3.8°C) with respect to the surrounding healthy skin. ΔT is 2 – 2.8°C in the subcutaneous portion and 2.8 – 3.2°C in the superficial portion of the lesion. Lesion area ratio: $Area_{IR}/Area_{WL} = 2.2$ Color differences: $\Delta E_{avg} = 13.05$ (superficial, healthy skin) and $\Delta E_{avg} = 11.95$ (subcutaneous, healthy skin).

more reddish ($\Delta a^* = 7$) and bluish hues ($\Delta b^* = -11$) when compared to the healthy skin color.

From the WL image, the dimensions of the superficial portion of the lesion are 2.1 cm (major axis), 1.8 cm (minor axis) with a surface area of 3.0 cm^2. The IR images (shown in Figure 4.19(d)) and (e)) show that a larger portion of the arm is affected than detected in the WL image. The dashed black arrows point to the subcutaneous portion of the lesion in Figure 4.19 (d) - (e). The total affected area was mapped onto the WL image and the result is visualized in Figure 4.19(b). The subcutaneous portion extends from the top right to the bottom left of the superficial portion, as illustrated in Figure 4.19 (b) and (e).

The lesion was significantly warmer by 2.0 – 3.2°C (Figure 4.19(f)) with respect to the surrounding healthy skin temperature of 33.2°C (Figure 4.19(d)). Figure 4.19(f) shows that the temperature elevation of the right half (3 – 3.2°C) is larger than the left half (2.6 – 2.8°C) of the superficial visible component. This temperature distribution can be associated with the regressing left half of the lesion. The entire affected area measured from the IR image, was 3.9 cm (major axis) by 2.2 cm (minor axis) large with a total surface area of 6.8 cm^2. This area is 2.2 times larger than the area measured from the WL image. This result suggests that again the affected area is likely to be underestimated if the visible portion of lesion is considered alone.

Case VII Involuting IH of the glabella: Figure 4.20(a) shows an involuting, deep hemangioma of the glabella in a 29-month-old Caucasian female. The focal hemangioma resembled a soft compressible, subcutaneous nodule that has some coarse overlying telangiectasia with an overlying purple hue. The lesion was treated with Propranolol. Figure 4.19(c) shows that the lesion is darker in appearance ($\Delta L^* = -15.2$), has similar

redness (Δa* = 1.8) and dark bluish (Δb* = -10.5) hues when compared to the healthy skin color. The superficial portion of the lesion was identified on the basis of light purple discoloration (green boundary in Figure 4.20 (a)) of the skin. From the WL image, the dimensions of the superficial portion were measured as 1.6 cm (major axis), 0.8 cm (minor axis) and a surface area of 1.0 cm^2 (Figure 4.20 (a)). The IR images in Figure 4.20 (d)-(e)

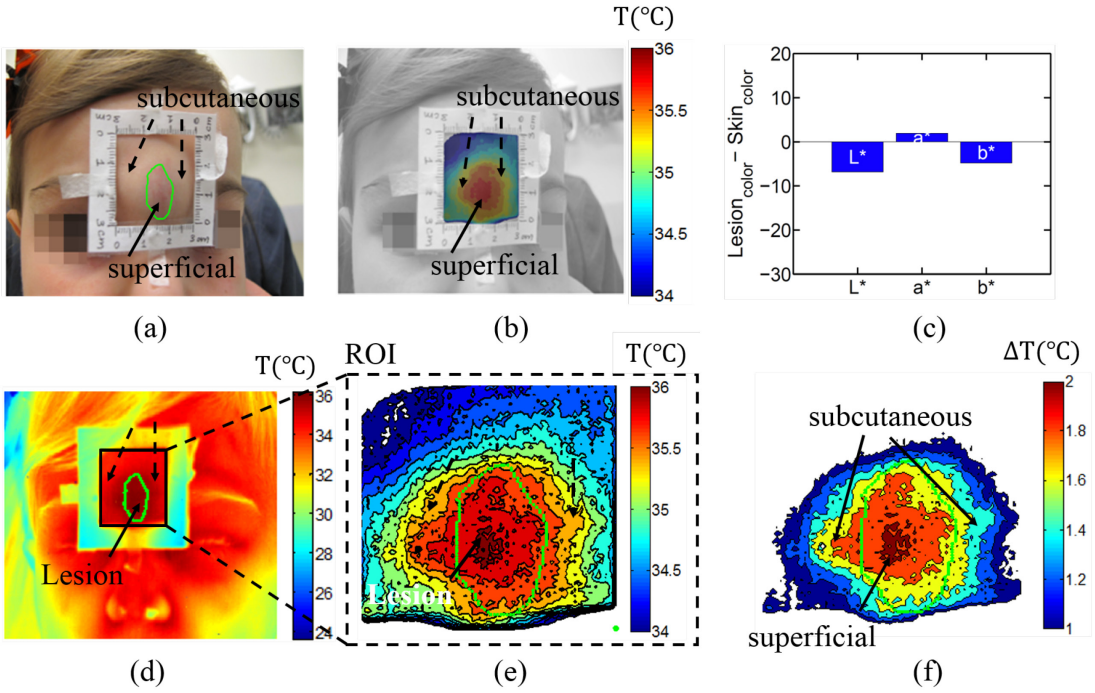

Figure 4.20 Case VII - Involuting, deep hemangioma of glabella in a 29-month-old Caucasian female [139]. The lesion resembled a soft, compressible subcutaneous nodule that has some coarse overlying telangiectasia with an overlying purple hue. It was treated with Propranolol. (a) WL image. (b) Total affected area (color-coded temperature map) mapped onto the WL image. (c) Color difference between the lesion and healthy skin in terms of L^*, a^* and b^*.(d) The color-coded IR image. The solid black arrow points to the superficial portion of lesion and the black dashed arrows point to the subcutaneous portion. The black rectangle outlines the ROI. (e) Magnified IR image showing temperature in the ROI and (f) temperature elevation at the lesion location (1 – 2°C) with respect to the surrounding healthy skin. ΔT is 1 – 1.8°C in the subcutaneous portion and 1.6 – 2°C in the superficial portion of the lesion. Lesion area ratio: $Area_{IR}/Area_{WL} = 4$. Color differences: $\Delta E_{avg} = 18.57$ (superficial, healthy skin) and $\Delta E_{avg} = 11.56$ (subcutaneous, healthy skin).

display the temperature distributions at the superficial and surrounding subcutaneous portions of the deep IH lesion. The entire lesion, as measured from the IR image, was 2.5 cm (major axis) by 2.1 cm (minor axis) large with an area of 4.1 cm^2. This area is 4 times larger than the area measured from the WL image. The total affected area (as color-coded IR thermal map) was mapped onto the WL image and the result is visualized in Figure 4.20 (b). With respect to the healthy skin temperature of 34°C (Figure 4.20(d)), the temperature increase is in the range of 1.0 – 1.4°C at the subcutaneous portion and 1.4 – 2.0°C at the superficial portion, as illustrated in Figure 4.20 (f). The superficial and subcutaneous portions are marked by solid black arrows. This temperature distribution can be attributed to the presence of the healthy skin layer overlying the subcutaneous portion that decreases the effect of the subcutaneous vasculature on the skin temperature.

Summary for the involution phase IHs – Cases V through VII demonstrated the applicability of the combined IR – WL imaging technique in quantitatively assessing involution phase IHs. The color, thermal and geometrical features of the involuting phase IHs are summarized in Table 4.6 and Table 4.7. Two lesions were of mixed subtype (case V, upper back and case VI, left arm) and one was classified as a deep IH (case VII, glabella). Case V was a flat raised lesion, case VI was elevated dome-shaped and case VII was a subcutaneous nodule. The measured color differences between the superficial lesion and healthy skin are larger than those between the subcutaneous portion and healthy skin. By comparing lesion outlines in WL and IR images, we showed that the total affected area extends well beyond the visible superficial boundary. We quantified the extent of subcutaneous involvement from the IR images. When compared to the area measured from the WL image, the total affected area measured from the IR images was 2.1 times larger

for case V, 2.2 times larger for case VI and 4 times larger for case VII. The temperature decrease observed at the central portion in cases V and VII can be explained by the involution phase characteristics of the IH lesions. The less perfused fibrous fatty tissue replaces the highly perfused tumor, causing decrease in lesion vascularity and subsequent decreases in skin temperature. These results demonstrate the applicability of IR imaging in identifying regressing portions of the lesion during the involution phase.

Table 4.6 WL image based color differences between lesion and healthy skin for the involuting IHs

Case No	**Description**	**Location**	ΔE_{avg} **(superficial, healthy skin)**	ΔE_{avg} **(subcutaneous, healthy skin)**
V	Mixed	Upper back	12.09	6.15
VI	Mixed	Left arm	13.05	11.95
VII	Deep	Glabella	18.57	11.56

Table 4.7 Geometrical and thermal features of the involuting IHs (from WL and IR images)

Case No	**Maximum lesion temperature Tmax** (℃)	**Temperature rise** Δ**T** (℃)	**Major Axis(WL) Minor Axis(WL)** (cm)	**Major Axis(IR) Minor Axis(IR)** (cm)	$\mathbf{Area_{WL}}$ (cm^2)	$\mathbf{Area_{IR}}$ (cm^2)	**Area ratio** $(\frac{Area_{IR}}{Area_{WL}})$
V	36.2	0.7-2.1	4.4, 2.3	5.1, 4.2	7.8	16.3	2.1
VI	36.4	2.0-3.2	2.1, 1.8	3.9, 2.2	3.0	6.8	2.2
VII	36.1	1.0-2.0	1.6, 0.8	2.5, 2.1	1.0	4.1	4.0

4.5.5 Quantitative visualization of IH colors and healthy skin colors

The Munsell color representations (HC/V values) for IHs and healthy skin colors were computed from the CIELAB coordinates of the colors, as discussed in section 4.4.1.3. Table 4.8 summarizes the quantitative color data for IHs and the healthy skin for the cases considered in this study. The measured hue (H), value (V) and the chroma (C) values for these cases are expressed in the HC/V notation of the Munsell representation. The hues and chroma values for the color of IHs and the corresponding healthy skin are visualized in the Munsell hue circle in Figure 4.21. The blue radial arrows represent IH cases and the red radial arrows correspond to the healthy skin colors. The numbers next to the arrows refer to the cases (Table 4.8). The color lightness varies along the y – axis (perpendicular to the

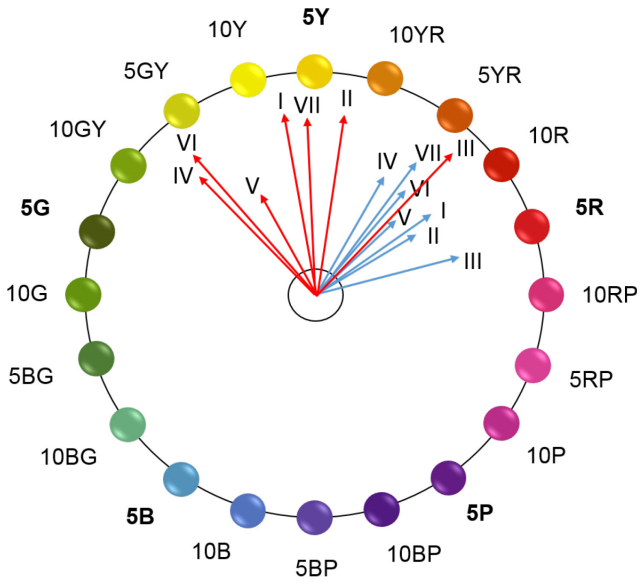

Figure 4.21 Quantitative visualization of IH and healthy skin colors on the Munsell hue circle. The blue arrows represent the IH lesions and the red arrows represent the corresponding healthy skin colors.

Table 4.8 Quantitative color representations for IHs and healthy skin colors using the HC/V Munsell color notation

Case No	HC/V (IH)	HC/V (healthy skin)
I	9.5R 3.4/7	7.5Y 6/4.3
II	0.6YR 3.3/7.4	1.2Y 6.2/6.2
III	4.8R 4.3/4.2	3YR 5.3/5.6
IV	6.8YR 2.8/5.7	8.5GY 5.6/6.5
V	3.3YR 2.6/6.1	4GY 4.0/7.3
VI	3.5YR 4.8/4.4	5.6GY 7/4.1
VII	5YR 5.7/3.8	5.5Y 6.8/4.0

plane of the paper) and the lightness data are shown in Table 4.8. We measured red to yellow – red hues (with a larger red component) for the first three IH cases (Figure 4.21(b)) - 9.5R for case I (Figure 4.14(a)), 0.6YR for case II (Figure 4.15(a)), and 4.8R for case III (Figure 4.16(a)). We measured yellow – red hues (with a larger yellow component) for the next four cases (Figure 4.21(b)) - 6.8 YR for case IV (Figure 4.17(a)), 3.3 YR for case V (Figure 4.18 (a)), 3.5YR for case VI (Figure 4.19(a)), and 5YR for case VII (Figure 4.20(a)). The corresponding healthy skin colors demonstrate yellow, yellow – red and yellow – green hues, illustrated in Figure 4.21.

4.5.6 Follow-up imaging of a proliferative phase IH lesion

Follow–up of case II (proliferating IH of the nasal tip): We applied the non-dimensional temperature technique developed in section 4.4.2 to the IR images of case II (a proliferating lesion of the nasal tip), captured during two clinical visits. The results are illustrated in Figure 4.22. Figure 4.22(a) shows the WL image during the first imaging session. The WL image of the lesion captured three months after the first imaging session

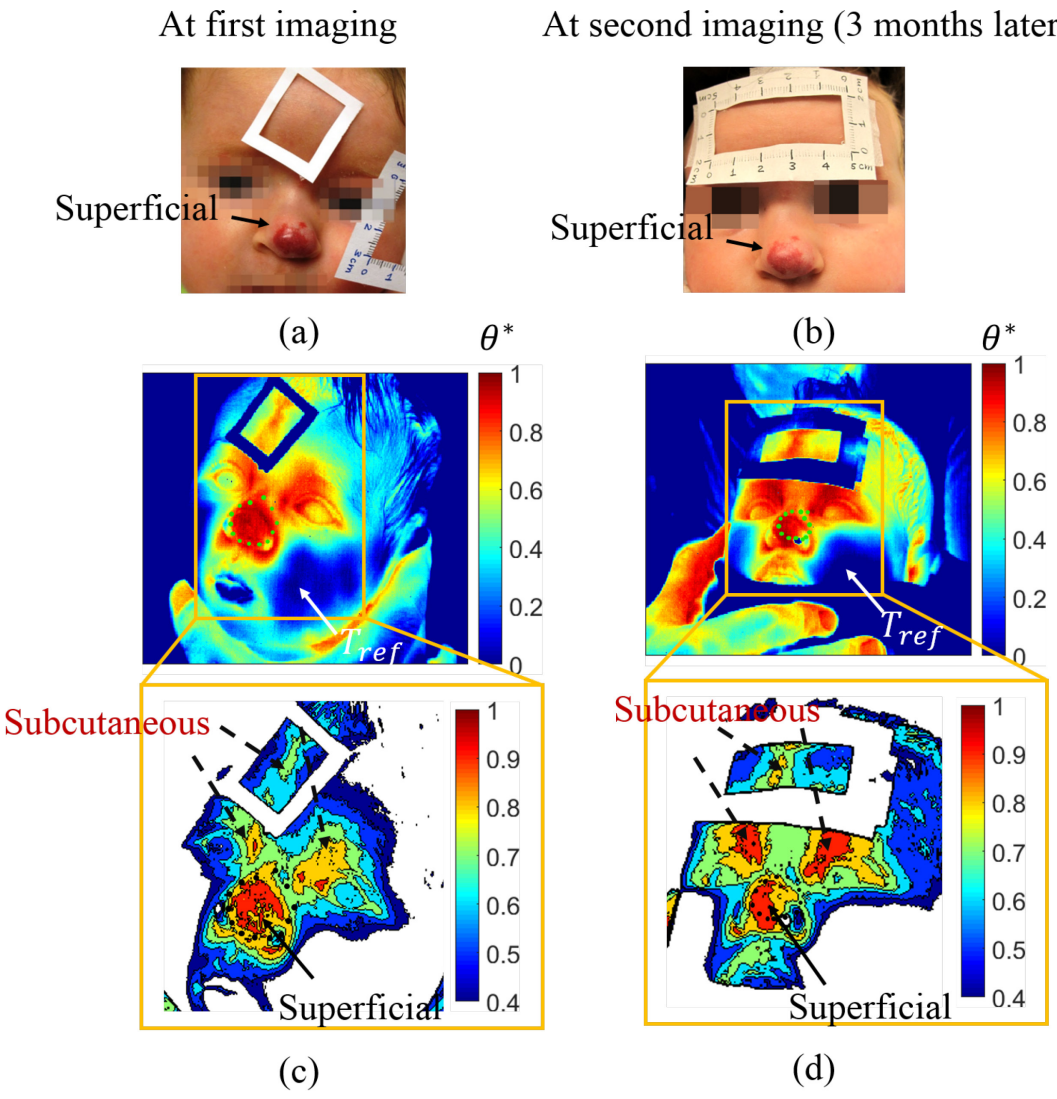

Figure 4.22 Non-dimensional temperature difference technique applied to the IR images of a proliferating lesion captured during two clinical visits. WL images captured during the (a) first and (b) second imaging session, three months later. (c) Dimensionless temperature difference (θ^*) map (top row) and the magnified image showing the dimensionless temperature difference in the ROI (bottom row) during the first visit. (d) Dimensionless temperature difference (θ^*) map (top row) and the magnified image showing the dimensionless temperature difference in the ROI (bottom row) during the second visit, three months later.

is displayed in Figure 4.22(b). The lesion was under treatment between the two visits. The lesion showed lighter discoloration at the second imaging session when compared to its

appearance during the first visit. The change in the color of the lesion from darker to lighter is induced by the regression due to treatment of the superficial lesion.

We generated the non-dimensional temperature difference (θ^*) maps using Equation 4.14. The left cheek temperature was chosen as the reference healthy skin temperature, as described in section 4.4.2. The non-dimensional temperature difference image for the first visit is shown in Figure 4.22(c) and for the second visit in Figure 4.22(d) (top rows). The bottom rows of Figure 4.22 (c) and (d) display the non-dimensional temperature differences in the ROI (yellow rectangle) using thermal contours. The results demonstrate the changes in the shape of the 0.9 intensity thermal contour from the first to the second visit. The 0.9 intensity contour at the nasal tip region is smaller at the second visit, when compared to the first. This decrease in non-dimensional temperature difference, demonstrated by the superficial portion of the lesion at the second visit, may be associated with the efficacy of the treatment. We detected suspiciously warm regions in the forehead region (also indicated in Figure 4.15(d) with dashed blue arrows) during both the first and second clinical visits. These regions (marked by dashed black arrows in bottom row of Figure 4.22s (c) and (d)) may be a part of the subcutaneous portion of the IH lesion, as explained for case II in section 4.5.2. The thermal contour of 0.9 intensity outlining the subcutaneous regions has increased in size, when compared to the first visit. This increase in non-dimensional temperature difference, manifested in the subcutaneous portions of the lesion at the second visit, may be associated with the proliferating subcutaneous vasculature of the lesion.

4.6 Discussion and conclusions

In this chapter, we demonstrated that the combined IR – WL imaging developed in this study can be used as an inexpensive, non-invasive tool for quantitative assessment of infantile hemangiomas. As the imaging technique does not require anesthesia or sedation, unlike MRI and CT, it is suitable for clinical imaging of young IH infants. We applied the WL and IR image processing techniques to quantitatively assess the IH color and temperature in different types of hemangiomas. Different classes of IH lesions (superficial, mixed and deep) were sampled from different regions of the body including the lip (case I), nasal region (case II), scalp (cases III and IV), back (case V), arm (case VI) and forehead (case VII). The lesions were in different phases (from proliferating to involuting) at the time of imaging and the subjects ranged from 1 to 30 months of age. Some subjects had received treatments (Propranolol or Timolol gel) prior to the time of imaging, while others had received no treatment. We summarize key findings and capabilities of the combined IR – WL steady state image analysis technique for quantitative assessment of all subjects in Figure 4.23. For presentation purposes, we plotted the results in the order of increasing age of the subjects (shown on the x axis) and grouped them by the IH stage (shown by horizontal arrows on the top). We present a comparison of lesion areas measured from the IR and WL images in Figure 4.23(a), temperature elevation distributions at lesion location with respect to the healthy skin temperature in Figure 4.23(b) and the color differences between lesion and healthy skin in Figure 4.23(c).

Analysis of IH size – We introduced an area ratio metric, $Area_{IR}/Area_{WL}$, to demonstrate the advantages of using quantitative IR imaging over conventional WL imaging for assessment of IH size. We observed that the total affected area extends well beyond the superficial portion that is visible in the WL images. According to Figure 4.23(a), the

measured surface area of the lesion from the IR images, $Area_{IR}$ (cm^2) was at least 1.6 times larger than the measured surface area from the WL images, $Area_{WL}$ (cm^2). We observed

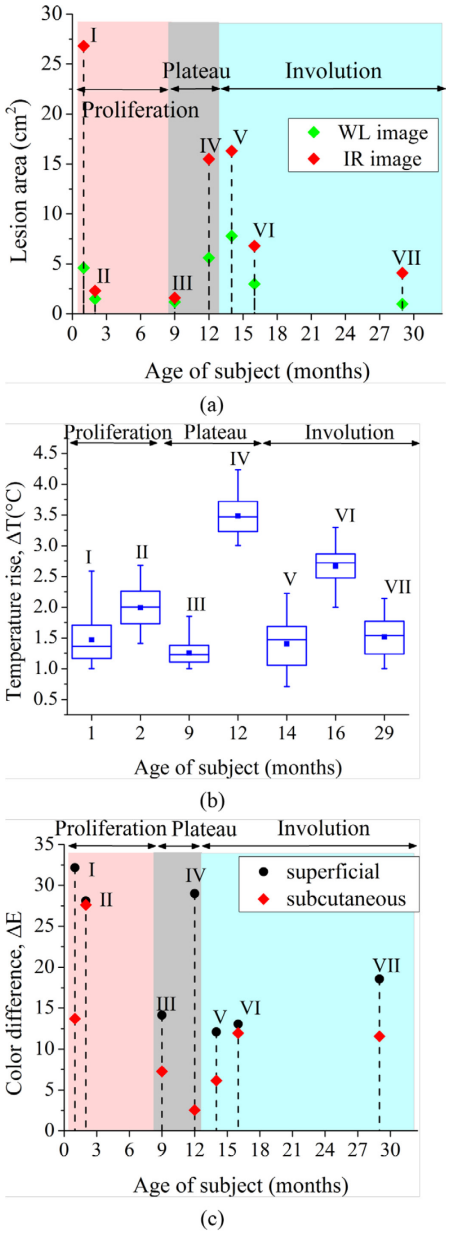

Figure 4.23 IH characteristics plotted as a function of the subject age and stage of evolution of the lesion. (a) Lesion area measured from the WL images and IR images, (b) temperature elevation at lesion location with respect to the surrounding healthy skin temperature and (c) color difference between the lesion and healthy skin in superficial and subcutaneous portions of the lesion.

this trend for all IH subtypes (superficial, mixed or deep). For most of the subjects (cases I and cases IV – VII), Area_{IR} was significantly larger than Area_{WL}. This result implies that the IR images provide a complete picture of the IHs by showing the subcutaneous involvement of IHs. For cases II (Figure 4.15) and III (Figure 4.16), for which smaller area ratios were observed, we cannot confirm with certainty whether the warm regions surrounding the superficial portion are the extensions of the subcutaneous involvement. Therefore, we did not include these areas in estimating the total affected area from the IR images. For superficial IH lesions, such as cases III (Figure 4.16) and IV (Figure 4.17), estimating the lesion area from the WL image, simply based on the redness or discoloration of the skin, may significantly underestimate the affected area. The subcutaneous portions of the mixed subtype IHs, such as cases I (Figure 4.14), II (Figure 4.15), V (Figure 4.18) and VI (Figure 4.19), and the deep IHs, such as case VII (Figure 4.20) are covered by an overlying layer of the healthy skin. Visible inspection alone cannot be used to accurately assess the subcutaneous portion of the IHs. Our thermal image overlay technique provides a unique capability to visualize and quantify the superficial and subcutaneous extent of the lesion simultaneously on the WL image.

Additionally, our current IR-WL image processing technique can be extended easily to estimate IH volume by including lesion depth information. The volume of the superficial portion may be computed by measuring the lesion elevation from the skin surface and combining it with the measured lesion surface area. In Chapter 3, we demonstrated that the depth of the lesion can be estimated non-invasively using inverse reconstruction algorithm using skin surface temperature as an input. The combined IR – WL imaging technique coupled with inverse reconstruction algorithms will allow

measuring the depth of the subcutaneous portion and subsequently the complete volume of the IH lesion non-invasively. Therefore, the combined IR – WL imaging approach is a suitable tool for quantitative assessment and long term monitoring of IH lesions.

Analysis of thermal signature of IHs: The box and whisker plot in Figure 4.23(b) shows the temperature elevation distributions for different IH cases. We considered the entire lesion area (including the subcutaneous and superficial portions) in contrast to one or two points for quantifying the thermal signatures of IH lesions. For each case, the minimum and maximum values of the whisker plots provide the range of temperature elevation at lesion location relative to the surrounding healthy skin temperature (Figure 4.23(b)). The mean and median temperature rise (from 1.5 – 3.5°C) is shown by the middle line and the dot of the box plot respectively. The upper and bottom limits represent the first and fourth quartiles of the temperature elevation distribution. In proliferating and plateau phase lesions, the subcutaneous portions exhibited lower temperature rise compared to the superficial portions (Figure 4.14(e) for case I and Figure 4.15(e) for case II, Figure 4.17(e) for case IV). The lower temperature rise of the subcutaneous portions is due to the overlaying layer of the healthy skin. The regressing portions of the involution phase IHs (identified by greying of the lesion) demonstrated smaller temperature elevations when compared to the non-regressed portions (shown in Figure 4.16(e) for case III; Figure 4.18(e) for case V and Figure 4.19 for case VI).

Analysis of color difference between lesion and healthy skin: In this study, we demonstrated that the color difference between the lesion and healthy skin in terms of ΔE (from CIELAB color model) [126] offers an objective and quantitative method to quantify changes in IH color with respect to the surrounding healthy skin. The visually perceived

color differences between the superficial portion and healthy skin are larger than those between the subcutaneous portion and healthy skin (from the WL images in cases I to VII). The ΔE values shown in Table 4.2, Table 4.4 and Table 4.6 align with this observation i.e. the superficial portions of lesions have larger ΔE than the subcutaneous portions in cases I through VII (also shown in Figure 4.23 (c)). After the completion of this study, we identified some of the limitations of our imaging technique. The temperature distributions for IHs involving the eyes are difficult to interpret, as illustrated by the IR images for case II (Figure 4.15). The eyes themselves emit more heat, making the process of differentiating the hemangioma's vasculature from the eye's vasculature challenging. Additionally, the estimates of area ratios for cases II and III are relatively smaller when compared to other cases (Figure 4.23(a)). The 2D projective registration of the lesion boundary is less accurate for the curved regions because the assumption that all the points to be registered lie in the same plane is not accurate for the curved areas. We detected suspiciously warm regions for these cases, however, we cannot confirm whether these areas belong the subcutaneous component of the lesions. Additional imaging by ultrasound or MRI would be needed to more accurately interpret the causes of the elevated temperatures in these cases. The presence of shadows due to elevated portions of the lesions and the non-uniform distribution of lighting pose limitations for color analysis. To overcome these effects, we selected the healthy skin regions where the illumination levels matched with that of the lesion for computing color differences between the lesion and healthy skin.

In conclusion, the successful analysis of this broad range of hemangiomas (different locations, subtypes and morphological characteristics) shows the feasibility and flexibility of the combined IR thermography with WL imaging in assessing these vascular tumors.

We developed color analysis tools for hemangiomas, which allow us to measure the color differences between lesion and healthy skin and provide quantitative visualization for the colors. We demonstrated that steady state infrared imaging in combination with the white – light imaging can quantify the total affected area (including the superficial and subcutaneous involvement) by the IHs. By applying WL – IR image registration, we can compare the areas of the visible portion of the IH with its thermal signature in the same image. This comparison shows that the IR image gives a more complete picture of the hemangioma area showing both the superficial and subcutaneous components. When coupled with inverse reconstruction techniques, the IR image may also provide the depth of the subcutaneous involvement allowing for volume measurements, which is a subject of future research. We combined the clinical knowledge of lesion phase and subtype with the lesion shape and temperature distribution to interpret the thermal signatures of IHs. This thermal analysis allowed us to quantitatively characterize the proliferating or involuting portions of the lesion and measure their surface areas. Finally, we developed a dimensionless temperature difference formulation, which allowed us to quantify the temperature elevations with respect to the surrounding healthy skin on a scale of 0 to 1. We used this technique to compare IR images of a proliferating lesion during different clinical visits (before and after starting treatment). We demonstrated that the intensity and shape of the dimensionless temperature difference contours can be associated with the increase or decrease in lesion size and vascular activity. The image processing methods presented in this chapter are used to measure the thermal and color signatures of other types of pigmented and vascular lesions in the next chapter.

Chapter 5 Thermal signatures of skin lesions

5.1 Motivation

The aim of this chapter is to initiate an atlas of thermal signatures of skin lesions varying in clinical and physiological characteristics, sizes and depths. A collection of thermal signatures serves as a reference for the studies using quantitative infrared imaging for evaluation and assessment of skin lesions as well as a reference for clinicians interpreting the images.

5.2 Methods

The details of the imaging equipment, setup and protocol used for imaging vascular lesions were described in Chapter 4, in sections 4.4 to 4.5. The data for pigmented skin lesions were acquired in 2009 in a patient study (protocol: NA00016040, Using High Resolution Functional Infrared Imaging to Detect Melanoma and Dysplastic Nevi) at the JHU Department of Dermatology, Pigmented Lesion Clinic at the Johns Hopkins Hospital Outpatient Center. The inclusion criteria consisted of clinical indication of biopsy as identified by the dermatologists [15]. For pigmented skin lesions, cooling was achieved by blowing cold air onto the skin using a vortex tube [15]. For vascular lesions, cooling was achieved by applying a cold gel pack onto the skin, as described in Chapter 4, in section 4.5. The thermal signatures of lesions were analyzed using the combined WL – IR image processing techniques described in Chapter 4, in section 4.6.

5.3 Results

The thermal characterization of skin lesions using the combined WL – IR imaging approach is illustrated by considering five sample cases in this study. The key clinical features of skin lesions are summarized in Table 5.1. For descriptive purposes, the cases are grouped into their respective categories.

Table 5.1 Summary of features of skin lesions included in this study

Case No	Lesion description	Category	Location	Depth of lesion involvement
I	Port wine stain	Vascular malformation	Left cheek	Dermis[b]
II	Venous malformation with superficial telangiectasias	Vascular malformation	Left side of the neck, middle upper back	Can be both superficial and deep[c]
III	Junctional dysplastic nevus with moderate atypia	Atypical pigmented lesion	Lower back	Epidermis – dermis junction[a]
IV	Compound dysplastic nevus with moderate atypia	Atypical pigmented lesion	Left thigh	Both epidermis and dermis[a]
V	Hand injury	Soft tissue injury	Left hand	Entire skin tissue[d]

a – [149]
b – [150]
c – [151]
d – Case V was a case of a bone fracture injury.

5.3.1 Vascular malformations

Vascular malformations are the anomalies of the vascular system that may involve either of the vascular segments – arteries, capillaries, veins and lymph vessels [152]. They are present at birth and do not undergo proliferation or involution. In this study, we considered two types of vascular anomalies – port wine stains that consist of dilated

capillaries in the dermis and venous malformations that consist of dilated venous vessels [152].

5.3.1.1 Port-Wine Stain

Case I - Figure 5.1(a) shows a 2 cm (major axis) x 2 cm (minor axis) large port-wine stain of the left cheek in an Asian female. Figure 5.1(c) displays the quantitative color differences between lesion and healthy skin measured from the WL image. The color difference values were calculated at every lesion pixel yielding a color–coded color difference map, where red represents larger color differences and blue smaller color differences. The superficial boundary of the lesion was identified on the basis of the dark red-purple discoloration (green boundary in Figure 5.1(a)) of the skin. The temperature distribution mapped onto the WL image and the result are visualized in Figure 5.1(b).The color-coded steady state IR images in Figure 5.1 (d) and the temperature elevation map in Figure 5.1(e) did not show any differences between lesion temperature and surrounding healthy skin temperature. This finding is consistent with the steady state temperature measurements reported in prior literature for port wine stains [153].

In order to study the transient thermal signature, we subjected the lesion and its surroundings to a mild cooling excitation and measured their thermal recoveries. We introduced a dimensionless temperature, $T^* = (T - T_{cooling})/(T_{steady\ state} - T_{cooling})$, where $T_{cooling}$ is the cooling temperature and $T_{steady\ state}$ is the steady state temperature of the pixel obtained from the steady state image. The dimensionless temperature allows us to scale the thermal recoveries of each pixel in the range of 0 to 1 and eliminate the impact of non-uniform cooling. Figure 5.1(f) shows the dimensionless temperature distribution for

the lesion and healthy skin as well as the temperature difference between them, as a function of time. The lesion recovered at almost the same rate as the surrounding healthy skin until t = 120s. The rate of lesion recovery slowed down from t = 120s to 380s, yielding a maximum dimensionless temperature difference, ΔT^*= -0.15°C between lesion and healthy skin. The slower recovery and a temperature decrease can be attributed to a lower value for the average blood perfusion rate of the lesion when compared to that of the healthy skin. We observed a very small temperature difference (-0.15°C) between port-wine stain and healthy skin during transient thermal recovery. This result, however,

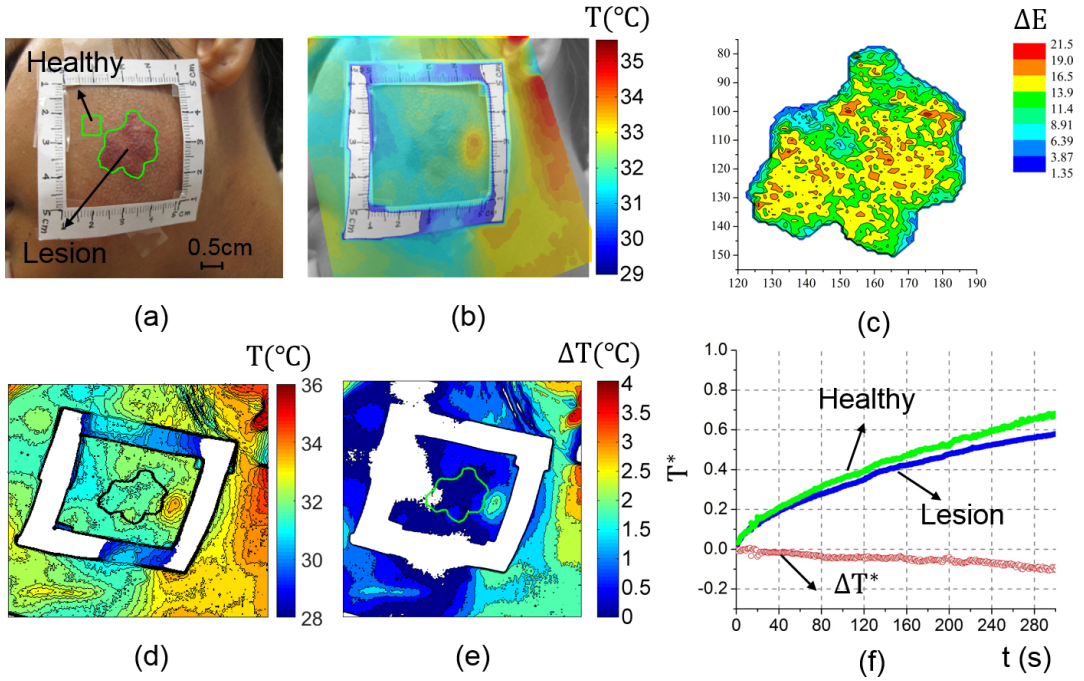

Figure 5.1 Case I - Port wine stain of the left cheek (before laser treatment), in an Asian female. (a) WL image, (b) color-coded temperature map mapped onto the WL image, (c) color difference (ΔE) distribution between lesion and healthy skin, (d) IR image showing temperature distribution at left cheek. The region within the black boundary belongs to the lesion. (e) Temperature elevation distribution at left cheek with respect to healthy skin temperature. (f) Dimensionless temperature distribution as a function of time for the port wine stain and healthy tissue.

demonstrates the enhanced skin temperature sensitivity to blood perfusion of the underlying tissue, which we also observed from the sensitivity analysis study (Chapter 1, in section 2.3.2).

For case I, we also compared skin temperatures before treatment with skin temperatures after laser treatment of the lesion. Both measurements were performed on the same day. It should be noted that a gel was applied to the subject's left cheek after the laser treatment. The top and bottom rows of images in Figure 5.2 display the WL images (Figures 5.2 (a) and (d)), the steady state IR images (Figures 5.2(b) and (e)) and the magnified IR images showing the temperature distribution at lesion location (Figures 5.2(c)

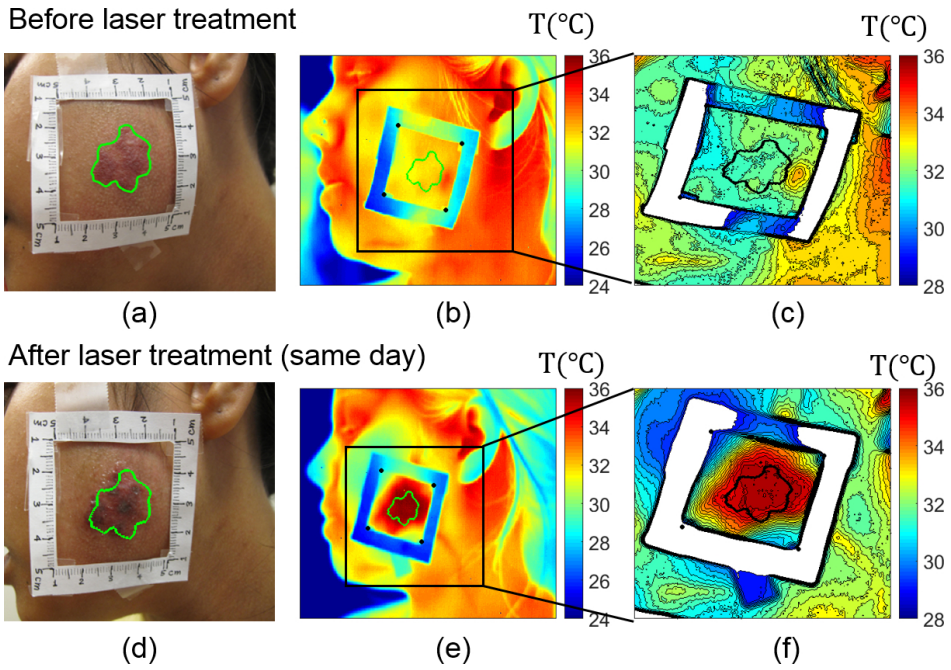

Figure 5.2 Before and after laser treatment comparison for case I. (a) WL image, (b) IR image. The black rectangle outlines the ROI and the green boundary outlines the lesion, (c) magnified IR image in the ROI showing temperature distribution at lesion location, captured before treatment. (c) WL image, (d) IR image and (e) magnified IR image in the ROI showing temperature at lesion location, captured immediately after treatment. Both set of images were captured on the same day

and (f)), before and after treatment, respectively. As described earlier, the lesion did not show any temperature difference with respect to the surrounding skin before treatment (Figures 5.2(c)). After laser treatment, the lesion showed a significant temperature increase (4 - 5°C) compared to surrounding healthy skin. The temperature increase can be attributed the heating and the body response to the heating of the tissue during laser treatment. Huang et al [154] demonstrated that an increase in the blood perfusion of the tissue may occur immediately after the laser treatment in order to remove excess heat from the tissue. This temporary dilation of the blood vessels might contribute to the increase in skin temperature in our case.

5.3.1.2 Venous malformation

Case II - Figure 5.3 illustrates a venous malformation having superficial telangiectasias (blood vessels located just below the surface of the skin) in a young Caucasian male subject. The lesion covered some portions of the left side of the neck (identified as lesion 1 in Figure 5.3(a)) as well as the middle upper back (identified as lesion 2 in Figure 5.3(b)). The superficial portions of both lesions were identified on the basis of the light red purple discoloration (green boundaries in Figures 5.3(a) and (b)) of the skin. The steady state IR images in Figures (c) and (d) display the temperature distributions at the superficial and subcutaneous portions of the venous malformation. With respect to the healthy skin temperature of 34°C (Figures (c)), the temperature increase was in the range of 1 – 2.5°C at the subcutaneous portion and 1.5 – 2°C at the superficial portions. The subcutaneous portions are marked by solid black arrows. The significant increases in skin

temperatures can be attributed to higher blood flow due to the combined effect of the superficial blood vessels and the dilated venous vessels of the lesion.

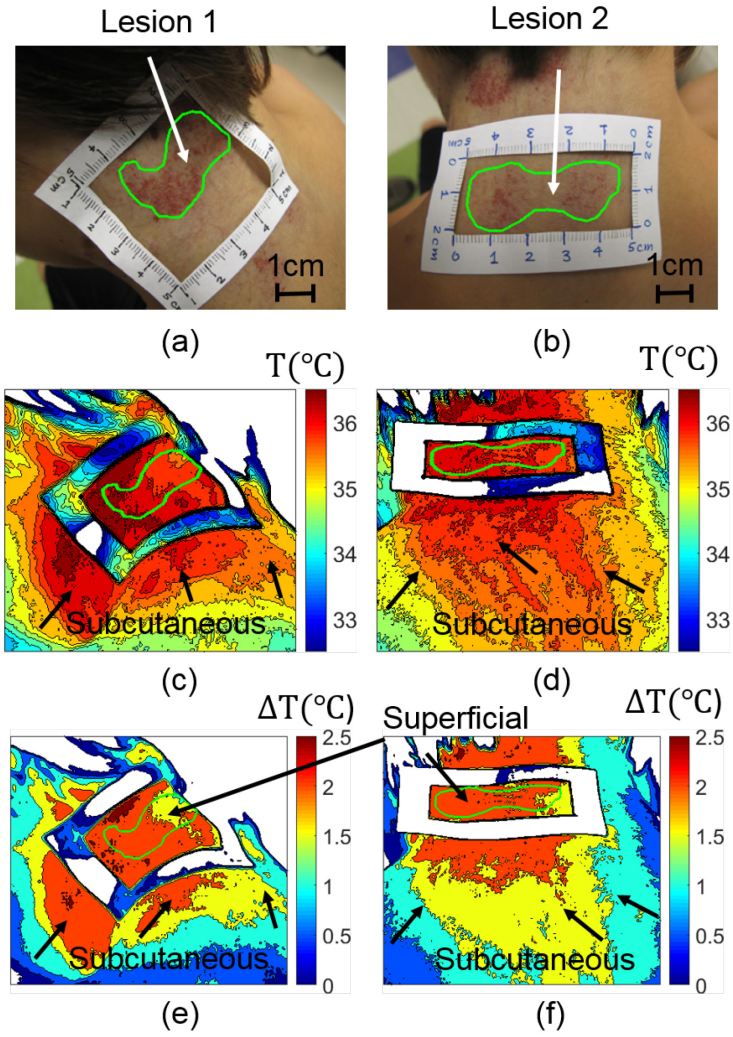

Figure 5.3 Case II - Venous malformation of the neck and the upper back with superficial telangiectasias. (a) WL image of the lesion on the neck (lesion 1) and (b) WL image of the lesion on the upper back (lesion 2). Color-coded steady state IR image of (c) lesion 1 and (d) lesion 2. The solid black lines mark the subcutaneous portion of the lesion. Temperature elevation distribution (1-2.5°C) at (e) lesion 1 and (f) lesion 2 locations.

5.3.2 Pigmented lesions

5.3.2.1 Junctional dysplastic nevus

Case III - Figure 5.4(a) shows a 7mm (major axis) x 5 mm (minor axis) large atypical lesion of the lower left back that was clinically identified as a junctional dysplastic nevus. The lesion possessed moderate atypia and was referred for biopsy. Figure 5.4(b) shows the dermoscope image of the lesion. It was used to measure the color differences between lesion and healthy skin and compute the color difference map at lesion location (Figure 3.4(c)). The non-uniformity of lesion color (Figure 5.4(b)) is well illustrated by the contours of the color difference map (Figure 5.3(c)). From the steady state temperature distributions displayed in Figures 5.4(c) and (d), we did not observe any differences in lesion temperature and surrounding healthy skin temperature, which indicate that the lesion is benign. For better visualization of lesion temperature, the color-coded thermal map is mapped onto the WL image, as shown in Figure 5.4(b). Figure 5.4(h) illustrates the transient temperature distributions at lesion location and its surroundings at t = 0s, 2s, 10s, 15s, 30s and 58s into thermal recovery. Again, we did not observe any temperature differences between lesion and healthy skin from the transient temperature contours. Both the steady state and transient thermal signatures suggest that the lesion is benign. The results of the biopsy also showed that the lesion is benign.

5.3.2.2 Compound dysplastic nevus

Case IV - Figure 5.5(a) shows a 5 mm (major axis) x 5 mm (minor axis) large atypical lesion of the left thigh that was clinically identified as a compound dysplastic nevus. The

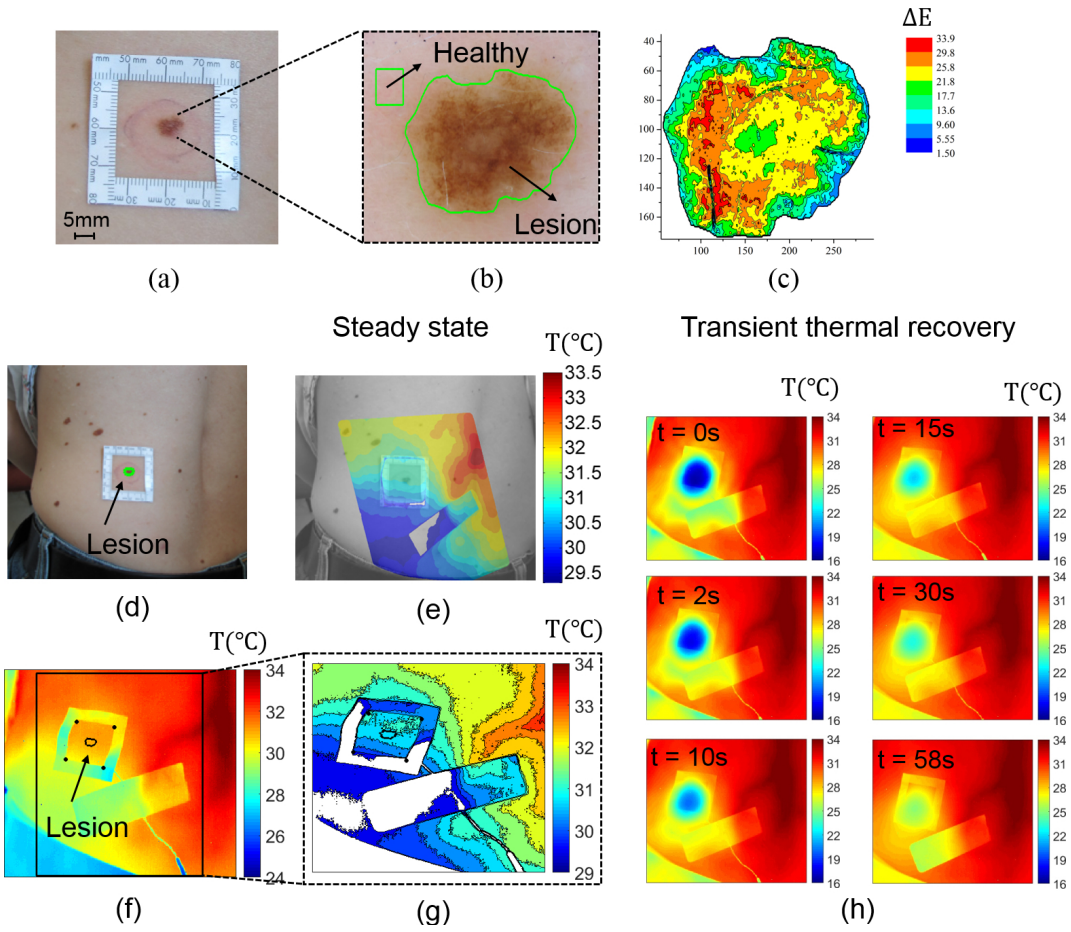

Figure 5.4 Case III - Junctional dysplastic nevus of the lower left back. (a) Magnified WL image, (b) dermoscopic image and (c) color difference (ΔE) distribution between lesion and healthy skin computed using dermoscopic image. (d) Original WL image, (e) color-coded temperature map mapped onto the WL image, (f) color-coded, steady state IR image. The black rectangle outlines the ROI. (g) Magnified IR image in the ROI showing temperature distribution at lesion location. (h) Color-coded IR images after 1 min of cooling. Temperature distribution at ROI is shown for t = 0s, 2s, 10s, 15s, 30s and 58s into thermal recovery.

lesion possessed moderate atypia and was referred for biopsy. A dermoscope image of the lesion is shown in the top right corner of Figure 5.5(a). The IR image in Figure 5.5(b) displays the temperature distribution at lesion location and its surroundings. The temperature distribution in the top right corner of the image is dominated by a blood vessel that increases the skin temperature locally. A better visualization of the temperature

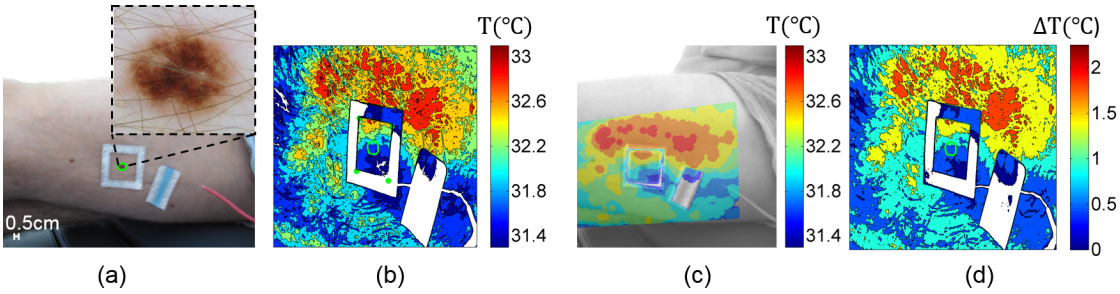

Figure 5.5 Case IV - Compound dysplastic nevus of the left thigh. (a) WL image. The top left image shows the dermoscope image. (b) Color-coded IR image showing temperature distribution at lesion location and its surroundings. The green boundary outlines the lesion. (c) Color-coded temperature map mapped onto the WL image and (d) temperature elevation distribution at lesion location and its surroundings, with respect to healthy skin temperature.

distribution is provided by the WL-IR image overlay in Figure 5.5(c). The temperature elevation distribution was computed with respect to a healthy skin temperature of 31.4°C (the region that is not influenced by the blood vessel), as shown in Figure 5.5(d). We observed a temperature rise of 0.2 - 0.5°C at lesion location (Figure 5.5(d)). Since, there is a large region of high temperature surrounding the lesion location, we cannot conclude from the steady state analysis whether the 0.2-0.5°C rise is due to lesion malignancy (high blood flow and metabolic activity) or is an effect of the nearby blood vessel. Transient thermal recovery of the lesion and surrounding healthy skin can provide more information about the lesion. The results of the biopsy showed that the lesion is benign.

5.3.3 Soft tissue injury and bone fracture

Case VI - Figure 5.6 illustrates qualitative follow-up of a soft tissue injury and bone fracture of the middle finger of the left hand, in a female subject. A bone fracture repair surgery was performed using metal pins that held the bone of the middle finger in place.

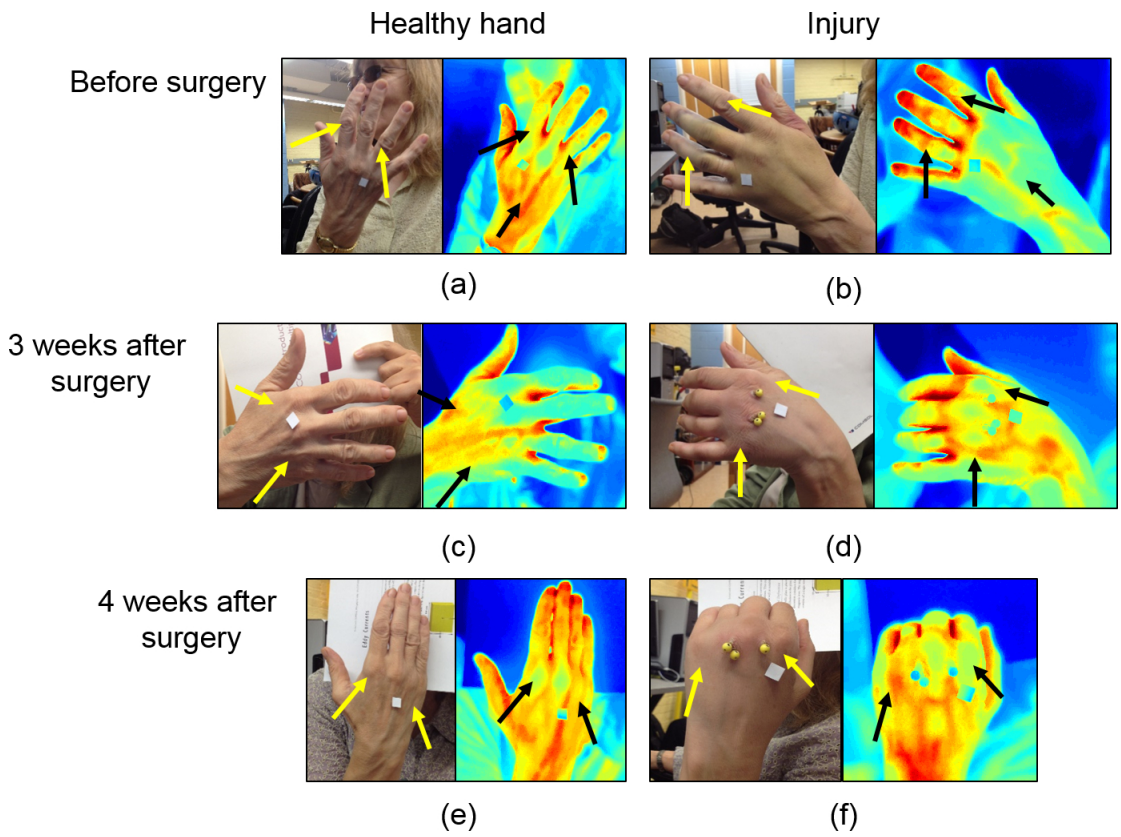

Figure 5.6 Qualitative follow-up of a soft tissue injury of the hand. Combined WL – IR images of (a) healthy and (b) injured hand captured before surgery; (c) healthy and (d) injured hand captured 3 weeks after surgery; and (e) healthy and (f) injured hand captured 4 weeks after surgery.

The WL and greyscale IR images of the right (healthy) and left (injured) hands were first acquired before the surgery (Figure 5.6 (a) and (b)) and then 3 weeks (Figures 5.6 (c) and (d)) and 4 weeks (Figures 5.6(e) and (f)) after the surgery. The greyscale IR images are color coded, where red indicates high temperature and blue low temperature. The black arrows in the IR images point to the symmetrically opposite locations and allow qualitative comparison of temperatures between two hands. The yellow arrows point to the corresponding locations in the WL images and allow qualitative comparison of swelling and skin color.

Before surgery, the WL image of the left hand (Figure 5.6 (b)) showed swelling and a relatively pale skin color in contrast to the healthy skin color (shown in Figure 5.6 (a)). The corresponding IR image (Figure 5.6 (b)) indicated inflammation in fingers (high temperature) and an impaired blood flow (low temperature) in back of the palm, contrasted to the temperature distribution of the healthy hand (Figure 5.6 (a)). The WL image showed improvement in skin color, three weeks after the surgery (Figure 5.6(d)). The corresponding IR image indicated inflammation in the entire hand (high temperature regions), when compared to healthy hand temperatures in Figure 5.6 (c). By the fourth week after surgery, both WL and IR images of the left hand were similar to those of the right hand, indicating improvements in skin color and temperature.

5.4 Conclusions

We analyzed thermal signatures of skin lesions of varying physiologies, sizes and depths in this study. The transient analysis for the port wine stain lesion demonstrate that more information about lesion can be obtained by using dynamic thermal imaging. We believe that a collection of thermal signatures of skin lesions in this study would facilitate the analysis and interpretation of other vascular anomalies, pigmented lesions and soft tissue injuries.

Chapter 6 Conclusion

This dissertation addressed a subset of fundamental and practical questions relevant for quantitative thermographic characterization of thermal signatures of skin lesions as well as subcutaneous lesions. The overall aim was to explore the feasibility of steady state and transient IR imaging for early detection and staging of deep tissue injuries and quantitative assessment of skin lesions (including pigmented lesions and vascular tumors), using computational thermal modeling combined with quantitative WL – IR imaging and image processing tools. Our modeling efforts and the interpretation of thermal signatures benefit from the fundamental understanding of the thermal behavior of skin, gained by conducting a comprehensive sensitivity analysis of healthy skin temperature variations with respect to variations in tissue thermophysical properties and layer thicknesses. Our imaging and image analysis framework uses a combined WL-IR imaging approach that allows quantitative, objective assessment of growth and regression needed for long term monitoring of lesion history for treatment evaluation.

In Chapter 2, we performed a sensitivity analysis of healthy skin temperature variations with respect to small changes of 36 tissue parameters (30 thermophysical properties and 6 layer thicknesses) in order to gain insights into the complex thermal behavior of the skin tissue. The sensitivity analysis is essential for a better understanding of the influence of individual variations and uncertainties in property values describing a biophysical system on the measured skin temperature, with implications for clinical diagnostic applications. The insights from the sensitivity analysis provide guidelines for the design of the clinical measurement system and interpretation of measurement data.

Both steady state skin temperatures and transient thermal recovery of the skin to a cooling excitation were included in the analysis, as they are important for medical diagnostic applications of static and dynamic IR imaging (that relies on cooling). The partial derivative based normalized sensitivities allow us to quantify and compare the independent effects of input parameters on skin temperatures.

Our analysis demonstrated that large variations in key tissue parameters (thermal conductivity of the fat layer, blood perfusion rates of dermis layers and the fat layer thickness) had a negligible influence on the computed skin temperatures. Additionally, we found that the metabolic heat generation rate is among the least influential parameters affecting the steady state skin temperature and the transient thermal recovery of skin from a cooling excitation. Larger values of the transient sensitivity coefficients compared to their steady state values demonstrate that the thermal recovery of the skin from a cooling excitation is a better indicator of the thermal state of the tissue underneath and provides more information than the steady state skin temperature. This means that in diagnostic applications of IR imaging, thermal contrasts between lesion and healthy skin can be enhanced by subjecting the skin to cooling. This leads to a conclusion that dynamic IR imaging should be used in clinical applications when the lesion is small or deep, and no significant temperature difference is detected in a static analysis.

We also analyzed the contributions of the thermal and physiological characteristics of each layer to the transient thermal recovery of the skin, in order to gain insights for improving the dynamic IR measurement system design. Fat and muscle layers exhibited late onset of thermal recovery (largest temperature difference reached after 2 and 5 minutes, respectively, following the removal of the cooling load) and subsequently led to

late maxima in the sensitivity curves in comparison to the epidermis and dermis layers. This implies that a deep tissue lesion (situated in the fat or muscle layers) would present the strongest measurement signal late into the thermal recovery (t = 2 to 10 mins, as indicated in our analysis). A near surface lesion (involving the epidermis or dermis layers) would present the strongest measurement signal early (t = 0 to 2 mins). Therefore, the optimum duration for a thermographic scan, that gives the best measurement signal and sensitivity, would vary with the depth of the lesion. Additionally, the differences in the thermal behavior of different skin layers during cooling and thermal recovery can be employed for improving skin cooling techniques for dynamic IR imaging applications. The fundamental understanding of the thermal system of the skin gained from this study is invaluable for the design of dynamic IR measurement systems and lays the foundations for interpreting the thermal signatures of lesions in Chapters 3 -5.

In Chapter 3, we developed a computational thermal model of a heel deep tissue injury (DTI) to demonstrate that incipient DTIs can be detected and characterized quantitatively and non-invasively in a clinical setting using IR imaging. First, to explain the inconsistencies reported in prior literature on pressure related injuries, we accounted for ischemia and ischemia reperfusion processes (etiologies for DTI) in our thermal model by incorporating ischemia and inflammation as thermal variables. Next, we proposed new and more accurate clinical staging criteria for DTIs, which classifies them into reversible and irreversible DTIs, and characterized thermal signatures of each stage using our thermal model. To assess the feasibility of early thermographic detection (before the lesion becomes visible on the skin surface), we considered an incipient 1.5 cm by 0.5 cm lesion. Our steady state computational models demonstrate that the measurement signals

associated with DTI ischemia and inflammation for lesion depths of 8mm, 6 mm and 3.8 mm can be detected using static IR imaging, yielding a static thermographic detection capability for reversible DTIs. We, however, observed that steady state IR imaging alone cannot distinguish between DTI inflammation and multilayer DTI (inner ischemic core surrounded by inflammation mantel). To overcome this limitation, we included a transient analysis in our model to test the dynamic infrared imaging capability. We observed that the measurement signal in a clinical setting can be enhanced by subjecting the skin to cooling and comparing the transient thermal recovery of tissue affected by the DTI with healthy tissue. Furthermore, dynamic IR imaging can detect both ischemia and inflammation in the case of a multilayer DTIs, yielding a thermographic detection capability for both reversible and irreversible DTIs.

We also demonstrated the feasibility of IR imaging coupled with inverse reconstruction methods to non-invasively measure key DTI properties such as the lesion depth, size and blood perfusion rate. The thermal staging criteria proposed in this dissertation offer an objective, convenient and quantitative method to document the severity and property of the injury, yielding a thermographic diagnosis and assessment capability.

We applied combined IR-WL image processing approaches for quantitative assessment of skin lesions in Chapters 4 and 5. We developed color analysis tools, which allowed us to measure the color differences between lesion and healthy skin and quantitatively visualize their colors. However, considering that the WL images may present shadows that add noise to the measurement, it is desirable to have a standardized uniform lighting source in the examination room.

The combined IR-WL imaging and image processing tools developed in the Heat Transfer Lab of the Johns Hopkins University were applied to analyze infantile hemangioma (IH) lesions first. A comparison of the IH area visible in the WL image (detected by a clinician by visual inspection) with the total affected area measured in the IR image leads to the conclusion that the IR image provides a more complete picture of the IH lesion, by visualizing both its superficial and subcutaneous components. The quantification of the extent of subcutaneous involvement is especially useful for the problematic IH lesions (that interfere with vital functions), as the combined IR – WL imaging can be performed with relative simplicity without requiring sedation or anesthesia in young subjects.

As demonstrated in Chapter 3, the measured temperature data can be coupled with inverse reconstruction methods to obtain the depth estimates for the subcutaneous portion, allowing for volume measurements, which is the subject of future research efforts. An accurate assessment of the IH volume, early in the proliferative stage, can prevent complications and allows better tailoring of treatment strategies. Using dimensionless temperature maps to compare IR images of a proliferating lesion captured during different clinical visits (before and after starting treatment, 3 months weeks apart), we demonstrated that IR imaging can be used to assess increase/decrease in lesion size and activity over time. The follow-up imaging and quantitative assessment of a tumor under treatment using the combined IR – WL imaging could be improved by standardizing the imaging conditions such the light source and illumination conditions for WL imaging and controlling the ambient temperature, camera focal length, imaging time, the positioning of the patient with respect to the IR camera.

The measured temperature data for skin lesions in Chapters 4 and 5 demonstrate that the lesion type, geometry and vascularity affect the temperature elevation distributions. The characteristic thermal signatures of skin lesions of different types (IHs, port-wine stain ,

venous malformation, benign and malignant atypical lesions), shapes (dome – shaped, flat-raised, flat) and sizes and locations (face, back, legs), depths from the skin surface have been summarized in these chapters. The broad range of lesions analyzed in this dissertation demonstrates the flexibility and feasibility of IR imaging as an effective clinical assessment tool. We also identified potential limitations of IR imaging as a quantitative assessment tool. The temperature distributions for IHs involving the eyes were difficult to interpret. The eyes themselves emit more heat, making the process of differentiating the hemangioma's vasculature from the eye's vasculature challenging. Furthermore, we noticed that some IH lesions of the face exhibited warm regions, which may or may not belong to the subcutaneous component of the lesion. Additional imaging by ultrasound or MRI would be needed to accurately interpret the causes of elevated temperatures in such cases.

In summary, the improved understanding of the biophysical system of the skin gained from this study will be very useful for the design of IR measurement systems suitable for lesion detection and quantification. The collection of thermal signatures provides a knowledge database that will facilitate the analysis and interpretation of clinical thermographic images of other skin and subcutaneous lesions and help expand the clinical applications of quantitative IR imaging.

Appendix

Levenberg-Marquardt method for measuring properties of DTI

We describe the Levenberg-Marquardt (LM) method [104] based inverse bioheat transfer approach [103] to simultaneously estimate two DTI parameters from the measured steady state skin surface temperature data. The relevant DTI properties are the depth, h, size (i.e. length of the major axis), d_1 and blood perfusion rate, ω. To demonstrate the workflow, we explain the steps to simultaneously estimate DTI depth, h and the size, d_1, from a given skin surface temperature profile, Y. Let $P = \begin{bmatrix} P_1 \\ P_2 \end{bmatrix}$ be the vector of the unknown parameters, i.e. $P_1 = h$ and $P_2 = d_1$.

Step 1: Guess values for the unknown parameter vector P and solve for the corresponding skin temperature profile, $T(P)$.

Step 2: Compute the objective function, S, which is the sum of squared error between the measured temperature profile (Y) and the computed temperature profile, $T(P)$.

$$S(P) = [Y - T(P)]^T [Y - T(P)] \quad (1)$$

Step 3: Exit, if $S(P) < 10^{-5}$. Otherwise, proceed to Step 4.

Step 4: Calculate the sensitivity matrix, $J(P)$, using the temperature information from i number of points on the skin surface

$$J(P) = \frac{\partial T^T(P)}{\partial P} = \begin{bmatrix} \frac{\partial T_1}{\partial P_1} & \frac{\partial T_1}{\partial P_2} \\ \vdots & \vdots \\ \frac{\partial T_i}{\partial P_1} & \frac{\partial T_i}{\partial P_2} \end{bmatrix} \quad (2)$$

The partial derivatives in Equation 2 may be approximated using finite difference approximation.

Step 5: Solve for the next best set of parameters using the LM algorithm [104]. If μ is the damping parameter, the parameter values during the $m+1^{th}$ iteration i.e. P^{m+1} are obtained using

$$P^{m+1} = P^m + [(J^m)^T J^m + \mu^m \Omega^m]^{-1}(J^m)[Y - T(P^m)] \quad (3)$$

In Equation 3, $\Omega^m = diag[(J^m)^T J^m]$ is the diagonal matrix computed at the m^{th} iteration.

Step 6: Substitute $\mu = 10\mu$ in Equation 3, if the parameter values computed at Step 5 are not realistic, i.e. the corresponding temperature data $T(P^{m+1}) < 0$. Repeat Step 5 until realistic parameter values are obtained. Otherwise, proceed to Step 7.

Step 7: If $S(P^{m+1}) < S(P^m)$, make $\mu = \sqrt{10}\mu$ and go to Step 3. If $S(P^{m+1}) > S(P^m)$, make $\mu = 10\mu$ and go to Step 5.

Bibliography

[1] Ring, E. F., 1998, "Progress in the Measurement of Human Body Temperature," IEEE Engineering in Medicine and Biology Magazine : The Quarterly Magazine of the Engineering in Medicine & Biology Society, **17**(4) pp. 19-24.

[2] Anbar, M., 1998, "Clinical Thermal Imaging Today," IEEE Engineering in Medicine and Biology Magazine : The Quarterly Magazine of the Engineering in Medicine & Biology Society, **17**(4) pp. 25-33.

[3] Deng, Z. S., and Liu, J., 2004, "Mathematical Modeling of Temperature Mapping Over Skin Surface and its Implementation in Thermal Disease Diagnostics," Computers in Biology and Medicine, **34**(6) pp. 495-521.

[4] Jones, B. F., 1998, "A Reappraisal of the use of Infrared Thermal Image Analysis in Medicine," IEEE Transactions on Medical Imaging, **17**(6) pp. 1019-1027.

[5] Pirtini Çetingül, M., and Herman, C., 2011, "Quantification of the Thermal Signature of a Melanoma Lesion," International Journal of Thermal Sciences, **50**(4) pp. 421-431.

[6] Lahiri, B. B., Bagavathiappan, S., Jayakumar, T., 2012, "Medical Applications of Infrared Thermography: A Review," Infrared Physics & Technology, **55**(4) pp. 221-235.

[7] Xu, F., Lu, T. J., Seffen, K. A., 2009, "Mathematical Modeling of Skin Bioheat Transfer," Applied Mechanics Reviews, **62**(5) pp. 050801-050801.

[8] Wilson, S. B., and Spence, V. A., 1988, "A Tissue Heat Transfer Model for Relating Dynamic Skin Temperature Changes to Physiological Parameters," Physics in Medicine and Biology, **33**(8) pp. 895-912.

[9] Mcintosh, R. L., and Anderson, V., 2010, "A Comprehensive Tissue Properties Database Provided for the Thermal Assessment of a Human at Rest," Biophysical Reviews and Letters, **05**(03) pp. 129-151.

[10] Torvi, D. A., and Dale, J. D., 1994, "A Finite Element Model of Skin Subjected to a Flash Fire," Journal of Biomechanical Engineering, **116**(3) pp. 250-255.

[11] Cohen, M. L., 1977, "Measurement of the Thermal Properties of Human Skin. a Review," Journal of Investigative Dermatology, **69**(3) pp. 333-338.

[12] Valvano, J., 1995, Springer US, pp. 445-488.

[13] Çetingül, M. P., Herman, C., and Alani, R. M., 2009, "Skin imaging with infrared thermography and confocal microscopy," ASME 2009 Heat Transfer Summer Conference collocated with the InterPACK09 and 3rd Energy Sustainability Conferences, Anonymous American Society of Mechanical Engineers, pp. 731-739.

[14] Jones, B. F., and Plassmann, P., 2002, "Digital Infrared Thermal Imaging of Human Skin," IEEE Engineering in Medicine and Biology Magazine : The Quarterly Magazine of the Engineering in Medicine & Biology Society, **21**(6) pp. 41-48.

[15] Pirtini Çetingül, M., and Herman, C., 2011, "The Assessment of Melanoma Risk using the Dynamic Infrared Imaging Technique," Journal of Thermal Science and Engineering Applications, **3**(3) pp. 031006-031006.

[16] Bagavathiappan, S., Philip, J., Jayakumar, T., 2010, "Correlation between Plantar Foot Temperature and Diabetic Neuropathy: A Case Study by using an Infrared Thermal Imaging Technique," Journal of Diabetes Science and Technology, **4**(6) pp. 1386-1392.

[17] Benbow, S. J., Chan, A. W., Bowsher, D. R., 1994, "The Prediction of Diabetic Neuropathic Plantar Foot Ulceration by Liquid-Crystal Contact Thermography," Diabetes Care, **17**(8) pp. 835-839.

[18] Bagavathiappan, S., Saravanan, T., Philip, J., 2009, "Infrared Thermal Imaging for Detection of Peripheral Vascular Disorders," Journal of Medical Physics / Association of Medical Physicists of India, **34**(1) pp. 43-47.

[19] Sun, P., Lin, H., Jao, S. E., 2006, "Relationship of Skin Temperature to Sympathetic Dysfunction in Diabetic at-Risk Feet," Diabetes Research and Clinical Practice, **73**(1) pp. 41-46.

[20] Saxena, A. K., and Willital, G. H., 2008, "Infrared Thermography: Experience from a Decade of Pediatric Imaging," European Journal of Pediatrics, **167**(7) pp. 757-764.

[21] Mercer, J. B., Nielsen, S. P., and Hoffmann, G., 2008, "Improvement of Wound Healing by Water-Filtered Infrared-A (wIRA) in Patients with Chronic Venous Stasis

Ulcers of the Lower Legs Including Evaluation using Infrared Thermography," German Medical Science : GMS E-Journal, **6**pp. Doc11.

[22] Bouzida, N., Bendada, A., and Maldague, X. P., 2009, "Visualization of Body Thermoregulation by Infrared Imaging," Journal of Thermal Biology, **34**(3) pp. 120-126.

[23] Deng, Z. S., and Liu, J., 2005, "Enhancement of Thermal Diagnostics on Tumors Underneath the Skin by Induced Evaporation," Conference Proceedings : ...Annual International Conference of the IEEE Engineering in Medicine and Biology Society.IEEE Engineering in Medicine and Biology Society.Annual Conference, **7**pp. 7525-7528.

[24] Flores-Sahagun, J. H., Vargas, J. V. C., and Mulinari-Brenner, F. A., 2011, "Analysis and Diagnosis of Basal Cell Carcinoma (BCC) Via Infrared Imaging," Infrared Physics & Technology, **54**(5) pp. 367-378.

[25] Borchartt, T. B., Conci, A., Lima, R. C. F., 2013, "Breast Thermography from an Image Processing Viewpoint: A Survey," Signal Processing, **93**(10) pp. 2785-2803.

[26] Mohammed, J. A., Balma-Mena, A., Chakkittakandiyil, A., 2014, "Infrared Thermography to Assess Proliferation and Involution of Infantile Hemangiomas: A Prospective Cohort Study," JAMA Dermatology, **150**(9) pp. 964-969.

[27] Renkielska, A., Nowakowski, A., Kaczmarek, M., 2006, "Burn Depths Evaluation Based on Active Dynamic IR Thermal Imaging--a Preliminary Study," Burns : Journal of the International Society for Burn Injuries, **32**(7) pp. 867-875.

[28] Park, J., Hyun, J. K., and Seo, J., 2007, "The Effectiveness of Digital Infrared Thermographic Imaging in Patients with Shoulder Impingement Syndrome," Journal of Shoulder and Elbow Surgery, **16**(5) pp. 548-554.

[29] de Weerd, L., Mercer, J. B., and Weum, S., 2011, "Dynamic Infrared Thermography," Clinics in Plastic Surgery, **38**(2) pp. 277-292.

[30] NPUAP., 2016, "*National-Pressure-Ulcer-Advisory-Panel-Npuap-Announces-a-Change-in-Terminology-from-Pressure-Ulcer-to-Pressure-Injury-and-Updates-the-Stages-of-Pressure-Injury*," **2016**(07,08) .

[31] Kottner, J., Dassen, T., and Lahmann, N., 2010, "Prevalence of Deep Tissue Injuries in Hospitals and Nursing Homes: Two Cross-Sectional Studies," International Journal of Nursing Studies, **47**(6) pp. 665-670.

[32] VanGilder, C., MacFarlane, G. D., Harrison, P., 2010, "The Demographics of Suspected Deep Tissue Injury in the United States: An Analysis of the International Pressure Ulcer Prevalence Survey 2006-2009," Advances in Skin & Wound Care, **23**(6) pp. 254-261.

[33] Gefen, A., Farid, K. J., and Shaywitz, I., 2013, "A Review of Deep Tissue Injury Development, Detection, and Prevention: Shear Savvy," Ostomy/Wound Management, **59**(2) pp. 26-35.

[34] Bhargava, A., Chanmugam, A., and Herman, C., 2014, "Heat Transfer Model for Deep Tissue Injury: A Step Towards an Early Thermographic Diagnostic Capability," Diagnostic Pathology, **9**pp. 36-1596-9-36.

[35] Zheng, J. W., Zhang, L., Zhou, Q., 2013, "A Practical Guide to Treatment of Infantile Hemangiomas of the Head and Neck," International Journal of Clinical and Experimental Medicine, **6**(10) pp. 851-860.

[36] Katona, G., Csakanyi, Z., Gacs, E., 2012, "Propranolol for Infantile Haemangioma: Striking Effect in the First Weeks," International Journal of Pediatric Otorhinolaryngology, **76**(12) pp. 1746-1750.

[37] Kalicki, B., Jung, A., Ring, F., 2012, "Infrared Thermography Assessment of Infantile Hemangjoma Treatment by Propanolol," Thermology International, **22**(3) pp. 102-103.

[38] Garcia-Romero, M. T., Chakkittakandiyil, A., and Pope, E., 2014, "The Role of Infrared Thermography in Evaluation of Proliferative Infantile Hemangiomas. Results of a Pilot Study," International Journal of Dermatology, **53**(3) pp. e216-7.

[39] Chang, L. C., Haggstrom, A. N., Drolet, B. A., 2008, "Growth Characteristics of Infantile Hemangiomas: Implications for Management," Pediatrics, **122**(2) pp. 360-367.

[40] Anbar, M., 2002, "Assessment of Physiologic and Pathologic Radiative Heat Dissipation using Dynamic Infrared Imaging," Annals of the New York Academy of Sciences, **972**pp. 111-118.

[41] Cetingul, M. P., and Herman, C., 2010, "A Heat Transfer Model of Skin Tissue for the Detection of Lesions: Sensitivity Analysis," Physics in Medicine and Biology, **55**(19) pp. 5933-5951.

[42] Huang, H., and Liauh, C., 2012, "Review: Therapeutical Applications of Heat in Cancer Therapy," Journal of Medical and Biological Engineering, **32**(1) pp. 1-11.

[43] He, X., and Bischof, J. C., 2003, "Quantification of Temperature and Injury Response in Thermal Therapy and Cryosurgery," Critical Reviews in Biomedical Engineering, **31**(5-6) pp. 355-422.

[44] Jaunich, M., Raje, S., Kim, K., 2008, "Bio-Heat Transfer Analysis during Short Pulse Laser Irradiation of Tissues," International Journal of Heat and Mass Transfer, **51**(23) pp. 5511-5521.

[45] Rabin, Y., 2003, "A General Model for the Propagation of Uncertainty in Measurements into Heat Transfer Simulations and its Application to Cryosurgery," Cryobiology, **46**(2) pp. 109-120.

[46] Jamil, M., and Ng, E. Y. K., 2013, "Ranking of Parameters in Bioheat Transfer using Taguchi Analysis," International Journal of Thermal Sciences, **63**(0) pp. 15-21.

[47] Johnson, N. N., Abraham, J. P., Helgeson, Z. I., 2011, "An Archive of Skin-Layer Thicknesses and Properties and Calculations of Scald Burns with Comparisons to Experimental Observations," Journal of Thermal Science and Engineering Applications, **3**(1) pp. 011003-011003.

[48] Frank, P., 1978, "Introduction to system sensitivity theory," Academic press, .

[49] Saltelli, A., Ratto, M., Tarantola, S., 2005, "Sensitivity Analysis for Chemical Models," Chemical Reviews, **105**(7) pp. 2811-2828.

[50] Vuilleumier, L., Harley, R. A., and Brown, N. J., 1997, "First- and Second-Order Sensitivity Analysis of a Photochemically Reactive System (a Green's Function Approach)," Environmental Science & Technology, **31**(4) pp. 1206-1217.

[51] Hamby, D. M., 1994, "A Review of Techniques for Parameter Sensitivity Analysis of Environmental Models," Environmental Monitoring and Assessment, **32**(2) pp. 135-154.

[52] Ingalls, B., 2008, "Sensitivity Analysis: From Model Parameters to System Behaviour," Essays in Biochemistry, **45**pp. 177-193.

[53] Pannell, D. J., 1997, "Sensitivity Analysis of Normative Economic Models: Theoretical Framework and Practical Strategies," Agricultural Economics, **16**(2) pp. 139-152.

[54] Liu, J., 2001, "Uncertainty Analysis for Temperature Prediction of Biological Bodies Subject to Randomly Spatial Heating," Journal of Biomechanics, **34**(12) pp. 1637-1642.

[55] Jasiński, M., 2009, "Sensitivity Analysis of Transient Bioheat Transfer with Perfusion Rate Dependent on Tissue Injury," Computer Assisted Mechanics and Engineering Sciences, **16, No. 3/4**pp. 267-277.

[56] Davies, C. R., Saidel, G. M., and Harasaki, H., 1997, "Sensitivity Analysis of One-Dimensional Heat Transfer in Tissue with Temperature-Dependent Perfusion," Journal of Biomechanical Engineering, **119**(1) pp. 77-80.

[57] Autrique, L., and Lormel, C., 2008, "Numerical Design of Experiment for Sensitivity Analysis--Application to Skin Burn Injury Prediction," IEEE Transactions on Bio-Medical Engineering, **55**(4) pp. 1279-1290.

[58] Ng, E. Y., Tan, H. M., and Ooi, E. H., 2010, "Prediction and Parametric Analysis of Thermal Profiles within Heated Human Skin using the Boundary Element Method," Philosophical Transactions.Series A, Mathematical, Physical, and Engineering Sciences, **368**(1912) pp. 655-678.

[59] Jasiński, M., 2003, "Sensitivity Analysis of Burn Integrals with Respect to Thickness of Epidermis," Scientific Research of the Institute of Mathematics and Computer Science, **2**(1) pp. 45-54.

[60] Sudharsan, N. M., and Ng, E. Y., 2000, "Parametric Optimization for Tumour Identification: Bioheat Equation using ANOVA and the Taguchi Method," Proceedings of the Institution of Mechanical Engineers.Part H, Journal of Engineering in Medicine, **214**(5) pp. 505-512.

[61] Yamazaki, F., 2015, "The Cutaneous Vasoconstrictor Response in Lower Extremities during Whole-Body and Local Skin Cooling in Young Women with a Cold Constitution," The Journal of Physiological Sciences, **65**(5) pp. 397-405.

[62] Pennes, H. H., 1948, "Analysis of Tissue and Arterial Blood Temperatures in the Resting Human Forearm." Journal of Applied Physiology, **85**(1) pp. 5-34.

[63] Bhowmik, A., Singh, R., Repaka, R., 2013, "Conventional and Newly Developed Bioheat Transport Models in Vascularized Tissues: A Review," Journal of Thermal Biology, **38**(3) pp. 107-125.

[64] Cheng, T., and Herman, C., 2014, "Analysis of Skin Cooling for Quantitative Dynamic Infrared Imaging of Near-Surface Lesions," International Journal of Thermal Sciences, **86**(0) pp. 175-188.

[65] Hamby, D. M., 1995, "A Comparison of Sensitivity Analysis Techniques," Health Physics, **68**(2) pp. 195-204.

[66] Saltelli, A., Tarantola, S., and Campolongo, F., 2000, "Sensitivity Analysis as an Ingredient of Modeling," Statistical Science, **15**(4) pp. 377-395.

[67] Di Carlo, A., 1995, "Thermography and the Possibilities for its Applications in Clinical and Experimental Dermatology," Clinics in Dermatology, **13**(4) pp. 329-336.

[68] Buzug, T. M., Schumann, S., Pfaffmann, L., 2006, "Functional Infrared Imaging for Skin-Cancer Screening," Conference Proceedings : ...Annual International Conference of the IEEE Engineering in Medicine and Biology Society.IEEE Engineering in Medicine and Biology Society.Annual Conference, **1**pp. 2766-2769.

[69] Smith, D.,E, Szidarovszky, F., Karnavas, J., W., 2008, "Sensitivity Analysis, a Powerful System Validation Technique," The Open Cybernetics and Systems Journal, **2**pp. 39 - 56.

[70] Stekelenburg, A., Gawlitta, D., Bader, D. L., 2008, "Deep Tissue Injury: How Deep is our Understanding?" Archives of Physical Medicine and Rehabilitation, **89**(7) pp. 1410-1413.

[71] Ahn, H., Cowan, L., Garvan, C., 2016, "Risk Factors for Pressure Ulcers Including Suspected Deep Tissue Injury in Nursing Home Facility Residents: Analysis of National Minimum Data Set 3.0," Advances in Skin & Wound Care, **29**(4) pp. 178-190.

[72] White-Chu, E. F., Flock, P., Struck, B., 2011, "Pressure Ulcers in Long-Term Care," Clinics in Geriatric Medicine, **27**(2) pp. 241-258.

[73] Black, J., Baharestani, M., Cuddigan, J., 2007, "National Pressure Ulcer Advisory Panel's Updated Pressure Ulcer Staging System," Urologic Nursing, **27**(2) pp. 144-50, 156.

[74] Mak, A. F., Zhang, M., and Tam, E. W., 2010, "Biomechanics of Pressure Ulcer in Body Tissues Interacting with External Forces during Locomotion," Annual Review of Biomedical Engineering, **12**pp. 29-53.

[75] Black, J. M., Brindle, C. T., and Honaker, J. S., 2015, "Differential Diagnosis of Suspected Deep Tissue Injury," International Wound Journal, .

[76] Deprez, J. F., Brusseau, E., Fromageau, J., 2011, "On the Potential of Ultrasound Elastography for Pressure Ulcer Early Detection," Medical Physics, **38**(4) pp. 1943-1950.

[77] Aoi, N., Yoshimura, K., Kadono, T., 2009, "Ultrasound Assessment of Deep Tissue Injury in Pressure Ulcers: Possible Prediction of Pressure Ulcer Progression," Plastic and Reconstructive Surgery, **124**(2) pp. 540-550.

[78] Quintavalle, P. R., Lyder, C. H., Mertz, P. J., 2006, "Use of High-Resolution, High-Frequency Diagnostic Ultrasound to Investigate the Pathogenesis of Pressure Ulcer Development," Advances in Skin & Wound Care, **19**(9) pp. 498-505.

[79] Hamaluik, K., Moussa, W., and Ferguson-Pell, M., 2014, "Numerical Characterization of Quasi-Static Ultrasound Elastography for the Detection of Deep Tissue Injuries," IEEE Transactions on Medical Imaging, **33**(7) pp. 1410-1421.

[80] Minematsu, T., Nakagami, G., Sari, Y., 2010, "Candidate Biomarkers for Deep Tissue Damage from Molecular Biological and Biochemical Aspects," Journal of Tissue Viability, **19**(2) pp. 77-83.

[81] Angelidis, I., Lidman, D., SjÃ¶berg, F., 2009, "Decubitus Ulcer Development: Pressure Alone Increases Tissue Temperature," **32**(5) pp. 241-244.

[82] Schubert, V., and Fagrell, B., 1991, "Evaluation of the Dynamic Cutaneous Post-Ischaemic Hyperaemia and Thermal Response in Elderly Subjects and in an Area at Risk for Pressure Sores," Clinical Physiology (Oxford, England), **11**(2) pp. 169-182.

[83] Sato, M., Sanada, H., Konya, C., 2006, "Prognosis of Stage I Pressure Ulcers and Related Factors," International Wound Journal, **3**(4) pp. 355-362.

[84] Goller, H., Lewis, D. W., and McLaughlin, R. E., 1971, "Thermographic Studies of Human Skin Subjected to Localized Pressure," The American Journal of Roentgenology, Radium Therapy, and Nuclear Medicine, **113**(4) pp. 749-754.

[85] Sprigle, S., Linden, M., McKenna, D., 2001, "Clinical Skin Temperature Measurement to Predict Incipient Pressure Ulcers," Advances in Skin & Wound Care, **14**(3) pp. 133-137.

[86] Mahanty, S. D., and Roemer, R. B., 1979, "Thermal Response of Skin to Application of Localized Pressure," Archives of Physical Medicine and Rehabilitation, **60**(12) pp. 584-590.

[87] Loerakker, S., Stekelenburg, A., Strijkers, G. J., 2010, "Temporal Effects of Mechanical Loading on Deformation-Induced Damage in Skeletal Muscle Tissue," Annals of Biomedical Engineering, **38**(8) pp. 2577-2587.

[88] Loerakker, S., Manders, E., Strijkers, G. J., 2011, "The Effects of Deformation, Ischemia, and Reperfusion on the Development of Muscle Damage during Prolonged Loading," Journal of Applied Physiology (Bethesda, Md.: 1985), **111**(4) pp. 1168-1177.

[89] Mak, A. F., Yu, Y., Kwan, L. P., 2011, "Deformation and Reperfusion Damages and their Accumulation in Subcutaneous Tissues during Loading and Unloading: A

Theoretical Modeling of Deep Tissue Injuries," Journal of Theoretical Biology, **289**pp. 65-73.

[90] Salcido, R., Lee, A., and Ahn, C., 2011, "Heel Pressure Ulcers: Purple Heel and Deep Tissue Injury," Advances in Skin & Wound Care, **24**(8) pp. 374-80; quiz 381-2.

[91] Cichowitz, A., Pan, W. R., and Ashton, M., 2009, "The Heel: Anatomy, Blood Supply, and the Pathophysiology of Pressure Ulcers," Annals of Plastic Surgery, **62**(4) pp. 423-429.

[92] Jennings, R. B., and Reimer, K. A., 1991, "The Cell Biology of Acute Myocardial Ischemia," Annual Review of Medicine, **42**pp. 225-246.

[93] Walker, P. M., 1991, "Ischemia/Reperfusion Injury in Skeletal Muscle," Annals of Vascular Surgery, **5**(4) pp. 399-402.

[94] Herrman, E. C., Knapp, C. F., Donofrio, J. C., 1999, "Skin Perfusion Responses to Surface Pressure-Induced Ischemia: Implication for the Developing Pressure Ulcer," Journal of Rehabilitation Research and Development, **36**(2) pp. 109-120.

[95] Pye, G., and Bowker, P., 1976, "Skin Temperature as an Indicator of Stress in Soft Tissue," Engineering in Medicine, **5**(3) pp. 58-60.

[96] Carden, D. L., and Granger, D. N., 2000, "Pathophysiology of Ischaemia-Reperfusion Injury," The Journal of Pathology, **190**(3) pp. 255-266.

[97] Eltzschig, H. K., and Collard, C. D., 2004, "Vascular Ischaemia and Reperfusion Injury," British Medical Bulletin, **70**pp. 71-86.

[98] Mayrovitz, H. N., and Smith, J., 1998, "Heel-Skin Microvascular Blood Perfusion Responses to Sustained Pressure Loading and Unloading," Microcirculation, **5**(2-3) pp. 227-233.

[99] Tsuji, S., Ichioka, S., Sekiya, N., 2005, "Analysis of Ischemia-Reperfusion Injury in a Microcirculatory Model of Pressure Ulcers," Wound Repair and Regeneration, **13**(2) pp. 209-215.

[100] Emery, A. F., and Sekins, K. M., 1982, "The use of Heat Transfer Principles in Designing Optimal Diathermy and Cancer Treatment Modalities," International Journal of Heat and Mass Transfer, **25**(6) pp. 823-834.

[101] Ruschkewitz, Y., and Gefen, A., 2010, "Cell-Level Temperature Distributions in Skeletal Muscle Post Spinal Cord Injury as Related to Deep Tissue Injury," Medical & Biological Engineering & Computing, **48**(2) pp. 113-122.

[102] Fukushima, H., Hashimoto, Y., Yoshiya, S., 2002, "Conduction Analysis of Cement Interface Temperature in Total Knee Arthroplasty," The Kobe Journal of Medical Sciences, **48**(1-2) pp. 63-72.

[103] Mital, M., and Pidaparti, R. M., 2008, "Breast Tumor Simulation and Parameters Estimation using Evolutionary Algorithms," Modelling and Simulation in Engineering, **2008**.

[104] Ozisik, N., and Orlande, H., 2000, "Inverse Heat Transfer: Fundamentals and Applications," CRC Press, pp. 3-195.

[105] Hatwar, R., 2015, "Personel Communication," .

[106] Holland, K. E., and Drolet, B. A., 2010, "Infantile Hemangioma," Pediatric Clinics of North America, **57**(5) pp. 1069-1083.

[107] Haggstrom, A. N., Drolet, B. A., Baselga, E., 2006, "Prospective Study of Infantile Hemangiomas: Clinical Characteristics Predicting Complications and Treatment," Pediatrics, **118**(3) pp. 882-887.

[108] Kilcline, C., and Frieden, I. J., 2008, "Infantile Hemangiomas: How Common are they? A Systematic Review of the Medical Literature," Pediatric Dermatology, **25**(2) pp. 168-173.

[109] Drolet, B. A., Esterly, N. B., and Frieden, I. J., 1999, "Hemangiomas in Children," N Engl J Med, **341**(3) pp. 173-181.

[110] Richter, G. T., and Friedman, A. B., 2012, "Hemangiomas and Vascular Malformations: Current Theory and Management," International Journal of Pediatrics, **2012**pp. 645678.

[111] Hemangioma Investigator Group, Haggstrom, A. N., Drolet, B. A., 2007, "Prospective Study of Infantile Hemangiomas: Demographic, Prenatal, and Perinatal Characteristics," The Journal of Pediatrics, **150**(3) pp. 291-294.

[112] Bhat, V., Salins, P. C., and Bhat, V., 2014, "Imaging Spectrum of Hemangioma and Vascular Malformations of the Head and Neck in Children and Adolescents," Journal of Clinical Imaging Science, **4**pp. 31-7514.135179. eCollection 2014.

[113] Storch, C. H., and Hoeger, P. H., 2010, "Propranolol for Infantile Haemangiomas: Insights into the Molecular Mechanisms of Action," The British Journal of Dermatology, **163**(2) pp. 269-274.

[114] Khan, I. S., Kiehna, E. N., Satti, K. F., 2014, "Surgical Management of Large Scalp Infantile Hemangiomas," Surgical Neurology International, **5**pp. 41-7806.129560. eCollection 2014.

[115] Drolet, B. A., Frommelt, P. C., Chamlin, S. L., 2013, "Initiation and use of Propranolol for Infantile Hemangioma: Report of a Consensus Conference," Pediatrics, **131**(1) pp. 128-140.

[116] Kutz, A. M., Aranibar, L., Lobos, N., 2015, "Color Doppler Ultrasound Follow-Up of Infantile Hemangiomas and Peripheral Vascularity in Patients Treated with Propranolol," Pediatric Dermatology, **32**(4) pp. 468-475.

[117] Desmons, F., Houdas, Y., Deffrenne, C., 1976, "Thermographic Study of Hemangiomas of Children," Angiology, **27**(9) pp. 494-501.

[118] Lindberg, R.M., 2016, "Diagnostic Pathology: Soft Tissue Tumors," Elsevier, Philadelphia, pp. 408-436.

[119] Hartley, R.I., and Zisserman, A., 2004, "Multiple View Geometry in Computer Vision," Cambridge University Press, ISBN: 0521540518, .

[120] Fairchild, D.M., 2013, "Color Appearance Models," Wiley, pp. 56-115.

[121] Robertson, A. R., 1977, "The CIE 1976 Color-Difference Formulae," Color Research & Application, **2**(1) pp. 7-11.

[122] Weatherall, I. L., and Coombs, B. D., 1992, "Skin Color Measurements in Terms of CIELAB Color Space Values," The Journal of Investigative Dermatology, **99**(4) pp. 468-473.

[123] Ford, A., and Roberts, A., 1998, "Colour Space Conversions," .

[124] Madooei, A., and Drew, S. M., 2013, "A Colour Palette for Automatic Detection of Blue-White Veil," Society for Imaging Science and Technology, .

[125] Ohta, Y., Kanade, T., and Sakai, T., 1980, "Color Information for Region Segmentation," Computer Graphics and Image Processing, **13**(3) pp. 222-241.

[126] Kim, S. C., Kim, D. W., Hong, J. P., 2000, "A Quantitative Evaluation of Pigmented Skin Lesions using the L*a*b* Color Coordinates," Yonsei Med J, **41**(3) pp. 333-339.

[127] Szychta, P., Al-Nakib, K., Anderson, W., 2013, "Quantitative Method for Evaluation of Aesthetic Results After Laser Treatment for Birthmarks," Lasers in Medical Science, **28**(6) pp. 1567-1572.

[128] Ahmad Fadzil, M. H., Ihtatho, D., Mohd Affandi, A., 2009, "Objective Assessment of Psoriasis Erythema for PASI Scoring," Journal of Medical Engineering & Technology, **33**(7) pp. 516-524.

[129] Nischik, M., and Forster, C., 1997, "Analysis of Skin Erythema using True-Color Images," IEEE Transactions on Medical Imaging, **16**(6) pp. 711-716.

[130] Centore, P., 2010, "The Munsell Toolbox. Code Available at Http://Www.99main.Com/~centore/ MunsellToolbox/MunsellToolbox.Html," **2010**.

[131] Tsang, M. W., Garzon, M. C., and Frieden, I. J., 2006, "How to Measure a Growing Hemangioma and Assess Response to Therapy," Pediatric Dermatology, **23**(2) pp. 187-190.

[132] Hogeling, M., Adams, S., and Wargon, O., 2011, "A Randomized Controlled Trial of Propranolol for Infantile Hemangiomas," Pediatrics, **128**(2) pp. e259-66.

[133] Léauté-Labrèze, C., de, l. R., Hubiche, T., 2008, "Propranolol for Severe Hemangiomas of Infancy," N Engl J Med, **358**(24) pp. 2649-2651.

[134] Laranjo, S., Costa, G., Parames, F., 2014, "The Role of Propranolol in the Treatment of Infantile Hemangioma," Revista Portuguesa De Cardiologia : Orgao Oficial Da Sociedade Portuguesa De Cardiologia = Portuguese Journal of Cardiology : An Official Journal of the Portuguese Society of Cardiology, **33**(5) pp. 289-295.

[135] Burrows, P. E., Laor, T., Paltiel, H., 1998, "Diagnostic Imaging in the Evaluation of Vascular Birthmarks," Dermatologic Clinics, **16**(3) pp. 455-488.

[136] Herman, C., 2013, "The Role of Dynamic Infrared Imaging in Melanoma Diagnosis," Expert Review of Dermatology, **8**(2) pp. 177-184.

[137] Burkes, S. A., Patel, M., Adams, D. M., 2016, "Infantile Hemangioma Status by Dynamic Infrared Thermography: A Preliminary Study," International Journal of Dermatology, .

[138] Miki, Y., 1975, "Thermographic Evaluations of Haemangiomas," The Australasian Journal of Dermatology, **16**(3) pp. 114-117.

[139] Cheng, T., 2015, "Improving Quantitative Infrared Imaging for Medical Diagnostic Applications," .

[140] You, X., 2014, "Quantitative Infrared Thermography for Infantile Hemangioma Assessment," .

[141] Incropera, F.P., DeWitt, D.P., Bergman, T.L., 2006, "Fundamentals of heat and mass transfer," Wiley, India, pp. 700-736.

[142] Steketee, J., 1973, "Spectral Emissivity of Skin and Pericardium," Physics in Medicine and Biology, **18**(5) pp. 686-694.

[143] Cetas, T. C., 1978, "Practical Thermometry with a Thermographic Camera-Calibration, Transmittance, and Emittance Measurements," The Review of Scientific Instruments, **49**(2) pp. 245.

[144] Hamrelius, T., 1991, "Accurate temperature measurement in thermography: an overview of relevant features, parameters, and definitions," Proceedings of SPIE - The International Society for Optical Engineering, Anonymous **1467,** pp. 448.

[145] Ibarra-Castanedo, C., González, D., Klein, M., 2004, "Infrared Image Processing and Data Analysis," Infrared Physics & Technology, **46**(1–2) pp. 75-83.

[146] Cheng, T., and Herman, C., 2014, "Motion Tracking in Infrared Imaging for Quantitative Medical Diagnostic Applications," Infrared Physics & Technology, **62**(0) pp. 70-80.

[147] Cetingul, M. P., Herman, C., and Alani, R. M., 2009, "Skin Imaging With Infrared Thermography and Confocal Microscopy," ASME 2009 Heat Transfer Summer Conference collocated with the InterPACK09 and 3rd Energy Sustainability Conferences, Anonymous **3,** pp. 731 - 739.

[148] Celenk, M., 1990, "A Color Clustering Technique for Image Segmentation," Computer Vision, Graphics, and Image Processing, **52**(2) pp. 145-170.

[149] Busam, K.J., 2014, "Dermatopathology: a volume in the series Foundations in Diagnostic Pathology," Elsevier, China, pp. 447-513.

[150] Gabay, S., Lucassen, G. W., Verkruysse, W., 1997, "Modelling the Assessment of Port Wine Stain Parameters from Skin Surface Temperature Following a Diagnostic Laser Pulse," Lasers in Surgery and Medicine, **20**(2) pp. 179-187.

[151] Puig, S., Casati, B., Staudenherz, A., 2005, "Vascular Low-Flow Malformations in Children: Current Concepts for Classification, Diagnosis and Therapy," European Journal of Radiology, **53**(1) pp. 35-45.

[152] Cox, J. A., Bartlett, E., and Lee, E. I., 2014, "Vascular Malformations: A Review," Seminars in Plastic Surgery, **28**(2) pp. 58-63.

[153] Troilius, A., Wardell, K., Bornmyr, S., 1992, "Evaluation of Port Wine Stain Perfusion by Laser Doppler Imaging and Thermography before and After Argon Laser Treatment," Acta Dermato-Venereologica, **72**(1) pp. 6-10.

[154] Huang, Y. C., Tran, N., Shumaker, P. R., 2009, "Blood Flow Dynamics After Laser Therapy of Port Wine Stain Birthmarks," Lasers in Surgery and Medicine, **41**(8) pp. 563-571.

Vita

Akanksha Bhargava received her Bachelor's degree in Mechanical and Energy Engineering in 2010 from Vellore Institute of Technology University (VITU), Vellore, India. After working as a research intern in the Department of Mechanical and Materials Engineering at Florida International University (FIU), Miami, FL; she moved to Baltimore, MD in 2010 to pursue her PhD in Mechanical Engineering at the Johns Hopkins University (JHU). In 2013, she received her Master's degree in Mechanical Engineering from JHU. She worked as a research intern at Constellation Energy, Baltimore, MD in 2014 and completed her PhD in 2016.